UAB
Universitat Autònoma de Barcelona

A 3D bioprinted hydrogel gut-on-chip model with integrated TEER sensing capabilities

Daniel Vera Ibáñez

Universitat Autònoma
de Barcelona
Tesi doctoral

A 3D bioprinted hydrogel gut-on-chip model with integrated TEER sensing capabilities

Daniel Vera Ibáñez

Directors:
Dr. María del Mar Álvarez Sánchez
Dr. Elena Martínez Fraiz

Tutor:
Dr. Francesc Serra Graells

Universitat Autònoma de Barcelona
Departament de Microelectrònica i Sistemes Electrònics
Programa de Doctorat en Enginyeria Electrònica i de Telecomunicació

Bellaterra (Barcelona), Setembre 2023

I certify that I have read the dissertation "*A 3D bioprinted hydrogel gut-on-chip model with integrated TEER sensing capabilities*" and that, in my opinion, it is fully adequate in scope and quality as a dissertation for the degree of Doctor of Philosophy.

Dr. María del Mar Álvarez Sánchez, Dr. Elena Martínez Fraiz and Dr. Francesc Serra Graells

Universitat Autònoma de Barcelona
Departamentd e Microelectrònica i Sistemes Electrònics
Programa de Doctorat en Enginyeria Electrònica i de Telecomunicació

This work was carried out at Institut de Microelectrònica de Barcelona- Centre Nacional de Microelectrònica (IMB-CNM CSIC) and Institute for Bioengineering of Catalonia (IBEC).

Acknowledgements

En primer lugar, me gustaría agradecer a mis directoras de tesis, Dr. Mar Álvarez y Dr. Elena Martínez, por haberme dado la oportunidad de hacer mi tesis doctoral. A pesar de todos los problemas relacionados con la pandemia, han continuado apoyándome y ayudándome durante todo mi proyecto. También me gustaría dar las gracias a la Dr. Rosa Villa por haberme permitido hacer mi investigación en su grupo.

También querría expresar mi gratitud con la gente con la que estado trabajando estos tres años. En especial a José, que me enseñó muchas de las cosas que me fueron útiles durante la tesis. También a Miguel, una de las personas con las que tuve la suerte de coincidir y que hicieron esta experiencia mucho más amena gracias a su buen humor y su alegría. También a Xavi y al resto de miembros del grupo GAB y del CNM, a los que deseo lo mejor en lo profesional. De mis compañeros del IBEC, querría agradecer a María y Núria su ayuda y contribución activa a este proyecto. Gracias a ellas, pude llevar a cabo gran parte de la tesis y sin ellas no hubiese sido posible. Gracias también a Angela, Vero, Oscar, Aina y Melika por el apoyo y el aprecio que tuvisteis durante los meses que estuve en el instituto.

Querría agradecer a mi familia, en especial a mi madre, todo el apoyo emocional que tuve durante estos tres años. Significó mucho para mí. Y también a Tammy, la mejor persona que pude descubrir durante estos años y con la que espero estar muchos más.

Abstract

During the last decade, organ-on-chips have become a promising alternative to conventional *in vitro* and animal-based *in vivo* models. By integrating microfluidics with cell culture, these systems can recreate key mechanical forces to which epithelial and endothelial barriers are exposed to in their dynamic cell microenvironment. Among the different tissue models developed in the field, gut-on-chips have been largely studied due to the key role of the small intestine in nutrient absorption and drug uptake. However, most of the currently proposed gut-on-chip devices only represent the intestinal epithelium, neglecting other important elements of the intestinal mucosa. As these models are based on stiff and flat semi-porous membranes, they are unable to recapitulate the compartmentalized structure of the barrier. The intestinal mucosa organizes as a multicellular and three-dimensional (3D) architecture, shaped in finger-like protrusions called villi and invaginations called crypts where stromal cells embedded in the extracellular matrix (ECM) interact with the epithelium to maintain their integrity and function. To reproduce these *in vivo*-like conditions, hydrogels have been proposed as suitable cell substrates, as they can support both barrier formation and cell embedding. Structured as porous networks of polymer chains able to absorb large amounts of fluids, they possess highly tunable mechanical and chemical properties that can be adjusted to match those of soft tissues while allowing the diffusion of oxygen and nutrients for cell culture. Also, recent adoption of microfabrication techniques has resulted in the generation of scaffolds that mimic key 3D topographical features of the intestinal tissue. Considering all these benefits, the combination of engineered 3D hydrogels and microfluidic technology could push the physiological relevance of gut-on-chips even further.

In this work, I present a novel gut-on-chip based on a biomimetic hydrogel channel that recapitulates the epithelial and stromal compartments. The hydrogel was fabricated with a visible-light 3D bioprinting technique to generate villi-like structures reproducing key spatial features of the intestinal epithelium. The hydrogel composition was a mix of poly(ethylene) glycol diacrylate (PEGDA), a synthetic polymer that provides mechanical stability to the scaffold, and gelatin methacryloyl (GelMA), a biocompatible natural hydrogel that enables cell encapsulation. Printing parameters were initially optimized to obtain lateral pillar structures that matched the physiological dimensions of intestinal villi. After this, the hydrogel channel was placed within a microfluidic chip for continuous perfusion. Using this configuration, the system can support the cell culture of hydrogel-embedded stromal cells for several days under flow. It was also proved that the gut-on-chip could support the co-culture of epithelial cells and their barrier formation for 2 weeks, mimicking the 3D compartmentalized architecture of the intestinal mucosa under *in vivo*-like dynamic conditions. As a step further, I successfully integrated electrodes within the 3D bioprinted gut-on-chip device for real time trans-epithelial electrical resistance (TEER) quantification. Using electrochemical impedance spectroscopy (EIS), the evolution and formation of the epithelial barrier was monitored during the experiment, demonstrating the capabilities of the 3D hydrogel gut-on-chip as a potential tool to finely assess barrier permeability changes for tissue modeling in healthy and pathophysiological conditions along with drug assessment studies.

Resumen

En la última década, los ´organ-on-chips´ se han convertido en una alternativa prometedora a los modelos *in vitro* convencionales y a los *in vivo* basados en animales. Mediante la integración de la microfluídica en los cultivos celulares, estos sistemas pueden recrear fuerzas mecánicas a las que las células epiteliales y endoteliales están expuestas en su microentorno celular dinámico. Entre los diferentes modelos de tejido desarrollados en este campo, los ´gut-on-chips´ han sido ampliamente estudiados debido al rol clave del intestino delgado en la absorción de nutrientes y fármacos. Sin embargo, muchos de los dispositivos de gut-on-chips actualmente propuestos solo representan el epitelio intestinal, obviando otros elementos importantes de la mucosa intestinal. Al estar basados en membranas semi porosas rígidas y planas, estos modelos son incapaces de reproducir la estructura compartimentalizada de la barrera. La mucosa intestinal se organiza con un arquitectura multicelular y tridimensional (3D), conformada por protrusiones en forma de dedos llamadas vellosidades, e invaginaciones denominadas criptas, en la cual las células estromales embebidas dentro de la matriz extracelular (ECM) interactúan con el epitelio para mantener su integridad y función. Con el fin de reproducir condiciones similares al *in vivo*, los hidrogeles han sido propuestos como sustratos celulares idóneos, ya que pueden dar soporte tanto a la formación de una barrera como a la incorporación de otras células. Estos materiales están estructurados como matrices porosas de cadenas poliméricas capaces de absorber grandes cantidades de fluidos. Poseen propiedades mecánicas y químicas adaptables que pueden ser ajustadas para que correspondan a las de los tejidos blandos, al igual que permiten la difusión de oxígeno y nutrientes para cultivos celulares. Además, la adopción reciente de técnicas de microfabricación ha permitido la generación de sustratos que replican aspectos topográficos 3D claves del tejido intestinal. Teniendo en cuenta todos estos beneficios, la combinación de los hidrogeles 3D con la tecnología microfluídica podría llevar la relevancia fisiológica de los `gut-on-chips´ aún más lejos.

En este trabajo, presento un nuevo `gut-on-chip´ basado en un canal de hidrogel biomimético que recapitula los compartimentos epiteliales y estromales. El hidrogel fue fabricado mediante una técnica de bioimpresión 3D con luz visible para generar estructuras con forma de vellosidades que reprodujesen elementos espaciales clave del epitelio intestinal. La composición del hidrogel fue una mezcla de polietilenglicol diacrilado (PEGDA), un polímero sintético que provee estabilidad mecánica al sustrato, y anhídrido metacrílico de gelatina (GelMA), un hidrogel natural biocompatible que permite la encapsulación de células. Los parámetros de impresión fueron inicialmente optimizados para obtener estructuras con pilares laterales que replicasen las dimensiones fisiológicas de las vellosidades intestinales. Tras esto, el canal de hidrogel fue colocado dentro de un chip microfluídico para perfusión continua. Utilizando esta configuración, se pudo comprobar que el sistema permite cultivar células estromales embebidas dentro del hidrogel durante varios días bajo flujo. También se demostró que el gut-on-chip permite el co-cultivo de células epiteliales y la formación de una barrera durante 2 semanas, imitando la arquitectura 3D compartimentalizada de la mucosa intestinal bajo condiciones dinámicas similares al *in vivo*. Dando un paso más allá, logré integrar electrodos dentro del `gut-on-chip´ 3D bioimprimido para la cuantificación de la resistencia eléctrica trans-epitelial (TEER) en tiempo real. Utilizando espectroscopía de impedancia electroquímica (EIS), la formación de una barrera epitelial pudo ser monitorizada

periódicamente durante el experimento, demostrando las capacidades de nuestro `gut-on-chip´ basado en un hidrogel 3D bioimprimido como potencial herramienta para evaluar cambios precisos de permeabilidad en modelos de tejidos en condiciones sanas y patofisiológicas al igual que estudios de evaluación de fármacos.

List of abbreviations

Ag/AgCl: silver/ silver chloride

Au: gold

BBB: blood brain barrier

CPE: constant phase element

CE: counter electrode

COP: cyclic olefin polymer

Caco-2: human epithelial colorectal adenocarcinoma cells

DLP: digital light projection

DMEM: Dulbecco's modified eagle medium

DAPI: 4',6-diamidino-2-phenylindole

ECM: extracellular matrix

EIS: electrochemical impedance spectroscopy

EDTA: ethylenediaminetetraacetic acid

FBS: fetal bovine serum

GelMA: gelatin methacryloyl

LAP: lithium (2,4,6-trimethylbenzoyl) phosphinate

PC: polycarbonate

Pt: platinum

PEDOT:PSS: poly(3.4-ethylenedioxythiophene):polystyrenesulfonate

PBS: phosphate buffer saline

PEG: poly(ethylene) glycol

PEGDA: poly(ethylene) glycol diacrylate

PSA: pressure-sensitive adhesive

PDMS: polydimethylsiloxane

PET: polyethylene terephthalate

P/S: penicilin/streptomycin

RE: reference electrode

SLA: stereolithography

TEER: trans-epithelial electrical resistance

TMSPMA: 3-(Trimethoxysilyl)propryl methacrylate

UV: ultraviolet

WE: working electrode

ZO-1: Zonula-Occludens-1

Table of Contents

List of Figures

List of Tables

Motivation

One of the major challenges of the pharmaceutical industry is the increasing cost of drug development due to the high failure rates of compound candidates. Animal models have been widely used as *in vivo* models for pre-clinical studies. But the lack of physiological resemblance with humans limits their predictive potential for drug screening applications. Also, ethical concerns related to *in vivo* testing have led to a progressive shift towards animal-free methods. In this context, standard *in vitro* models have been a gold standard in pre-clinical testing as they are inexpensive and easy to implement. In these models, epithelial or endothelial cells are cultured on flat substrates under static conditions for drug absorption and permeability assays. However, their oversimplified structure cannot recapitulate the complexity of the target tissue barrier. Thus, there is an increasing need to develop new advanced *in vitro* systems that can better mimic key aspects of the dynamic cell microenvironment of tissue barriers and improve the effectiveness in the drug research pipeline.

Recent adoption of microfabrication techniques within the bioengineering field has led to the development of new advanced microfluidic devices that support cell culture under perfusion, often referred as ´organ-on-chips´. These systems provide a more realistic microenvironment for the cells, as tissue barriers are often exposed to dynamic mechanical forces such as shear stress and hydrostatic pressures. Among the different models, several groups have focused in establishing gut-on-chips due to the critical function of the intestine in human homeostasis, regulating nutrient absorption while protecting against pathogens. These advanced *in vitro* gut models have successfully recapitulated key properties and function of intestinal tissues. However, conventional gut-on-chips only represent the epithelial compartment and do not include other important elements of the intestinal mucosa such as stromal cells. This is due to the configuration of these microfluidic devices, based on stiff and flat membranes that cannot support the complex architecture of the intestinal mucosa.

As a promising alternative, hydrogels have been introduced as cell substrates within microfluidic devices. These ECM-like scaffolds can support both the encapsulation of stromal cells and the formation of mature cell barriers, thus increasing the physiological relevance of the models. Current hydrogel gut-on-chips have successfully replicated key aspects of the intestinal mucosa, such as the 3D topography and the compartmentalized structure of the tissue. However, the proposed microfabrication techniques in these models have several drawbacks as they rely either on cumbersome procedures or expensive equipment, limiting their potential applications in the field. Thus, new technologies that comprise both easy and affordable microfabrication techniques are required to develop the next hydrogel gut-on-chips.

In addition, cell barrier characterization in these microfluidic devices mostly relies on permeability and immunostaining assays, which cannot provide fast readouts about the state of the tissue monolayer during its formation. To solve these limitations, several groups have successfully integrated electrodes within organ-on-chips to perform trans-epithelial electrical resistance (TEER) measurements, a non-invasive technique that correlates the electrical properties of the tissue barrier with their integrity and tightness. By placing them close to the cell culture area, fast and accurate readouts of the electrical impedance of the cell monolayers can be obtained in real time to monitor their development and function under dynamic conditions. This approach has only been implemented for membrane-based microfluidic chips and, to this day, no 3D hydrogel organ-on-chips have been developed to integrate electrodes for real time TEER quantification.

The thesis is divided in five chapters:

- In the first chapter, we provide general knowledge about engineered tissue barrier models. A review of the different microfabrication techniques that have been used to establish hydrogel organ-on-chips is presented. Examples of tissue barrier models based on hydrogel microfluidic systems are also described here, with a special focus on gut models.

- For the second chapter, we give a general overview on the principles of electrical monitoring of cell barriers within organs-on-chips. The different strategies adopted in the field are reviewed, along with examples of devices with TEER sensors for gut-on-chip models.

- The third chapter focuses on the optimization of the bioprinting parameters that has been performed to generate hydrogel channels with lateral villi-like structures. We also discuss the assembly process of the hydrogel microfluidic device and the experimental validation of the system to support long-term perfusion for dynamic cell culture.

- In the fourth chapter, a 3D gut-on-chip model based on the bioprinted hydrogel channel is presented. In this model, stromal cells are embedded in the scaffold while epithelial cells are grown on top to form a full barrier and to recapitulate the compartmentalization of the intestinal mucosa. Through different types of assays, the properties and function of the formed epithelial barrier are assessed.

- Finally, the fifth chapter presents a new version of the 3D bioprinted hydrogel gut-on-chip with integrated electrodes. The fabrication and characterization of the electrodes is described, and the device is experimentally validated to perform real time TEER monitoring of the forming epithelial barrier inside the hydrogel channel.

1. Engineering *in vitro* tissue barrier models

1.1. *In vitro* models of tissue barriers

1.1.1. Physiology of epithelial and endothelial cell barriers

Cell barriers are key elements to maintain the homeostasis of the human body [1]. Delimiting the boundaries between tissue compartments, both epithelia and endothelia have major roles in supporting organ development and function. They ensure the transport of nutrients and oxygen, while regulating ion and solute concentrations, and preventing pathogenic infections as a first line of defense in the immune system. At the organ level, these barriers fulfil different tasks. Endothelial cells form the vascular networks of the circulatory system, and, in the case of the blood-brain barrier (BBB), they tightly regulate the crossing of solutes to avoid potential damage to the central nervous system. Epithelial barriers are also essential in other organ functions, such as in the gut, where they absorb nutrients, or in the kidney, where solutes are filtered and reabsorbed. Deregulation of cell barrier function has been linked to numerous diseases such as Crohn's disease [2] for the gastrointestinal tract and liver fibrosis for the liver sinusoidal endothelium [3].

Endothelial and epithelial cells form tight barriers by strongly attaching to each other via junctional protein complexes [4]. These protein junctions are generally classified in three groups, with different variations depending on the cell line: tight junctions, adherens junctions and desmosomes (Figure 1.1). Tight junctions have a major role in the control of the cell barrier integrity by sealing the interspace between adjacent cells [5]. They are mainly composed of claudin and occludin proteins that communicate with each other to regulate the transport through the barrier. Adherens junctions are also involved in cell-cell adhesion by forming cadherin-catenin complexes that ensure barrier tightness [6]. Desmosomes are located in the basal compartment of cells, and they are mostly formed by intracellular proteins that provide anchorage to filaments and mechanical stability to the tissue.

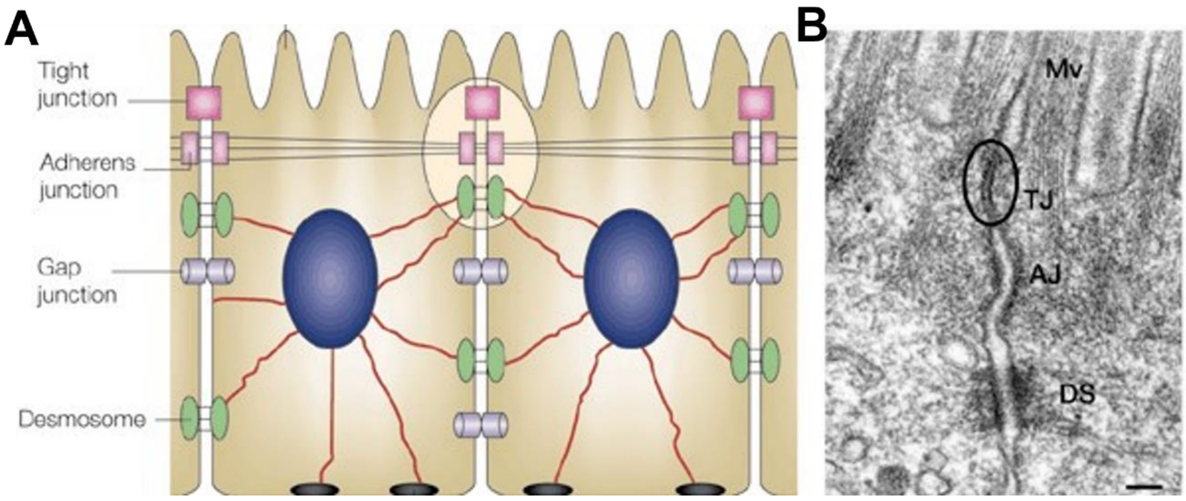

Figure 1.1: *Structure of cell-to-cell junctions. (A) Schematic of the protein junctional complex of two adjacent cells of a cell barrier. (B) Electron micrograph of the junctional complex in mouse intestinal epithelial cells (Mv: microvilli; TJ: tight junction; AJ: adherens junction; DS: desmosome). Scale bar: 200 µm. Adapted with permission from Nature Reviews Molecular Cell Biology, 2001 [5].*

The permeability of the cell barrier is dynamically regulated by the external microenvironment of the tissue, where different biochemical stimuli can trigger specific responses to the paracellular (between the cells) and transcellular (through the cells) transport of solutes via cellular signaling pathways [7]. Among them, cell-to-cell communication is a crucial interaction to sustain tissue homeostasis. These interactions are based on the release of chemical signals in the form of proteins or metabolites secreted by cells that can be detected by their neighbors. Cell-to-cell signaling is generally classified in four main categories, depending on the distance between the sender and the receiver: endocrine signaling, where signals travel through long distances; paracrine signaling, where cells communicate locally through chemical messengers; autocrine signaling, where cells release signals that are picked up by themselves; and direct cell contact, where adjacent cells physically interact via protein junctions (Figure 1.2). The complexity of certain tissues requires multicellular interactions to support tissue barrier function, such as in the gut, where mesenchymal cells of the lamina propria play a critical role in epithelial barrier permeability [8], or in the BBB, where pericytes control vascular development and blood flow [9].

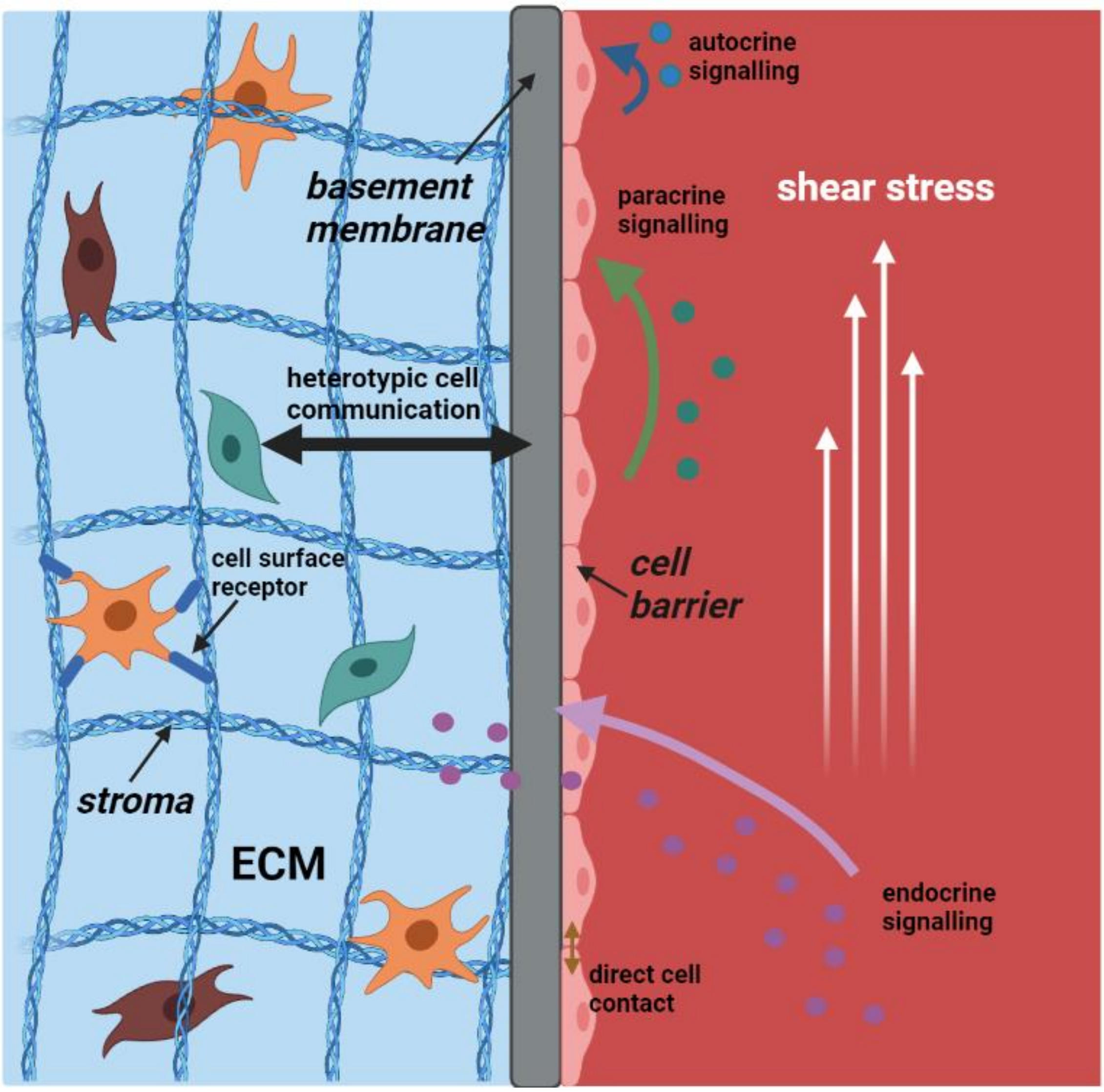

Figure 1.2: *Biochemical and physical stimuli of the cell barrier microenvironment. Schematic representation of biochemical and physical stimuli in the microenvironment of cell barriers, including cell-to-cell signaling, cell-ECM interactions, and flow-induced shear stress.*

The ECM also plays a relevant role in the regulation of the tissue barrier state. This three-dimensional network of proteins and polysaccharides is produced and modified by cells, providing physical support to tissues in the body [10]. Cell barriers are located on top of the basement membrane, a specific thin ECM sheet that dictates cell polarization, the biological process by which a cell organizes spatially to adopt a specific structure and function, and the sealing of intercellular spaces via cell adhesion motifs [11]. Below the basement membrane, the stroma is formed of an ECM that gives structural and mechanical stability to many different types of cells such as immune cells, blood vessels, fibroblasts and other mesenchymal cells [12]. While having a defined spatial architecture, the ECM is also under constant dynamic remodeling conditions in contact with surrounding cells. Cell-ECM interactions are mediated via cell surface receptors that trigger various intracellular cellular pathways. Through these interactions, the ECM acts as a key regulator of many cell functions such as growth, migration, and differentiation. Moreover, cells can sense the stiffness and morphology of the ECM through specific integrin-based cell surface adhesion complexes (Figure 1.2). For example, 3D topographical features in the intestinal ECM have been reported to play a crucial role in stem cell differentiation within the crypts [13].

Tissue barriers are also exposed to external physical stimuli when interfacing flowing fluids. Epithelial and endothelial cells are subjected to fluid shear stress, a tangential mechanical force generated by fluid flow, and hydrostatic pressure (Figure 1.2). In the vasculature, the effect of constant shear stress on endothelial cells induces cell alignment and proliferation, while it also regulates vascular permeability [14]. On the opposite side, it can also lead to the progression of physiological diseases, as it happens during atherosclerosis, where some arterial regions are exposed to lower shear stress levels [15]. In epithelial barriers, fluid flow can also have an important role in barrier function. For instance, peristaltic flow can have a significant impact on bacterial growth, affecting the composition of the gut microbiota [16].

1.1.2. Conventional in vitro models of cell barriers

Conventional *in vitro* models of cell barriers rely on commercial cell culture inserts, often referred to as Transwell®. These Transwell® cups are compatible with different types of well plates and they can be used for cell culture in static conditions (Figure 1.3 A). They have a porous plastic membrane attached at the bottom that is often coated with ECM proteins such as collagen or laminin to facilitate cell attachment. These membranes have pore sizes ranging from 0.1 µm to 10 µm and they are generally made of polyethylene terephthalate (PET), polycarbonate (PC) or polytetrafluoroethylene (PTFE). They also provide a separation between the apical and the basolateral compartment within the well (Figure 1.3 B). This configuration better recreates the *in vivo* microenvironment of the cell barrier than standard cell culture dishes, as it allows nutrient uptake and solute secretion from its basolateral side, which promotes cell polarization.

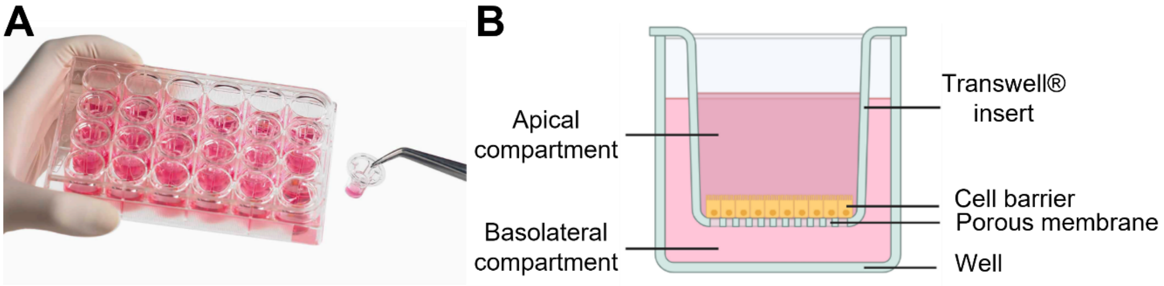

Figure 1.3: *Transwell® cell culture inserts. (A) Image of Transwell® cell culture inserts. (B) Schematic of an in vitro Transwell®-based model of a cell barrier.*

Another advantage of these systems is the possibility to perform permeability assays to characterize the properties of a cell barrier by using fluorescent labels [17]. In these assays, a tracer, such as a fluorescent dye, is loaded in the apical compartment and its concentration in the basolateral compartment is monitored over time (Figure 1.4). The diffusion across the cell barrier can thus be quantified and compared under different cell culture conditions. Also, some fluorescent dyes, such as dextrans, have different molecular weights that can be used to characterize the tightness of the cell barrier by assessing the size selectivity of the tight junctions. This approach is applied in pharmaceutical research to determine the drug permeability of certain cell barriers such as the gut [18,19].

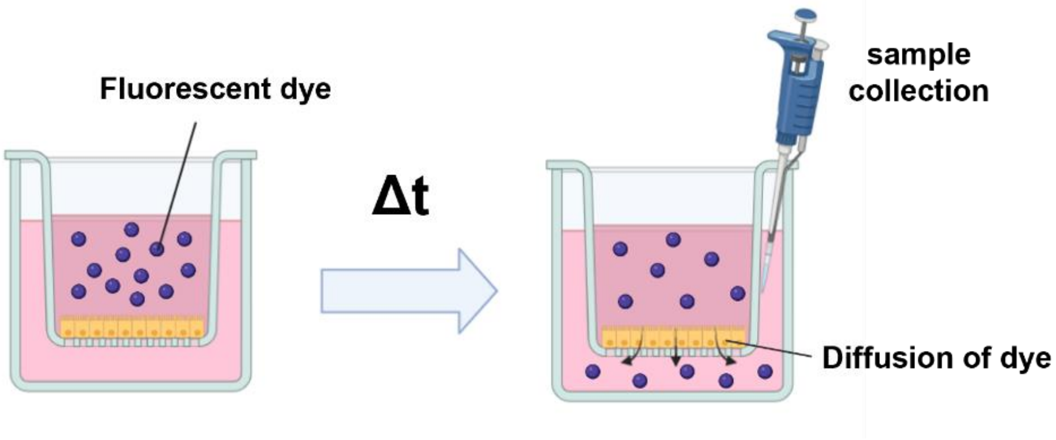

Figure 1.4: *Schematic of a permeability assay in a Transwell® insert.*

Due to its simplicity and easy handling, several cell barrier models have been established on culture inserts. For example, conventional *in vitro* models of the gut have been mostly based on Transwells®. Early intestinal models used epithelial cells to perform permeability studies [20]. Later, they became more complex by co-culturing other relevant cell lines, such as immune cells on the opposite side of the membrane or the bottom of the well [21]. By adding these cells, heterotypic cell interactions could be recapitulated *in vitro* and their effect on the barrier tightness could be observed. Other examples of co-culture on Transwell® inserts were done for the BBB [22], the alveolar epithelium [23], and the renal tubule [24].

However, despite being a gold standard to study cell barrier properties and perform drug screening studies *in vitro*, Transwell® systems have major limitations to mimic *in vivo*-like environments, resulting in poor predictive capabilities [25]. Their thickness, generally around 10 µm, prevents direct cell contact interactions between cells seeded on different compartments of the insert. Thus, cell-to-cell signaling is physically limited. Also, as the substrates are flat plastic membranes, they cannot reproduce the topographical features nor the mechanical properties of the *in vivo* ECM [26]. Finally, Transwell®-based models are established in static conditions. Thus, endothelial and epithelial cells are not exposed to the shear stress forces from fluid flows, lacking key dynamic stimuli for cell alignment and barrier permeability.

1.1.3. Organ-on-chip models

During this last decade, organ-on-chips have emerged as a promising alternative to overcome the limitations of static *in vitro* models [27,28]. These microdevices combine cell culture and microfluidics, allowing spatiotemporal control of media perfusion within the channels or chambers where cells are grown (Figure 1.5). As these systems are highly versatile, fluid rates can be finely adjusted to recapitulate physiological values of shear stress and hydrostatic pressure found in the *in vivo* cell barrier microenvironment. Another functionality of organ-on-chip platforms is the generation of biochemical gradients that can better mimic spatial concentrations of oxygen, nutrients, and solutes for specific tissues [29].

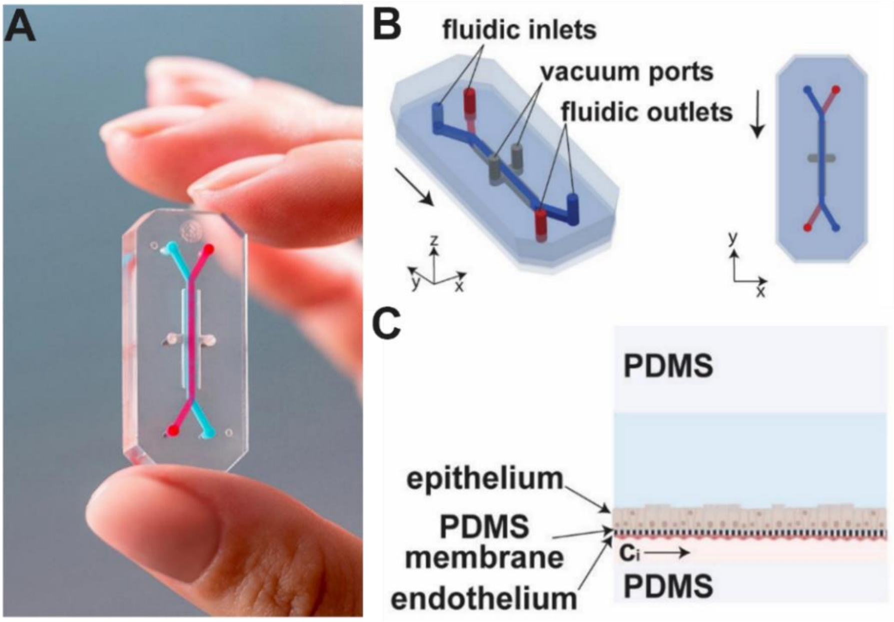

Figure 1.5: *Working principle of organ-on-chips. (A) Image of a PDMS-based organ-on-chip device (Emulate Inc.). (B) Schematic of the Emulate device with vacuum ports and two microfluidic channels. (C) Schematic of the epithelial/endothelial cell co-culture in the device. Adapted with permission from the Royal Society of Chemistry, 2021* [30].

The first organ-on-chip model reported in the literature was a lung alveolar-capillary barrier [31]. In this publication, a microfluidic platform was built, with an upper and bottom channel interfaced by a porous poly(dimethylsiloxane) (PDMS) membrane. On each side of the membrane, alveolar epithelial cells and pulmonary microvascular endothelial cells were seeded and cultured. During the experiment, endothelial cells were exposed to the shear forces of the media flow, while the epithelial compartment was filled with air. Two adjacent hollow compartments were connected to a vacuum system to generate a cyclic stretch on the membrane that mimicked breathing movements (Figure 1.6 A). This mechanical strain enhanced both epithelial and endothelial uptake of nanoparticles, stimulating their transport to the vascular compartment and better mimicking their physiological absorption in animal models. Several other organ-on-chip models have been established following this architecture with porous plastic membranes, such as liver-on-chips [32], kidney-on-chips [33] and BBB-on-chips [34]. A gut-on-chip was also established. In this case, intestinal epithelial Caco-2 cells were grown under fluid flow and peristaltic stimulation by cyclically stretching the membrane [35]. In these conditions, the cells formed 3D villi protrusions that recreated the *in vivo* intestinal epithelium. Also, they could differentiate into four different types of cells present in the intestinal barrier, while also showing an enhanced absorptive efficiency and drug metabolizing activity (Figure 1.6 B).

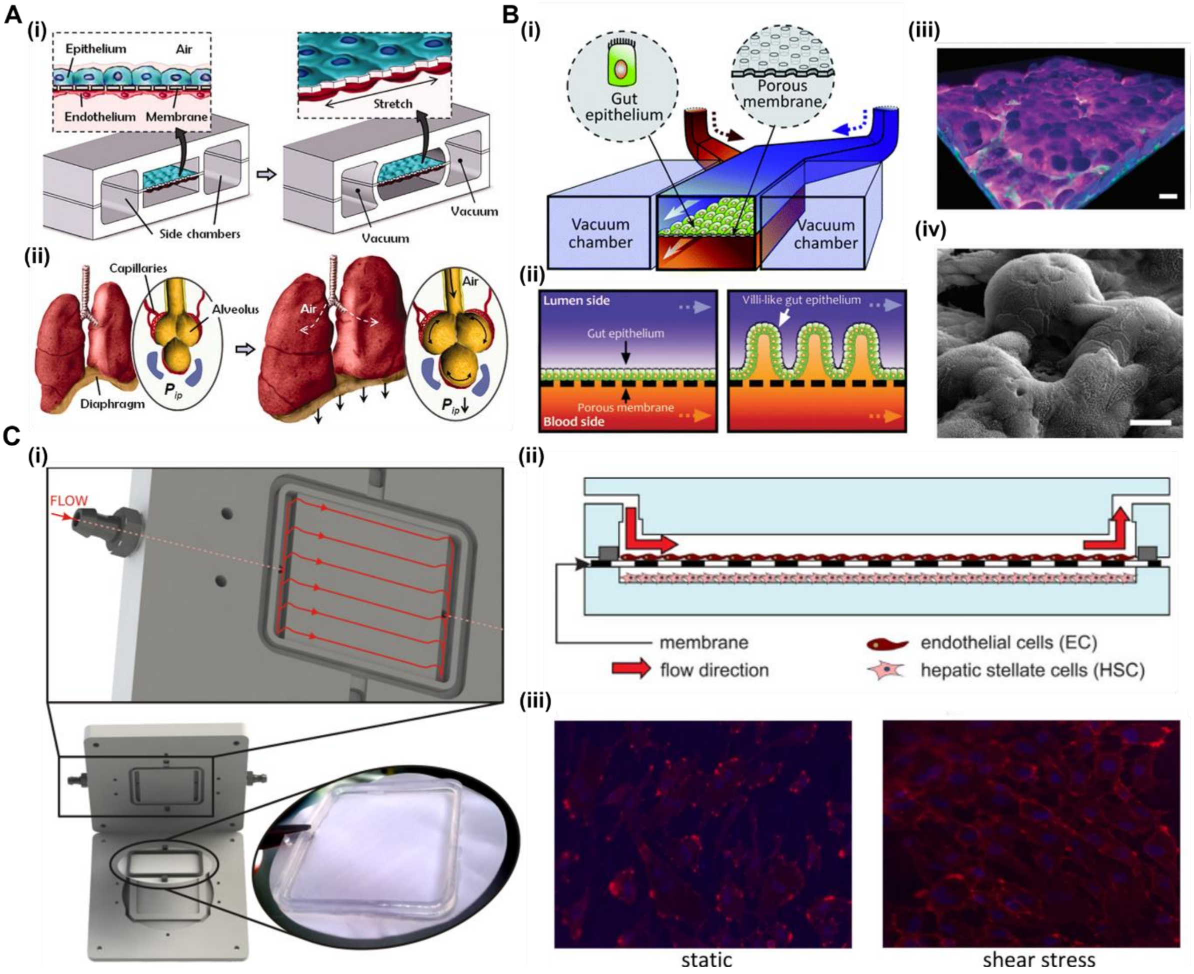

Figure 1.6: *Examples of membrane-based organ-on-chips. (A) Lung alveolar-capillary barrier model. (i) Schematic of the device with two microchannels interfaced by a PDMS membrane with lateral vacuum channels for stretching. (ii) Schematic of the mechanical stretching of the lung alveoli during breathing mimicked by the device. Adapted with permission from AAAS, 2010* [31]*. (B) Gut-on-chip model. (i) Schematic of the PDMS chip where intestinal Caco-2 cells are grown. (ii) Effect of the fluid flow on the villus formation of the intestinal barrier on-chip. (iii) 3D confocal reconstruction and (iv) SEM images of the Caco-2 villi. Samples were stained for nuclei (blue), F-actin (green), and mucin 2 (magenta). Scale bar: 25 µm. Adapted with permission from the Royal Society of Chemistry, 2013* [35]*. (C) Organ-on-chip model of the hepatic sinusoid. (i) Schematic of the plastic bioreactor with lateral connectors on the sides and the custom membrane. Red arrows represent the flow paths. (ii) Cross-section of the mounted bioreactor with the endothelial cells on top of the membrane and the hepatic cells on the lower plate. (iii) Imaging of the endothelial cells cultured under static conditions (left) and under continuous perfusion inside the bioreactor (right). Alpha-smooth muscle actin (α-SMA) is stained in red and nuclei, in blue. Adapted with permission from PLOS, 2014* [36]*.*

However, an important limitation of PDMS as a substrate for organ-on-chips is its ability to absorb small hydrophobic molecules, hindering potential applications in drug permeability and absorption studies [37,38]. Alternatively, thermoplastics such as (PMMA), polycarbonate (PC) and cyclic olefin polymer (COP) have been proposed as suitable materials for microfluidic platforms as they are inexpensive, biocompatible, optically transparent, and resistant to solvents [39]. Using rapid prototyping techniques, microchannels can be easily fabricated for cell culture in organ-on-chip applications. For example, a model of the hepatic sinusoid was established in a modular bioreactor made of PMMA [36]. The plastic plates were fabricated by computer numerical control (CNC) machining to include inlet connections and a central chamber where a microporous membrane was allocated. Endothelial cells and hepatic stellate cells were co-cultured under continuous perfusion, resulting in the formation of a confluent endothelial monolayer and an improved phenotype of the hepatic cells (Figure 1.6 C).

Despite being a clear step forward in the field, conventional membrane-based organ-on-chips employ hard and non-permeable materials that limit their relevance as *in vitro* models of tissue barriers. When cultured on the polymeric membrane of the device, cells lack the proper cell-ECM interactions, essential for tissue formation and remodeling [40]. Also, as for Transwell® models, key 3D topographical features of the modeled organs or tissues are also missing for these organ-on-chip platforms [41]. So, the compartmentalized structure of the tissue cannot be reproduced for *in vitro* studies.

1.2. Hydrogel-based *in vitro* models

Hydrogels have been intensively studied as excellent candidates to act as ECM surrogates in tissue engineering for *in vitro* and *in vivo* applications [42]. They are three-dimensional (3D) networks of polymer chains able to absorb large amounts of fluids. They possess highly tunable mechanical and chemical properties that can be adjusted to match those of soft tissues [43]. In addition, their porous nature enables the embedding of cells, as oxygen and nutrients can easily diffuse through their structure [44]. As these scaffolds can also support the formation of cell monolayers on top, researchers can establish 3D multicellular *in vitro* models of tissue barriers. An overview on hydrogels used for cell culture applications and specific examples of hydrogel-based *in vitro* models of cell barriers is addressed in this section.

1.2.1. Types of hydrogels

Depending on their source and combination, hydrogels can be classified in three main groups: natural, synthetic and hybrid hydrogels. Natural hydrogels are derived from macromolecules found in the native tissue ECMs, mostly polysaccharides and proteins [45]. Because of their origin, they are inherently biocompatible and bioactive, thus suitable for cell culture applications. They can contain cell binding sequences such as arginine-glycine-aspartate (RGD) peptides, that allow for cell adhesion and can also contain cell-degradable motifs[44]. Because of these properties, they support cell encapsulation and promote the remodeling of the cell microenvironment via matrix metalloproteinases (MMPs). However, degradation might also limit long-term cell culture applications as it compromises the mechanical stability of the scaffold. Among the different types of natural hydrogels, collagen and Matrigel are the most used proteins in cell culture applications (Figure 1.7 A). Collagen is the primary component in the ECM, being type I the most abundant in tissues. Its ubiquity and commercial availability make it a suitable biomaterial for cell culture models [46]. Matrigel is a basement membrane-derived protein mixture containing laminin, collagen type IV, entactin and other constituents. It is used as an ECM substitute for cell growth and migration but due to its non-defined composition, there is a significant batch-to-batch variability and experimental uncertainty [47]. Gelatin, an amorphous form of collagen, is also a common hydrogel material in tissue engineering applications (Figure 1.7 A). It is produced from the hydrolysis and denaturation process of collagen, which still preserves its biocompatibility and biodegradability properties. However, due to its thermal instability at 37ºC, gelatin is chemically modified with methacrylic anhydride to form GelMA, obtaining stable structures at body temperature [48]. Moreover, polysaccharides such as hyaluronic acid [49], agarose [50] and alginate [51] have also been adapted as scaffolds for cell culture models (Figure 1.7 B).

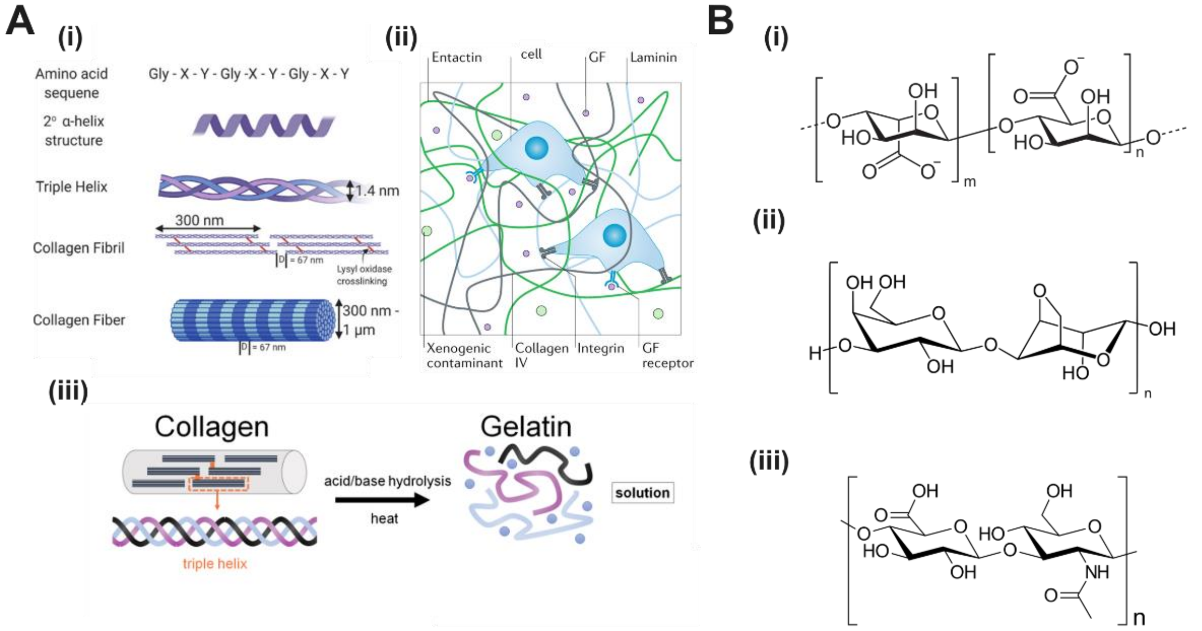

Figure 1.7: *Natural hydrogels for cell culture. (A) Structure and composition of protein-based natural hydrogels. (i) Structure of collagen, from the amino acid sequence to the collagen fiber. Adapted with permission from MDPI 2020 [54]. (ii) Main components of Matrigel. Adapted with permission from Nature Reviews Materials 2020 [52]. (iii) Fabrication process of gelatin from the hydrolysis and denaturation of collagen. (B) Chemical composition of polysaccharides used for hydrogel-based models: (i) alginate (ii) agarose and (iii) hyaluronic acid.*

While the physicochemical properties of natural hydrogels are not easy to tune, hydrogels derived from synthetic polymers can be easily customized in terms of mechanical and structural properties for long-term cell culture [53]. They are inherently inert, biocompatible and have low biodegradability properties. But they do not promote cell adhesion, so they are usually functionalized to include RGD cell adhesion motifs or ECM adhesion proteins such as fibronectin, collagen, or laminin (Figure 1.8 A). They can also be a reservoir of other biomolecules like growth factors or contain MMP-cleavable peptide sequences to make them biodegradable in cell culture (Figure 1.8 A) [54]. These incorporated properties have allowed them to be suitable scaffolds for cell-culture applications [55]. The most popular synthetic hydrogels are poly(2-hydroxyethyl methacrylate) (pHEMA), poly acrylate (PAA) and poly (ethylene glycol) (PEG) [56,57]. PEG is the most used synthetic polymer in bioengineering studies

(Figure 1.8 B) [58]. It is commercially available with different molecular weights and chemical compositions for cell adhesion and biodegradability. It is also hydrophilic, non-cytotoxic and has low protein adsorption. To polymerize PEG-based hydrogels, functional groups such as acrylate or ester groups are added for chemical cross-linking. The most common example of this is PEGDA, which has been used in numerous *in vitro* models (Figure 1.8 B) [59].

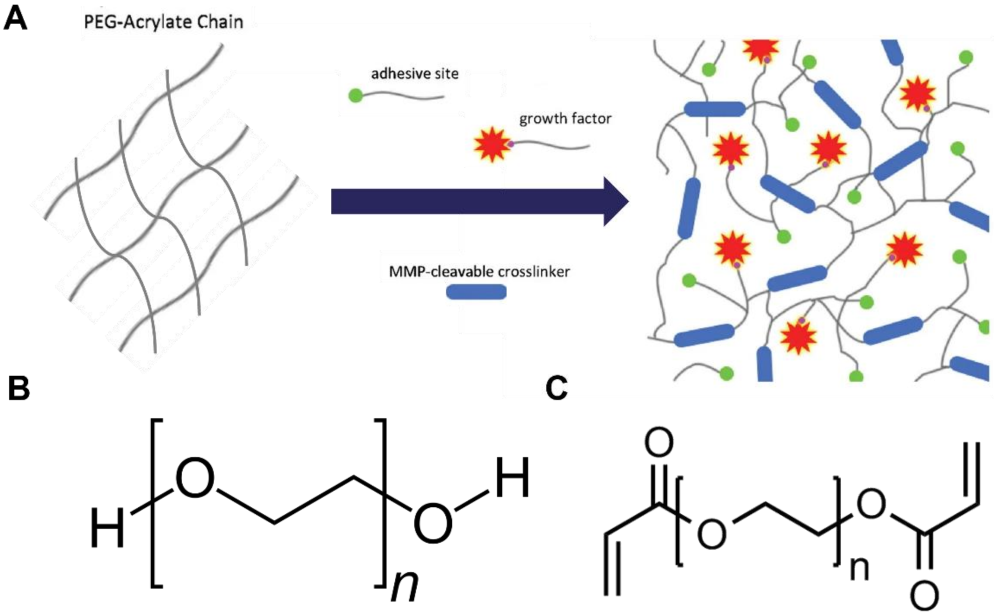

Figure 1.8: *Synthetic hydrogels for cell culture. (A) Schematic of the functionalization of PEG-acrylate polymers with cell adhesion ligands, growth factors and MMP-cleavable cross-linkers as bioactive sites for cell culture. Adapted with permission from PNAS, 2009 [60]. (B) Chemical composition of PEG and (C) PEGDA.*

To take advantage of the benefits of both natural and synthetic polymers while overcoming their drawbacks, hybrid blends have been proposed [61]. These hydrogels have bioactive sites and can support cell encapsulation while also demonstrating improved long-term mechanical stability. These properties can be finely tuned by changing the total polymer concentration and the ratio between synthetic and natural hydrogel polymers. Depending on the nature of the polymeric chains and the cross-linking method employed, co-networks, fully or semi-interpenetrating polymer networks can be obtained [42]. Among the possible combinations, co-polymerizing PEGDA and GelMA has become a popular strategy when addressing the fabrication of tissue barrier models [62] and tissue remodeling scaffolds [63].

1.2.2. Cross-linking methods

Polymer chain cross-linking reactions allow the formation of insoluble solid hydrogel networks from pre-polymer solutions. Depending on the chemistry of the polymers, different cross-linking strategies, which can be reversible or irreversible, can be employed to generate hydrogels. The choice on this strategy can yield different results on the control of the reaction and the mechanical properties of the scaffold [43,64].

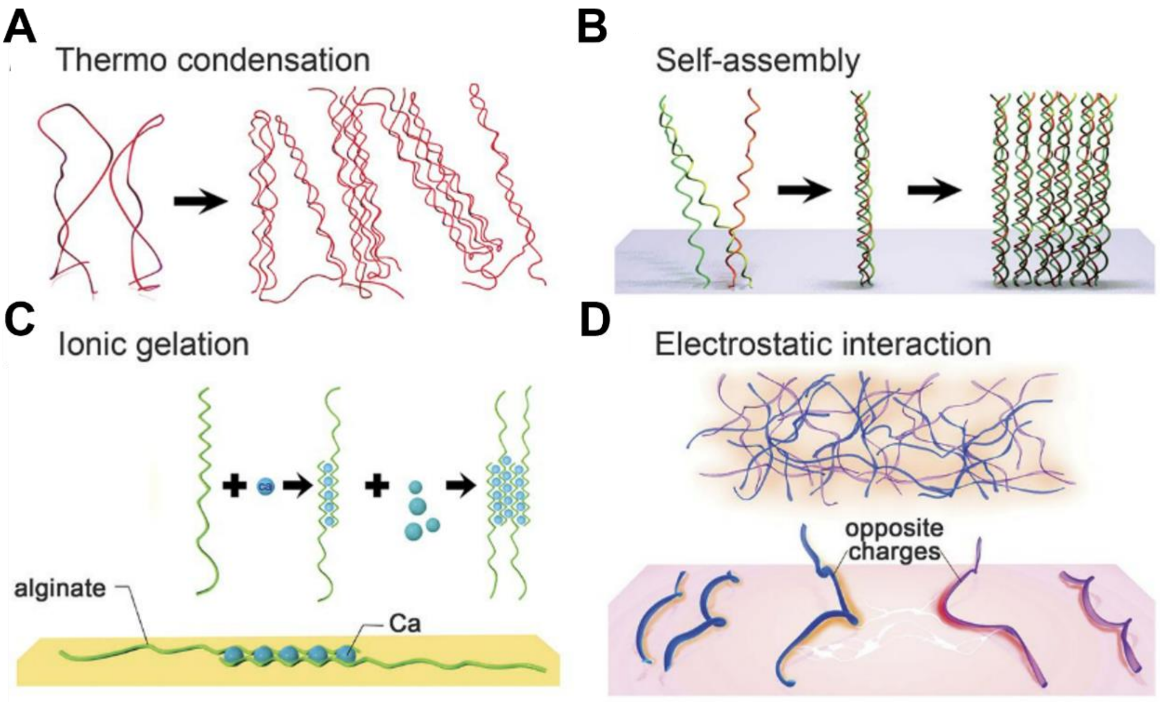

Figure 1.9: *Physical cross-linking methods of hydrogels. (A) Thermally induced gelation. (B) Self-assembly via hydrophobic interactions or hydrogen bonding. (C) Ionic and (D) electrostatic interactions. Adapted with permission from AAAS, 2017* [67].

Physically cross-linked hydrogels are obtained from the reversible binding of the polymer chains by molecular entanglements, hydrogen bonding, electrostatic or ionic interactions (Figure 1.9) [65]. Most natural polymers have residues that allow for cross-linking reactions based on electrostatic interactions. For example, collagen contains charged functional groups that enable the self-assembly formation of fibrils via thermal gelation at 37ºC [66]. On the other hand, alginate cross-linking is ensured by ionic interactions with bivalent cations such as Ca^{2+} and Mg^{2+} [67]. Physical gelation is usually highly compatible with cell embedding, but it is strongly affected by external conditions such as the pH and the temperature which, along with the polymer concentration, modulate the network structure and mechanical properties of the hydrogels. While physical cross-linking approaches are technologically simple to implement, the obtained structures are typically very soft and prone to degrade. Therefore, their mechanical integrity represents a challenge to build self-standing structures.

Unlike physical cross-linking, chemical cross-linking consists in the permanent and irreversible covalent bonding of polymers to generate hydrogels [65]. This type of cross-linking results in more mechanically stable structures over time than physical gelation techniques. However, the cross-linking reaction requires the chemical functionalization of the polymeric chain, which can be controlled by the adding of a cross-linking agent. Chemically cross-linked hydrogels can be obtained via enzyme-catalyzed reaction, click chemistry or photopolymerization. Enzyme-based cross-linking is a cell-compatible strategy that consists in the attachment of the enzyme to the polymer that catalyzes the binding of the polymeric chains (Figure 1.10 A) [68]. Some examples of enzymes used for hydrogel cross-linking are transglutaminases, peroxidases, and transferases. Transglutaminases have been used to cross-link gelatin hydrogels for cell culture models [69]. Fibrin, a natural hydrogel, has also been reported to be polymerized via thrombin-mediated reaction [70]. However, despite the benefits of the rapid gelation process for cell culture applications, there is no control on the reaction kinetics, as it starts immediately once the enzyme is added to the mixture. Cell-enzyme interactions can also interfere with the reaction, adding more uncertainty over the resulting hydrogel structure. Moreover, click chemistry-based cross-linking consists in a highly selective and fast reaction between two functional groups present in the polymeric chains (Figure 1.10 B). Some examples are thiol-ene and azyde-alkyne reactions [71]. However, while the reaction has a high-selectivity and does not require external compounds to initiate it, click chemistry cross-linking cannot be easily controlled as the functional groups on the polymeric chains spontaneously react with each other.

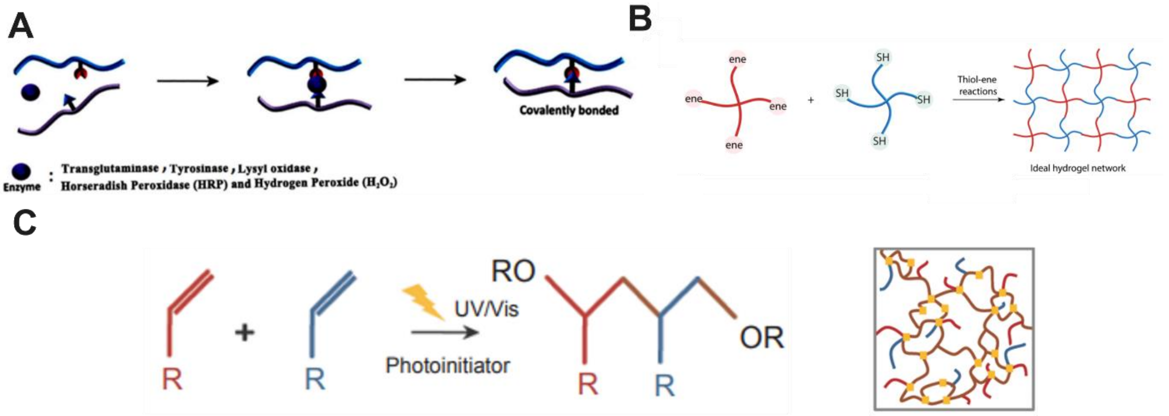

Figure 1.10: *Chemical cross-linking methods of hydrogels. (A) Schematic of enzyme-catalyzed reaction. Adapted with permission from International Journal of Biological Macromolecules, 2019* [75]*. (B) Schematic and chemical representation of a thiol-ene click reaction. Adapted with permission from American Chemical Society, 2018* [72]*. (C) Representation of a free radical photopolymerization and the resulting mesh. Adapted with permission from Elsevier, 2015* [73]*.*

Polymerization triggered by easily controlled external stimuli such as light has been proposed as another method for chemical cross-linking of hydrogels (Figure 1.10 C) [74]. Among the different available approaches, free radical photopolymerization is a well-known and common method to obtain hydrogels from photosensitive polymers, as the reaction can be finely controlled without harming embedded cells during the process [75]. A photosensitive molecule, referred to as radical photoinitiator, is initially mixed with a pre-polymer solution. Upon light exposure, the photoinitiator is activated, decomposing into free radicals. These radicals react with the monomer chains that contain specific chemical groups, creating monomers with free radicals. The new radical monomers attach to the polymeric chains, inducing chain growth propagation. This propagation step continues until there are no free monomers left, and the reaction terminates. Photoinitiators are generally classified in two types. Type I photoinitiators, like 1-[4-(2-Hydroxyethoxy)-phenyl]-2-hydroxy-2-methyl-1-propane-1-one (Irgacure 2959) and Lithium phenyl (2,4,6-trimethylbenzoyl) phosphinate (LAP), absorb photons and decompose into two free radicals. Type II photoinitiators, such as Eosin Y and riboflavin, need a co-initiator to produce radicals and start the photopolymerization. UV or visible light is employed depending on the absorption spectrum of the photoinitiator. Visible light is preferred for cell-laden hydrogels to avoid potential phototoxic effects [76]. In addition, the choice of a photoinitiator and its concentration is crucial for both the resulting hydrogel properties and the viability of the embedded cells [77]. A popular free radical photopolymerization reaction is that based on acrylates. Derivatives of natural polymers such as gelatin methacryloyl (GelMA), methacrylated hyaluronic acid (MeHA) or methacrylated alginate (MeAlg) as well as derivatives of synthetic polymers such as PEGDA have been used to produce hydrogels through this cross-linking method [76,78–80] .

1.2.3. Hydrogels for 3D cell culture

As opposed to conventional Transwell®-based models, hydrogels can act as ECM mimics to support multicellular and compartmentalized cell models in complex *in vitro* studies [42,81]. For tissue barriers, hydrogels have been used to encapsulate different tissue-resident cells inside the polymeric mesh while seeding epithelial or endothelial cells on top to form monolayers. For example, hydrogels have been used as ECM analogs to encapsulate stromal cells and support the formation of epithelial monolayers [82]. Pereira et al. developed a 3D intestinal model comprising intestinal CCD-18Co myofibroblasts embedded in Matrigel™, on which epithelial Caco-2 cells and mucus-producing HT29-MTX cells were seeded on top (Figure 1.11 A) [83]. Myofibroblasts were able to remodel the surrounding ECM matrix as shown by the production of fibronectin while supporting epithelial cell growth (Figure 1.11 A). Also, due to epithelial-stromal interactions, insulin permeability values were closer to the ones found *in vivo*. However, the model was based on Matrigel™, a natural hydrogel with a high batch-to-batch variability and partially unknown composition, thus reducing the reproducibility of the results [52]. As an alternative, our group proposed the use of cell-laden GelMA-PEGDA hydrogels to establish a 3D *in vitro* model of the intestinal mucosa [62]. With this hybrid composition, 3T3 fibroblasts were encapsulated inside the hydrogel while Caco-2 were grown on top to form a mature epithelial monolayer for several weeks (Figure 1.11 B). The co-culture of stromal cells with epithelial cells was shown to both promote barrier formation and accelerate barrier recovery upon temporary disruption, recapitulating key functionalities of *in vivo* intestinal tissues. Moreover, in a recent publication, a tri-layer 3D intestinal model consisting of an epithelial monolayer, stromal fibroblasts and an endothelial barrier was presented. Human intestinal fibroblasts (HIF) were embedded in a collagen layer on a Transwell® membrane [84]. Caco-2 enterocytes and HT29-MTX Goblet cells were seeded on top of the hydrogel, while human pulmonary microvascular endothelial (HPMEC-ST1.6R) cells were grown on the bottom side of the insert (Figure 1.11 B). After 21 days of cell culture, expression of efflux transporters Multidrug Resistance Protein (MRP-2) and P-glycoprotein (P-gp) was observed to be lower in 3D tri-culture models compared to the other ones, similar to physiological observations. Also, tight junction markers ZO-1 and Claudin-1 were positive for the complete models, indicating the presence of both epithelial and endothelial monolayers, while MUC-2 expression confirmed the presence of Goblet cells (Figure 1.11 C). These results, along with permeability values closer to *in vivo* ranges, proved the capabilities of the multicellular *in vitro* model to mimic the vascularized intestinal mucosa.

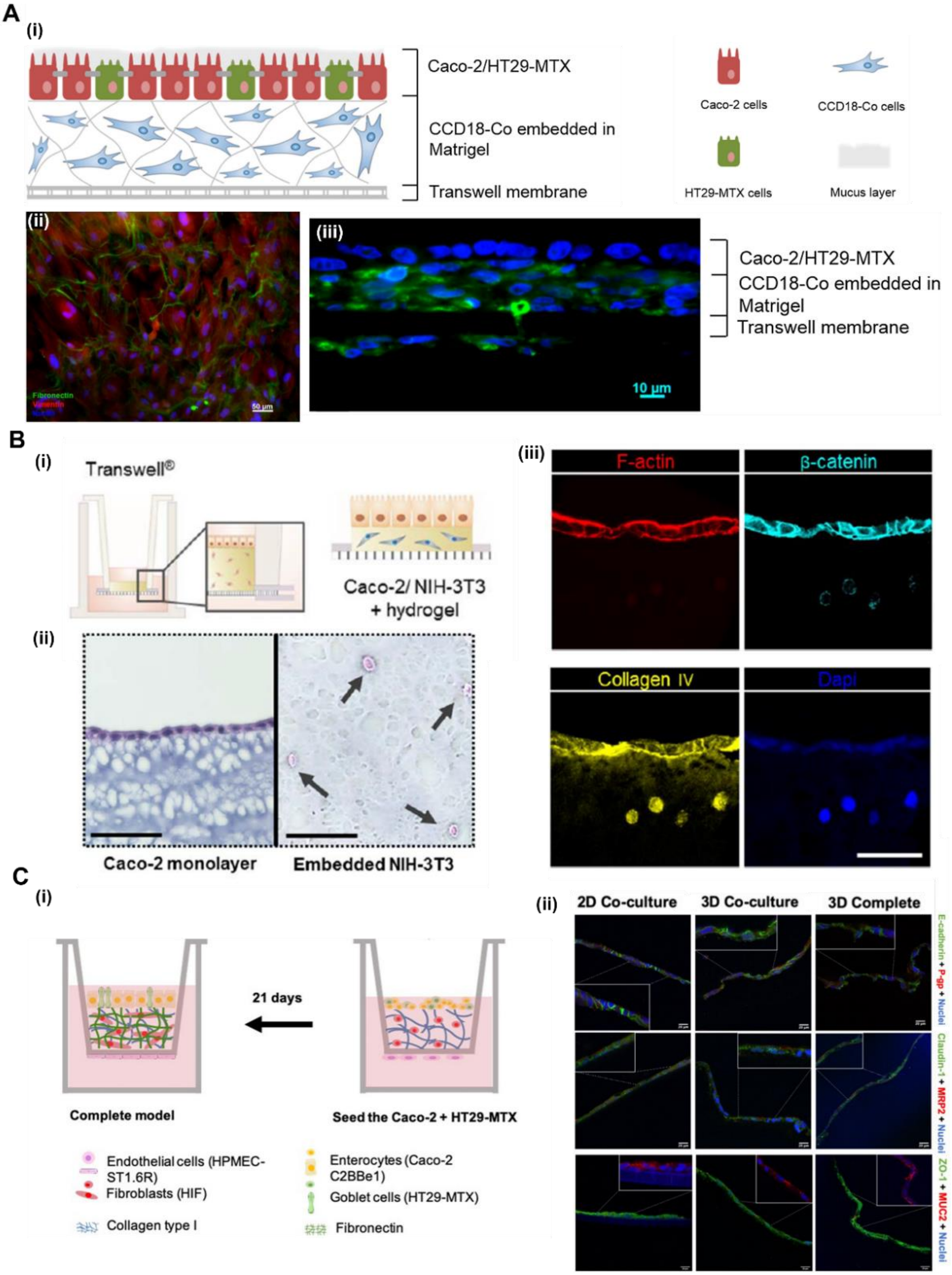

***Figure 1.11:** Hydrogel-based models of the intestinal mucosa. (A) 3D intestinal model on Matrigel^{TM} for epithelial-stromal cross-talk. (i) Illustration of the tri-culture 3D model. (ii) Staining of fibronectin for CCD18-Co fibroblasts in the 3D hydrogel. Fibronectin was labelled with Alexa-Fluor 488 (green), vimentin with Alexa-Fluor 594 (red) and nuclei, with DAPI (blue). (iii) Expression of fibronectin (green) on a cross-section of the triple-culture 3D model. Nuclei were stained for DAPI (blue). Adapted with permission from Elsevier, 2015 [83]. (B) In vitro model of the intestinal mucosa on PEGDA-GelMA hydrogels. (i) Schematic of the intestinal model, with 3T3 fibroblasts embedded in the scaffold and Caco-2 cells forming a monolayer on top. (ii) Detailed views of a cross-section of haematoxylin and*

eosin-stained hydrogel samples showing an intact epithelial monolayer at the top (right) and a uniform distribution of the NIH-3T3 fibroblasts (arrows) in the hydrogel (left). Scale bar: 50 µm. (iii) Immunostainings for F-actin, β-catenin, and Collagen IV of a co-culture sample in the hydrogel. Scale bar: 50 µm. DAPI was used to stain the nuclei. All samples were fixed and stained after 21 days of cell culture. Adapted with permission from IOP Publishing, 2020 [62]*. (C) 3D intestinal tri-culture model with an endothelial barrier. (i) Representation of the tri-culture model where human intestinal fibroblasts are encapsulated in a collagen layer while Caco-2 and Goblet cells are seeded on top, and endothelial cells are grown on the bottom side of the insert. (ii) Expression of efflux markers MRP-2 and P-gp (stained in red), tight junctions E-Cadherin, Claudin-1, and ZO-1 (in green) and mucus-producing cell marker MUC2 (in red) for 2D cell co-culture models with epithelial cells only, 3D co-cultures with epithelial and stromal cells only, and 3D complete models including endothelial cells at 21 days of cell culture. Nuclei are stained in blue. Scale bar: 20 µm. Adapted with permission from Elsevier, 2022* [84]*.*

Also, at the organ level, topographical and structural cues are critical in the polarization and maturation of tissue barriers by generating biochemical gradients that promote cell compartmentalization [85]. The progress in high-resolution microfabrication techniques has led to the generation of 3D hydrogels that can closely reproduce the spatial architecture of cell barriers [86,87]. In Martinez's group, 3D PEGDA hydrogels with villus-like protrusions were fabricated using a mold-free photopolymerization approach to mimic the configuration of the small intestinal epithelium (Figure 1.12 A) [88]. Intestinal epithelial cells were seeded and gradually grew over the vertical hydrogel micropillars until they formed a tight and mature monolayer over them. The effect of the curvature and stiffness of the hydrogel on the cell barrier was observed through the polarization of the tight junctions of the enterocytes, showing the importance of 3D topographical features in the formation and development of intestinal barriers. To further increase the predictive capabilities of such 3D models, stromal cells have been also included within the microfabricated scaffolds to mimic the lamina propria of the intestinal mucosa, allowing stromal-epithelial interactions as *in vivo*. For instance, NIH-3T3 cell-laden PEGDA-GelMA hydrogels were printed and served as a support for the growth of Caco-2 epithelial barriers. It was observed that 3T3 fibroblasts promoted tighter barriers than in the case of epithelial cell monocultures after 21 days of cell culture. Also, spatial organization of the epithelial and stromal cells closely mimicked *in vivo* intestinal tissues, with Caco-2 cells covering the villous and crypt structures while most 3T3 cells were located close to the tips of the villi and crypt regions of the hydrogel (Figure 1.12 B).

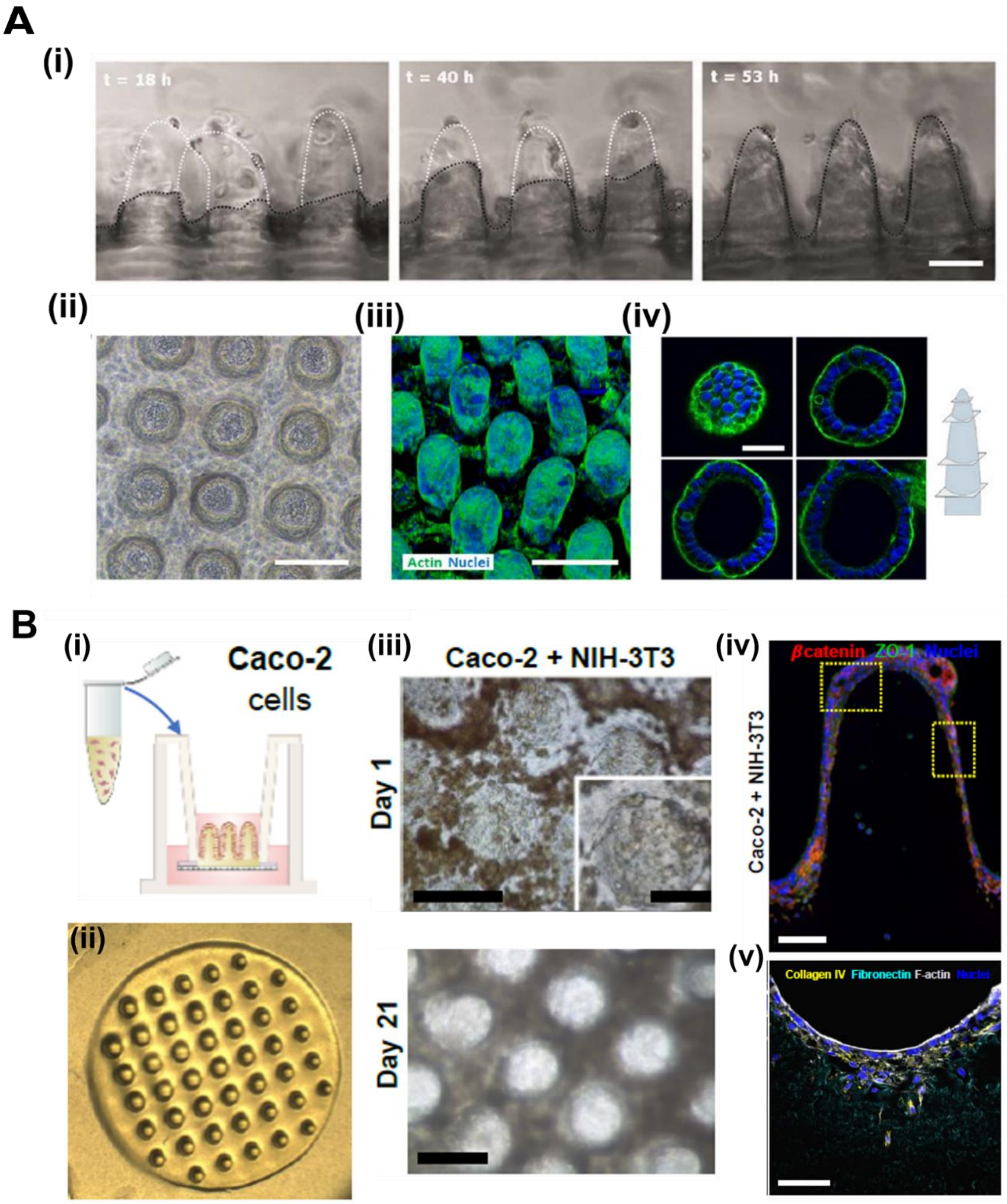

Figure 1.12: *3D biomimetic hydrogels for tissue barrier modelling. (A) Caco-2 cell culture on PEGDA-AA villi-like 3D scaffolds. (i) Time-lapse microscopy images of Caco-2 cells growing along the PEGDA-AA micropillars. Scale bar: 150 µm. (ii) Top view brightfield image of the micropillars with the epithelial cells. Scale bar: 50 µm. (iii) Confocal projection of Caco-2 cells growing on the 3D scaffolds for 21 days. Scale bar: 50 µm. (iv) Sliced cross-section of a Caco-2 cell covered micropillar. Nuclei are shown in blue; F-actin is shown in green. Scale bar: 50 µm. Adapted with permission from IOP Publishing, 2019* [88]*. (B) Bioprinted cell-laden crypt-villous hydrogels for a 3D gut model. (i) Illustration of the Caco-2 cell seeding on 3D cell-laden PEGDA-GelMA hydrogels assembled on Transwells®. (ii) Brightfield image of the printed hydrogel. (iii) Top view brightfield images of the Caco-2 cells forming a monolayer on the 3T3 cell-laden hydrogels at day 1 and 21. Scale bar: 100 µm, 50 µm (inset). (iv) Expression of β-catenin (red) and ZO-1 (green) markers showing Caco-2 epithelial cells polarization along the villi-like structure at day 21. Nuclei are stained blue. Scale bar = 100 µm. (v) Expression of Collagen IV (yellow) and*

fibronectin (cyan) for fibroblast activity within the hydrogels. F-actin is stained in white and nuclei, in blue. Scale bar = 50 μm. Adapted with permission from Elsevier, 2023 [89]*.*

1.2.4. Considerations about hydrogel microfluidic models

Despite their biocompatibility and mechanical tunability, hydrogel-based static models are still unable to reproduce the dynamic external conditions of the tissue barrier microenvironment, where fluid flows exert mechanical forces over the different types of cell barriers and modulate the transport of nutrients and oxygen (Figure 1.13 A). Recently, major efforts have been put to integrate hydrogels within microfluidic devices to combine the benefits of both approaches and increase the physiological relevance of tissue barrier-on-chips (Figure 1.13 B) [40,90]. Both as matrices embedded within the microfluidic chips, and as self-contained perfusable devices, hydrogel microfluidic platforms are the ideal candidates to include the cellular and acellular components of tissue barriers while providing fluid perfusion. This approach, however, is still technologically challenging in different aspects. When selecting hydrogels as building blocks for microfluidic platforms in tissue modeling applications, specific considerations affecting their mechanical properties and structural features should be considered (Figure 1.14).

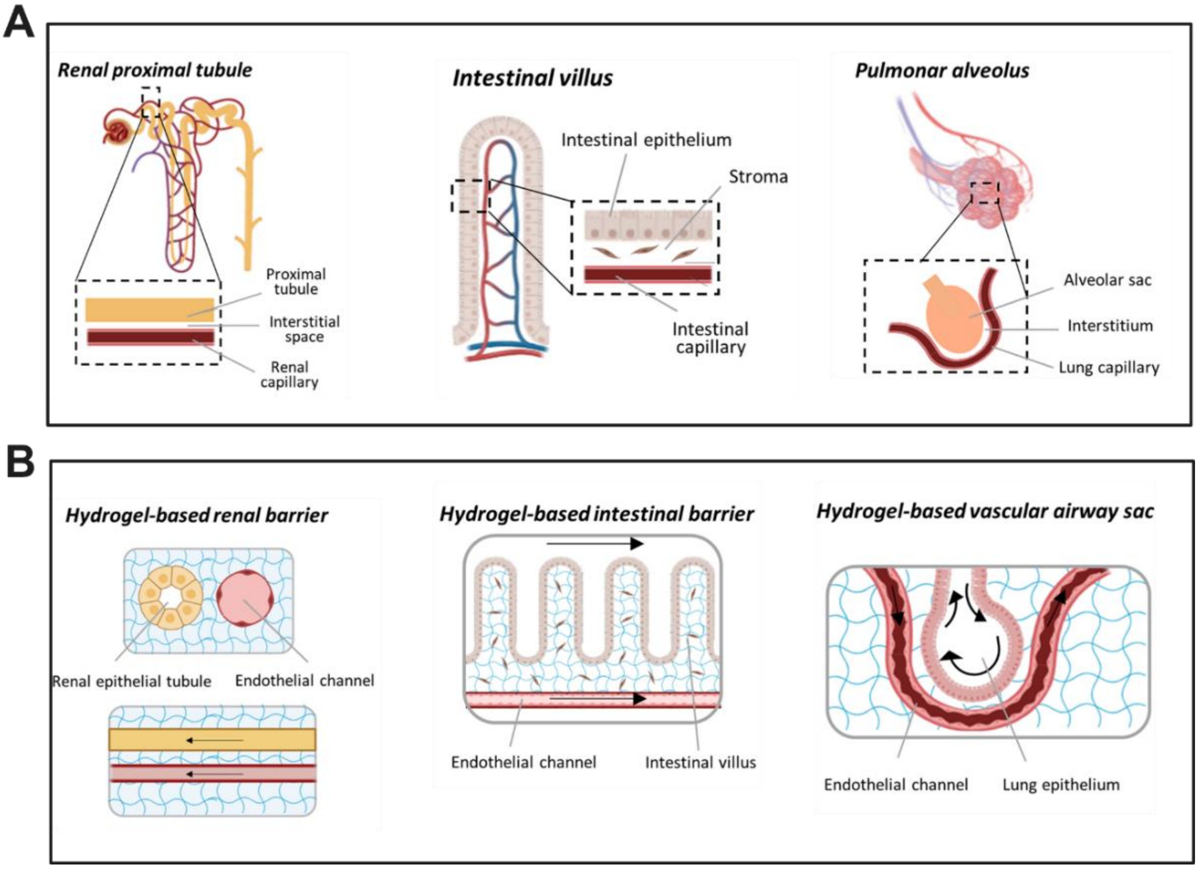

Figure 1.13: *Hydrogel microfluidic tissue barrier models. Schematic comparison of the structure of (A) some tissue barriers in vivo and (B) hydrogel-based organ-on-chip platforms aiming to model tissue barrier functions in vitro.*

As tunable biomaterials, the mechanical properties of hydrogels depend on multiple parameters such as the nature, structure and molecular weight of polymer chains composing the network, the polymer content, the cross-linking process, and density [91]. This extensive selection of parameters offers a broad range of mechanical stiffness that can match the one of the ECM of the target tissue found *in vivo*. Dynamic mechanical forces from microfluidic perfusion can subject both the tissue barrier and the hydrogels to hydrostatic pressure and fluid shear stress, having a significant impact on their integrity [92,93]. Thus, these forces must be accounted for when hydrogels are included in microfluidic applications as they might be a limiting factor to achieve self-standing structures such as microchannels.

Another key aspect of hydrogels that must be carefully considered when exploring microfluidic applications is swelling [94]. Hydrogel networks can absorb high amounts of surrounding liquids, inducing their volume enlargement. Swelling depends on the material composition and concentration, along with the porosity of the cross-linked network and the medium where the swelling happens. Moreover, when removed from the liquid environment, dehydration can happen and induce the shrinkage of the hydrogel structures. In both cases, the potential impact of swelling or shrinkage on the mechanical stability and spatial dimensions of the hydrogels must be considered when designing the microfluidic platforms. Moreover, pore size and porosity are key parameters to facilitate diffusion-based transport of nutrients to embedded cells within hydrogel [95]. By the convective forces of fluid perfusion, this transport can be further improved in microfluidic setups, overall increasing cell viability. However, too small pores can restrict cell movement, which is highly relevant for cells in stromal compartments of tissue barriers, while too big ones can compromise the mechanical integrity of the hydrogel scaffold [96,97].

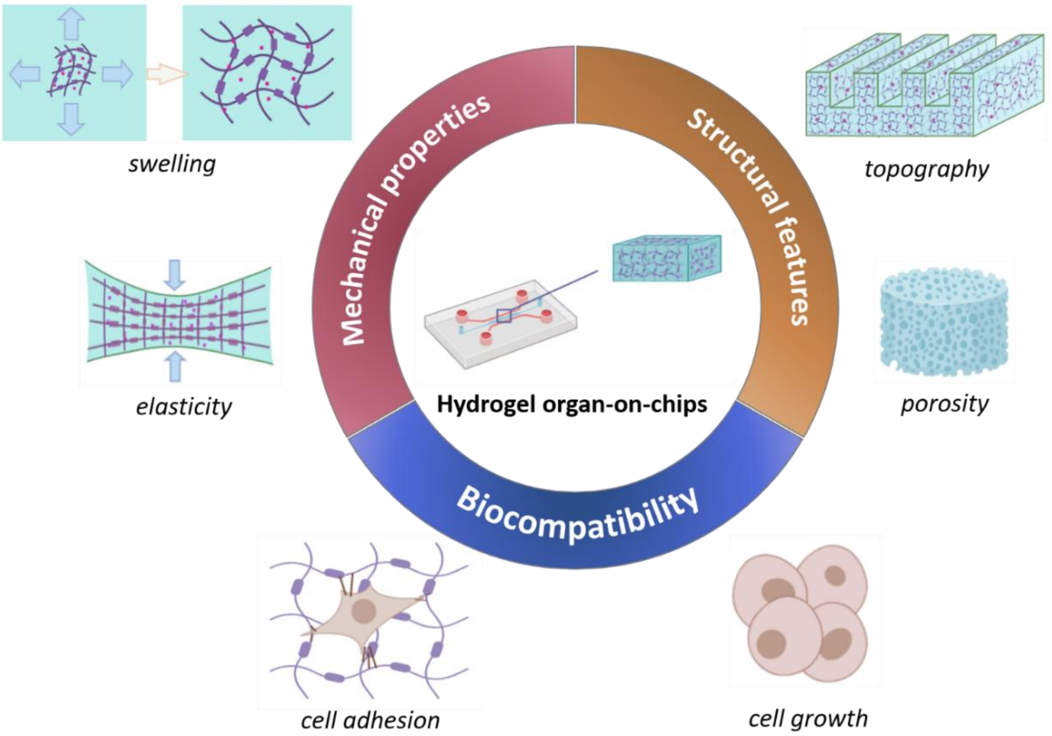

Figure 1.14: *Relevant features of hydrogels for organ-on-chip applications.*

Finally, when considering hydrogels for microfluidic applications, the compatibility of these materials to deliver 3D structures by employing microfabrication techniques is a crucial point. These approaches need to be compatible with the chemical nature and the cross-linking capabilities of the hydrogels and they should generate polymeric networks with suitable properties for the *in vitro* modelling of tissue barriers. The main microfabrication techniques used in the field are described in the following section.

1.3. Microfabrication techniques for hydrogel microfluidic devices

Initially adapted from the microfabrication of silicon-based materials, microfabrication tools have been adopted by the bioengineering community to generate tissue barrier models in organ-on-chips [27]. Recent advances in the field have pushed this concept even further by introducing hydrogels as ECM analogs to potentially revolutionize its impact in *in vitro* studies [40,41,98]. The main microfabrication methods used to build hydrogel microfluidic platforms for tissue barrier-on-chip applications are presented in this section and summarized in Table 1.1.

Microfabrication method (resolution)	Advantages	Drawbacks	Hydrogel	Tissue barrier models	Ref
Soft lithography (100 µm)	Simplicity Compatible with many hydrogels	Only simple shapes Alignment issues Low resolution	Collagen pHEMA GelMA PEG Agarose Fibrin Alginate Collagen/Matrigel	Endothelial barrier Blood−brain barrier Intestinal barrier	99–105
Extrusion-based bioprinting (100 µm)	Fine spatial control of cell-laden hydrogels Reduced number of precursors	High cell shear stress Nozzle-imposed geometrical constraints Poor structural stability	dECM/gelatin GelMA/PEG Gelbrin ECM Gelatin/fibrinogen Collagen Gelatin MeAlg MeHA GelMA	Liver-on-chip Renal proximal tubule model Vessel-on-chip	76,106–110
Light-based 3D bioprinting (10µm)	3D complex structures Automated procedure High resolution	Only photocrosslinkable polymers UV/photoinitiator-induced cytotoxicity	PEGDA	Vascular networks	111,112
Laser-based photopatterning (10 µm)	In situ patterning in cell-laden hydrogels High resolution	Complex setup Expensive equipment Laser-induced cytotoxicity	Photodegradable PEG PEG	Vascular networks	112,113

Table 1.1: *Summary of the main microfabrication techniques employed to engineer hydrogel microfluidic platforms.*

1.3.1. Soft lithography

Soft lithography, traditionally used to produce PDMS replicas, can be adapted to produce hydrogel microstructures in a variety of technological approaches [115], thanks to its high flexibility, reproducibility, and in general, its compatibility with a wide range of hydrogels and cell culture requirements. This technique is relatively inexpensive, easy to perform and does not need a clean room environment, thus making soft lithography-based approaches a popular choice for hydrogel microfluidic platforms. Among them, micromolding is one of the preferred options. In micromolding, a prepolymer solution is usually cast onto a patterned PDMS mold, which is then removed after polymer gelation to generate 3D structural features. This technique has been used to produce microfluidic channels made from enzymatically cross-linked gelatin [69], thermally cross-linked collagen [116], agarose [117], and photo cross-linkable PEGDA [59], among other materials (Figure 1.15 A). Wires [118], needles [119], and helical springs [120] (Figure 1.15 B) have also been used as molds.

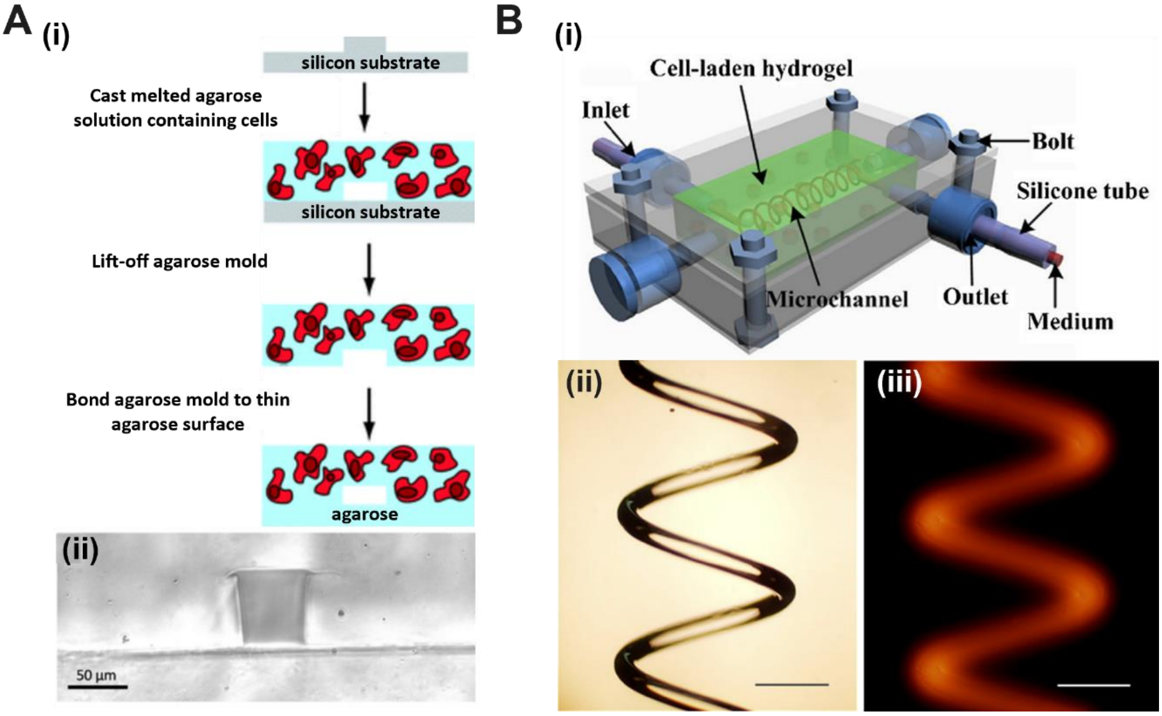

Figure 1.15: *Replica molding of perfusable hydrogels. (A) Mold-based fabrication of cell-laden agarose microchannels. (i) Schematic of the microfabrication process. (ii) Cross-sectional view of the hollow hydrogel channel. Adapted with permission from the Royal Society of Chemistry, 2007* [117]*. (B) Fabrication of microfluidic hydrogels based on a helical spring template. (i) Schematic of the custom-built platform to mold the helical agarose hydrogel channel. (ii) Brightfield image of the helical microchannel. Scale bar: 1 mm. (iii) Fluorescence image of the helical microchannel filled with Rhodamine B (RhB) solution. Scale bar: 1 mm. Adapted with permission from Biotechnology and Bioengineering, 2013* [120]*.*

Aside from being used to produce hydrogel-based microfluidic channels, soft lithography approaches have also been exploited to integrate hydrogels within conventional PDMS microfluidic channels. A simple strategy is the fabrication of localized supporting gels by surface tension-assisted patterning [121]. With this technique, a PDMS chip is designed with microposts or micropillars lining a microchannel where the hydrogel precursor is loaded. This way, the precursor volume is spatially constrained by surface tension, allowing its localized gelation (Figure 1.16 A). Typically, the central hydrogel-loaded channel has two parallel outer channels, where culture medium can be perfused. Endothelial or epithelial cells can form functional barriers at the hydrogel−liquid interface and interact with hydrogel-embedded cells (Figure 1.16 A). Kamm's group has extensively used this configuration with cell-laden fibrin and collagen hydrogels to recreate BBB models [103,122,123]. A similar approach is used in the commercially available OrganoPlate® system. By capillary force, a collagen solution is filled into the microchannel where chip-integrated bottom stripes, referred as phaseguides, spatially confine the hydrogels by meniscus pinning [124]. This technology has been applied to vascular [125] and intestinal studies [105]. Another approach based on surface tension is the so-called viscous finger patterning, developed by Beebe's group, to line the interior of PDMS channels with a layer of hydrogel materials [104]. There, circular hollow lumens are obtained by passive pumping of culture media that displaces the central portion of the hydrogel precursor due to a viscosity gradient between the two fluids [126] (Figure 1.16 B). After polymerization, cells can adhere and line the inner part of the channel. BBB models where brain endothelial cells were cocultured with hydrogel-embedded astrocytes and pericytes to study neurovascular inflammation and drug screening have been developed by employing this procedure [127,128]. Although the method does not require intricate setups, it is necessary to precisely optimize the process to avoid the complete removal of the precursor or the formation of incomplete structures.

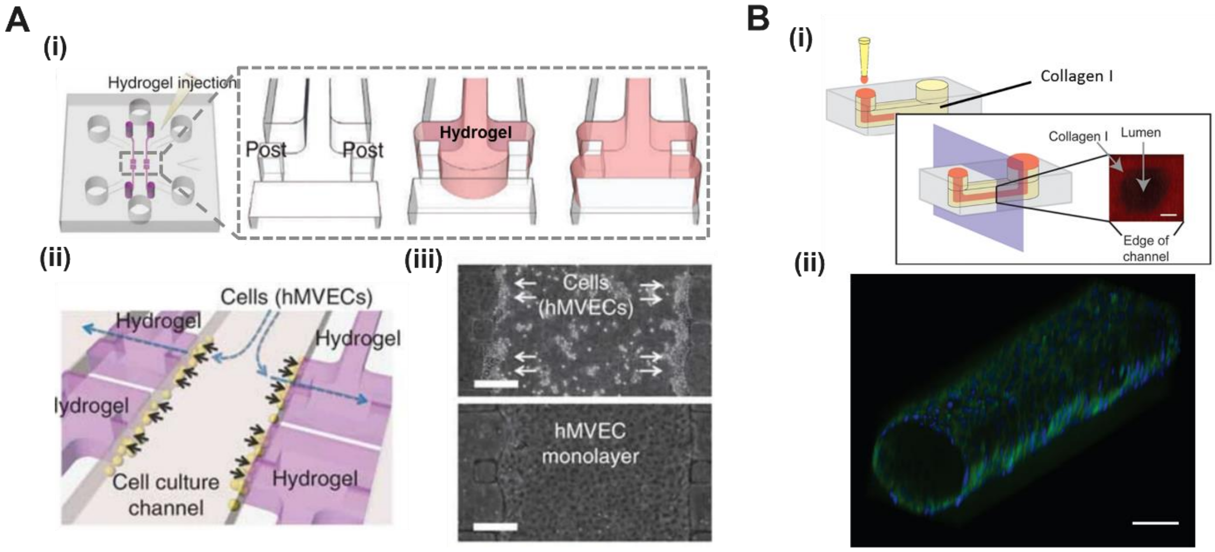

Figure 1.16: *Hydrogel integration via soft lithography. (A) Phase-guided patterning of collagen-based channels. (i) Schematic of the surface tension-assisted hydrogel loading in the chip. (ii) Representation of the seeding of endothelial cells in the central channel. (iii) Images of the human microvascular endothelial cells (hMVECs) after seeding (top) and 1 day of cell culture (bottom). Scale bar: 250 µm. Adapted with permission from Nature Protocols, 2012 [121]. (B) Viscous finger patterning of perfusable hydrogels. (i) Schematic representation of the fabrication of collagen-based hollow microchannels. Adapted with permission from SAGE, 2012 [126]. (ii) 3D volume-rendered image of an endothelial-lined lumen in a microchannel. Blue corresponds to nuclei, green corresponds to CD31. Scale bar: 100 µm. Adapted with permission from Biomaterials, 2013 [104] .*

1.3.2. Laser-based photopatterning

Photopatterning relies on the photodegradation of small focal volumes of polymer by laser focusing due to multiphoton absorption [129]. By adjusting the laser frequency and the pulse time, hollow microchannels can be precisely formed via continuous degradation of hydrogel voxels with nano to femtosecond laser pulses without compromising the overall structure

[130,131]. Lutolf's group has employed this approach to generate vascular channels and intestinal models on PEG-based, collagen I, and Matrigel hydrogels [113,132]. In one of the studies, new vessel branches could be microfabricated in situ from existing ones without damaging the embedded cells, allowing spatiotemporal control over the vascular pattern (Figure 1.17 A) [113].

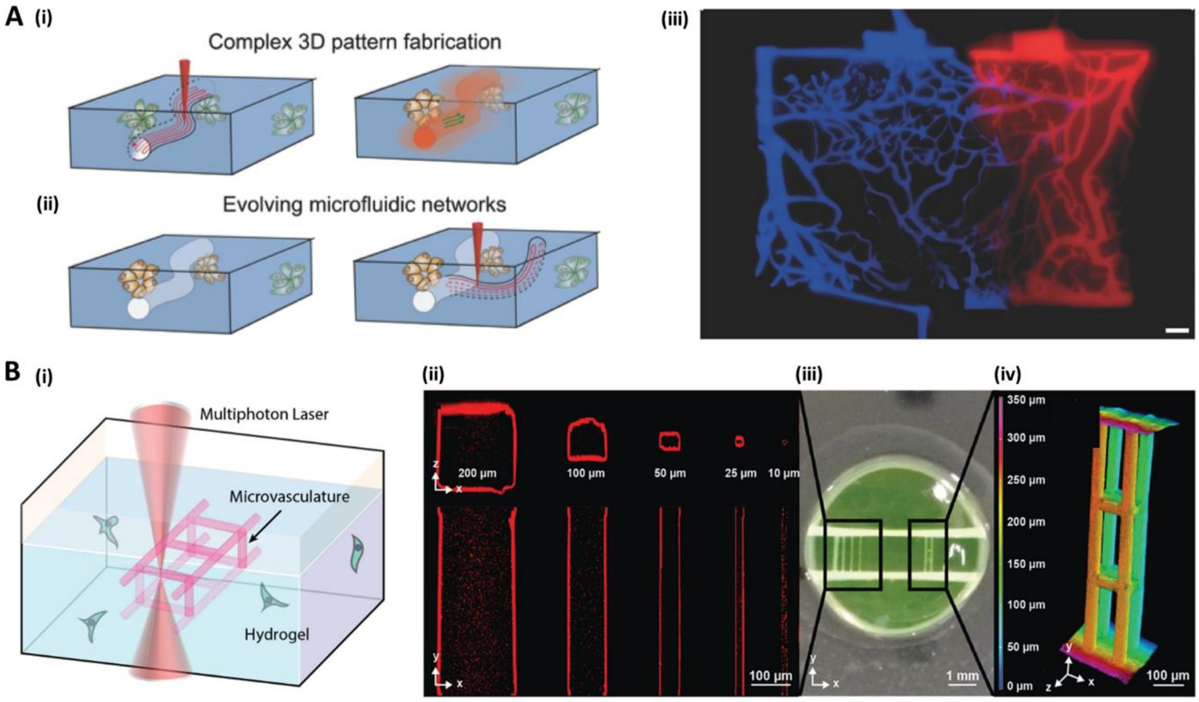

Figure 1.17: *Fabrication of hydrogel-based microfluidics by laser-based photopatterning. (A) Photopatterning of complex microfluidic networks. (i) Schematic illustration of the microfabrication of channels in cell-laden hydrogels by laser photodegradation. (ii) Spatiotemporal control over the microchannel structure. (iii) Photograph of micropatterned capillary network perfused with dyes mimicking arteriovenous circulation. Reprinted with permission from John Wiley and Sons, 2016* [113]*. (B) Laser photoscission of synthetic photolabile hydrogels. (i) Schematic illustration of the fabrication of microchannels in the presence of encapsulated stromal cells by multiphoton excitation that induces a localized photocleavage of the hydrogel. (ii) Cross-sectional view of perfused hydrogel with red fluorescent beads to visualize different diameters of the photocleaved microchannels. (iii) Photograph of photopatterned hydrogel with parallel channels (left) and 3D multilayered channels (right). (iv) Color-mapped 3D representation of fabricated interconnected channels. Reprinted with permission from John Wiley and Sons, 2017* [114]*.*

Hydrogels with photolabile groups have also been developed to induce controlled photo-scission of polymeric chains. Arakawa et al. employed a cytocompatible laser-based strategy to create vascular networks within a photosensitive hydrogel [114]. The prepolymer composition was a mixture of a PEG derivative covalently linked with a synthetic peptide containing a photodegradable moiety, cell adhesion, and cleavable motifs. Photopatterned vessel sizes were in the physiological range, with diameters as small as 10 µm and supported both endothelial cell attachment, proliferation and the co-culture of stromal cells (Figure 1.17 B) [114]. Despite the progress, the high cost and complexity of the equipment, along with the long fabrication times limit the use of this approach in the bioengineering field.

1.3.3. Extrusion-based 3D bioprinting

In extrusion-based bioprinting, a cell-laden hydrogel precursor or bioink is loaded into a syringe and extruded through the nozzle by continuous pressure while it moves along the printing bed, thus creating stacked layers of the extruded filaments. A critical step in the printing process is the choice of bioinks. Hydrogel precursors must possess optimal viscosity and good structural stability. Gelatin [133], GelMA [110], methacrylated hyaluronic acid (MeHA), and methacrylated alginate (MeAlg) [76] are considered as appropriate bioinks. They are often copolymerized with PEG derivatives to increase the mechanical stability of the constructs and produce perfusable hydrogel structures [106]. However, they tend to have relatively high gelation times, which can be a problem in terms of mechanical integrity and resolution for the bioprinted structures. On top of that, shear stress caused by the nozzle extrusion can produce cell stress and damage. To overcome these drawbacks, two main approaches have been proposed: the use of sacrificial inks and the coaxial extrusion of bioinks.

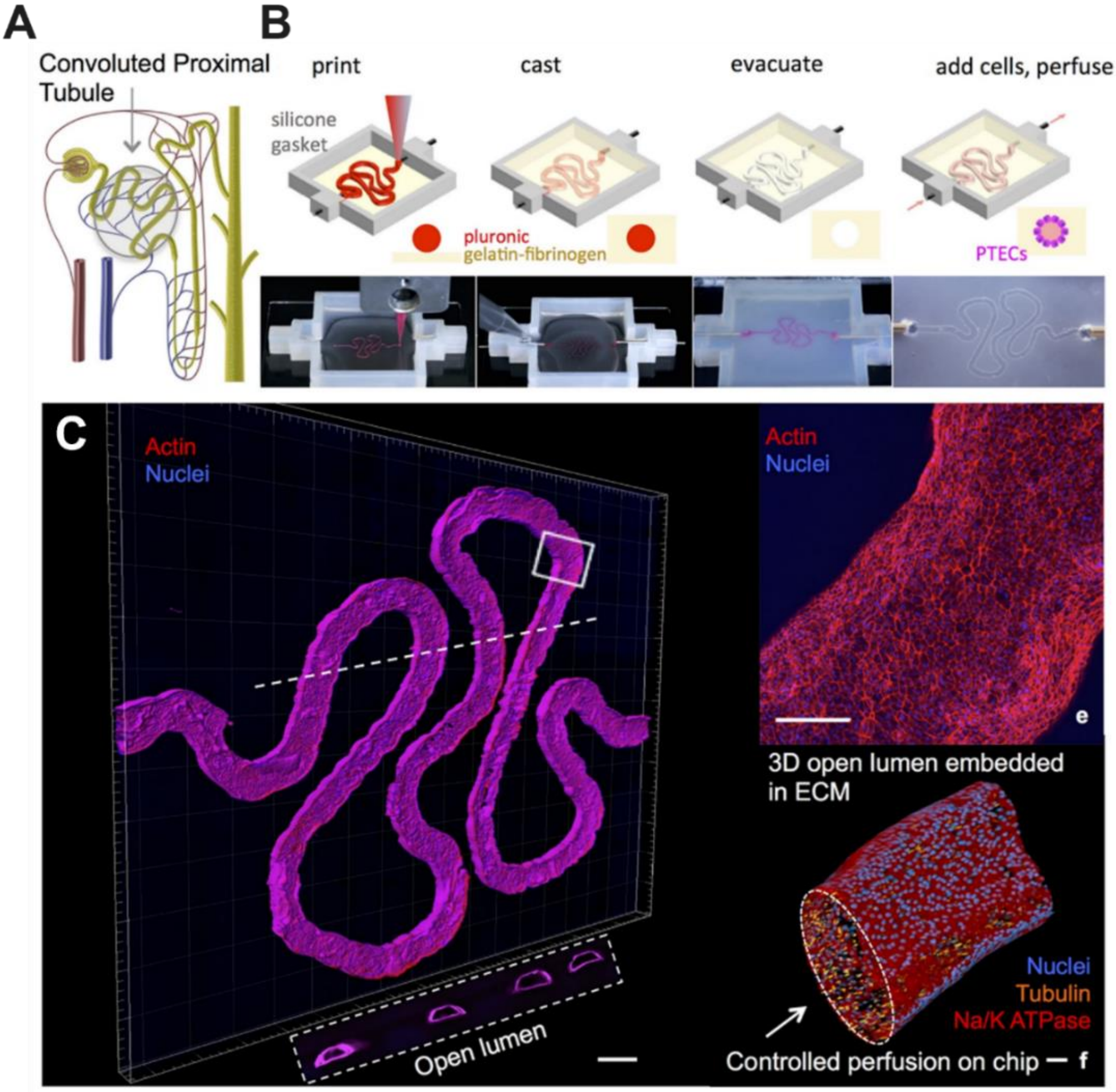

Figure 1.18: *Sacrificial ink-based bioprinting of perfusable hydrogels. (A) Schematic illustration of the proximal renal tubule. (B) Schematic and images of the printing process. The vascular ink that contains Pluronic is printed, and the ink with gelatin and fibrinogen is cast on the perfusion chip. Finally, the fugitive ink is evacuated creating the renal proximal tube (PTECs, primary tubular epithelial cells). (C)*

3D rendered confocal images of the printed convoluted proximal tubule (blue, nuclei; red, actin or NaK ATPase; orange, tubulin). Adapted with permission from Springer Nature, 2016 [107]*.*

The use of sacrificial inks in 3D bioprinting has been proven suitable to create stable hollow structures that can mimic *in vivo* tissue lumens [107,108]. These inks are initially printed to act as mechanical supports and then, they are removed once the bioink is cross-linked. Usually, materials with temperature-based gelation properties such as triblock copolymers of poly(ethylene oxide)-poly(propylene oxide)-poly(ethylene oxide) (PEO−PPO−PEO), trademarked as Pluronic, are used [110]. For example, 3D renal proximal tubules were formed on cell-laden gelatin-fibrin hydrogels cast on top of a 3D Pluronic bioprinted filament (Figure 1.18 A, B) [107]. Once the sacrificial ink was evacuated by thermal cooling, the resulting hollow network was epithelialized with proximal tubule epithelial cells that formed a polarized epithelium with improved phenotypic and functional properties (Figure 1.18 C).

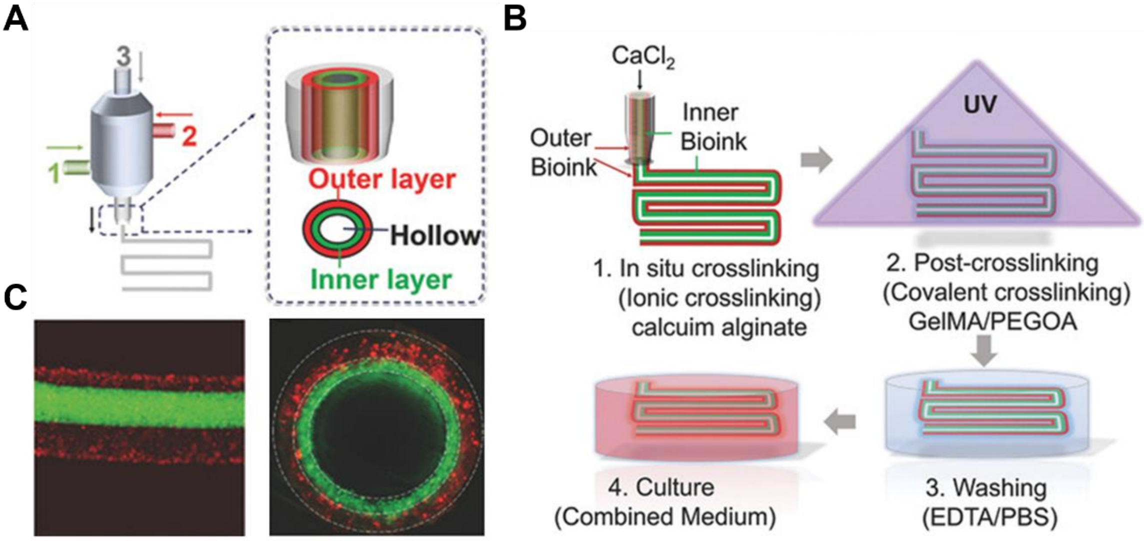

Figure 1.19: *Coaxial extrusion-based bioprinting of hollow tubules. (A) Schematic illustration of the coaxial nozzle to generate multilayer structures. (B) Fabrication process of the PEGOA-GelMA-alginate multilayered hollow tubes. (C) Fluorescent images of longitudinal and cross-sectional views of double-layered hollow fibers. Reprinted with permission from John Wiley and Sons, 2018* [106]*.*

On the other hand, the generation of perfusable multilayer hydrogel structures has been recently investigated via coaxial extrusion of bioinks [106,134,135]. In this approach, the nozzle can extrude several bioink layers simultaneously in a coaxial configuration through concentrically assembled needles. It can combine several hydrogels and cross-linking methods to spatially control the number of layers and shape of the extruded tubules along the process, offering high versatility on the design. For instance, a PEG-derivative polymer (PEGOA) loaded with urothelial smooth muscle cells and GelMA/alginate loaded with urothelial cells were simultaneously extruded (Figure 1.19 A, B) [106]. The two-step cross-linking strategy, with $CaCl_2$ and UV light resulted in cell-embedded tubular structures mimicking the epithelium of the urinary tract [106] (Figure 1.19 C).

1.3.4. Digital light projection stereolithographic (DLP-SLA) 3D bioprinting

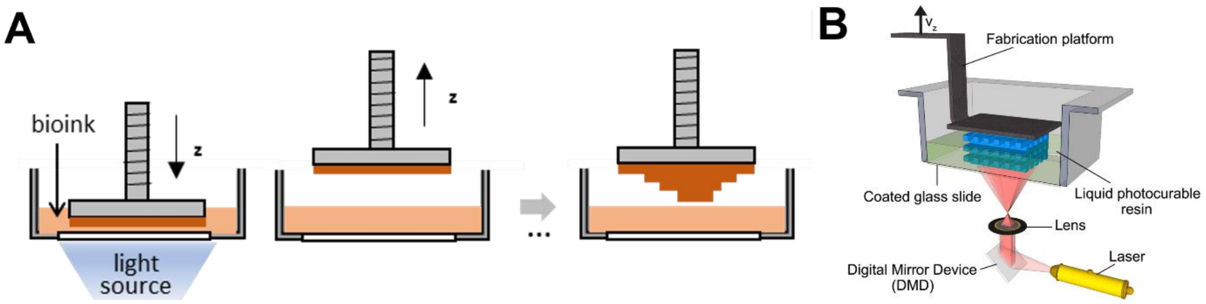

Figure 1.20: *Working principle of DLP-SLA 3D bioprinting. (A) Schematic illustration of the working principle of DLP-SLA to print hydrogel structures based on a layer-by-layer procedure. (B) Schematic of a DLP-SLA bioprinting platform where each layer of the hydrogel is polymerized all at once in a bottom-up configuration. Adapted with permission from Elsevier, 2012* [136].

Light-based bioprinting, also named stereolithographic (SLA) bioprinting, has been increasingly adopted as a versatile fabrication technique to generate high-resolution hydrogel structures in a precise and reproducible manner [137–139]. In this approach, a photosensitive bioink is loaded into a vat or cuvette and then photo cross-linked by a light source in a layer-by-layer process to form 3D hydrogels (Figure 1.20 A). These light sources can be either laser platforms (laser-assisted SLA) or light projectors (DLP-SLA). [137,264]. In DLP-SLA, a digital mask generated by a liquid crystal display (LCD) or a digital mirror device (DMD) is projected onto the vat where the precursor solution is loaded, allowing full layer polymerization at once and reducing printing times in comparison with laser-based techniques (Figure 1.20 B) [112,140].

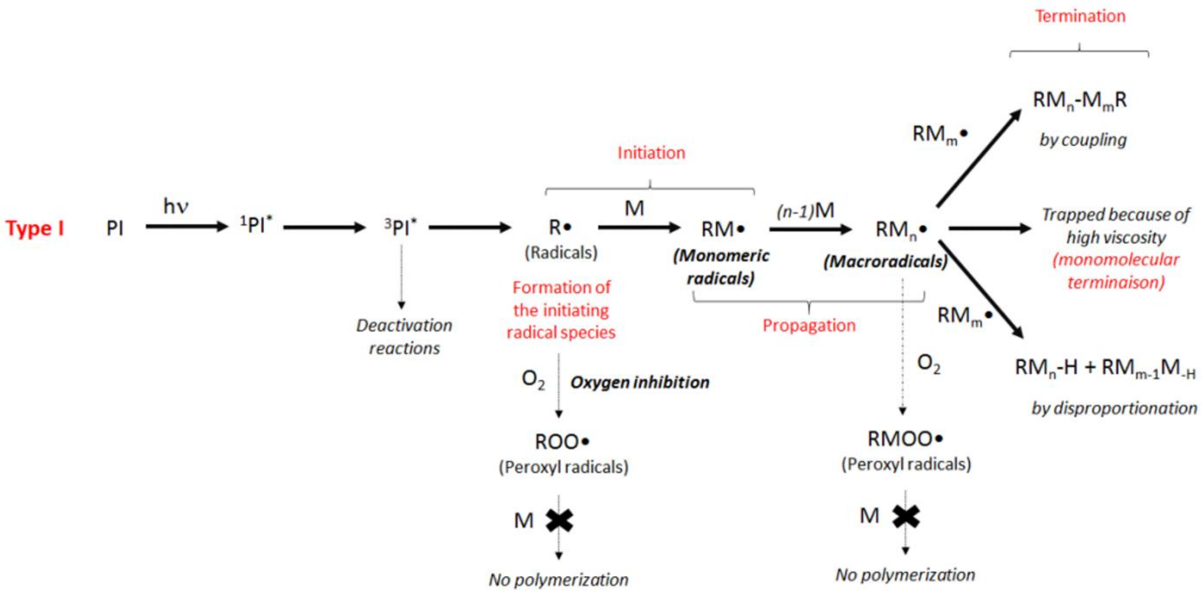

Figure 1.21.: *Schematic of the different phases of a free-radical photopolymerization based on a type-I photoinitiator. Adapted with permission from MDPI, 2021* [15].

Light-based 3D bioprinting is generally based on the free-radical photopolymerization of a bioink solution. Monomers containing acrylate groups are mixed with photosensitive molecules referred to as photoinitiators. Upon light exposure, the photoinitiator absorbs the energy from a photon and decomposes into free radicals to initiate a chain growth reaction [141]. These free radicals bind the monomers present in the solution to form polymeric chains during the propagation step. Chain growth is terminated either by coupling of two polymeric chains, by monomolecular termination due to spatial trapping in the solution or by a disproportionation reaction, in which a radical is transferred from one polymeric chain to another (Figure 1.21) [142,143]. A relevant aspect to consider about the photopolymerization reaction is the presence of oxygen molecules, as free radicals from photoinitiator molecules can react with them to form peroxyl radicals, limiting or inhibiting the reaction kinetics and the hydrogel formation (Figure 1.21) [88,144]. The type of light source and the exposure time are other critical parameters for hydrogel printing in cell culture models [145]. Commonly used type-I photoinitiators for SLA bioprinting applications, such as Irgacure 2959, are activated upon UV light exposure, inducing potential cell damage during prolonged printing times [146]. To avoid this, the use of visible-light photoinitiators such as LAP has been proposed, allowing 3D bioprinting of cell-laden hydrogel structures in the visible range [89,147,148].

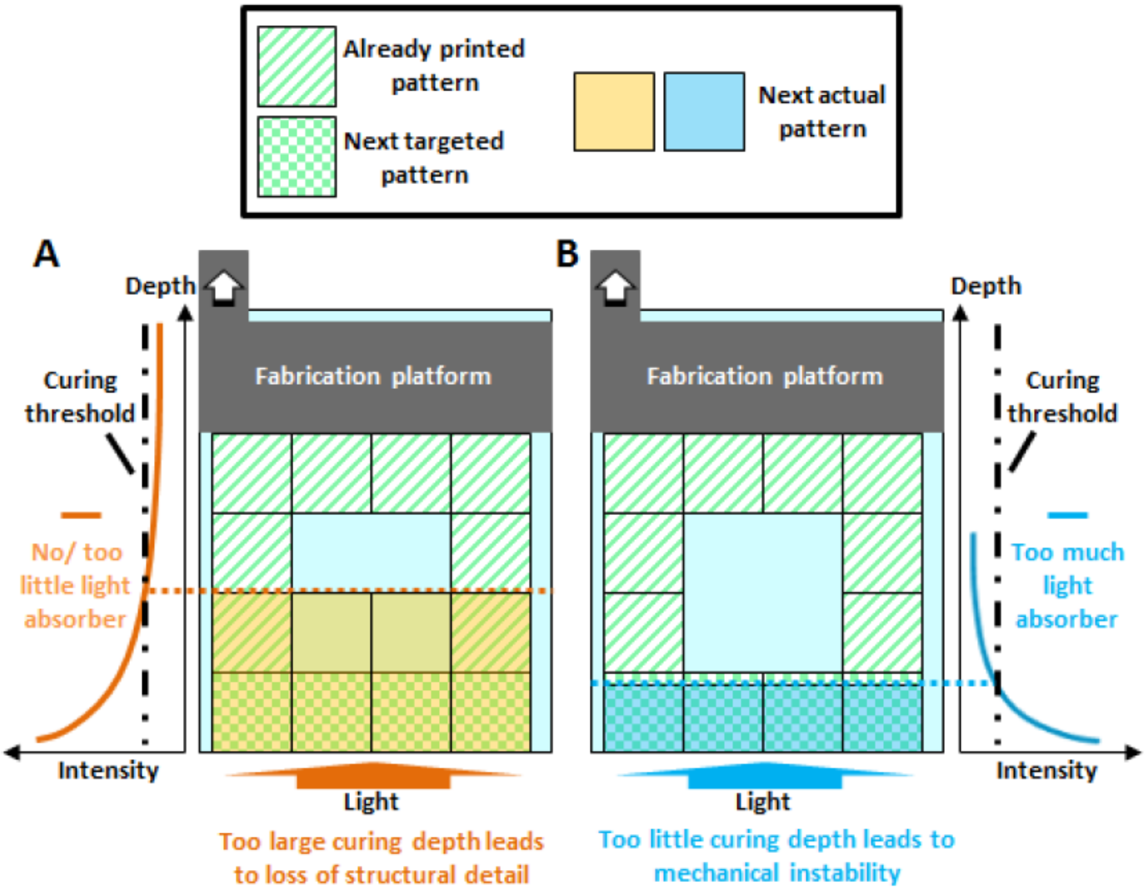

Figure 1.22: *Schematic of the effect of curing depth on SLA 3D printing of hydrogel channels. (A) For large curing depths, light penetrates beyond the targeted patterned layer and polymerizes unwanted areas of the already printed layer, resulting in reduced spatial resolution. (B) For short curing depths, light penetration is not sufficient for the targeted layer to polymerize and bond the previous one, resulting in mechanical instability. Adapted with permission from* [149].

In DLP-SLA bioprinting, the curing depth C_d is the key parameter of a specific pre-polymer solution to characterize the thickness of the polymerized layers [150]. It is directly linked to the energy dose E the bioink is exposed to at each step, following Jacob's equation [151]:

$$\textbf{\textit{(eq. 3.1)}} \quad C_d = D_p \ln\left(\frac{E}{E_c}\right)$$

where D_p is the optical penetration depth and E_c, the minimal energy to induce polymerization of the bioink solution. This energy threshold is highly dependent on the concentration of the photoinitiators, oxygen gradients and other inhibiting species [152]. D_p is defined by the composition of the used pre-polymer solution and, specifically, the photoinitiator:

$$\textbf{\textit{(eq 3.2)}}\quad D_p \propto \frac{2}{2.303\,\varepsilon\,[PI]}$$

Where ε is the molar extinction coefficient and $[\mathrm{PI}]$ is the molar concentration of the photoinitiator [138]. Optimal curing depth should be slightly larger than the designed layer thickness to ensure bonding between adjacent layers by polymerizing unreacted groups from the previous layer with the next one [152]. Larger curing depths can result in excessive light penetration into neighboring layers and overcuring of certain areas while shorter ones can reduce the definition of small features and compromise the stability of the hydrogels (Figure 3.9). To precisely control this parameter, different strategies based on the bioink composition can be adopted. Increasing the concentration of the photoinitiator can reduce the curing depth by increasing the light absorption of the bioink. However, several studies have shown the cytotoxic effects of photoinitiators in cell-laden hydrogels for high concentrations [77]. To prevent this, photoabsorbers are often added to the pre-polymer solution to finely tune the curing depth at each printed layer [138,153]. They can be selected according to the light source and the type of photoinitiator to compete in light absorption and confine the polymerization reaction to a thin layer for an improved spatial resolution, depending on their concentration. Grigoryan et al. found that food dyes such as tartrazine and curcumin are effective photoabsorbers to print intravascular networks within PEGDA hydrogels [111]. Using a custom DLP-SLA platform, they achieved remarkable complex structures, such as 3D static mixers, bicuspid valves, and entangled helical networks, which were applied in studies of red blood cell oxygenation and blood flow changes during ventilation in vascularized alveolar models (Figure 1.23).

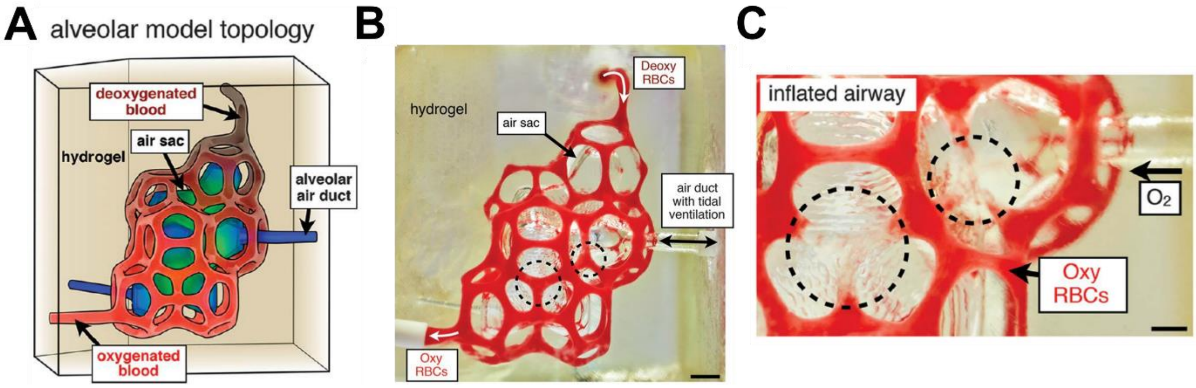

Figure 1.23: *Fabrication of hydrogel-based microfluidics by light-based DLP-SLA 3D bioprinting. (A) Schematic illustration of an alveolar model topology. (B) Photograph of a printed hydrogel during perfusion of red blood cells while the air sac is ventilated with O_2. Scale bar: 1 mm. (C) Photograph of an inflated air sac that obstructs adjacent vessels and red blood cell flow in the concave areas. Scale bar: 500 µm. Adapted with permission from AAAS, 2019* [111].

1.4. Models of tissue barriers in hydrogel microfluidic platforms

Combining hydrogels and microfluidics has allowed researchers to overcome some of the limitations of conventional tissue barrier-on-chips based on flat membranes [40]. Targeted tissue barriers for organ-on-chip applications have been primarily those used in pharmaceutical research for absorption, distribution, metabolism, and excretion (ADME) studies, including the vascular system, the BBB, the liver, the kidney and the gut. Advanced hydrogel microfluidic platforms can provide both physiological and pathological models of these tissues. This might improve the drug development process and provide a mechanistic insight of these physiological compartments for future therapeutic target predictions. In the following section, some representative examples of hydrogel microfluidic platforms that have been demonstrated to recapitulate key functions of these organ-specific barriers are discussed.

1.4.1. Vascular models

Vascular networks are organized in complex 3D geometries to ensure nutrient and oxygen supply to organ tissues. Blood vessels are lined by endothelial cells that form tight barriers and interact with the surrounding connective tissues to modulate their state. Under blood flow, endothelial barriers are exposed to mechanical forces such as lateral blood pressure, which can range from 1 to 15 kPa [93]. The diameter of blood vessels, which ranges from a few micrometers for capillaries to 25 mm for the aorta, and the elasticity of the vascular ECM also affect the endothelial barrier microenvironment. The structural and mechanical tunability of hydrogels allows the engineering of intricate and complex architectures with different dimensions and mechanical properties, mimicking the ones found *in vivo* [92,154].

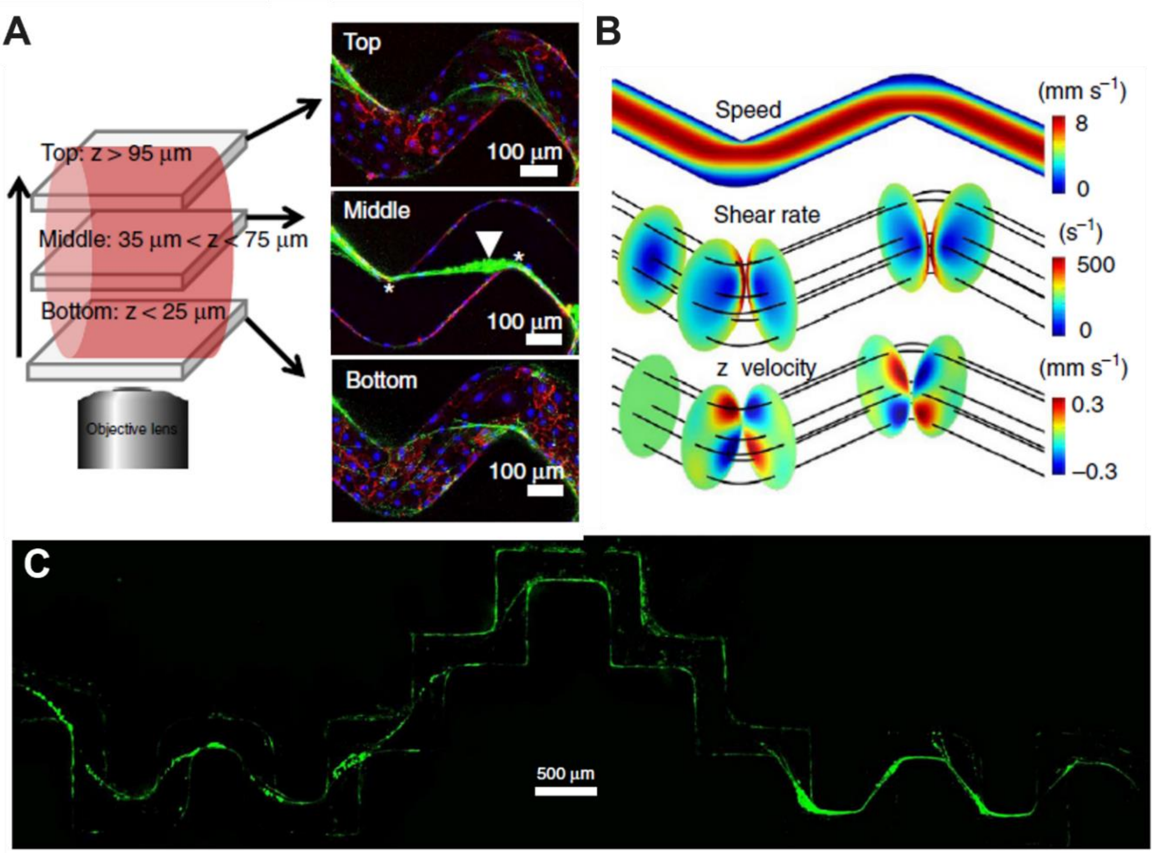

Figure 1.24: *Micromolded perfusable collagen I channels to study endothelial cell secretion of von Willebrand factor (VWF) proteins. (A) Confocal images at different z planes to visualize VWF fiber*

formation (green staining) within a tortuous channel covered by endothelial cells (blue and red staining). (B) Computational simulation of fluid flow within the vessels to correlate channel geometry and shear stress with VWF strand morphology and location. (C) A continuous VWF strand of around 5 cm in length (in green) extending through a torturous vessel along the shortest flow path. Reprinted with permission from Springer Nature, 2015 [155].

Two main strategies have been adopted to fabricate vessel-on-chip systems. One relies on the predesign of vascular channel networks within hydrogels, based on one or several of the microfabrication techniques previously explained, that later on will be seeded with endothelial cells to create functional barriers[155–157] . The main advantage of using microfabrication techniques is the precise tailoring of the geometry and the size of the channels, thus controlling key dynamic parameters such as fluid flow and solute gradients. For example, micromolding was applied to create collagen-based microvessel networks to form endothelial barriers. Under dynamic conditions, it was shown that fluid shear stress and vessel geometry modulate the formation and morphology of cell-secreted von Willebrand factor bundles and fibers (Figure 1.24) [155].

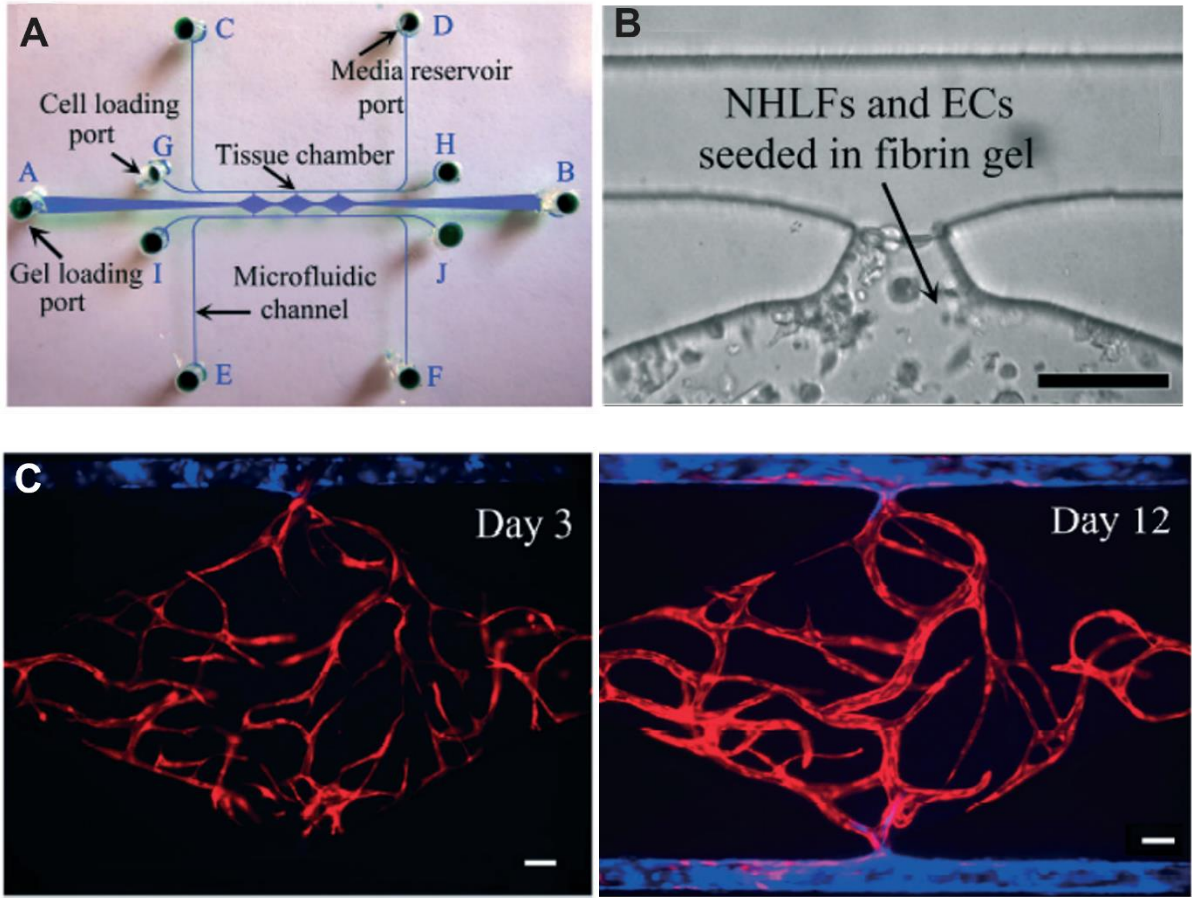

Figure 1.25: *Self-assembled vascular channels. (A) Top view photograph of the chip with the three channels for gel and cell loading, and media perfusion. (B) Fibrin hydrogel loaded in the microfluidic chamber with endothelial cells (ECs) and fibroblasts (NHLFs). (C) Self-formation of a vascular network in a multistep manner (white arrows indicate interconnection between the blue-stained endothelial cells located at the outer channels and the red-stained vascular network embedded in the hydrogel. Reprinted with permission from The Royal Society of Chemistry, 2016 [162].*

The second strategy pursued to fabricate vessel-on-chip devices relies on the intrinsic properties of endothelial cells, which can spatially self-assemble to form vascular networks when seeded within 3D matrices [158–160]. These matrices are formed from natural polymers such as fibrin [161], which can be remodeled by the cells while being mechanically stable to avoid their collapse during cell culture. To study the multistep process of vascular formation that occurs *in vivo,* the integration of hydrogels within microfluidic devices has been exploited. For instance, a microvascular model-on-chip combined the capillary network formation and engineered vessels to better recapitulate vasculogenesis [159,162]. To support this model, a PDMS chip was designed and micromolded to obtain multiple central chambers for hydrogel loading where the capillary network self-assembled, lined by two outer laminin-coated microchannels mimicking the artery/vein (Figure 1.25 A, B). Endothelial cells, along with perivascular fibroblasts formed a lumenized network within the fibrin gels that was tightly interconnected to the engineered artery/vein channel and showed *in vivo*-like barrier properties (Figure 1.25 C) [162]. This microvascular chip represents a model to study the transport across the endothelial barrier in a more physiologically relevant microenvironment than traditional Transwell® assays. Furthermore, perivascular cells found in the surrounding tissues such as fibroblasts, pericytes, or smooth muscle cells can be incorporated in the hydrogel channel, dramatically enhancing the potential of hydrogel-based vessel-on-chip models [163].

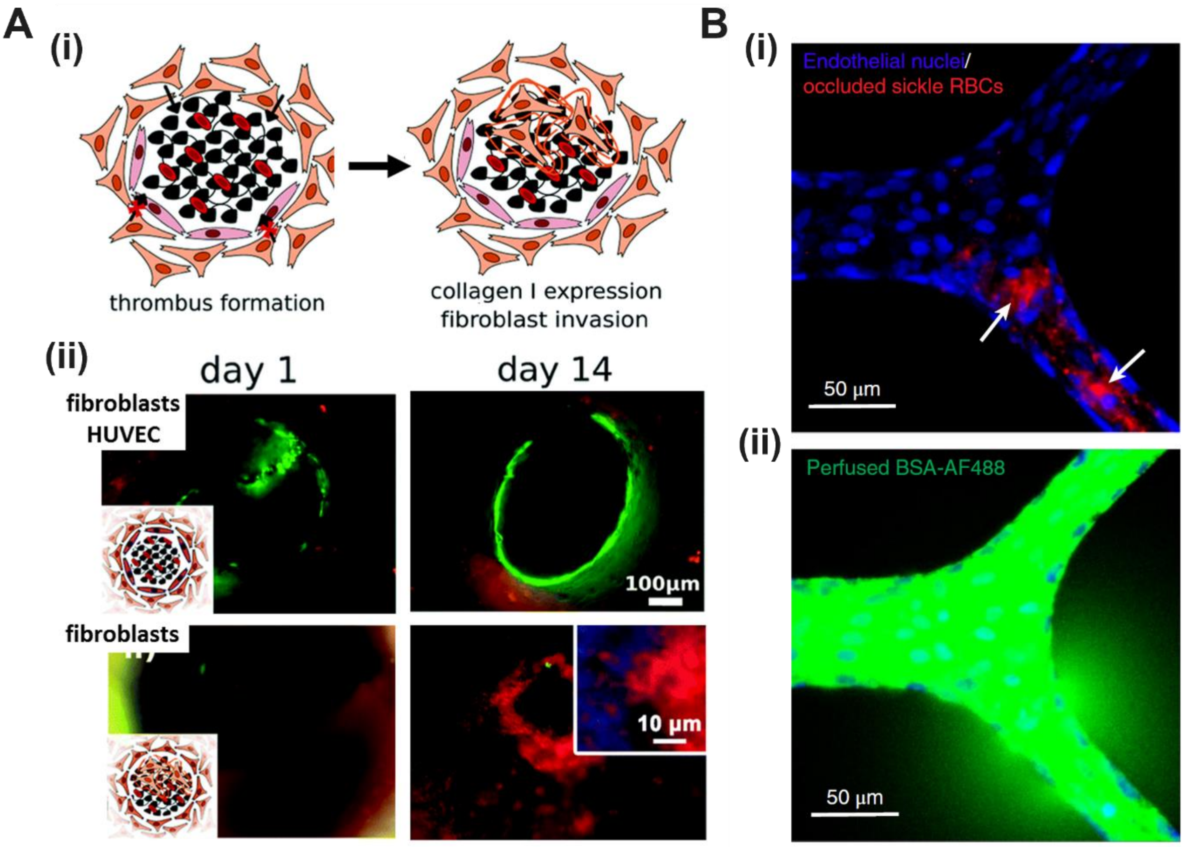

Figure 1.26: *Disease modelling in hydrogel vessel-on-chips. (A) Vascular thrombosis-on-chip. (i) Schematic representation of thrombus formation in a vessel lumen. (ii) Confocal images of collagen I deposition (red) by hydrogel embedded fibroblasts with and without endothelial cell barrier (green) to model the early stage of thrombus formation and the formation of a fibrotic clot over 14 days. Reprinted with permission from The Royal Society of Chemistry, 2016 [110]. (B) Study of sickle red blood cell disease with hydrogel microfluidic chips. (i) Confocal images of endothelialized channels (DAPI staining)*

occluded with sickle red blood cells (red staining) and (ii) colocalized leakage of perfused fluorescent protein (BSA-AF488). Reprinted with permission from Springer Nature, 2018 [164].

These complex microvascular networks can also serve as platforms for disease modelling [110,164]. For example, Zhang et al. established a thrombosis-on-chip model by using a sacrificial bioprinting technique (Figure 1.26 A) [110]. Pluronic ink was used to generate GelMA hollow channels where endothelial cells formed a confluent monolayer. Perfusion of whole blood supplemented with calcium chloride induced both endothelial damage and formation of blood clots and thrombi, which were cleared from the lumen by a thrombolytic agent. By using fibroblasts loaded within the GelMA channels, this chip also modelled fibrotic thrombosis. Fibroblasts migrated within the hydrogel toward the blood clots, releasing ECM proteins and forming fibrotic microtissues within the vessel lumen (Figure 1.26 A) [110]. Furthermore, employing hydrogel microfluidic devices allows for the visualization of endothelial permeability changes in pathological situations such as hematological disorders or infectious diseases like malaria [164]. In one publication, microvessels made of agarose-gelatin via micromolding were exposed to patient-derived sickle red blood cells (Figure 1.26 B). By using fluorescence dyes, increased barrier permeability and vessel obstruction were observed in the channels [164].

1.4.2. BBB models

The central nervous system is a challenging target for therapeutic drugs. The BBB protects the neural tissues from toxic compounds in a very efficient manner by selectively restricting the uptake of small molecules and drugs. This BBB barrier is formed by endothelial cells lining the capillary walls, astrocytes unsheathing the walls, and pericytes embedded in the basement membrane. To develop efficient therapeutic strategies that selectively cross the BBB, a better understanding of this multicellular and complex barrier is required. Conventional neurovascular studies rely on *in vivo* animal models and *in vitro* static cell culture platforms. Both approaches show limitations, either in terms of low throughput and ethical concerns or in the lack of mimicking faithfully the cell microenvironment, respectively. Conventional microfluidic systems consisting of PDMS chips with a semipermeable membrane have been used to better mimic the BBB microenvironment by supporting endothelial cells and neural cells on each side under perfusion [165]. Even though this configuration recreates the fluid flow the BBB is exposed to, it does not allow the formation of 3D architectures where different neural cell types can interact with each other [166]. Thus, there is a growing interest in including ECM analogs within these models to obtain more biomimetic systems.

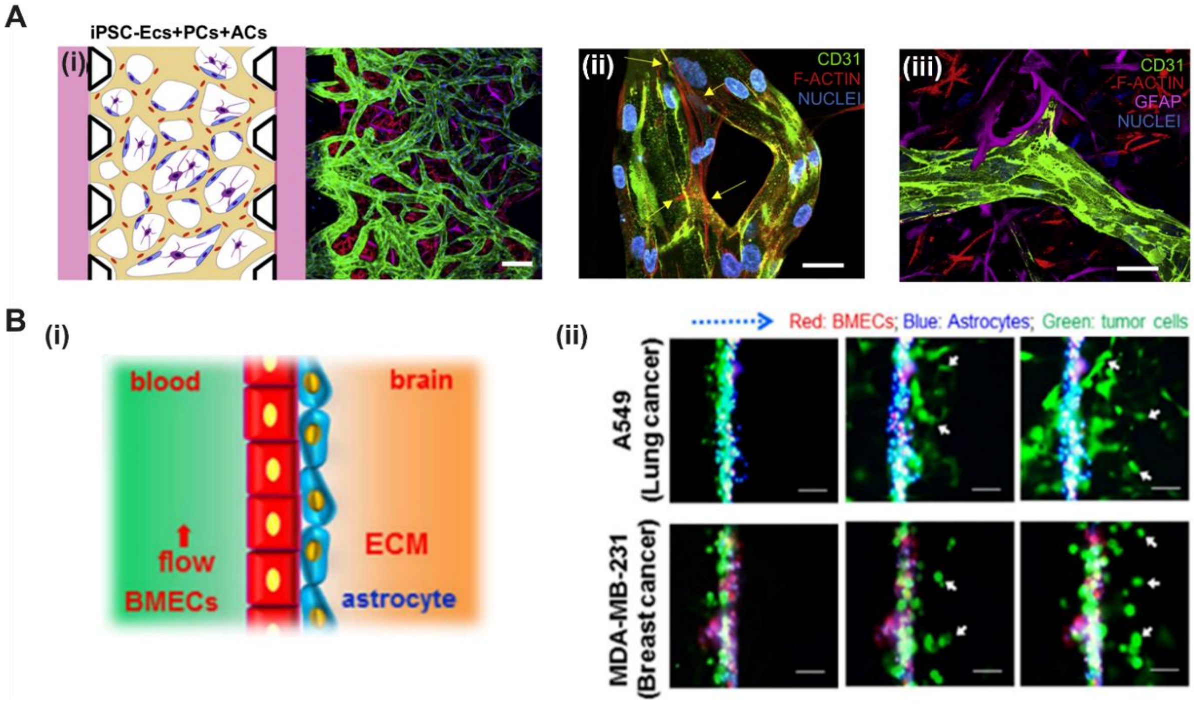

Figure 1.27: *Hydrogel BBB-on-chip models. (A) Neurovascular BBB model. (i) Schematic view of the monoculture of induced pluripotent stem cell-derived endothelial cells (iPSC ECs), co-cultured with pericytes (PCs), and tri cultured with astrocytes (ACs) within a fibrin hydrogel on-chip. Cross-sectional view of hollow microvessels (green) surrounded by (ii) pericytes (blue) and (iii) astrocytes (magenta). Reprinted with permission from Elsevier, 2018* [122]*. (B) BBB model to study metastatic brain tumors. (i) Schematic illustration of the device design to allow the co-culture of brain microvascular endothelial cells (BMECs) and astrocytes. (ii) Time-lapse fluorescence images of the migration of breast and lung cancer cells across the BBB model. Reprinted with permission from Springer Nature, 2016* [167]*.*

Novel hydrogel microfluidic platforms have been shown to support the co-culture of different types of neural cells under flow. Surface tension-based patterning is the preferred microfabrication technique to shape cell-laden hydrogels in BBB models because of its simplicity. It has been employed to establish an *in vitro* neurovascular model where endothelial cells, derived from induced pluripotent stem cells, pericytes and astrocytes were embedded in a fibrin matrix (Figure 1.27 A) [122]. Endothelial cells self-assembled into perfusable microvessels with low permeability and strong tight junctions within the hydrogel. Direct interactions of the microvessels with astrocytes and pericytes improved cell barrier maturation and function, compared to endothelial cell only models, as shown in other studies [103,128]. These improved properties were recently exploited to study PEG-coated nanoparticle transport across the barrier [123]. Using time-dependent image analysis of nanoparticle distribution inside and outside the microvasculature, the impact of size and functionalization of the nanoparticles on their permeability could be assessed, proving the suitability of this *in vitro* model for preclinical drug screening evaluations.

In addition to its relevancy in drug delivery, the BBB is involved in pathological processes such as tumor metastasis. By including hydrogels in the microfluidic device, tumor cell extravasation in the central nervous system could be studied [167]. In this work, replica molding was employed to fabricate a multiplexed PDMS microfluidic chip consisting of a vascular channel and another one in which a cell-laden collagen hydrogel was loaded. The extravasation of lung and breast cancer cells across the formed BBB was observed, reproducing similar results of brain metastasis seen *in vivo* (Figure 1.27 B) [167]. This chip was used for testing chemotherapeutic drugs approved for brain cancer treatment as a preclinical screening tool. By targeting hydrogel-embedded glioma cells, different efficacy results were obtained for each drug in the presence of the BBB.

1.4.3. Hepatic models

The liver sustains critical physiological functions within the human body such as detoxification, drug metabolism, bile acid production and protein synthesis. Exchange of metabolites and oxygen occurs at the liver sinusoid, where hepatocytes interact with a defenestrated barrier of endothelial cells. In preclinical studies, hepatoxicity tests are a standard procedure to assess the risks of discovered drugs on human health. However, several drug withdrawals due to their hepatoxic effects have shown the limitations of current toxicological models [168]. Because of this, great effort has been put into developing functional liver-on-chips that could be implemented in the preclinical testing pipeline. Conventional microfluidics have proven success in this field [36]. However, they lack an *in vivo*-like 3D matrix where hepatocytes can develop and interact directly with the endothelial barrier.

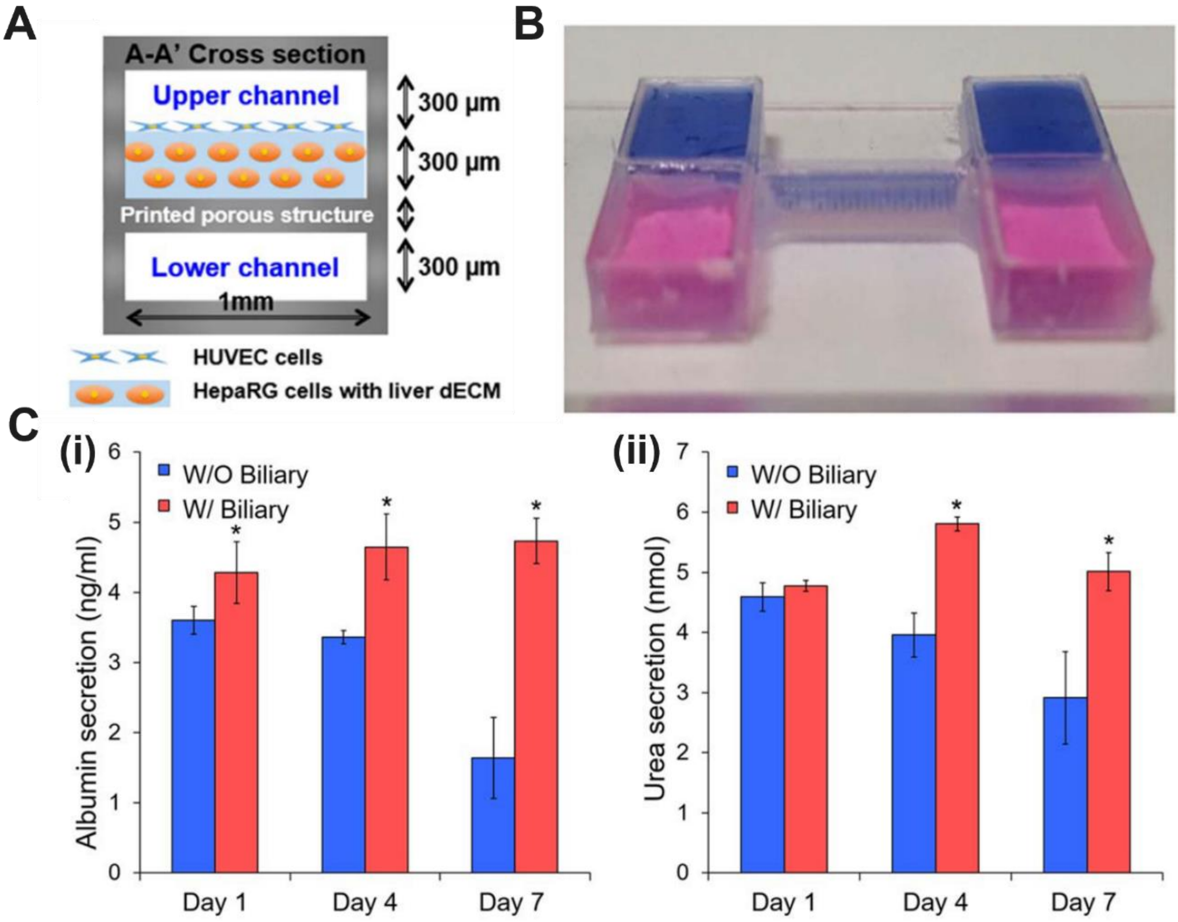

Figure 1.28: *Bioprinted hydrogel liver-on-chip model. (A) Schematic of the 3D printed device with an upper and lower channel for co-culture of endothelial cells (HUVEC) and hepatic cells (HepaRG). (B) Image of the two-channel device. (C) (i) Albumin and (ii) urea secretion levels with and without lower biliary channel. Reprinted with permission from IOP Publishing, 2019* [109].

Hydrogels are well suited to reproduce the spatial architecture of hepatic tissue barriers. Bioprinting has been proven to be a useful technique to spatially define the heterotypic interactions between hepatic cells and vascular endothelial cells. This technique was employed to print cell-laden hydrogels within a polycaprolactone (PCL) microfluidic chip, allowing the localized formation of an endothelial barrier on top of the 3D hepatocyte-embedded hydrogel [133]. The composition of the cell-laden bioinks was a mixture of gelatin and collagen type I. The bioprinted liver-on-chip showed high cell viability and increased albumin and urea synthesis, essential functions of the liver, compared to cell culture in static conditions. The same model was updated by including a biliary-like lower channel (Figure 1.28 A, B) [109]. In this case, liver dECM was used to embed the hepatic cells and support the endothelial barrier on top. In this configuration, liver functionalities such as albumin and urea secretion levels, along with drug metabolism capabilities were further improved (Figure 1.28 C). The liver-on-chip model also showed sensitivity to drug toxicity analysis.

1.4.4. Renal models

Kidneys are responsible for filtering and reabsorbing specific solutes in a selective manner according to their size and charge. Their functional units, called nephrons, regulate the exchange of these solutes through specific barriers. Among these, glomeruli are networks of blood vessels that are encapsulated in a cup-like sac and located at the proximal site of the kidney, where the filtrate enters the tubular nephron. Glomeruli have been reproduced on-chip to construct a model of diabetic nephropathy, a vascular pathology induced by high blood glucose levels [169]. Micromolding was used to produce a PDMS chip, consisting of a capillary channel mimicking the vascular lumen, a hydrogel channel representing the glomerular basement membrane, and a collection channel that acts as the glomerular capsule (Figure 1.29 A). The hydrogel channel was filled with Matrigel to support the growth of primary glomerular microtissues. The collection channel allowed collection of renal filtrates for further characterization. Under high glucose medium perfusion, the glomerular barrier showed higher permeability values and protein leakage was observed, reproducing the *in vivo* pathological responses of the glomeruli to hyperglycemia (Figure 1.29 A) [169].

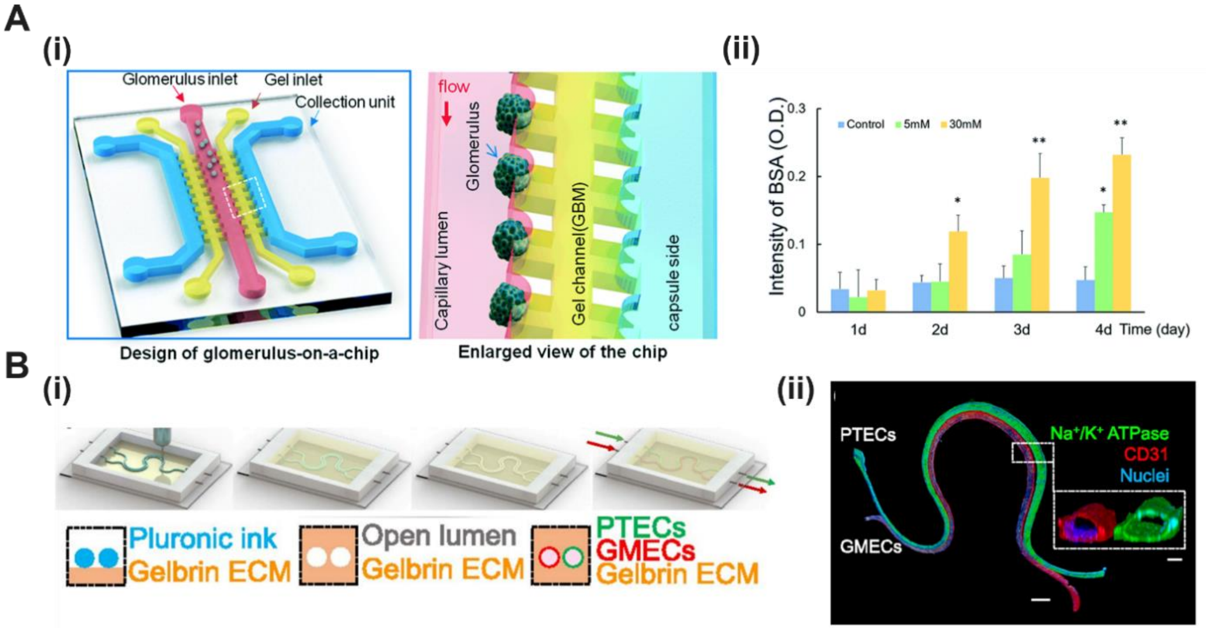

Figure 1.29: *Hydrogel kidney-on-chip. (A) Renal glomerulus-on-chip. (i) Schematic illustration of the microchip device with a capillary channel, a hydrogel loading channel and a collection channel*

mimicking the compartments of the renal glomerulus. (ii) Bovine serum albumin (BSA) filtration rate through the glomerular barrier under different glucose concentrations to quantify barrier permeability. Reprinted with permission from The Royal Society of Chemistry, 2017 [169]*. (B) Vascularized proximal tubule model. (i) Schematic view of the bioprinting process of the channels using sacrificial inks. (ii) Immunostaining image of the glomerular microvascular endothelial cells (GMECs, red) and proximal tubule epithelial cells (PTECs, green). Reprinted with permission from Proceedings of the National Academy of Sciences, 2019* [108]*.*

Another important part of the nephron is the proximal tubule, which plays an essential role in nutrient transport of the renal filtrate from the nephron to the bloodstream. Different studies with hydrogel microfluidic platforms have modelled it by generating hollow perfusable structures [170,171]. Convoluted proximal tubules were produced using 3D bioprinting techniques to fabricate their complex shape. For instance, twisted hollow channels within enzymatically cross-linked gelatin/fibrin matrix were produced by sacrificial templating using Pluronic, allowing epithelial cells to grow and form a functional barrier under flow [107]. Recently, the same approach was employed to mimic the proximal tubule endothelial barrier through bioprinting of two adjacent microchannels (Figure 1.29 B) [108]. Reabsorption of proteins such as albumin and glucose were confirmed with this model. Furthermore, exposing the renal epithelial barrier to a hyperglycemic state induced a dysfunction of the endothelial barrier, suggesting a cross-talk between the two barriers.

1.4.5. Intestinal models

The small intestine is the main site of absorption of nutrients and water within the gastrointestinal tract (GI) [172]. Shaped as a long tube connecting the stomach with the large intestine, it can be divided into three main parts: the duodenum, the jejunum and the ileum (Figure 1.30 A) [173,174]. The duodenum directly connects with the stomach and has a large surface area for nutrient uptake and digestion. The jejunum also plays a significant role in nutrient absorption while being smaller in diameter. The ileum is the final section of the small intestine, joining it to the large intestine. Moreover, the small intestine is organized in multiple layers with different functions (Figure 1.30 B) [175]. The intestinal mucosa is the innermost layer of the organ, directly in contact with the intestinal lumen to absorb nutrients. Found below the intestinal mucosa, the submucosa is a dense layer of connective tissue where nerves, lymphatic and blood vessels are located. The *muscularis propria* organizes in two layers of inner circular smooth muscle cells and outer longitudinal smooth muscle cells, ensuring peristaltic movement of ingested nutrients along the GI. Finally, the serosa, also referred as adventitia, is the outer sheet of fibrous connective tissue surrounding the small intestine.

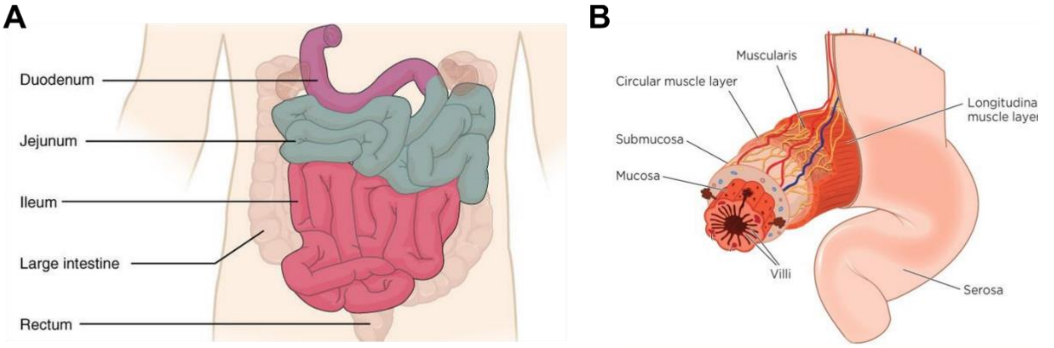

Figure 1.30: *Structure of the small intestine. (A) Schematic of the different parts of the small intestine. Adapted with permission from* [5]*. (B) Illustration of the different layers of the small intestine. Adapted with permission from* [6]*.*

The intestinal mucosa is composed of three main compartments: the epithelium, the lamina propria, also named intestinal stroma, and the *muscularis mucosae* (Figure 1.31 A). The epithelial layer acts as a semi-permeable barrier for selective nutrient uptake and pathogen protection [176]. Covered by a protective mucus layer, the cell monolayer lines the intestinal lumen while being exposed to peristaltic flow. It organizes itself in a three-dimensional (3D) manner, with finger-like protrusions called villi, formed mostly by polarized enterocytes, and tissue invaginations called crypts, where intestinal stem cells (ISC) differentiate and migrate to the villi, self-renewing the epithelial layer periodically to support its function [177] (Figure 1.31 B). The epithelium also hosts the gut microbiota, a vast group of symbiotic bacteria responsible for nutrient digestion and intestinal homeostasis [178]. Moreover, the lamina propria is a connective tissue layer found below the epithelium and made of extracellular proteins, such as structural collagens, glycoproteins, and proteoglycans. It contains various types of stromal cells, including mesenchymal cells and fibroblasts [179], along with smooth muscle cells and immune cells like macrophages, neutrophils, and lymphocytes [180,181]. Blood vessels and capillaries organize within the stromal compartment to transport the nutrients to the rest of the body (Figure 1.31 B). The third layer is the *muscularis mucosae*, a thin layer of smooth muscle cells that facilitates peristaltic flow within the lumen and separates the mucosa from the submucosa [182].

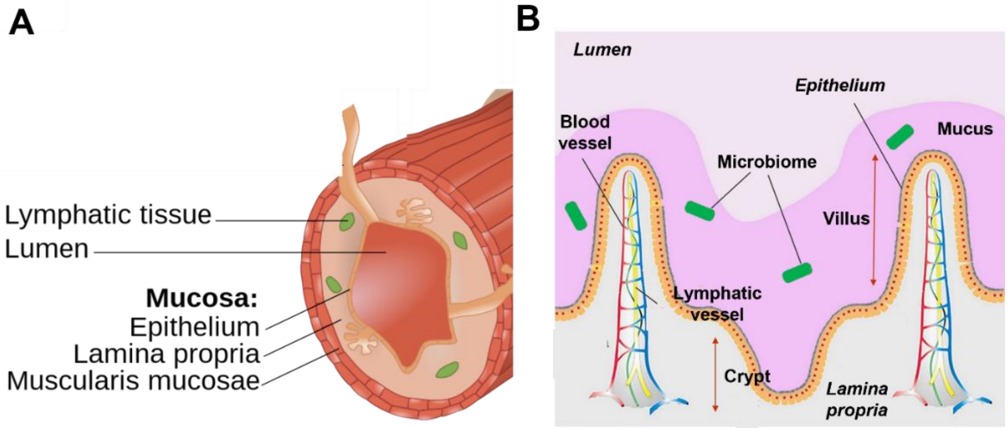

Figure 1.31: *Overview of the intestinal mucosa. (A) Illustration of the different layers and (B) spatial distribution of the intestinal cells along the crypt-villus axis. Adapted with permission from SAGE Journals, 2020* [14]*.*

The multicellularity and 3D architecture of the epithelium are very important parameters to properly perform these functions, as well as the basement membrane and stromal compartment forming the lamina propria of the tissue [87]. In addition, flow conditions are highly relevant for cell microenvironment and barrier function. For this reason, hydrogel gut-on-chip models have been developed to combine the benefits of biomimetic 3D hydrogels with microfluidic intestinal cell culture [105,183]. For instance, replica molding has been used to produce villus-like microstructures using collagen (Figure 1.32 A) [184]. A mechanical stage was then used to expose cells to gravity-driven fluid flow. The combination of flow-induced shear stress and 3D topography enhanced cell polarization and key cellular functions such as metabolic activity and permeability compared to static cell cultures. In another approach, hydrogels have been included in the microfluidic channels mimicking the gut tube to account for the lamina propria compartment with the focus placed on high throughput testing and easy visualization of the barrier leakiness. A popular approach is surface tension-based patterning of collagen I, which was loaded and shaped on a central channel, supporting the intestinal epithelial monolayer. This technology has been employed to create enterocyte cell tubules in a multiplexed microfluidic platform for high throughput testing of compounds on barrier integrity using fluorescent dyes (Figure 1.32 B) [105]. The same technology has also been used to model intestinal bowel disease *in vitro* [185]. In there, epithelial cells were exposed to inflammatory cytokines, inducing cell barrier leakiness. It was shown that this inflammatory-induced disruption could be modulated with specific inhibitors, showing its potential to design therapeutic targets.

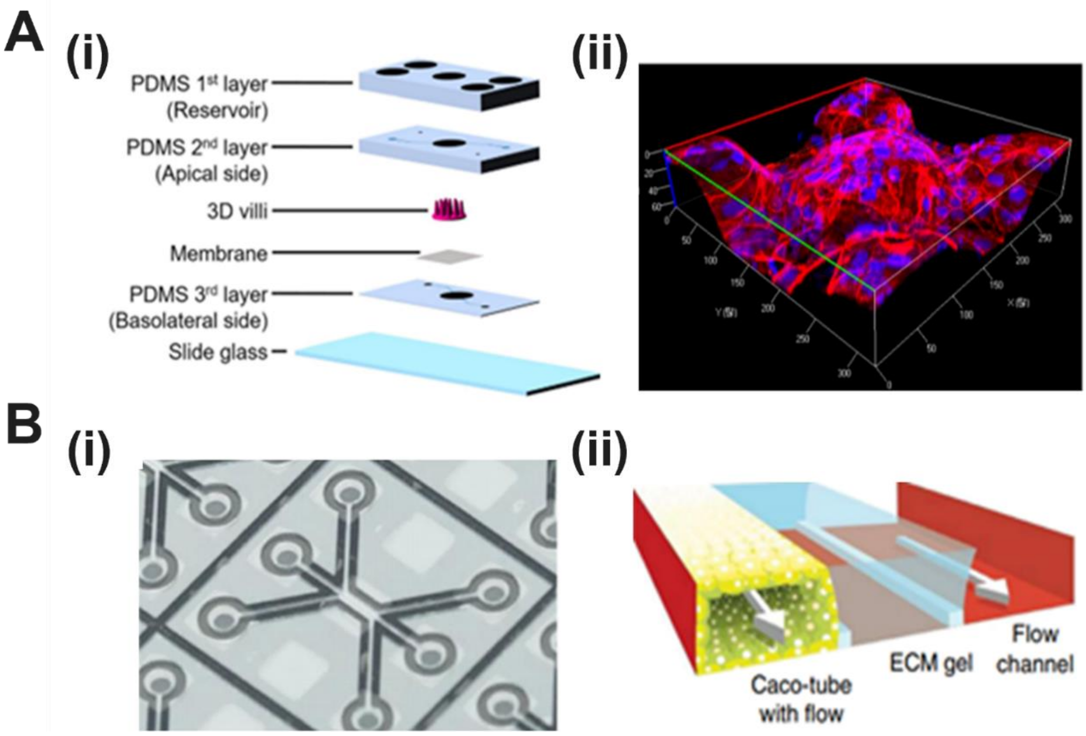

Figure 1.32: *Hydrogel gut-on-chip models. (A) Microfluidic intestinal model with a 3D villi-like scaffold. (i) Detailed view of the gut-on-chip. (ii) Confocal image of intestinal enterocytes (Caco-2 cells) cultured on top of the hydrogel. Reprinted with permission from Springer Nature, 2017* [184]*. (B) Tubular gut-on-chip. (i) Photograph of the multiplexed three-lane microfluidic chip OrganoPlate®. (ii) Schematic view of collagen-based scaffold to support Caco-2 cell barrier formation within the chip. Reprinted with permission from Springer Nature, 2017* [105]*.*

Some of these gut-on-chips have also included the stromal compartment within microfabricated hydrogels to recapitulate the multicellular organization and topography of the intestinal mucosa. For example, collagen scaffolds reproducing the shape and dimensions of mouse crypts and villi were micropatterned via replica molding for a gut-on-chip device (Figure 1.33 A) [186]. Primary mouse intestinal fibroblasts were embedded within the 3D hydrogels to reproduce the stromal compartment while organoid-derived mouse epithelial cells were seeded on top for dynamic cell culture. Under these conditions, it was shown that shear stress improved the maintenance of a polarized epithelial monolayer on the cell-laden scaffolds for long-term cell culture conditions, with proper differentiation and spatial segregation of intestinal cells along the crypt-villus axis (Figure 1.33 A). In another study, Nikolaev et al. generated cell-laden hydrogel channels recreating intestinal crypt-like invaginations for co-culture using laser photopatterning (Figure 1.33 B) [132]. Epithelial cells were co-cultured with different cell types present in the intestinal lamina propria embedded in the hydrogel channel, such as immune cells (macrophages) and mouse intestinal myofibroblasts. For the latter, myofibroblasts migrated within the scaffold, displayed elongated morphologies, and interacted with epithelial cells for one week under perfusion, demonstrating the ability of the intestinal model to establish an *in vivo*-like compartmentalized organization (Figure 1.33 B). However, even though these gut-on-chip models have successfully recapitulated key aspects of the intestinal mucosa, the proposed microfabrication techniques have several drawbacks as they either rely on cumbersome procedures or expensive equipment, limiting their potential applications in the field.

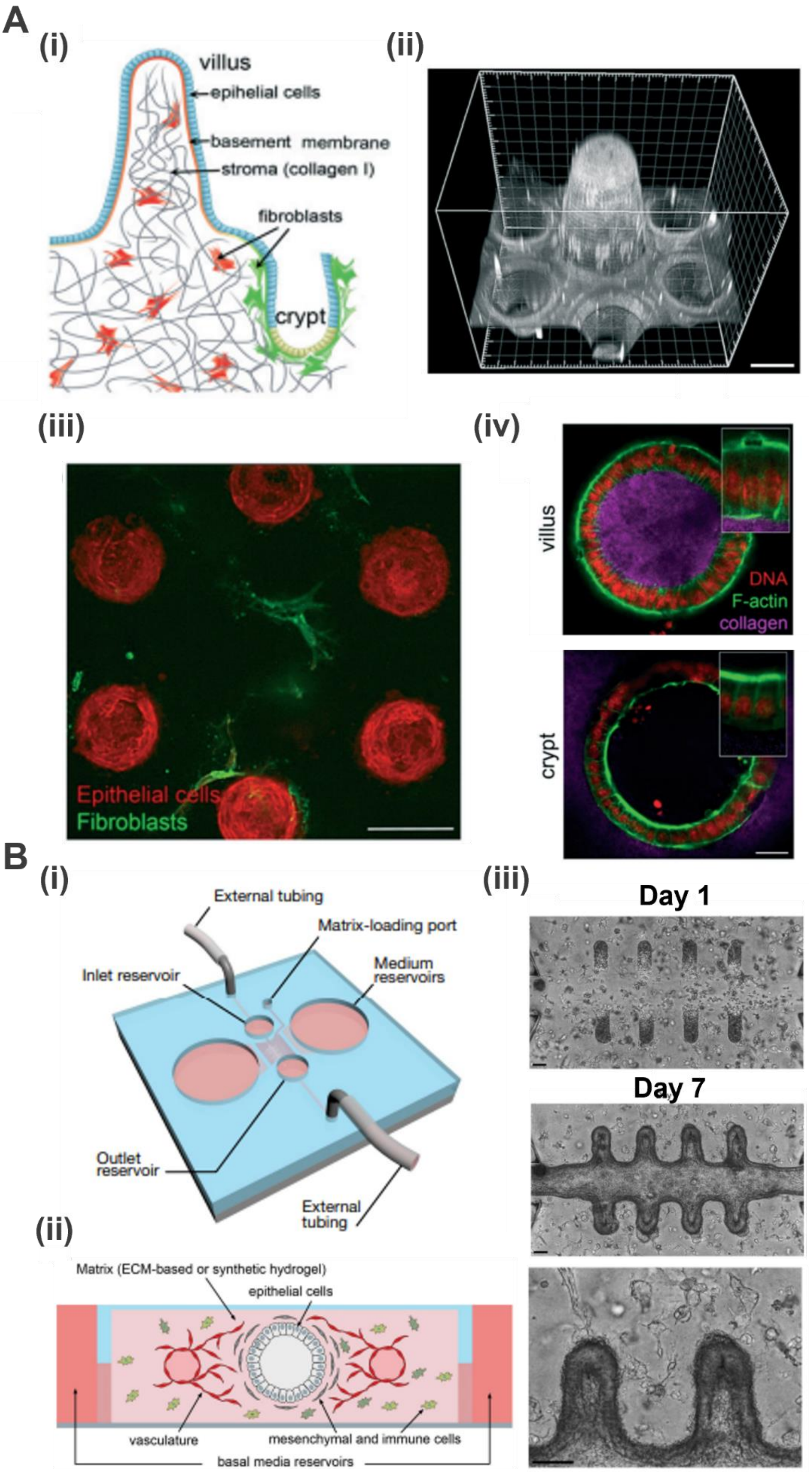

Figure 1.33: *Modelling the intestinal mucosa on hydrogel gut-on-chips. (A) 3D hydrogel gut-on-chip model representing the crypt-villus axis to study stromal-epithelial interactions. (i) Schematic*

representation of the intestinal mucosa in the small intestine. (ii) Image of the PDMS mold coated with laminin showing one villus surrounded by six crypts. Scale bar: 150 µm. (iii) Top confocal view of an epithelial monolayer (F-actin labelled in red) on the collagen scaffold containing fibroblasts (expressing αSMA, green) 4 days after seeding the organoids. Scale bar: 150 µm. (iv) Cross-section of the villus and crypt on collagen scaffolds. Collagen type I (TAMRA-labelled in pink); F-actin (phalloidin labelled in green) and nuclei (DAPI, red) are stained. Scale bar: 20 µm. Adapted with permission from the Royal Society of Chemistry, 2021 [186]*. (B) 3D hydrogel gut-on-chips with lateral crypt-like structures to study organoid morphogenesis. (i) Schematic of the 3D gut-on-chip device consisting of a hydrogel chamber in the center with two external medium reservoirs and two inlet and outlet reservoirs for perfusion through the lumen. (ii) Schematic representation of the 3D hydrogel gut-on-chip with an epithelium and various non-parenchymal cell types seeded in the matrix surrounding it. (iii) Brightfield images of co-cultured organoid-derived epithelial cells with mouse intestinal myofibroblasts encapsulated in the hydrogel at day 1 (top) and day 7 (medium and bottom). Myofibroblasts extensively migrate through the gel, directly interacting with the epithelium. Scale bars: 50 µm. Adapted with permission from Nature, 2020* [132].

1.5. References

1. Marchiando, A. M., Graham, W. V. & Turner, J. R. Epithelial barriers in homeostasis and disease. *Annual Review of Pathology: Mechanisms of Disease* **5**, 119–144 (2010).
2. Salim, S. Y. & Söderholm, J. D. Importance of disrupted intestinal barrier in inflammatory bowel diseases. *Inflamm Bowel Dis* **17**, 362–381 (2011).
3. Poisson, J. *et al.* Liver sinusoidal endothelial cells: Physiology and role in liver diseases. *J Hepatol* **66**, 212–227 (2017).
4. Shin, K., Fogg, V. C. & Margolis, B. Tight Junctions and Cell Polarity. *https://doi.org/10.1146/annurev.cellbio.22.010305.104219* **22**, 207–235 (2006).
5. Tsukita, S., Furuse, M. & Itoh, M. Multifunctional strands in tight junctions. *Nat Rev Mol Cell Biol* **2**, 285–293 (2001).
6. Harris, T. J. C. & Tepass, U. Adherens junctions: from molecules to morphogenesis. *Nature Reviews Molecular Cell Biology 2010 11:7* **11**, 502–514 (2010).
7. Yuan, S. Y. & Rigor, R. R. Signaling Mechanisms in the Regulation of Endothelial Permeability. (2010).
8. Kurashima, Y. *et al.* Mucosal mesenchymal cells: Secondary barrier and peripheral educator for the gut immune system. *Front Immunol* **8**, 298053 (2017).
9. Brown, L. S. *et al.* Pericytes and neurovascular function in the healthy and diseased brain. *Front Cell Neurosci* **13**, 457589 (2019).
10. Theocharis, A. D., Skandalis, S. S., Gialeli, C. & Karamanos, N. K. Extracellular matrix structure. *Adv Drug Deliv Rev* **97**, 4–27 (2016).
11. Pozzi, A., Yurchenco, P. D. & Iozzo, R. V. The nature and biology of basement membranes. *Matrix Biology* **57–58**, 1–11 (2017).
12. Powell, D. W., Pinchuk, I. V., Saada, J. I., Chen, X. & Mifflin, R. C. Mesenchymal Cells of the Intestinal Lamina Propria. *Annu Rev Physiol* **73**, 213–237 (2011).
13. Pompili, S., Latella, G., Gaudio, E., Sferra, R. & Vetuschi, A. The Charming World of the Extracellular Matrix: A Dynamic and Protective Network of the Intestinal Wall. *Front Med (Lausanne)* **8**, 610189 (2021).
14. Roux, E., Bougaran, P., Dufourcq, P. & Couffinhal, T. Fluid Shear Stress Sensing by the Endothelial Layer. *Front Physiol* **11**, 533349 (2020).
15. Cunningham, K. S. & Gotlieb, A. I. The role of shear stress in the pathogenesis of atherosclerosis. *Laboratory Investigation* **85**, 9–23 (2005).

16. Cremer, J. *et al.* Effect of flow and peristaltic mixing on bacterial growth in a gut-like channel. *Proc Natl Acad Sci U S A* **113**, 11414–11419 (2016).
17. Palumbo, P. *et al.* A general approach to the apparent permeability index. *J Pharmacokinet Pharmacodyn* **35**, 235–248 (2008).
18. Hidalgo, I. J., Raub, T. J. & Borchardt, R. T. Characterization of the Human Colon Carcinoma Cell Line (Caco-2) as a Model System for Intestinal Epithelial Permeability. *Gastroenterology* **96**, 73649 (1989).
19. Hubatsch, I., Ragnarsson, E. G. E. & Artursson, P. Determination of drug permeability and prediction of drug absorption in Caco-2 monolayers. *Nature Protocols 2007 2:9* **2**, 2111–2119 (2007).
20. Hilgers A, C. R. B. P. Caco-2 Cell Monolayers as a Model for Drug Transport Across the Intestinal Mucosa. *Pharm Res* **7**, (1990).
21. Kämpfer, A. A. M. *et al.* Development of an in vitro co-culture model to mimic the human intestine in healthy and diseased state. *Toxicology in Vitro* **45**, 31–43 (2017).
22. Hatherell, K., Couraud, P. O., Romero, I. A., Weksler, B. & Pilkington, G. J. Development of a three-dimensional, all-human in vitro model of the blood–brain barrier using mono-, co-, and tri-cultivation Transwell models. *J Neurosci Methods* **199**, 223–229 (2011).
23. Costa, A., de Souza Carvalho-Wodarz, C., Seabra, V., Sarmento, B. & Lehr, C. M. Triple co-culture of human alveolar epithelium, endothelium and macrophages for studying the interaction of nanocarriers with the air-blood barrier. *Acta Biomater* **91**, 235–247 (2019).
24. Piossek, F. *et al.* Physiological oxygen and co-culture with human fibroblasts facilitate in vivo-like properties in human renal proximal tubular epithelial cells. *Chem Biol Interact* **361**, 109959 (2022).
25. Kelm, J. M., Lal-Nag, M., Sittampalam, G. S. & Ferrer, M. Translational in vitro research: integrating 3D drug discovery and development processes into the drug development pipeline. *Drug Discov Today* **24**, 26–30 (2019).
26. Mammoto, T., Mammoto, A. & Ingber, D. E. Mechanobiology and Developmental Control. (2013) doi:10.1146/annurev-cellbio-101512-122340.
27. Zhang, B., Korolj, A., Lai, B. F. L. & Radisic, M. Advances in organ-on-a-chip engineering. *Nature Reviews Materials 2018 3:8* **3**, 257–278 (2018).
28. Bhatia, S. N. & Ingber, D. E. Microfluidic organs-on-chips. *Nature Biotechnology 2014 32:8* **32**, 760–772 (2014).
29. Huh, D., Hamilton, G. A. & Ingber, D. E. From 3D cell culture to organs-on-chips. *Trends Cell Biol* **21**, 745–754 (2011).
30. Grant, J. *et al.* Simulating drug concentrations in PDMS microfluidic organ chips. *Lab Chip* **21**, 3509–3519 (2021).
31. Huh, D. *et al.* Reconstituting organ-level lung functions on a chip. *Science (1979)* **328**, 1662–1668 (2010).
32. Jang, K. J. *et al.* Reproducing human and cross-species drug toxicities using a Liver-Chip. *Sci Transl Med* **11**, (2019).
33. Jang, K. J. *et al.* Human kidney proximal tubule-on-a-chip for drug transport and nephrotoxicity assessment. *Integrative Biology* **5**, 1119–1129 (2013).
34. Achyuta, A. K. H. *et al.* A modular approach to create a neurovascular unit-on-a-chip. *Lab Chip* **13**, 542–553 (2013).
35. Kim, H. J. & Ingber, D. E. Gut-on-a-Chip microenvironment induces human intestinal cells to undergo villus differentiation. *Integrative Biology* **5**, 1130–1140 (2013).
36. Illa, X. *et al.* A novel modular bioreactor to in Vitro study the hepatic sinusoid. *PLoS One* **9**, 1–5 (2014).

37. Mukhopadhyay, R. When PDMS isn't the best. *Anal Chem* **79**, 3249–3253 (2007).
38. Berthier, E., Young, E. W. K. & Beebe, D. Engineers are from PDMS-land, Biologists are from Polystyrenia. *Lab Chip* **12**, 1224–1237 (2012).
39. Campbell, S. B. *et al.* Beyond Polydimethylsiloxane: Alternative Materials for Fabrication of Organ-on-a-Chip Devices and Microphysiological Systems. *ACS Biomater Sci Eng* **7**, 2880–2899 (2021).
40. Liu, H. *et al.* Advances in Hydrogels in Organoids and Organs-on-a-Chip. *Advanced Materials* **31**, 1–28 (2019).
41. Terrell, J. A., Jones, C. G., Kabandana, G. K. M. & Chen, C. From cells-on-a-chip to organs-on-a-chip: scaffolding materials for 3D cell culture in microfluidics. *J Mater Chem B* **8**, 6667–6685 (2020).
42. Tibbitt, M. W. & Anseth, K. S. Hydrogels as Extracellular Matrix Mimics for 3D Cell Culture. (2009) doi:10.1002/bit.22361.
43. Malda, J. *et al.* 25th Anniversary Article: Engineering Hydrogels for Biofabrication. *Advanced Materials* **25**, 5011–5028 (2013).
44. Caliari, S. R. & Burdick, J. A. A practical guide to hydrogels for cell culture. *Nature Methods 2016 13:5* **13**, 405–414 (2016).
45. Catoira, M. C., Fusaro, L., Di Francesco, D., Ramella, M. & Boccafoschi, F. Overview of natural hydrogels for regenerative medicine applications. *J Mater Sci Mater Med* **30**, 1–10 (2019).
46. Antoine, E. E., Vlachos, P. P. & Rylander, M. N. Review of Collagen I Hydrogels for Bioengineered Tissue Microenvironments: Characterization of Mechanics, Structure, and Transport. *Tissue Eng Part B Rev* **20**, 683 (2014).
47. Hughes, C. S., Postovit, L. M. & Lajoie, G. A. Matrigel: A complex protein mixture required for optimal growth of cell culture. *Proteomics* **10**, 1886–1890 (2010).
48. Yue, K. *et al.* Synthesis, properties, and biomedical applications of gelatin methacryloyl (GelMA) hydrogels. *Biomaterials* **73**, 254–271 (2015).
49. Xu, X., Jha, A. K., Harrington, D. A., Farach-Carson, M. C. & Jia, X. Hyaluronic acid-based hydrogels: from a natural polysaccharide to complex networks. *Soft Matter* **8**, 3280–3294 (2012).
50. Zarrintaj, P. *et al.* Agarose-based biomaterials for tissue engineering. *Carbohydr Polym* **187**, 66–84 (2018).
51. Neves, M. I., Moroni, L. & Barrias, C. C. Modulating Alginate Hydrogels for Improved Biological Performance as Cellular 3D Microenvironments. *Front Bioeng Biotechnol* **8**, 665 (2020).
52. Aisenbrey, E. A. & Murphy, W. L. Synthetic alternatives to Matrigel. *Nat Rev Mater* **5**, 539 (2020).
53. Lutolf, M. P. & Hubbell, J. A. Synthetic biomaterials as instructive extracellular microenvironments for morphogenesis in tissue engineering. *Nature Biotechnology 2005 23:1* **23**, 47–55 (2005).
54. Culver, J. C. *et al.* Three-dimensional biomimetic patterning in hydrogels to guide cellular organization. *Advanced Materials* **24**, 2344–2348 (2012).
55. Huebsch, N. Translational mechanobiology: Designing synthetic hydrogel matrices for improved in vitro models and cell-based therapies. *Acta Biomater* **94**, 97–111 (2019).
56. Slaughter, B. V, Khurshid, S. S., Fisher, O. Z., Khademhosseini, A. & Peppas Biomaterials, N. A. Hydrogels in Regenerative Medicine HHS Public Access. *Adv Mater* **21**, 3307–3329 (2009).

57. Lutolf, M. P. & Hubbell, J. A. Synthetic biomaterials as instructive extracellular microenvironments for morphogenesis in tissue engineering. *Nature Biotechnology 2005 23:1* **23**, 47–55 (2005).
58. D’souza, A. A. & Shegokar, R. Polyethylene glycol (PEG): a versatile polymer for pharmaceutical applications. *Expert Opin Drug Deliv* **13**, 1257–1275 (2016).
59. Cuchiara, M. P., Allen, A. C. B., Chen, T. M., Miller, J. S. & West, J. L. Multilayer microfluidic PEGDA hydrogels. *Biomaterials* **31**, 5491–5497 (2010).
60. Phelps, E. A., Landázuri, N., Thulé, P. M., Taylor, W. R. & García, A. J. Bioartificial matrices for therapeutic vascularization. *Proc Natl Acad Sci U S A* **107**, 3323–3328 (2010).
61. Zhao, Z. *et al.* Composite Hydrogels in Three-Dimensional in vitro Models. *Front Bioeng Biotechnol* **8**, 611 (2020).
62. Vila, A. *et al.* Hydrogel co-networks of gelatine methacrylate and poly(ethylene glycol) diacrylate sustain 3D functional in vitro models of intestinal mucosa. *Biofabrication* **12**, (2020).
63. Wang, Y. *et al.* Development of a Photo-Crosslinking, Biodegradable GelMA/PEGDA Hydrogel for Guided Bone Regeneration Materials. *Materials 2018, Vol. 11, Page 1345* **11**, 1345 (2018).
64. Tenje, M. *et al.* A practical guide to microfabrication and patterning of hydrogels for biomimetic cell culture scaffolds. *Organs-on-a-Chip* 100003 (2020) doi:10.1016/j.ooc.2020.100003.
65. Hu, W., Wang, Z., Xiao, Y., Zhang, S. & Wang, J. Advances in crosslinking strategies of biomedical hydrogels. *Biomater Sci* **7**, 843–855 (2019).
66. Walters, B. D. & Stegemann, J. P. Strategies for directing the structure and function of three-dimensional collagen biomaterials across length scales. *Acta Biomater* **10**, 1488–1501 (2014).
67. Bidarra, S. J., Barrias, C. C. & Granja, P. L. Injectable alginate hydrogels for cell delivery in tissue engineering. *Acta Biomater* **10**, 1646–1662 (2014).
68. Parhi, R. Cross-Linked Hydrogel for Pharmaceutical Applications: A Review. *Adv Pharm Bull* **7**, 515 (2017).
69. Paguirigan, A. & Beebe, D. J. Gelatin based microfluidic devices for cell culture. *Lab Chip* **6**, 407–413 (2006).
70. Rowe, S. L., Lee, S. Y. & Stegemann, J. P. Influence of thrombin concentration on the mechanical and morphological properties of cell-seeded fibrin hydrogels. *Acta Biomater* **3**, 59–67 (2007).
71. Li, X. & Xiong, Y. Application of ‘Click’ Chemistry in Biomedical Hydrogels. *ACS Omega* **7**, 36918–36928 (2022).
72. Xu, Z. & Bratlie, K. M. Click Chemistry and Material Selection for in Situ Fabrication of Hydrogels in Tissue Engineering Applications. *ACS Biomater Sci Eng* **4**, 2276–2291 (2018).
73. Pereira, R. F. & Bártolo, P. J. 3D Photo-Fabrication for Tissue Engineering and Drug Delivery. *Engineering* **1**, 090–112 (2015).
74. Yao, H., Wang, J. & Mi, S. Photo Processing for Biomedical Hydrogels Design and Functionality: A Review. *Polymers (Basel)* **10**, (2018).
75. Choi, J. R., Yong, K. W., Choi, J. Y. & Cowie, A. C. Recent advances in photo-crosslinkable hydrogels for biomedical applications. *Biotechniques* **66**, 40–53 (2019).
76. Ji, S., Almeida, E. & Guvendiren, M. 3D bioprinting of complex channels within cell-laden hydrogels. *Acta Biomater* **95**, 214–224 (2019).

77. Williams, C. G., Malik, A. N., Kim, T. K., Manson, P. N. & Elisseeff, J. H. Variable cytocompatibility of six cell lines with photoinitiators used for polymerizing hydrogels and cell encapsulation. *Biomaterials* **26**, 1211–1218 (2005).
78. Chen, M. B., Srigunapalan, S., Wheeler, A. R. & Simmons, C. A. A 3D microfluidic platform incorporating methacrylated gelatin hydrogels to study physiological cardiovascular cell-cell interactions. *Lab Chip* **13**, 2591–2598 (2013).
79. Zhu, W. *et al.* Direct 3D bioprinting of prevascularized tissue constructs with complex microarchitecture. *Biomaterials* **124**, 106–115 (2017).
80. Zhang, R. & Larsen, N. B. Stereolithographic hydrogel printing of 3D culture chips with biofunctionalized complex 3D perfusion networks. *Lab Chip* **17**, 4273–4282 (2017).
81. Baruffaldi, D., Palmara, G., Pirri, C. & Frascella, F. 3D Cell Culture: Recent Development in Materials with Tunable Stiffness. *ACS Appl Bio Mater* **4**, 2233–2250 (2021).
82. Roulis, M. & Flavell, R. A. Fibroblasts and myofibroblasts of the intestinal lamina propria in physiology and disease. *Differentiation* **92**, 116–131 (2016).
83. Pereira, C., Araújo, F., Barrias, C. C., Granja, P. L. & Sarmento, B. Dissecting stromal-epithelial interactions in a 3D in vitro cellularized intestinal model for permeability studies. *Biomaterials* **56**, 36–45 (2015).
84. Macedo, M. H., Barros, A. S., Martínez, E., Barrias, C. C. & Sarmento, B. All layers matter: Innovative three-dimensional epithelium-stroma-endothelium intestinal model for reliable permeability outcomes. *Journal of Controlled Release* **341**, 414–430 (2022).
85. Bollenbach, T. & Heisenberg, C. P. Gradients Are Shaping Up. *Cell* **161**, 431–432 (2015).
86. Khademhosseini, A. & Langer, R. Microengineered hydrogels for tissue engineering. *Biomaterials* **28**, 5087–5092 (2007).
87. Torras, N., García-Díaz, M., Fernández-Majada, V. & Martínez, E. Mimicking epithelial tissues in three-dimensional cell culture models. *Front Bioeng Biotechnol* **6**, 1–7 (2018).
88. Castaño, A. G. *et al.* Dynamic photopolymerization produces complex microstructures on hydrogels in a moldless approach to generate a 3D intestinal tissue model. *Biofabrication* vol. 11 https://iopscience.iop.org/article/10.1088/1758-5090/ab0478 (2019).
89. Torras, N. *et al.* A bioprinted 3D gut model with crypt-villus structures to mimic the intestinal epithelial-stromal microenvironment. *Biomaterials Advances* **153**, 213534 (2023).
90. van Duinen, V., Trietsch, S. J., Joore, J., Vulto, P. & Hankemeier, T. Microfluidic 3D cell culture: From tools to tissue models. *Curr Opin Biotechnol* **35**, 118–126 (2015).
91. Anseth, K. S., Bowman, C. N. & Brannon-Peppas, L. Mechanical properties of hydrogels and their experimental determination. *Biomaterials* **17**, (1996).
92. Hu, C., Chen, Y., Tan, M. J. A., Ren, K. & Wu, H. Microfluidic technologies for vasculature biomimicry. *Analyst* **144**, 4461–4471 (2019).
93. Pradhan, S. *et al.* Biofabrication Strategies and Engineered In Vitro Systems for Vascular Mechanobiology. *Adv Healthc Mater* **1901255**, 1901255 (2020).
94. Kamata, H., Li, X., Chung, U. Il & Sakai, T. Design of Hydrogels for Biomedical Applications. *Adv Healthc Mater* **4**, 2360–2374 (2015).
95. Loh, Q. L. & Choong, C. Three-dimensional scaffolds for tissue engineering applications: Role of porosity and pore size. *Tissue Eng Part B Rev* **19**, 485–502 (2013).
96. Wolf, K. *et al.* Physical limits of cell migration: Control by ECM space and nuclear deformation and tuning by proteolysis and traction force. *Journal of Cell Biology* **201**, 1069–1084 (2013).
97. Miron-Mendoza, M., Seemann, J. & Grinnell, F. The differential regulation of cell motile activity through matrix stiffness and porosity in three dimensional collagen matrices. *Biomaterials* **31**, 6425–6435 (2010).

98. Zhang, X., Li, L. & Luo, C. Gel integration for microfluidic applications. *Lab Chip* **16**, 1757–1776 (2016).
99. Baker, B. M., Trappmann, B., Stapleton, S. C., Toro, E. & Chen, C. S. Microfluidics embedded within extracellular matrix to define vascular architectures and pattern diffusive gradients. *Lab Chip* **13**, 3246–3252 (2013).
100. Miller, J. S. *et al.* Rapid casting of patterned vascular networks for perfusable engineered three-dimensional tissues. *Nat Mater* **11**, 768–774 (2012).
101. Cuchiara, M. P., Gould, D. J., McHale, M. K., Dickinson, M. E. & West, J. L. Integration of self-assembled microvascular networks with microfabricated PEG-based hydrogels. *Adv Funct Mater* **22**, 4511–4518 (2012).
102. Tocchio, A. *et al.* Versatile fabrication of vascularizable scaffolds for large tissue engineering in bioreactor. *Biomaterials* **45**, 124–131 (2015).
103. Adriani, G., Ma, D., Pavesi, A., Kamm, R. D. & Goh, E. L. K. A 3D neurovascular microfluidic model consisting of neurons, astrocytes and cerebral endothelial cells as a blood-brain barrier. *Lab Chip* **17**, 448–459 (2017).
104. Bischel, L. L., Young, E. W. K., Mader, B. R. & Beebe, D. J. Tubeless microfluidic angiogenesis assay with three-dimensional endothelial-lined microvessels. *Biomaterials* **34**, 1471–1477 (2013).
105. Trietsch, S. J. *et al.* Membrane-free culture and real-time barrier integrity assessment of perfused intestinal epithelium tubes. *Nat Commun* **8**, (2017).
106. Pi, Q. *et al.* Digitally Tunable Microfluidic Bioprinting of Multilayered Cannular Tissues. *Advanced Materials* **30**, 1–10 (2018).
107. Homan, K. A. *et al.* Bioprinting of 3D Convoluted Renal Proximal Tubules on Perfusable Chips. *Sci Rep* **6**, 1–13 (2016).
108. Lin, N. Y. C. *et al.* Renal reabsorption in 3D vascularized proximal tubule models. *Proc Natl Acad Sci U S A* **116**, 5399–5404 (2019).
109. Lee, H. *et al.* Cell-printed 3D liver-on-a-chip possessing a liver microenvironment and biliary system. *Biofabrication* **11**, (2019).
110. Zhang, Y. S. *et al.* Bioprinted thrombosis-on-a-chip. *Lab Chip* **16**, 4097–4105 (2016).
111. Grigoryan, B. *et al.* Multivascular networks and functional intravascular topologies within biocompatible hydrogels. *Science (1979)* **364**, 458–464 (2019).
112. Xue, D. *et al.* Projection-Based 3D Printing of Cell Patterning Scaffolds with Multiscale Channels. *ACS Appl Mater Interfaces* **10**, 19428–19435 (2018).
113. Brandenberg, N. & Lutolf, M. P. In Situ Patterning of Microfluidic Networks in 3D Cell-Laden Hydrogels. *Advanced Materials* **28**, 7450–7456 (2016).
114. Arakawa, C. K., Badeau, B. A., Zheng, Y. & DeForest, C. A. Multicellular Vascularized Engineered Tissues through User-Programmable Biomaterial Photodegradation. *Advanced Materials* **29**, 1–9 (2017).
115. Xia, Y. & Whitesides, G. M. SOFT LITHOGRAPHY. *Annual Review of Materials Science* **28**, 153–184 (1998).
116. Wang, J. C. *et al.* Pneumatic mold-aided construction of a three-dimensional hydrogel microvascular network in an integrated microfluidics and assay of cancer cell adhesion onto the endothelium. *Microfluid Nanofluidics* **15**, 519–532 (2013).
117. Ling, Y. *et al.* A cell-laden microfluidic hydrogel. *Lab Chip* **7**, 756–762 (2007).
118. Jocic, S., Mestres, G. & Tenje, M. Fabrication of user-friendly and biomimetic 1,1′-carbonyldiimidazole cross-linked gelatin/agar microfluidic devices. *Materials Science and Engineering C* **76**, 1175–1180 (2017).

119. Kageyama, T. *et al.* Rapid engineering of endothelial cell-lined vascular-like structures in in situ crosslinkable hydrogels. *Biofabrication* **6**, (2014).
120. Huang, G. *et al.* Helical spring template fabrication of cell-laden microfluidic hydrogels for tissue engineering. *Biotechnol Bioeng* **110**, 980–989 (2013).
121. Shin, Y. *et al.* Microfluidic assay for simultaneous culture of multiple cell types on surfaces or within hydrogels. *Nat Protoc* **7**, 1247–1259 (2012).
122. Campisi, M. *et al.* 3D self-organized microvascular model of the human blood-brain barrier with endothelial cells, pericytes and astrocytes. *Biomaterials* **180**, 117–129 (2018).
123. Lee, S. W. L. *et al.* Modeling Nanocarrier Transport across a 3D In Vitro Human Blood-Brain–Barrier Microvasculature. *Adv Healthc Mater* **1901486**, 1–12 (2020).
124. Vulto, P. *et al.* Phaseguides: A paradigm shift in microfluidic priming and emptying. *Lab Chip* **11**, 1596–1602 (2011).
125. van Duinen, V. *et al.* 96 Perfusable Blood Vessels To Study Vascular Permeability in Vitro. *Sci Rep* **7**, 1–11 (2017).
126. Bischel, L. L., Lee, S. H. & Beebe, D. J. A Practical method for patterning lumens through ECM hydrogels via viscous finger patterning. *J Lab Autom* **17**, 96–103 (2012).
127. Herland, A. *et al.* Distinct contributions of astrocytes and pericytes to neuroinflammation identified in a 3D human blood-brain barrier on a chip. *PLoS One* **11**, 1–21 (2016).
128. Yu, F. *et al.* A pump-free tricellular blood–brain barrier on-a-chip model to understand barrier property and evaluate drug response. *Biotechnol Bioeng* 0–1 (2019) doi:10.1002/bit.27260.
129. Pradhan, S., Keller, K. A., Sperduto, J. L. & Slater, J. H. Fundamentals of Laser-Based Hydrogel Degradation and Applications in Cell and Tissue Engineering. *Adv Healthc Mater* **6**, 1–28 (2017).
130. Hribar, K. C. *et al.* Three-dimensional direct cell patterning in collagen hydrogels with near-infrared femtosecond laser. *Sci Rep* **5**, 1–7 (2015).
131. Heintz, K. A. *et al.* Fabrication of 3D Biomimetic Microfluidic Networks in Hydrogels. *Adv Healthc Mater* **5**, 2153–2160 (2016).
132. Nikolaev, M. *et al.* Homeostatic mini-intestines through scaffold-guided organoid morphogenesis. *Nature* **585**, 574–578 (2020).
133. Lee, H. & Cho, D. W. One-step fabrication of an organ-on-a-chip with spatial heterogeneity using a 3D bioprinting technology. *Lab Chip* **16**, 2618–2625 (2016).
134. Liu, W. *et al.* Coaxial extrusion bioprinting of 3D microfibrous constructs with cell-favorable gelatin methacryloyl microenvironments. *Biofabrication* **10**, 024102 (2018).
135. Hong, S., Kim, J. S., Jung, B., Won, C. & Hwang, C. Coaxial bioprinting of cell-laden vascular constructs using a gelatin-tyramine bioink. *Biomater Sci* **7**, 4578–4587 (2019).
136. Billiet, T., Vandenhaute, M., Schelfhout, J., Van Vlierberghe, S. & Dubruel, P. A review of trends and limitations in hydrogel-rapid prototyping for tissue engineering. *Biomaterials* **33**, 6020–6041 (2012).
137. Soman, P., Chung, P. H., Zhang, A. P. & Chen, S. Digital microfabrication of user-defined 3D microstructures in cell-laden hydrogels. *Biotechnol Bioeng* **110**, 3038–3047 (2013).
138. Ng, W. L. *et al.* Vat polymerization-based bioprinting—process, materials, applications and regulatory challenges. *Biofabrication* **12**, 022001 (2020).
139. Skoog, S. A., Goering, P. L. & Narayan, R. J. Stereolithography in tissue engineering. *J Mater Sci Mater Med* **25**, 845–856 (2014).
140. Tumbleston, J. R. *et al.* Continuous liquid interface production of 3D objects. *Science (1979)* **347**, 1349–1352 (2015).

141. Ito, Y. Photochemistry for biomedical applications: From device fabrication to diagnosis and therapy. *Photochemistry for Biomedical Applications: From Device Fabrication to Diagnosis and Therapy* 1–313 (2018) doi:10.1007/978-981-13-0152-0/COVER.
142. Su, W.-F. Principles of Polymer Design and Synthesis.
143. Bowman, C. N. & Kloxin, C. J. Toward an enhanced understanding and implementation of photopolymerization reactions. *AIChE Journal* **54**, 2775–2795 (2008).
144. Jariwala, A. S. *et al.* Modeling effects of oxygen inhibition in mask-based stereolithography. *Rapid Prototyp J* **17**, 168–175 (2011).
145. Pereira, R. F. & Bártolo, P. J. 3D bioprinting of photocrosslinkable hydrogel constructs. *J Appl Polym Sci* **132**, (2015).
146. Hanasoge, S. & Ljungman, M. H2AX phosphorylation after UV irradiation is triggered by DNA repair intermediates and is mediated by the ATR kinase. *Carcinogenesis* **28**, 2298–2304 (2007).
147. Lin, H. *et al.* Application of visible light-based projection stereolithography for live cell-scaffold fabrication with designed architecture. *Biomaterials* **34**, 331–339 (2013).
148. Macedo, M. H. *et al. The shape of our gut: dissecting the importance of the villi architecture in a 3D bioprinted in vitro intestinal model*. https://ssrn.com/abstract=4166663.
149. Zhang, R. & Larsen, N. B. Stereolithographic hydrogel printing of 3D culture chips with biofunctionalized complex 3D perfusion networks. *Lab Chip* **17**, 4273–4282 (2017).
150. Lee, J. H., Prud'homme, R. K. & Aksay, I. A. Cure depth in photopolymerization: Experiments and theory. *J Mater Res* **16**, 3536–3544 (2001).
151. Rapid prototyping & manufacturing— Fundamentals of stereolithography. *J Manuf Syst* **12**, 430–433 (1993).
152. Melchels, F. P. W., Feijen, J. & Grijpma, D. W. A review on stereolithography and its applications in biomedical engineering. *Biomaterials* **31**, 6121–6130 (2010).
153. Gibson, I., Rosen, D. W. & Stucker, B. Additive manufacturing technologies: Rapid prototyping to direct digital manufacturing. *Additive Manufacturing Technologies: Rapid Prototyping to Direct Digital Manufacturing* 1–459 (2010) doi:10.1007/978-1-4419-1120-9/COVER.
154. Osaki, T., Sivathanu, V. & Kamm, R. D. Vascularized microfluidic organ-chips for drug screening, disease models and tissue engineering. *Curr Opin Biotechnol* **52**, 116–123 (2018).
155. Zheng, Y., Chen, J. & López, J. A. Flow-driven assembly of VWF fibres and webs in in vitro microvessels. *Nat Commun* **6**, (2015).
156. Morgan, J. P. *et al.* Formation of microvascular networks in vitro. *Nat Protoc* **8**, 1820–1836 (2013).
157. Nguyen, D. H. T. *et al.* Biomimetic model to reconstitute angiogenic sprouting morphogenesis in vitro. *Proc Natl Acad Sci U S A* **110**, 6712–6717 (2013).
158. Kim, S., Lee, H., Chung, M. & Jeon, N. L. Engineering of functional, perfusable 3D microvascular networks on a chip. *Lab Chip* **13**, 1489–1500 (2013).
159. Hsu, Y. H., Moya, M. L., Hughes, C. C. W., George, S. C. & Lee, A. P. A microfluidic platform for generating large-scale nearly identical human microphysiological vascularized tissue arrays. *Lab Chip* **13**, 2990–2998 (2013).
160. Park, Y. K. *et al.* In vitro microvessel growth and remodeling within a three-dimensional microfluidic environment. *Cell Mol Bioeng* **7**, 15–25 (2014).
161. Phan, D. T. T. *et al.* A vascularized and perfused organ-on-a-chip platform for large-scale drug screening applications. *Lab Chip* **17**, 511–520 (2017).

162. Wang, X. *et al.* Engineering anastomosis between living capillary networks and endothelial cell-lined microfluidic channels. *Lab Chip* **16**, 282–290 (2016).
163. Zheng, Y. *et al.* In vitro microvessels for the study of angiogenesis and thrombosis. *Proc Natl Acad Sci U S A* **109**, 9342–9347 (2012).
164. Qiu, Y. *et al.* Microvasculature-on-a-chip for the long-term study of endothelial barrier dysfunction and microvascular obstruction in disease. *Nat Biomed Eng* **2**, 453–463 (2018).
165. Kilic, O. *et al.* Brain-on-a-chip model enables analysis of human neuronal differentiation and chemotaxis. *Lab Chip* **16**, 4152–4162 (2016).
166. Oddo, A. *et al.* Advances in Microfluidic Blood–Brain Barrier (BBB) Models. *Trends Biotechnol* **37**, (2019).
167. Xu, H. *et al.* A dynamic in vivo-like organotypic blood-brain barrier model to probe metastatic brain tumors. *Sci Rep* **6**, 1–12 (2016).
168. Roth, A. & Singer, T. The application of 3D cell models to support drug safety assessment: Opportunities & challenges. *Adv Drug Deliv Rev* **69–70**, 179–189 (2014).
169. Wang, L. *et al.* A disease model of diabetic nephropathy in a glomerulus-on-a-chip microdevice. *Lab Chip* **17**, 1749–1760 (2017).
170. Weber, E. J. *et al.* Development of a microphysiological model of human kidney proximal tubule function. *Kidney Int* **90**, 627–637 (2016).
171. Mu, X., Zheng, W., Xiao, L., Zhang, W. & Jiang, X. Engineering a 3D vascular network in hydrogel for mimicking a nephron. *Lab Chip* **13**, 1612–1618 (2013).
172. Shroyer, N. F. & Kocoshis, S. A. Anatomy and Physiology of the Small and Large Intestines. *Pediatric Gastrointestinal and Liver Disease* 324-336.e2 (2011) doi:10.1016/B978-1-4377-0774-8.10031-4.
173. Small Intestine: Function, anatomy & Definition. https://my.clevelandclinic.org/health/body/22135-small-intestine.
174. Tortora, G. J. & Nielsen, M. T. (Mark T. Principles of human anatomy.
175. Volk, N. & Lacy, B. Anatomy and Physiology of the Small Bowel. *Gastrointest Endosc Clin N Am* **27**, 1–13 (2017).
176. Buckley, A. & Turner, J. R. Cell Biology of Tight Junction Barrier Regulation and Mucosal Disease. *Cold Spring Harb Perspect Biol* **10**, (2018).
177. Montgomery, R. K. & Grand, R. J. Development of the Gastrointestinal Tract. *Pediatric Gastrointestinal and Liver Disease* 2-9.e2 (2011) doi:10.1016/B978-1-4377-0774-8.10001-6.
178. Sekirov, I., Russell, S. L., Caetano M Antunes, L. & Finlay, B. B. Gut microbiota in health and disease. *Physiol Rev* **90**, 859–904 (2010).
179. Powell, D. W., Pinchuk, I. V., Saada, J. I., Chen, X. & Mifflin, R. C. Mesenchymal Cells of the Intestinal Lamina Propria. *Annu Rev Physiol* **73**, 213 (2011).
180. Vancamelbeke, M. & Vermeire, S. The intestinal barrier: a fundamental role in health and disease. (2017) doi:10.1080/17474124.2017.1343143.
181. Peterson, L. W. & Artis, D. Intestinal epithelial cells: regulators of barrier function and immune homeostasis. *Nature Reviews Immunology 2014 14:3* **14**, 141–153 (2014).
182. Uchida, K. & Kamikawa, Y. Muscularis mucosae - the forgotten sibling. *J Smooth Muscle Res* **43**, 157–177 (2007).
183. Shim, K. Y. *et al.* Microfluidic gut-on-a-chip with three-dimensional villi structure. *Biomed Microdevices* **19**, (2017).
184. Shim, K. Y. *et al.* Microfluidic gut-on-a-chip with three-dimensional villi structure. *Biomed Microdevices* **19**, (2017).
185. Beaurivage, C. *et al.* Development of a gut-on-a-chip model for high throughput disease modeling and drug discovery. *Int J Mol Sci* **20**, (2019).

186. Verhulsel, M. *et al.* Developing an advanced gut on chip model enabling the study of epithelial cell/fibroblast interactions. *Lab Chip* **21**, 365–377 (2021).

2. Electrical monitoring of cell barrier models in organ-on-chips

2.1. Overview on electrical measurements of cell barriers

As epithelial and endothelial cells grow and form cell monolayers, these barriers become tighter, restricting ion paracellular transport through the tight junctions. The integrity of a cell barrier can thus be directly correlated to its electrical resistance [1,2]. Trans-epithelial electrical resistance (TEER) measurements are a quantitative and non-invasive method to measure the tightness of tissue barriers, with lower values associated to leaky cell layers while tight barriers display high ones (Figure 2.1). Since the first electrical measurements on *in vivo* tissues were performed in the 1950s with Ussing chambers [3,4], this method has been widely adopted as a gold standard for *in vitro* assays [5]. Unlike conventional tracer-based permeability assays, TEER monitoring can be performed in real time and does not require any labeling nor complex analytical tools, providing fast and reliable readouts about the state of the barrier.

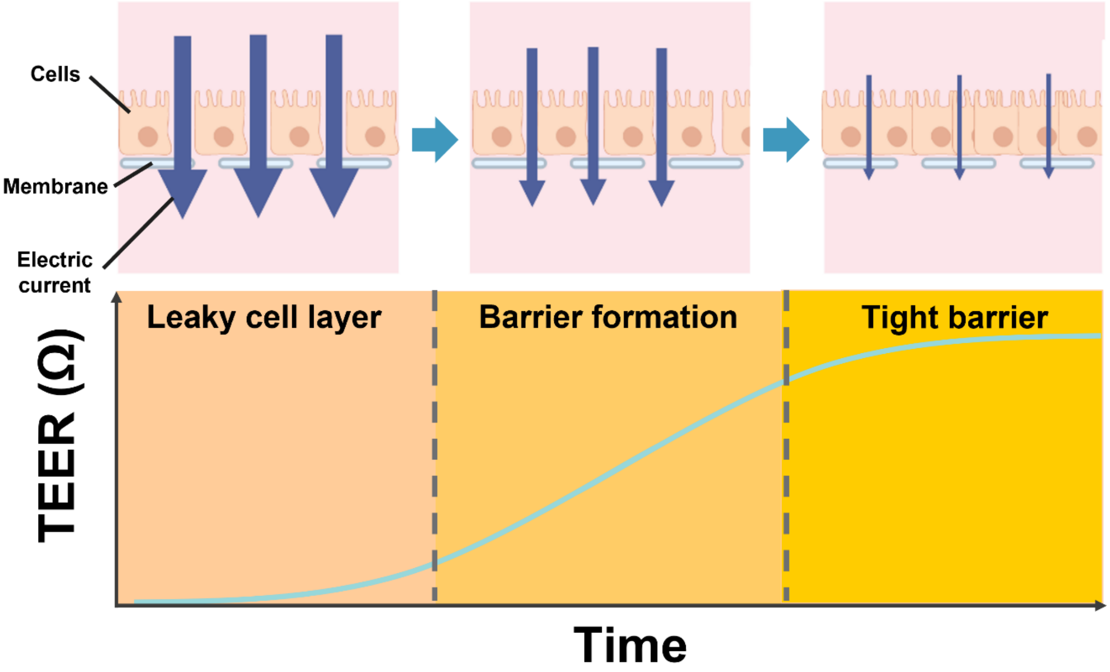

Figure 2.1: *Schematic of the evolution of TEER during the formation of a cell barrier.*

2.1.1. Equivalent electrical circuit of cell barriers

The electrical impedance of the cell monolayer can be represented by an equivalent electrical circuit, as shown in Figure 2.2 A. Transcellular transport of ions and electric charges across the cell membrane can be described by apical and basolateral capacitances and resistances. The capacitive behavior of the cell membrane can be associated to the lipid bilayer, which acts as an electrical insulator between the cell and the medium. The paracellular resistance represents the electrical ion permeability through the tight junctions of the cell barrier. By lumping this initial model, the number of parameters in the electrical circuit can be reduced to three by grouping the apical and basolateral capacitances, and resistances in one each, assuming they have similar values (Figure 2.2 B). By further simplifying the circuit, a two-variable model can be obtained by grouping the transcellular and paracellular resistances into TEER (Figure 2.2 C) [6]. To complete the circuit, the resistance of the medium is often added to account for its electrical properties. While cell layers are dynamic biological systems, this simplified model is a good approximation of their electrical behavior, allowing the extraction of key parameters linked to their formation and maturation.

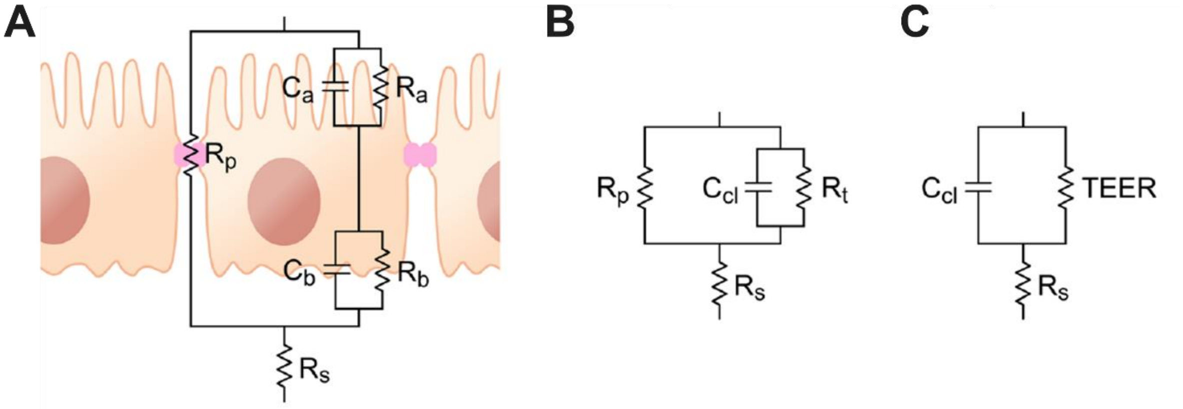

Figure 2.2: *Equivalent electric circuit of an epithelial cell barrier. (A) Schematic of the different electric parameters associated to the cell layer. (B) Lumped model with the apical and basolateral elements. (C) Lumped model with the cell layer capacitance and TEER. R_p: paracellular resistance; R_s: solution resistance; C_a: apical capacitance; C_b: basolateral capacitance; R_a: apical resistance; R_b: basolateral resistance; R_t: transcellular resistance; C_{cl}: cell layer capacitance. Adapted with permission from BMC* [5]*.*

In this model, TEER is the sum of the paracellular and transcellular resistances, the two main ion transportation pathways. In the case of leaky cell layers, TEER displays low values as the transcellular resistance dominates over the paracellular resistance due to larger gaps in between the cells. For tight barriers, TEER is higher as paracellular resistance increases and reaches similar values to the transcellular one due to the restriction of ion transport through the intercellular space. Depending on the studied tissue barrier model, TEER values can fall into one of the two mentioned categories. For instance, the endothelium of the hepatic sinusoid and the epithelium of the renal proximal tubule are categorized as leaky barriers as their main function involves nutrient and oxygen exchanges [7,8]. On the opposite side, the BBB displays high TEER values as it highly restricts the paracellular passage of potentially harmful compounds to the neural compartment [9].

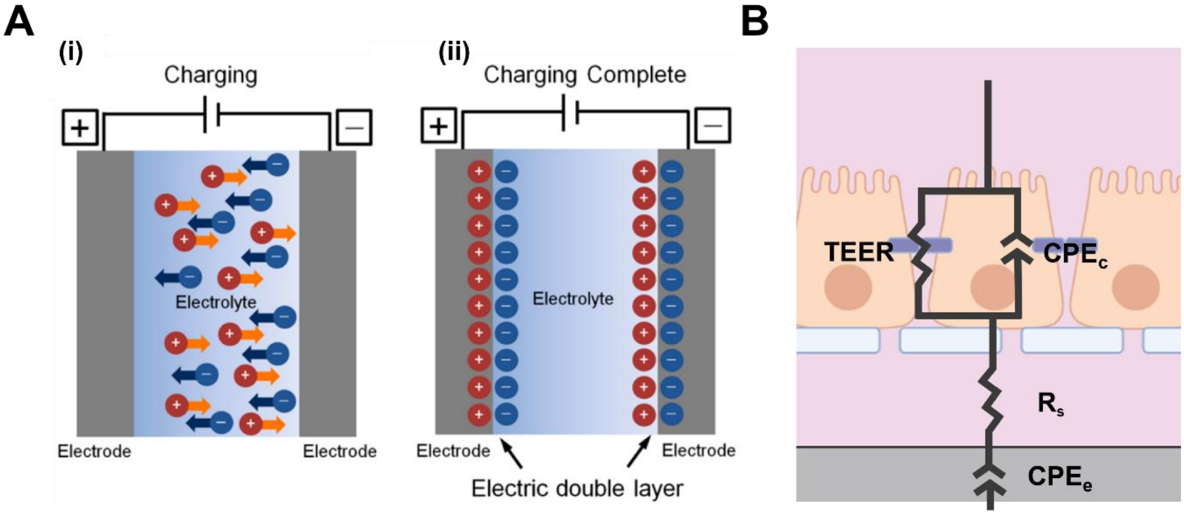

Figure 2.3: *Electric double layer capacitance and constant phase element. (A) Schematic of (i) the charging process and (ii) formation of the double layer capacitance at the interface between the*

electrode and the electrolyte under an external voltage. Adapted with permission from MDPI, 2019 [10]*. (B) Schematic of the equivalent electrical circuit including constant phase elements to model the electrode impedance and the cell layer capacitance.*

The electrodes also contribute to the overall impedance of the system. Depending on the type of material, they can be more prone to be polarized under certain electrical conditions. When a current or potential difference is applied in the system, they act as capacitors at the interface between the electrode surface and the electrolyte, when ions and electric charges cumulate during the charging phase, generating a double layer capacitance (Figure 2.3 A). This double layer capacitance can have a significant impact on impedance measurements, as it is inversely proportional to the electrode size [11,12]. To add the contribution of the electrode polarization to the total impedance of the system, a constant phase element (CPE) is often used as a modeling element and placed in series with the resistance of the medium within the equivalent electrical circuit:

$$\textbf{\textit{(eq. 2.1)}} \quad Z_{CPE} = \frac{1}{A(jw)^{\alpha}}$$

Where Z_{CPE} is the electrode polarization impedance, j is the imaginary unit, w is the angular frequency, A is the admittance of the electrode and α is an exponent linked to the ideality of the impedance, with 0 being a pure resistor and 1, a pure capacitor. Moreover, CPEs have also been used to model the capacitive behavior of the cell barrier as equivalent electrical circuits with these elements are generally better fit to experimental data than with normal cell layer capacitances (Figure 2.3 B). The reason for this could be due to the variety of cell membrane morphologies and the narrowing of intercellular clefts during barrier formation [13,14].

However, it is important to point out the large discrepancies on the reported TEER values within similar *in vitro* cell barrier models [15]. This variability is mainly due to the different techniques and measurement errors associated with them, along with experimental conditions that can affect the electrical resistance of the cell monolayer.

2.1.2. TEER measurement techniques

Different commercial devices are available to measure the cell barrier resistance on Transwell® inserts for conventional static models. Chopstick-like electrode probes are a common option to perform these measurements (Figure 2.4 A) [16]. The probe has two sticks with two silver/ silver chloride (Ag/AgCl) electrodes on each (Figure 2.4 B). But the readouts with this system can be inaccurate as the probe must be placed and held manually, reducing the repeatability between measurements. An alternative to chopstick electrodes is the EndOhm® chamber, where the Ag/AgCl concentric electrodes are fixed and placed facing each other vertically, with the membrane in between both, making TEER measurements more accurate and reproducible (Figure 2.4 C, D) [17]. With these systems, a single-frequency current signal is generated by two current-carrying electrodes and the resulting potential drop is picked up by two voltage-sensing electrodes to calculate the total resistance using Ohm's law. While Ag/AgCl electrodes are compatible with direct current (DC) measurements, commercial volt-ohm meters like the EVOM® system work with AC signals to avoid electrode and cell membrane polarization [18], which can be potentially harmful for the cells. The measurement is performed while the insert and the electrodes are submerged in medium, which have their own electrical resistances. To account for this, a blank measurement with a control sample without cells is initially performed to subtract it from the total resistance:

$$\textbf{\textit{(eq 2.2)}} \quad TEER = (R_{total} - R_{blank}) * A_{barrier}$$

Where R_{total} is the total measured resistance with cells, R_{blank} is the resistance of the control insert and media, and $A_{barrier}$ is the cell culture area (or the membrane area for commercial Transwells®). This normalization of the TEER value by the cell culture area is often performed to compare resistance values between inserts or substrates with different dimensions.

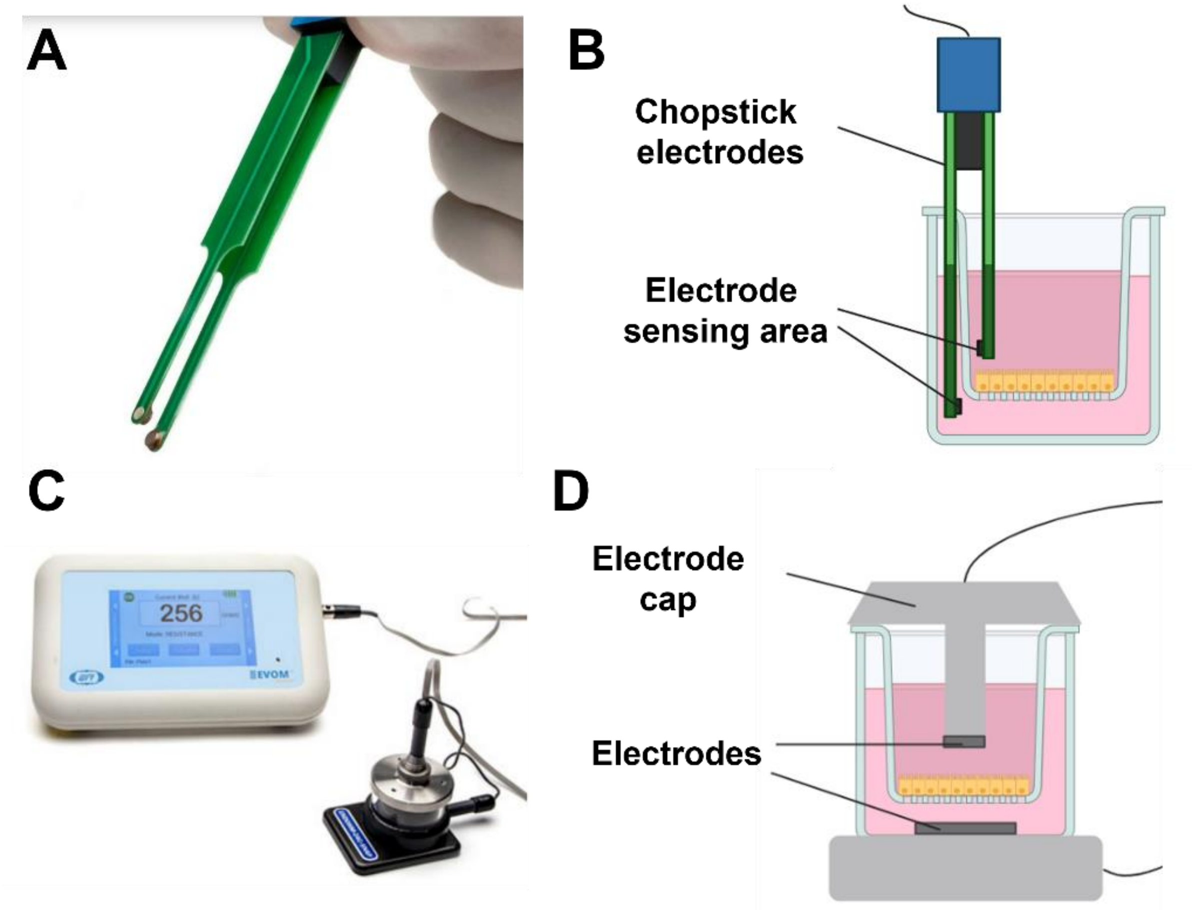

Figure 2.4: *TEER measurement systems for Transwell®-based cell barrier models. (A) Chopstick STX-2 electrode probe (World Precision Instruments). (B) Schematic of the TEER measurement in a Transwell® insert with chopstick electrodes. (C) Image of the EndOhm® chamber and the EVOM® epithelial volt-ohm meter (World Precision Instruments). (d) Schematic of the TEER measurement in a Transwell® insert with an EndOhm® chamber.*

Different factors can affect TEER measurements. It is well known that electrical cell layer resistances are temperature dependent [19]. Electrical conductivity is linked to ion mobility, which has an exponential relationship with temperature. Measurements can be performed either at 37ºC inside the incubator or at room temperature outside. In the first case, these types of measurements need specific electronic devices that can operate in high humidity conditions. In the second case, samples need to be placed outside for at least 20 minutes for the temperature to equilibrate and have stable readouts, which can compromise the integrity of the cell barrier for long waiting times. Another relevant aspect to consider is the electrode configuration. Chopstick-like probes have been shown to have large variability in their readouts due to current density distributions not being homogenous for large Transwells®, introducing errors on the measured values (Figure 2.5 A) [20]. These limitations are mostly overcome with EndOhm® chambers as electrodes are fixed in a central position at the apical and basolateral compartments of the cell culture inserts, generating a more uniform current density (Figure 2.5 B).

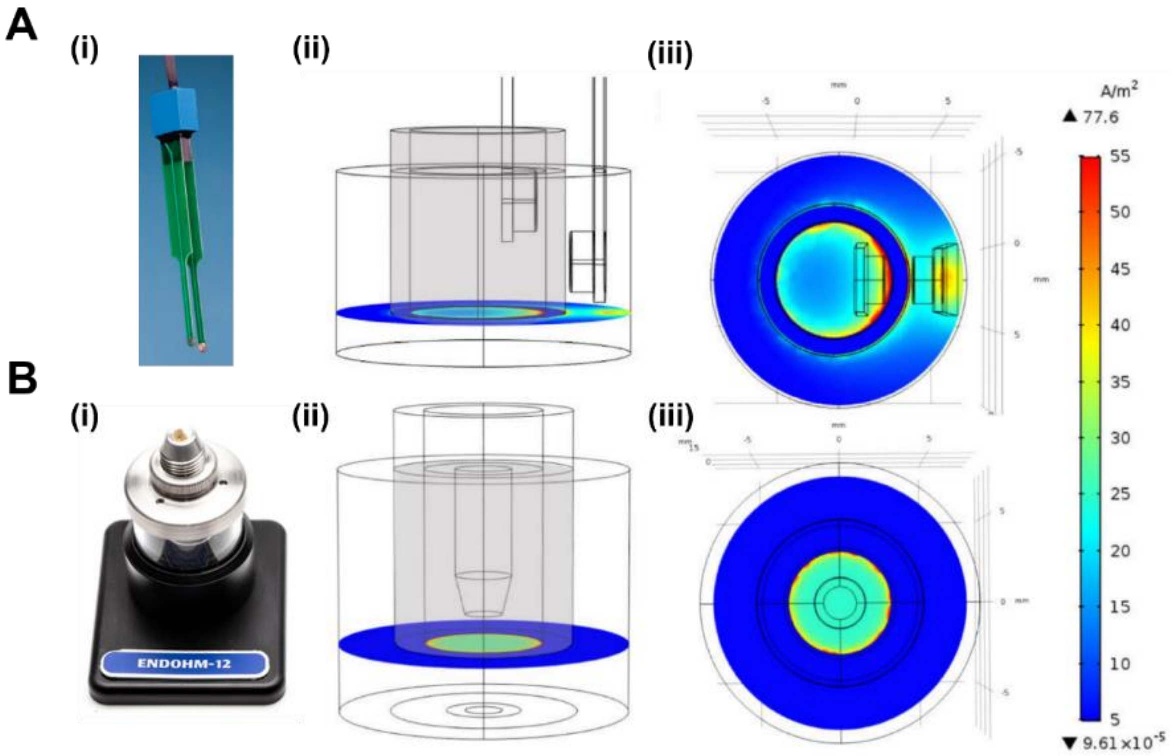

Figure 2.5: *Effect of electrode position on TEER measurements with (A) STX-2 chopstick-like probes and (B) EndOhm® chambers. (i) Image of the systems. (ii) Side and (iii) top view of the current density distribution on the membrane area simulated with COMSOL. The size of the modelled insert is 6.5 mm in diameter. Adapted with permission from MDPI, 2021* [20].

Despite most *in vitro* studies of tissue barriers relying on these electrical setups to monitor TEER progression over time, these systems have several limitations to extract meaningful data about their formation and tightness. As total resistances are measured with these systems, the contribution of each element present inside (medium, insert or cells) cannot be directly attributed without a blank measurement, making the process more cumbersome. Also, since standard TEER measuring devices operate with single frequency signals, frequency-dependent capacitive effects of the cell layers cannot be extracted, limiting the understanding of their behavior and function over time.

2.1.3. *Electrical impedance spectroscopy (EIS)*

Commercial TEER measuring devices are widespread in *in vitro* research as they provide a fast readout of cell barrier resistance, but they mostly operate either with DC or single-frequency AC signals, limiting the throughput of data related to their electrical properties. EIS is an impedance measuring technique in which an AC signal, either a current or a voltage, is applied at different frequencies to quantify the magnitude and phase shift of the resulting signal [21]. With this method, the different components of the equivalent electrical circuit of the tissue barrier can be represented as complex impedances to account for frequency-related phenomena such as the capacitive effects of the cell monolayer [22,23].

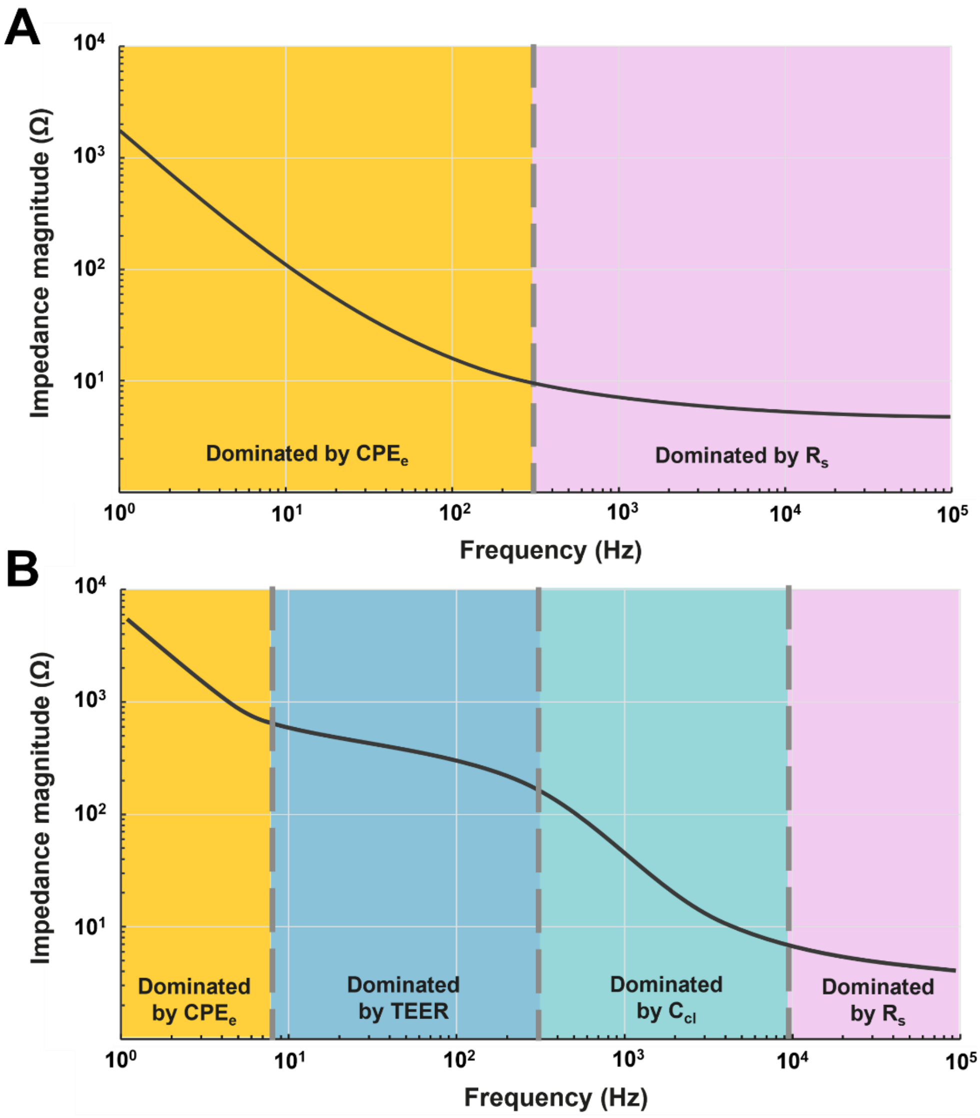

Figure 2.6: *Impedance spectra (A) without and (B) with a formed cell monolayer using a two-electrode configuration.*

Impedance spectra are often represented by Bode plots, where the impedance magnitude and the phase change are depicted as a function of frequency, usually on a logarithmic scale. For tissue barrier studies, the frequency sweep ranges between 10 Hz and 1 MHz. Different regions can be recognized within these plots depending on the stage of formation of the barrier. Initially, when cells have not formed any monolayer, two regions can be distinguished: in the low frequency, the impedance is dominated by the electrode polarization, represented by a CPE; in the high frequencies, the capacitive effect of the electrodes is less prominent, and the resistance of the medium is the dominant one (Figure 2.6 A). In the case the cell layer is well formed on the substrate, the contributions of the barrier show up on the graph, creating four distinct regions (Figure 2.6 B). At low frequencies, generally below 10 or 100 Hz, the CPE of the electrodes remains dominant. In the mid-range frequencies (100 – 10 kHz), the cell layer resistance TEER and capacitance C_{cl} contribute the most to the overall impedance. In the higher frequencies, above 10 kHz, the main component is the medium resistance. One of the main advantage of EIS measurements is the possibility to extract TEER values for cell barrier characterization without performing an initial blank adjustment, since the trans-epithelial resistance can be extracted from the difference of impedance magnitudes at the high and low frequencies (Figure 2.7 A). Also, shifts on the magnitude and phase plots can be associated to increasing C_{cl} values (Figure 2.7 B). The determination of TEER and C_{cl} is generally obtained by using model fitting algorithms based on least-squares methods.

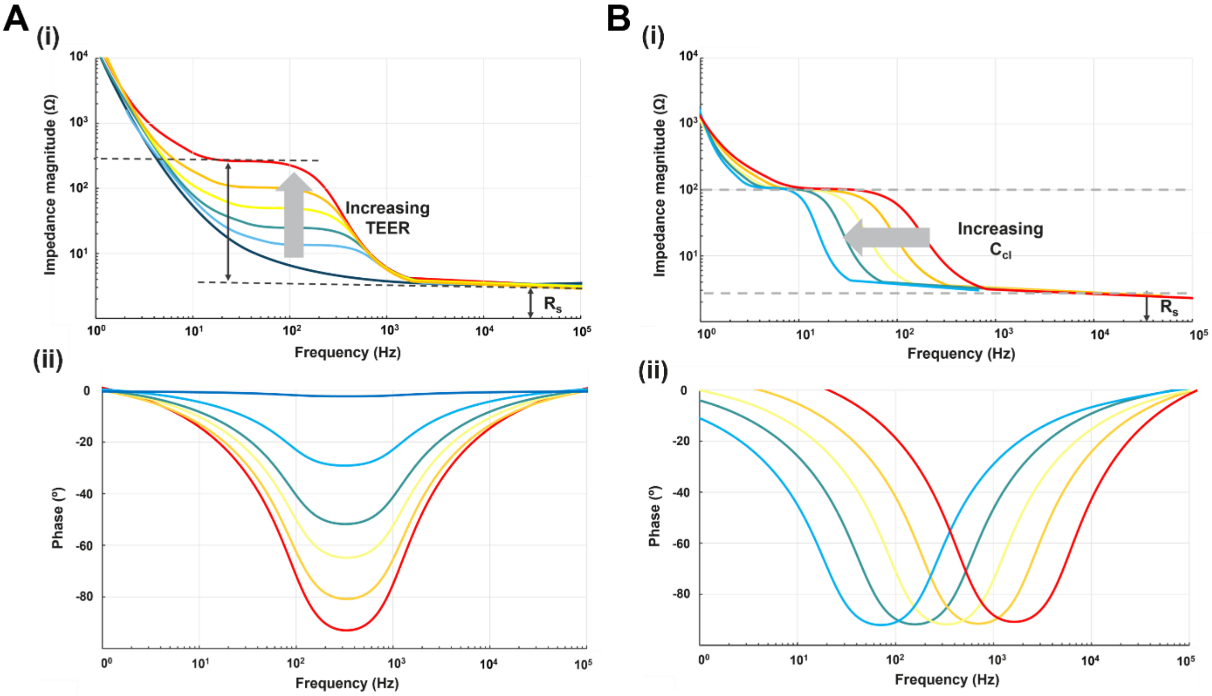

Figure 2.7: *Evolution of TEER and Ccl during barrier formation. (A) Effect of TEER increase in Bode (i) magnitude and (ii) phase plots. (B) Effect of Ccl in Bode (i) magnitude and (ii) phase plots.*

Currently, two commercial systems enable EIS measurements to study *in vitro* cell barrier systems: the CellZScope® (nanoAnalytics, Germany) and the ECIS system (Applied Biophysics, US). The CellZScope® is an automated device that can perform impedance measurements over a defined range of frequencies, between 1 Hz and 1 MHz, using AC signals (Figure 2.8 A) [24]. Several inserts (up to 24) can be placed inside the platform, that can operate under incubator conditions. Stainless steel electrodes are located at the top and bottom side of each insert to measure the electrical properties of the cell layer via EIS (Figure 2.8 A). Moreover, in the Electric Cell-substrate Impedance System (ECIS) Cultureware® platform, cells are cultured on the surface of an electrode-integrated substrate (Figure 2.8 B) [25]. The device operates in a bipolar configuration with an AC current signal between 25 Hz and 100 kHz. Various configurations of electrodes, from one electrode to an array of them, are available depending on the type of study, like cell migration, cell proliferation or cytotoxicity tests (Figure 2.8 B). In the one-electrode configuration (1E), a small circular gold (Au) electrode of around 250 µm acts as the working electrode (WE) while a concentric larger one works as the counter electrode (CE) (Figure 2.8 B). Since the sensing area is reduced to the size of the WE, increasing TEER values can be picked up when cells grow on top of the electrode, restricting the current signal passage through the formed barrier (Figure 2.8 B). However, this configuration does not allow diffusion or permeability studies as the basal compartment is absent. To overcome this issue, an insert support (8W TransFilter Adapter) was implemented as an adapter to make the ECIS system compatible with commercial Transwells® (Figure 2.8 B).

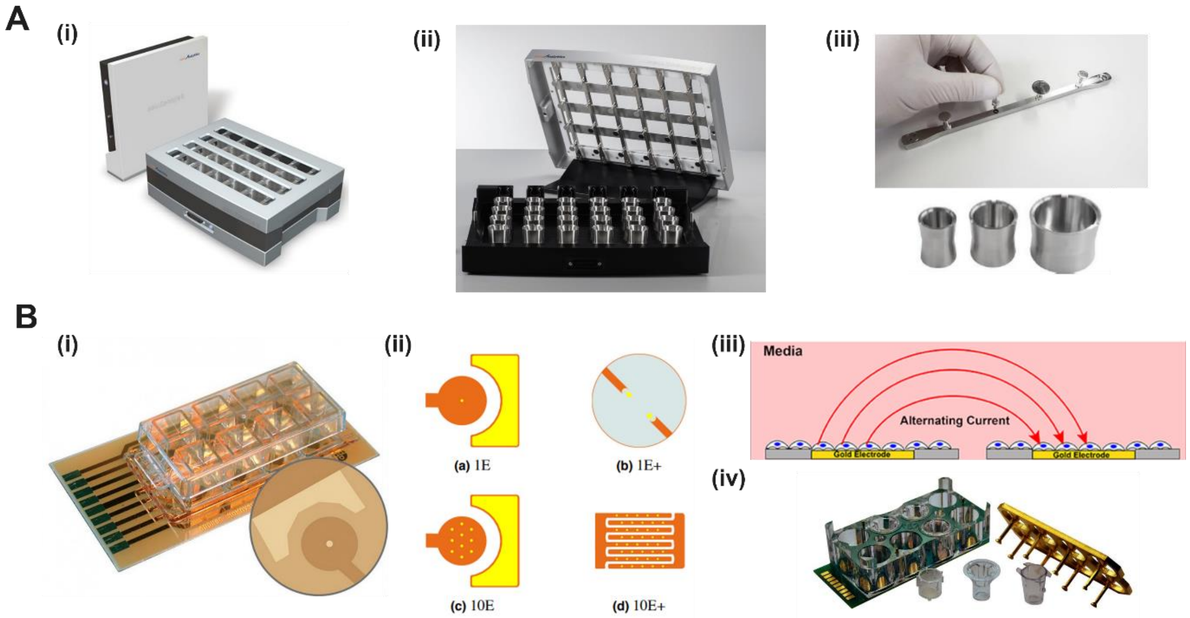

Figure 2.8: *Commercial devices for EIS-based characterization of cell barriers. (A) The CellZScope® system [26]. (i) Images of the complete device and (ii) the open cell culture platform. (iii) Photograph of the top and bottom stainless steel electrodes. (B) Electric Cell-substrate Impedance System (ECIS) [25]. (i) Image of the 8-well 1E Cultureware® device. (ii) Schematic of the different available electrode configurations. (iii) Working principle of TEER measurements on the grown cell layers. (iv) 8W TransFilter Adapter for commercial inserts.*

2.2. TEER measurement strategies for organ-on-chips

2.2.1. Materials for TEER electrodes

Due to their high electrical conductivity properties, metals are the privileged material for electrode fabrication in TEER monitoring of organ-on-chips [26]. Among them, Ag/AgCl is a common choice due to its high electrical stability and low polarization, making them suitable for DC and low-frequency AC signals. Already used in commercial TEER measuring devices for static *in vitro* models, Ag/AgCl electrodes have also been adapted to organ-on-chip devices [27–30]. For example, two AgCl thin film electrode pairs were placed in a microfluidic device to establish a BBB model (Figure 2.9 A) [30]. The electrodes were connected to an EVOM® volt-ohm meter to generate an AC current signal and measure the trans-epithelial resistance of endothelial b.End3 cells co-cultured with astrocytes. This dynamic model of the blood-brain barrier showed higher TEER values than both Transwell® models and dynamic cell cultures with endothelial cells only. However, while having numerous advantages for electrical monitoring, silver ions can leach into the medium after a prolonged use of the electrodes, inducing potential cytotoxic effects on the cells [31].

Other electrode materials have been implemented in organ-on-chip applications as they are more biocompatible and inert. Au has been integrated in different microfluidic devices to study barrier function in real time [32–34]. For instance, Au electrode pairs were patterned on PC substrates using clean room fabrication processes for EIS-based measurements [33]. The substrates were then assembled together with PDMS channels and a plastic membrane to obtain a two-channel microfluidic device with fully integrated electrodes for TEER monitoring (Figure 2.9 B). By culturing both human airway epithelial cells and intestinal epithelial cells in the chip under different conditions, TEER and cell layer capacitance were successfully measured during the experiment, thus validating the integration of the electrodes in the system. However, Au has a significantly high electrode polarization impedance in the low frequencies, potentially affecting TEER readouts of tissue barriers. Due to this, different strategies have been adopted to reduce the electrode impedance by increasing the surface area at the electrolyte-electrode interface and reducing the double layer capacitance. One option is to generate porous Au layers [35]. A second strategy is to increase the surface roughness by performing a black Pt deposition on the Au electrodes [36,37].

Platinum (Pt) is also a popular option for electrode fabrication as they are resistant to oxidation, and they have high durability [38–40]. For instance, human cerebral microvascular endothelial hCMEC/D3 cells were cultured in a membrane-based microfluidic platform and TEER values were recorded with two Pt wires, inserted at the top and bottom microchannel each (Figure 2.9 C) [38]. During 7 days of cell culture, TEER values could be successfully recorded with these electrodes placed close to the cell culture area. However, in certain configurations, placing electrodes close to the cell culture area can hinder optical inspection of cell layers, as most electrode materials are opaque.

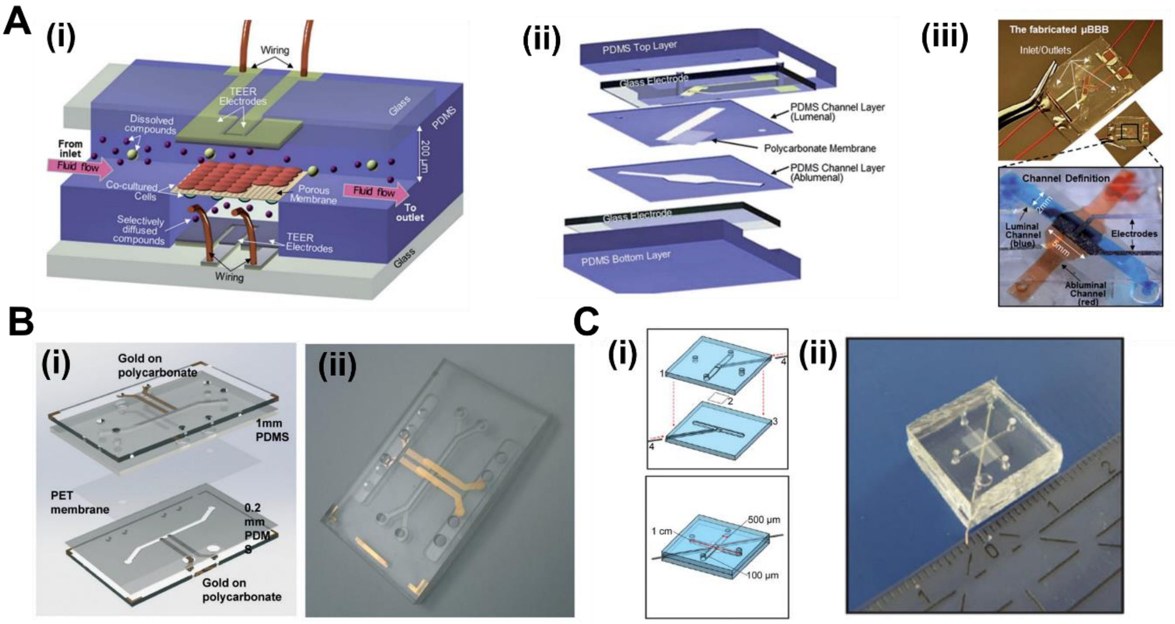

Figure 2.9: *Electrode materials for TEER monitoring in organ-on-chips. (A) Organ-on-chip with integrated Ag/AgCl electrodes. (i) 3D schematic of the two-channel microfluidic device with top/bottom electrodes. (ii) Exploded view of the different layers of the chip. (iii) Photograph of the electrode-integrated chip perfused with color dies. Adapted with permission from the Royal Society of Chemistry, 2012* [30]*. (B) Microfluidic device with fully integrated Au electrodes for in vitro cell barrier models. (i) 3D CAD schematic of the device with four Au electrodes patterned on PC substrates, PDMS channels and*

a plastic membrane. (ii) Image of the assembled device. Adapted with permission from the Royal Society of Chemistry, 2017 [33]*. (C) Organ-on-chip with inserted Pt wires. (i) Schematic view of the different parts of the device, consisting of top and bottom PDMS parts, a membrane and two Pt wires inserted and fixed on the sides of the channels. (ii) Image of the assembled PDMS device. Adapted with permission from Springer, 2013* [38]*.*

Some groups have proposed the use of transparent conductive materials for electrode fabrication to make them optically compatible with organ-on-chips. Indium tin oxide (ITO) is one of them, as it has been used on microfluidic devices to monitor trans-epithelial resistances [41–43]. For example, a gut-on-chip device was fabricated with ITO electrodes on PET sheets to assess the effect of micro-bubble formation on TEER [41]. Images of the formed bubbles in the central chamber were taken with an optical microscope and correlated to the recorded TEER values in order to correct them (Figure 2.10 A). However, while being fully transparent, ITO has a significant electrode contact impedance. To overcome this problem, poly(3,4-ethylenedioxythiophene) (PEDOT) doped with polystyrenesulfonate (PEDOT:PSS) is a conductive ionic polymer that has been suggested as an alternative due to is very low polarization impedance while being optically translucent [44,45]. In a recent work, a gut-on-chip with integrated PEDOT:PSS electrodes was developed using rapid prototyping and drop casting techniques (Figure 2.10 B) [46]. Electrodes were designed to preserve optical access to the cell culture area while guaranteeing uniform current density for reliable electrical measurements. As a demonstration, the development and maturation of intestinal epithelial cells to form a tight barrier was followed up via EIS-based TEER monitoring and validated with barrier disruption assays.

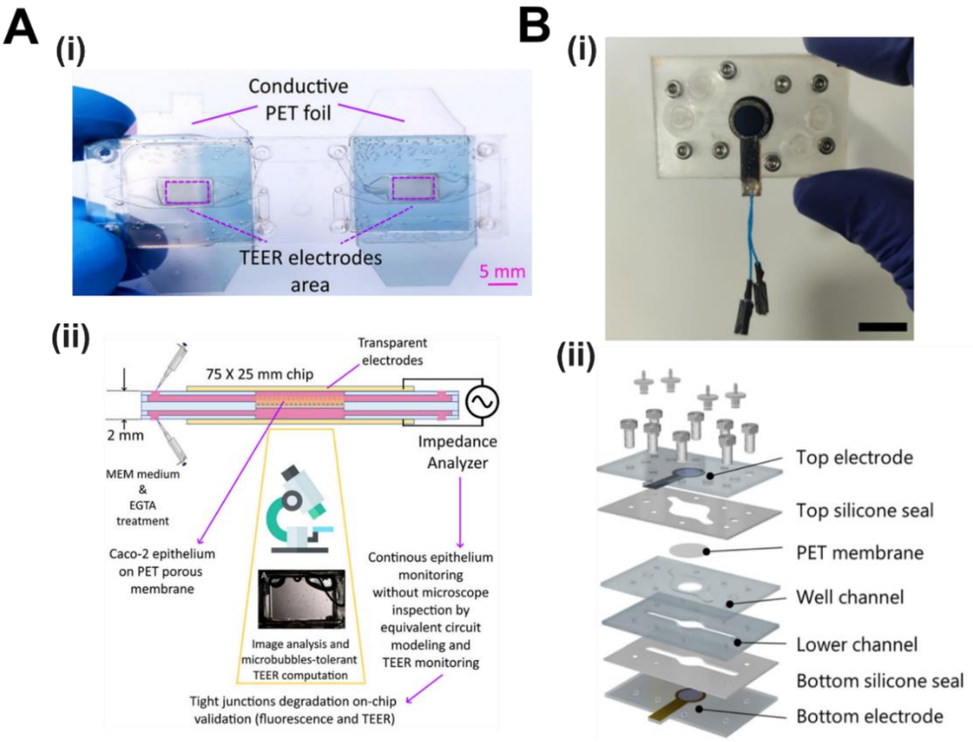

Figure 2.10: *Transparent and semi-transparent electrode materials for TEER measurement in organ-on-chips. (A) ITO electrode integration in an organ-on-chip device. (i) Photograph of the chip with the transparent embedded electrodes. (ii) Flowchart that depicts the algorithm for TEER calculation. Adapted with permission from IOP Publishing, 2022* [41]*. (B) Organ-on-chip device with integrated PEDOT:PSS electrodes. (i) Photograph of the chip. Scale bar: 1mm. (ii) Exploded view of the different*

components of the microfluidic system. Adapted with permission from the Royal Society of Chemistry, 2023 [46]*.*

2.2.2. Techniques for the integration of electrodes in organ-on-chips

Different engineering techniques have been adopted to implement electrodes within microfluidic devices for TEER monitoring. The insertion of Pt and Ag/AgCl wires was one of the first approaches used to study barrier function in organ-on-chips and it is still used to this day [40,47–49]. The wires are commercially available, and they can be easily adapted to the chip configuration. Generally, the electrode wires are placed at the inlets and outlets of the microfluidic platforms, where they can be in contact with the cell medium to measure the cell layer resistance. For example, two Ag and two Ag/Cl wire electrodes were placed at the inlet and outlet ports of a PDMS chip to monitor TEER evolution of Madin-Darbey canine kidney (MDCK) epithelial cells over time (Figure 2.11 A) [27]. After 7 days of cell culture under flow, the continuous monitoring of the cell layer showed a significant increase in TEER, and, by performing a barrier disruption assay with ehylenediaminetetraacetic acid (EDTA), the presence of a mature epithelial cell barrier could be confirmed. However, as electrodes are located relatively far away from the cell barrier, small changes in the resistivity of the cell medium can have a significant impact on the TEER readouts, making difficult the extraction of the cell layer parameters via model fittings. To solve this issue, it has been proposed to place the electrode wires closer to the cell culture substrate, reducing the signal-to-noise ratio [38,39]. This approach was used by Van der Helm et al. in a BBB-on-chip model (Figure 2.11 B) [39]. Four Pt wires were inserted near the cell culture area to create a more uniform current density and reduce potential measurement errors. Despite this improvement, the manual placement of the wires in the chip remains a source of variability for the electrical measurements, limiting the repeatability of the TEER quantification.

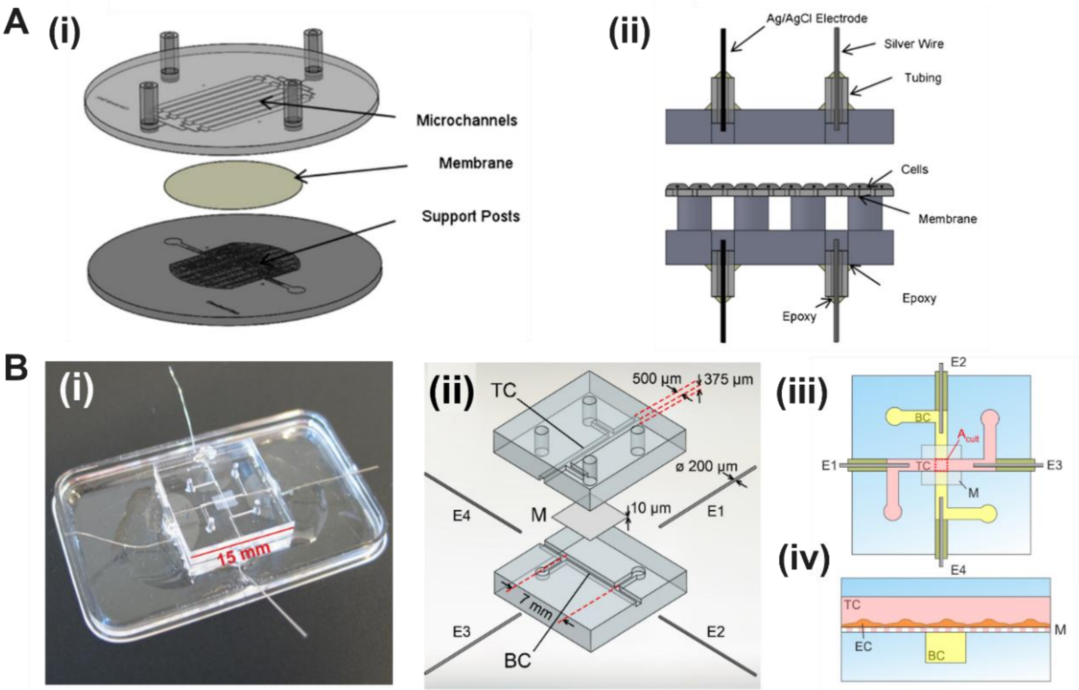

Figure 2.11: *Electrode wires in organ-on-chips for TEER monitoring. (A) Ag/AgCl wires inserted at the inlets for TEER monitoring. (i) Exploded view of the bioreactor (TEER electrodes not shown). (ii) Schematic of the TEER electrode configuration consisting of an Ag/AgCl electrode and a Ag electrode*

on each side of the membrane. Adapted with permission from Wiley and Sons, 2010 [27]*. (B) Pt wires inserted in an organ-on-chip for EIS-based measurements. (i) 3D Exploded view of the microfluidic chip, consisting of a top PDMS part with the top channel (TC), a membrane (M) and a bottom PDMS part with the bottom channel (BC). Four platinum wire electrodes (E1-4) are inserted and fixed on the side channels. (ii) Assembled chip, fixed to a plastic dish. (iii) Top schematic view of the chip with the inserted electrodes and the cell culture membrane. (iv) Schematic cross section showing the endothelial cells cultured in the top channel. Adapted with permission from Elsevier, 2016* [39]*.*

Initially developed for the microelectronic industry, thin film deposition is a microfabrication technique that has been adapted to engineer integrated electrodes in a precise and controlled manner in the organ-on-chip field. This type of deposition can be classified in two categories: physical vapor deposition (PVD) and chemical vapor deposition (CVD). Among PVD processes, sputtering and evaporation are the most common techniques. Sputtering consists in the gas ion bombardment (nitrogen or argon plasma) of a source material that ejects atoms to coat the surface of the substrate. Evaporation techniques also target a source material to generate a deposition layer on the substrate, either thermally or via electron beam bombardment. For both, the source electrode material is generally Au or Pt. An adhesion layer, often made of titanium (Ti), is initially deposited to optimize the attachment. Patterned structures can be obtained by combining thin film deposition with photolithography. Photolithography is based on the use of photomasks to pattern a photoresist on top of a substrate with micrometer range precision. In a process called lift-off, the photoresist is placed prior to the thin film deposition and then later removed to leave the patterned structures on the substrate (Figure 2.12 A). Alternatively, thin films can be deposited first and then etched to generate the patterned electrode. Among the different types of substrates used, silicon and glass are the most conventional ones but there have been examples of electrodes patterned on plastic, such as polycarbonate or COP [33,36,37]. By using plastic as a deposition substrate, the integration of the electrodes is compatible with rapid prototyping techniques to fabricate high-throughput microfluidic devices. Yeste et al. patterned interdigitated electrodes (IDE) based on Ti/Au thin films on plastic plates to establish a renal proximal tubule on-chip model (Figure 2.12 B) [36]. By performing EIS-based four-terminal measurements, the device could monitor in real time low TEER values of proximal tubule epithelial cells and transcellular chemical gradients of NaCl, which is linked to renal reabsorption functions *in vivo*. Moreover, CVD can also be used to generate thin films, such as oxide and nitride layers, by exposing the substrate surface to the precursor gas that chemically reacts to it. Titanium nitride (TiN) electrodes have been patterned with this technique to monitor TEER for *in vitro* cell barriers [50]. However, while thin film deposition allows precise microfabrication of electrodes for reliable TEER monitoring, the approach requires expensive equipment for clean room processing. As an alternative, some groups have proposed the use of clean room-free simplified techniques to integrate electrodes in organ-on-chips using, for example, screen printing [51,52].

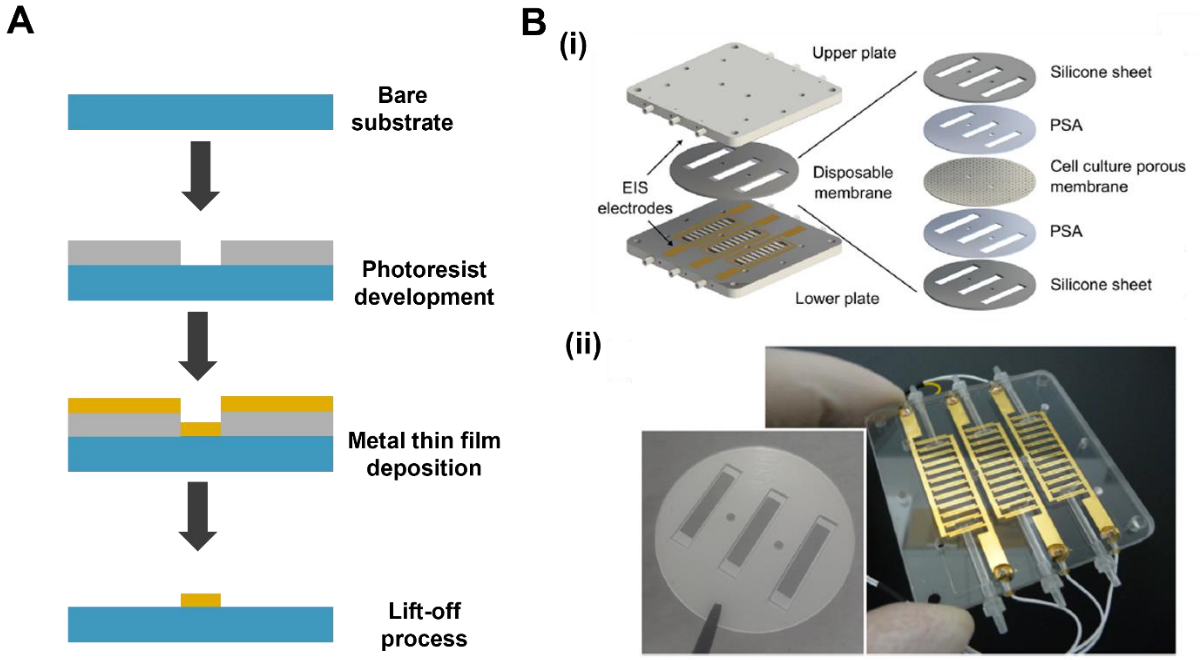

Figure 2.12: *Integration of electrodes in organ-on-chips for TEER sensing. (A) Schematic of a lift-off process for patterned thin film electrode fabrication. (B) Organ-on-chip device with fully integrated Au electrodes. (i) 3D exploded view of the different parts of the device, including top and bottom COP plates with IDEs for EIS measurements, and a membrane with attached silicone channels. (ii) Image of the disposable membrane and the patterned Au electrodes on the plastic substrate. Adapted with permission from Wiley and Sons, 2016* [36]*.*

2.2.3. Considerations about the electrode configuration

When designing a microfluidic device with TEER sensing electrodes, different critical aspects have to be considered. One of them is the type of measurement technique used. Cell barrier impedance can be quantified either with a two-terminal or a four-terminal approach [53,54]. In a two-terminal device, two electrodes generate a voltage or current signal across the cell layer (Figure 2.13 A). The resulting signal is picked up by the same electrodes to extract the resistance value. While this approach is simple to implement, it has a major drawback in terms of measurement accuracy. As the two electrodes are both carrying and sensing the electrical signals, the lead and contact resistances of the measuring equipment, along with the polarization impedance of the electrodes is added to the measured impedance, negatively affecting the readouts. In EIS-based applications, this effect can be observed in the low frequencies, where the double layer capacitance is dominant. Depending on the type of electrode material, the polarization impedance can have a different effect on the impedance spectra. However, if the contact impedance is accounted within an electrical equivalent circuit, for example, as a CPE, the model can still be fit, and the parameters associated with the cell barrier can be obtained.

In a four-terminal measurement, two electrodes act as the current or voltage carrying source while the other two serve as readout sensors (Figure 2.13 B). In this way, the contact and lead resistances of the equipment, along with the electrode polarization impedances, are greatly reduced compared to a two-terminal measurement. In spite of this, most commercial potentiostats are adapted to two-electrode configurations, thus limiting the applications based on four electrodes. Also, while the four-terminal approach improves readout accuracy, it can still be a source of measurement errors due to the geometry and the position of the electrodes in the device [55].

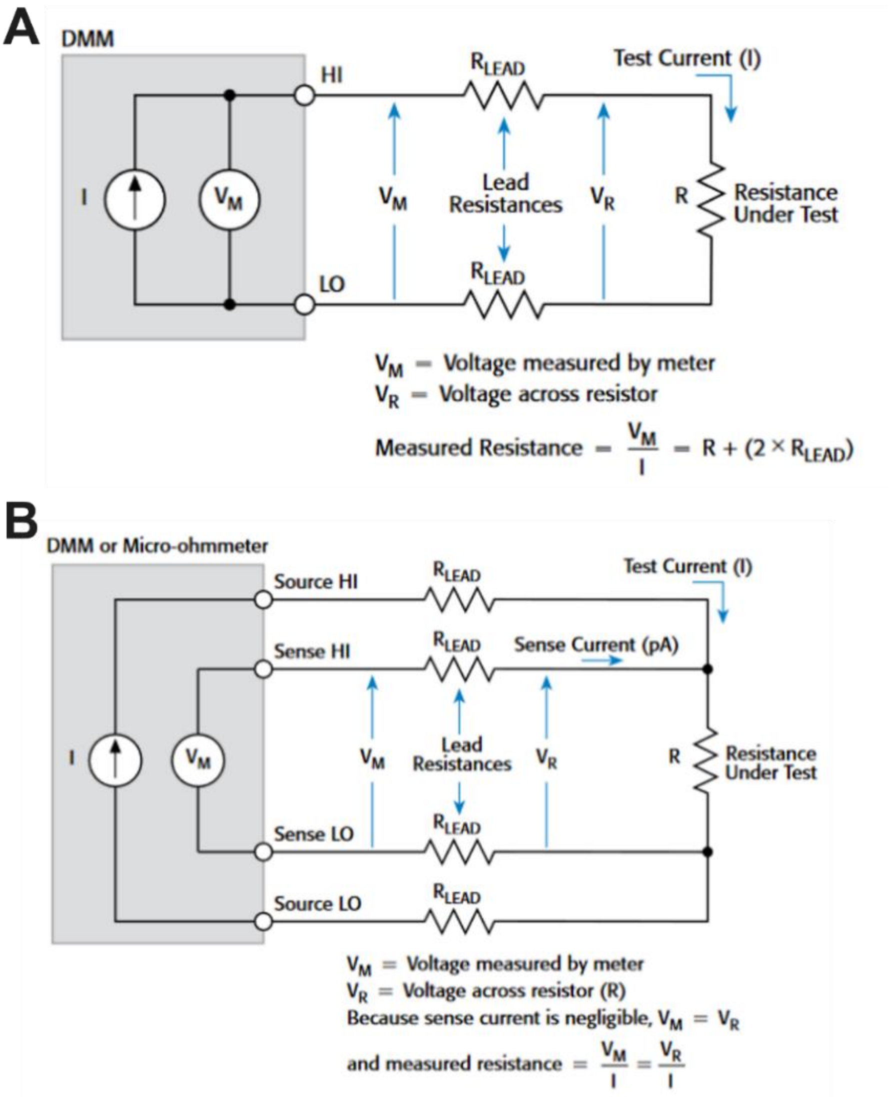

Figure 2.13: *Types of TEER measurement techniques. (A) Electrical circuit of a two-terminal measurement setup. (B) Electrical circuit of a four-terminal measurement setup. Adapted from [58].*

The spatial distribution of the electric field is another key element to determine the optimal configuration of the electrodes in a microfluidic device. When TEER measurements are performed on a cell barrier, not all regions of the cell layer contribute the same to the impedance values, as some areas are closer to the electrode than others depending on the system configuration. The contribution of each region to the total resistance is linked to the current density distribution. To quantify such distribution, the electrical sensitivity is often calculated:

$$\textbf{(eq. 2.3)} \quad S = \frac{J_1 * J_2}{I^2}$$

Where J_1 and J_2 are the current density fields when a current I is injected by the current-carrying electrodes and the voltage-sensing ones, respectively. In a bipolar configuration, both current densities are the same while in a tetrapolar configuration, each current density is associated to one of the electrode pairs. When the sensitivity of a specific volume has a high value, its contribution to the total impedance is higher than areas with lower values [13]. A numerical electrical model was established to determine the electrical sensitivity of the cell layer with different types of electrode sizes and positions for a four-terminal measurement setup (Figure 2.14) [56]. For an ideal uniform current distribution, the normalized value of sensitivity would be constant and equal to 1. Among the different simulated configurations, models A and C showed more uniform sensitivities than model B, where differences of current distribution can be observed between the center and the ends of the chamber due to the large distance between the electrodes. A dependency on TEER was also found, with low values associated with more uniform current distributions. Also, the channel dimensions can also affect the sensitivity of the system, as a decrease in height can have a negative impact on the uniformity of the current density. To compensate for these variations in other microfluidic setups, the authors proposed the use of a geometrical correction factor to account for the configuration of the device and the electrodes and to compare the corrected TEER values to others in the literature.

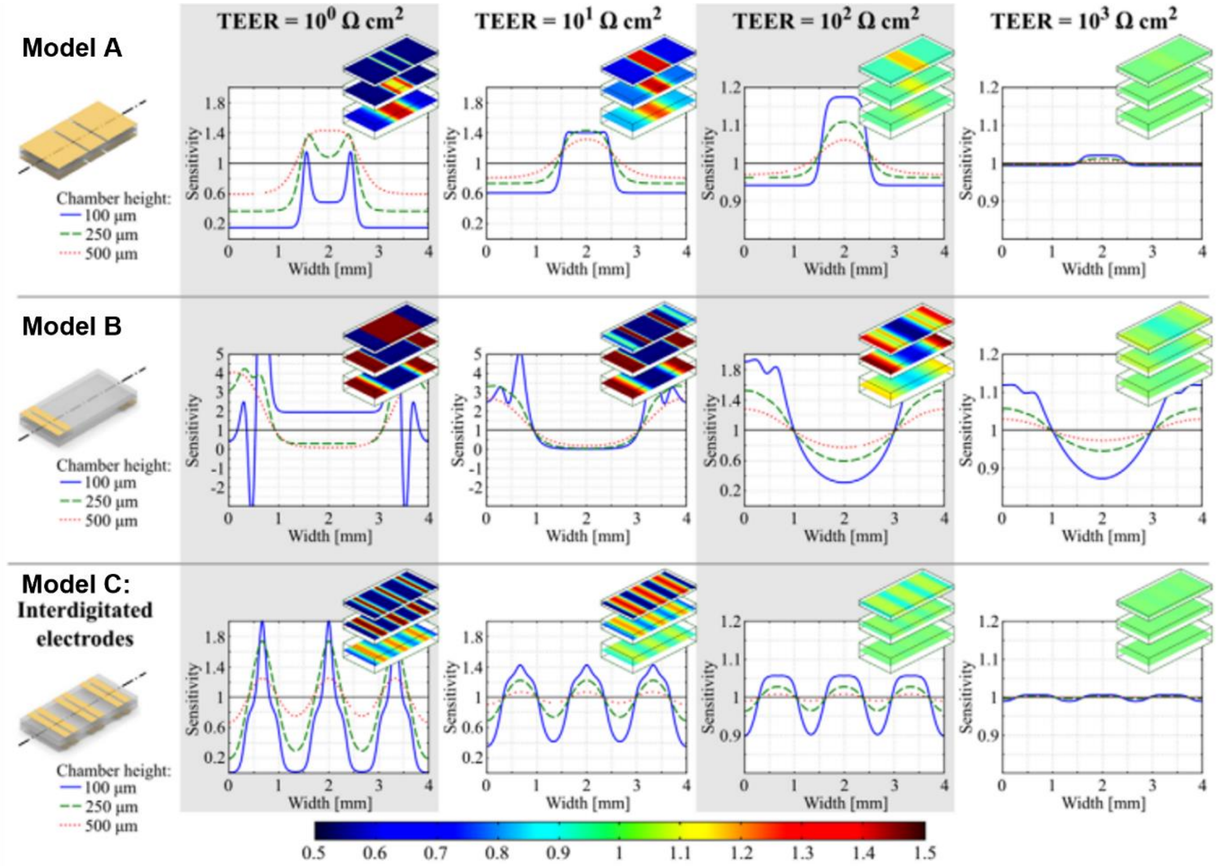

Figure 2.14: *Sensitivity distribution for different electrode configurations (3D schematics on the left column) across cell barriers in organ-on-chips. The results are computed from COMSOL simulations for different TEER values (from* 10^0 *to* 10^3 *Ω.cm*^{2}*) and different chamber heights (from 100 to 500 µm). The dashed lines on the schematics indicate the computed sensitivity section. Data are normalized by the squared cell culture area. Adapted with permission from Wiley and Sons, 2018* [56].

2.3. Examples of gut-on-chip models with integrated TEER sensing capabilities

The increasing complexity of tissue barrier models in organ-on-chips has led to the incorporation of TEER sensors within these devices to monitor the development and function of cell layers in real time [57–59]. These sensors can provide key quantitative information about the permeability of the cell barrier, essential for toxicology and drug screening studies. Such systems have been used in different *in vitro* models such as the blood brain barrier [60–64], the renal epithelium [36,65], the lung epithelium [66–68], the skin [69–71] and the heart [72].

The gut epithelium has also been one of the main targets of tissue barrier models with TEER sensing capabilities, as it tightly regulates the passage and absorption of oral compounds. While most *in vitro* models have relied on the cell culture of immortalized Caco-2 cells on commercial inserts to quantify the tightness of the epithelial monolayer, the reported values on these models have been shown to be abnormally high compared to *in vivo* studies. One of the reasons of the non-physiological tightening of the epithelial barriers *in vitro* is due to the properties of the cell culture membranes, as their stiffness and lack of 3D structural cues induce mechanobiological changes in cell morphology, promoting tighter cell-to-cell junctions and a lower intercellular permeability. To assess barrier integrity in more realistic cell micro-environments, gut-on-chips have been adapted to implement electrical monitoring of intestinal epithelial layers under dynamic conditions [73]. Wire insertion has been the main approach to measure cell layer resistance within the chip. To illustrate this, Odijk et al. developed a gut-on-chip to study the effect of the chip geometry and electrode position on TEER measurements [49]. Two Ag/AgCl wires were inserted at the inlet of the top channel and the outlet of the bottom one respectively, and DC TEER measurements were performed with a volt-ohm meter. By establishing a theoretical model of the cell layer, they found out that current density distribution was not spatially uniform within the chip, as the areas closer to the inlets and outlets had higher current densities than the rest (Figure 2.15 A). This non-uniformity of current distribution resulted in an over-estimation of TEER, with values on-chip artificially higher than Transwell®-based models. Moreover, great effort has been put to introduce intestinal microbiota in gut-on-chip models as they play a key role in gut homeostasis [48,74–76]. To investigate the effect of intestinal bacteria on epithelial permeability, a multi-layer microfluidic device, named HuMiX, was developed [76]. The device could support the cell co-culture of both aerobic and anaerobic bacteria of the microbiome with intestinal epithelial cells, by generating an oxygen gradient that could be monitored in-line with fixed optical oxygen sensors (Figure 2.15 B). In addition, commercial chopstick-like electrodes were inserted in the chip to assess the tightness of the epithelial barrier via end-point TEER measurements. After 7 days of cell culture under perfusion, Caco-2 cells formed a tight monolayer in co-culture with anaerobic bacteria *Lactobacillus rhamnosus GG* (LGG), with TEER values being significantly higher than static models (Figure 2.15 B).

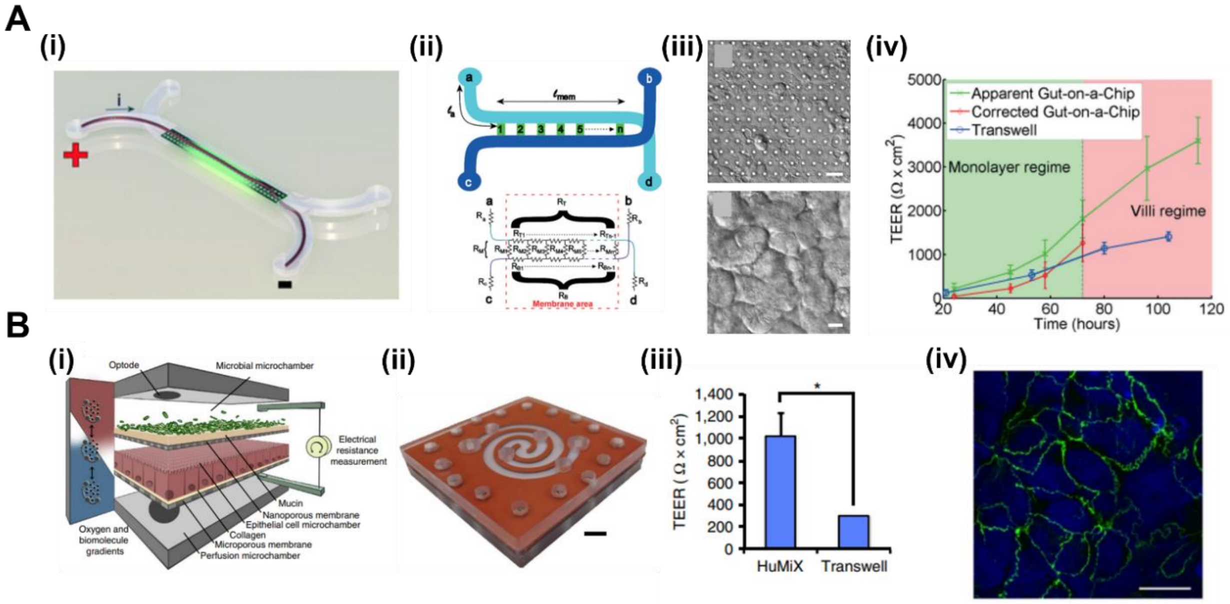

Figure 2.15: *Gut-on-chips with inserted wires for TEER monitoring. (A) Direct current TEER measurements on a gut-on-chip. (i) 3D schematic of the microfluidic device and the current flow. (ii) Chip layout and electrical equivalent circuit of the device. (iii) DIC images of Caco-2 cells grown on the cell culture membrane after 24h (top) and 100h (bottom). Scale bar: 50 μm. (iv) TEER plots of the gut-on-a-chip (green) and Transwell (blue) using human intestinal epithelial Caco-2 cells. The corrected gut-on-a-chip line (red) is calculated based on a theoretical model. Values are displayed as mean ± S.D. (for chip measurements,* n = *7, for Transwell measurements,* n = *12). Adapted with permission from the Royal Society of Chemistry, 2015* [49]*. (B) (i) Schematic diagram of the HuMiX model, where human intestinal epithelial cells and gastrointestinal microbiota are cultured on porous membranes under flow. (ii) Photograph of the assembled device. Scale bar: 1 mm. (iii) TEER plots of the Caco-2 cell layer after 7 days of cell culture in the HuMiX device and standard Transwells using standard chopstick electrodes. The error bars indicate the S.E.M. (n=3). * indicates a statistically significant difference (p<0.05). (iv) Immunofluorescence imaging of Caco-2 cells stained for ZO-1 (green) and nuclei (blue) after 24h of cell co-culture with anaerobic bacteria Lactobacillus rhamnosus GG (LGG). Scale bar: 10 μm. Adapted with permission from Nature, 2016* [76]*.*

Electrode-integrated gut-on-chips have also been developed to obtain more reliable electrical readouts of epithelial cell barrier properties [33,34,46,77]. For instance, a six-electrode chip was used to study 3D villus formation of intestinal epithelial Caco-2 cells [34]. Thin films of Au were patterned on PC substrates to fabricate semi-transparent electrodes for four-terminal EIS monitoring (Figure 2.16 A, B). Impedance analysis and 3D confocal imaging were compared at different time points over 12 days of cell culture to link the electrical properties of the tissue barrier with the morphology of the cell monolayer (Figure 2.16 C). Interestingly, it was observed that 3D villi formation in the gut-on-chip resulted in an increase of the cell layer capacitance, in accordance with simulated electrical models of the cell barrier (Figure 2.16 D, E). These results demonstrated the ability of electrical impedance characterization to determine the degree of differentiation of intestinal villi in gut-on-chips without the need of optical visualization.

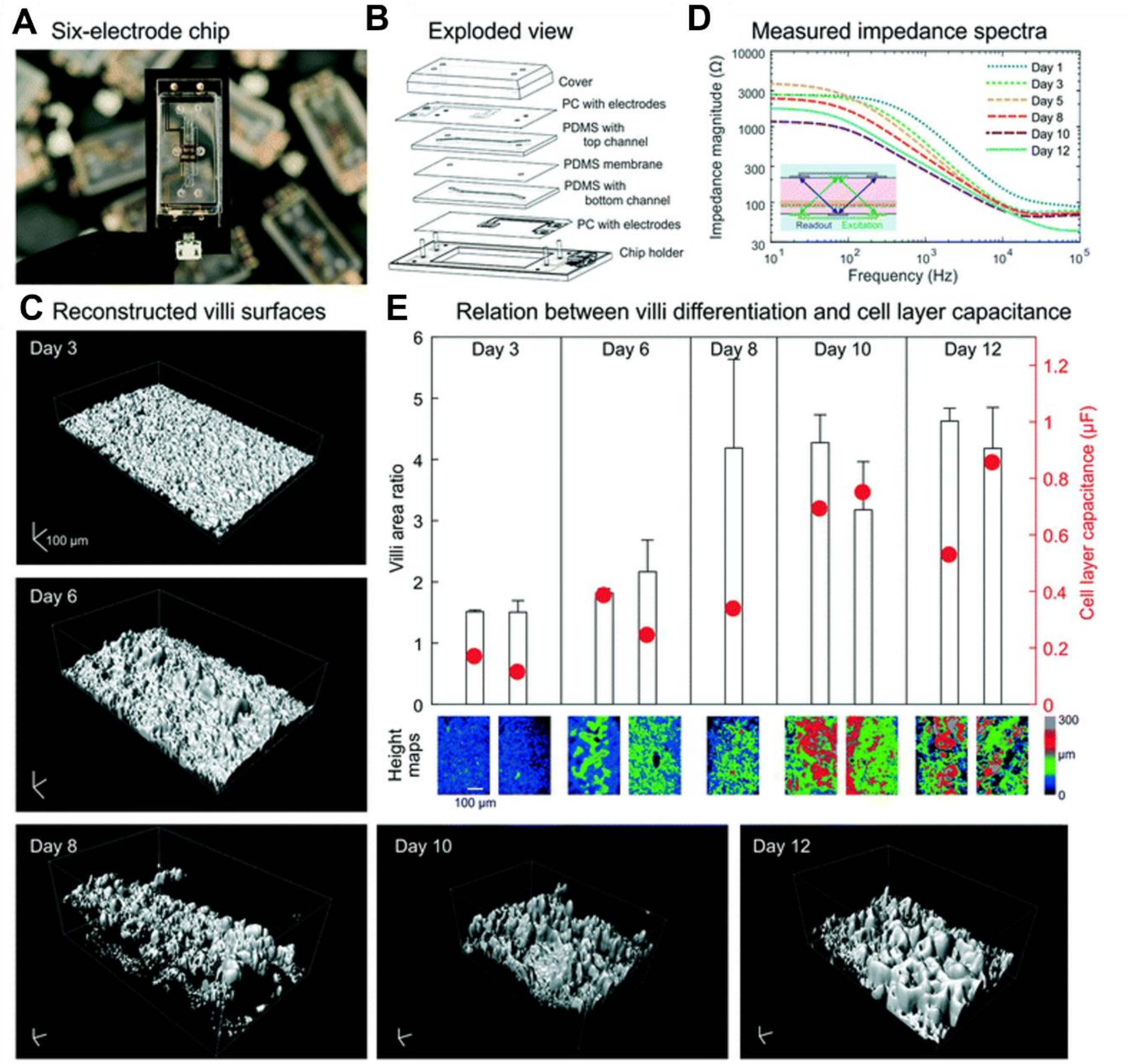

Figure 2.16: *Gut-on-chip with integrated sensors. (A) Image of the six-electrode device mounted in a chip holder. (B) Exploded view of the chip, showing two top and bottom PDMS channels separated by a porous PDMS membrane, sandwiched between two PC substrates with integrated semi-transparent Au electrodes. The chip holder contains a printed circuit board for electrical interfacing. (C) 3D reconstructed confocal images of the villus intestinal epithelium cultured on-chip at days 3, 6, 8, 10 and 12, showing an increase in number and height of villi over time. Scale bar: 100 µm. (D) Impedance magnitude Bode plots of the guts-on-chips after 12 days of cell culture. (E) Plot comparing the measured epithelial capacitance and the villi area ratio to quantify the degree of villus differentiation. Color scale indicates a height map. Scale bar: 100 µm. Adapted with permission from the Royal Society of Chemistry, 2019* [34]*.*

While some groups have reported TEER values on gut-on-chip models where intestinal epithelial cells self-formed 3D villi-like structures, most of these models are based on conventional stiff membranes that do not recapitulate the mechanical properties nor the compartmentalized organization of the intestinal mucosa *in vivo*, thus limiting the biological significance of cell layer resistance measurements based on these studies. To overcome these issues, hydrogels have been recently introduced in gut-on-chips with TEER sensing capabilities [78–80]. In one of these models, a high-throughput version of the commercially available OrganoPlate system was used to monitor TEER evolution on multiple Caco-2 tubules simultaneously [79]. For each chip of the platform, 8 stainless steel electrodes were inserted on different inlet and outlet ports to perform continuous four-terminal EIS measurements of the epithelial monolayers (Figure 2.17 A). The system was able to successfully monitor TEER during barrier formation, with maximum average values around 600 Ω.cm^2 after 4 days of cell culture. To further validate the model, Caco-2 cell tubules were exposed to staurosporine to assess the integrity of the barrier under drug-induced barrier disruption conditions. For increasing drug concentrations, TEER declines could be observed 1, 6 and 24h after exposure, and the apparent permeability coefficient to tracers with different molecular weights increased. However, the apparent permeability only increased from concentrations above 156 nM, while TEER decreases could be measured with concentrations as low as 10 nM, demonstrating the higher sensitivity of electrical measurements over fluorescent tracer-based permeability studies. Furthermore, timelapses of TEER with different concentrations of staurosporine showed the fast response of the cell barrier to high concentrations, with values reaching almost 0 Ω.cm2 in less than 3h, thus showing the advantages of real time TEER measurements with the system for drug screening applications (Figure 2.17 A). Following this, the same platform was used to study the inflammatory response of a four-cell co-culture for an *in vitro* dynamic intestinal model. For this work, epithelial Caco-2 cells and HT29-MTX-E12 goblet cells were co-cultured on the top adjacent channel to form a tight tubule after 4 days under perfusion, as confirmed by 3D confocal images (Figure 2.17 B). To establish an inflammatory model of the intestine, immune cells THP-1 and MUTZ-3 were added to the bottom adjacent channel and pro-inflammatory cytokines TNFα and IL-1β were perfused on both channels for up to 72h. EIS measurements revealed that exposure to the mix of cytokines induced a significant drop of cell layer resistance compared to non-exposed chips, with a decrease of more than 45% over control chips after 3 days. As a final application of the model, exposure to anti-inflammatory compound TPCA-1 resulted in a recovery of the barrier integrity, validating the model as a screening platform for drug testing. However, despite the high-throughput of these hydrogel gut-on-chip devices, their electrode configuration is based on the insertion of pairs of stainless steel rods at the inlet ports, which can be more prone to measurement errors due to the large distance between them.

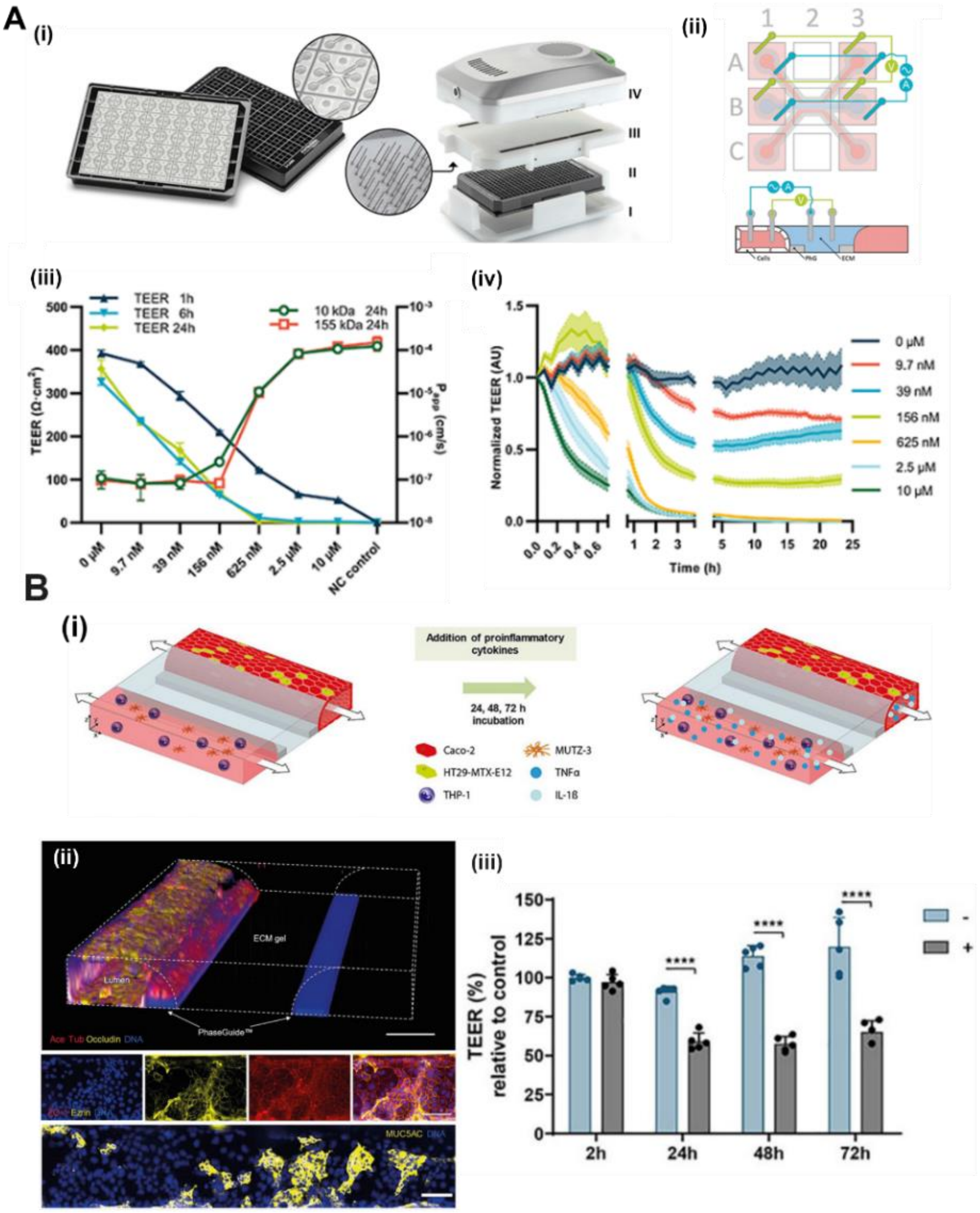

Figure 2.17: *Hydrogel gut-on-chip with TEER sensing capabilities. (A) OrganoTEER device for a gut-on-chip model. (i) Image of the multiplexed OrganoPlate platform (right), a microtiter plate with 40 three-channel microfluidic chips. Exploded view of the OrganoTEER device, consisting of a plate holder (I), the OrganoPlate (II), the electrode board (III) and the measurement module (IV). (Top) Schematic configuration of the electrodes on the chip inlet and outlet ports for four-point measurements. (Bottom) Schematic cross-section of the center of the chip, depicting the ECM gel, the phaseguides, the tube that is directly grown against the ECM gel, and a diagram of the electrical circuit formed from the apical to basal side of the tube. (iii) TEER (at 1, 6 and 24h) and apparent permeability P_{app} (at 24h) plots of Caco-2 cell barriers exposed to various concentrations of staurosporine. (iv) Timelapse of TEER of Caco-2 tubules exposed to different concentrations of staurosporine. Curves are plotted with standard deviation of the mean as shaded area with the mean value as central line. Axis breaks indicate a change in sampling rate within the continuous acquisition. n = 3–5 for the TEER data as well as the P_{app} data. Adapted with permission from the Royal Society of Chemistry, 2021 [79]. (B) Studies on inflammatory responses in OrganoTEER gut-on-chips. (i) Schematic illustration of the induction of inflammatory stimulation in the tetraculture intestinal model within the OrganoPlate three-lane chip upon exposure to TNFα and IL-1β (both at 200 ng/mL) on both lateral channels. (ii) Top image: 3D reconstruction of an*

epithelial tubule with Caco-2 and HT29-MTX cells against a collagen-I ECM patterned hydrogel in the middle compartment. The tube was stained for acetylated tubulin (red), occludin (yellow), and DNA (blue). Middle panel: immunofluorescent maximum projections of the epithelial tube in the tetraculture on day 4, stained for ezrin (yellow), ZO-1 (red), and DNA (blue). Bottom image: maximum projection of a stained tubular structure of Caco-2 and HT29-MTX cells in the top compartment of an OrganoPlate three-lane chip on day 4 of culture. The cells are stained for mucin 5AC (MUC5AC; yellow) and DNA (blue). Scale bar: 50 µm. (iii) TEER plots of the epithelial barriers assessed at 2, 24, 48, and 72 h after exposure to the inflammatory cytokines. Data are represented in percentage and normalized to the 2 h non-exposed condition (n = 4). Adapted with permission from SAGE Publications, 2020 [80].

2.4. References

1. Rutten, M. J., Hoover, R. L. & Karnovsky, M. J. Electrical resistance and macromolecular permeability of brain endothelial monolayer cultures. *Brain Res* **425**, 301–310 (1987).
2. Meza, I., Ibarra, G., Sabanero, M., Martinez-Palomo, A. & Cereijido, M. Occluding junctions and Cytoskeletal Components in a Cultured Transporting Epithelium 746. *J Cell Biol* **87**, 746–754 (1980).
3. USSING, H. H. & ZERAHN, K. Active Transport of Sodium as the Source of Electric Current in the Short-circuited Isolated Frog Skin. *Acta Physiol Scand* **23**, 110–127 (1951).
4. JOHNSEN, V. K., LEVI, H. & USSING, H. H. The Mode of Passage of Chloride Ions through the Isolated Frog Skin. *Acta Physiol Scand* **25**, 150–163 (1952).
5. Yeste, J., Illa, X., Alvarez, M. & Villa, R. Engineering and monitoring cellular barrier models. *J Biol Eng* **12**, 1–19 (2018).
6. Benson, K., Cramer, S. & Galla, H. J. Impedance-based cell monitoring: Barrier properties and beyond. *Fluids Barriers CNS* **10**, 1–11 (2013).
7. Poisson, J. *et al.* Liver sinusoidal endothelial cells: Physiology and role in liver diseases. *J Hepatol* **66**, 212–227 (2017).
8. Prozialeck, W. C., Edwards, J. R., Lamar, P. C. & Smith, C. S. Epithelial barrier characteristics and expression of cell adhesion molecules in proximal tubule-derived cell lines commonly used for in vitro toxicity studies. *Toxicol In Vitro* **20**, 942–953 (2006).
9. Smith, Q. R. & Rapoport, S. I. Cerebrovascular Permeability Coefficients to Sodium, Potassium, and Chloride. *J Neurochem* **46**, 1732–1742 (1986).
10. Liu, N., Chen, R. & Wan, Q. Recent Advances in Electric-Double-Layer Transistors for Bio-Chemical Sensing Applications. *Sensors 2019, Vol. 19, Page 3425* **19**, 3425 (2019).
11. Alexander, F., Eggert, S. & Price, D. Label-Free Monitoring of 3D Tissue Models via Electrical Impedance Spectroscopy. *Bioanal Rev* **2**, 111–134 (2019).
12. Kalvøy, H., Johnsen, G. K., Martinsen, Ø. G. & Grimnes, S. New Method for Separation of Electrode Polarization Impedance from Measured Tissue Impedance. *Open Biomed Eng J* **5**, 8–13 (2011).
13. Grimnes, S. & Martinsen, Ø. G. Bioimpedance and Bioelectricity Basics. *Bioimpedance and Bioelectricity Basics* (2008) doi:10.1016/B978-0-12-374004-5.X0001-3.
14. Guimera, A., Prats-Alfonso, E., Villa, R. & Javier Del Campo, F. Development of Microelectrode-based Biosensors for Biomedical Analysis. *RSC Detection Science* **2016-January**, 19–84 (2015).
15. Srinivasan, B. *et al.* TEER Measurement Techniques for In Vitro Barrier Model Systems. *SLAS Technol* **20**, 107–126 (2015).

16. World Precision Instruments | Cell & Tissue | TEER Measurement | STX2. https://www.wpi-europe.com/products/cell--tissue/teer-measurement/accessories-for-legacy-teer-meters/stx2.aspx.
17. World Precision Instruments | ENDOHM-12G EndOhm for 12mm Culture Cups (12 wells per plate). https://www.wpi-europe.com/products/cell--tissue/teer-measurement/accessories-for-legacy-teer-meters/8365-endohm-12g.aspx.
18. World Precision Instruments | EVM-MT-03-01 EVOM Manual for TEER Measurement. https://www.wpi-europe.com/products/cell--tissue/teer-measurement/evm-mt-03-01.aspx.
19. Blume, L.-F., Denker, M., Gieseler, F. & Kunze, T. Temperature corrected transepithelial electrical resistance (TEER) measurement to quantify rapid changes in paracellular permeability. *Pharmazie* (2010).
20. Vigh, J. P. *et al.* Transendothelial electrical resistance measurement across the blood–brain barrier: A critical review of methods. *Micromachines (Basel)* **12**, 685 (2021).
21. Macdonald, J. R. Impedance Spectroscopy. *Ann Biomed Eng* **20**, 289–305 (1992).
22. Gerasimenko, T. *et al.* Impedance Spectroscopy as a Tool for Monitoring Performance in 3D Models of Epithelial Tissues. *Front Bioeng Biotechnol* **7**, (2020).
23. Günzel, D. *et al.* From TER to trans- and paracellular resistance: lessons from impedance spectroscopy. *Ann N Y Acad Sci* **1257**, 142–151 (2012).
24. Automated TEER measurement systems - nanoAnalytics EN. https://www.nanoanalytics.com/en/products/cellzscope.html.
25. ECIS Cultureware - Applied BioPhysics. https://www.biophysics.com/cultureware.php.
26. Fuchs, S. *et al.* In-line analysis of organ-on-chip systems with sensors: Integration, fabrication, challenges, and potential. *ACS Biomater Sci Eng* **7**, 2926–2948 (2021).
27. Ferrell, N. *et al.* A microfluidic bioreactor with integrated transepithelial electrical resistance (TEER) measurement electrodes for evaluation of renal epithelial cells. *Biotechnol Bioeng* **107**, 707–716 (2010).
28. Douville, N. J. *et al.* Fabrication of two-layered channel system with embedded electrodes to measure resistance across epithelial and endothelial barriers. *Anal Chem* **82**, 2505–2511 (2010).
29. Ramadan, Q. & Ting, F. C. W. In vitro micro-physiological immune-competent model of the human skin. *Lab Chip* **16**, 1899–1908 (2016).
30. Booth, R. & Kim, H. Characterization of a microfluidic in vitro model of the blood-brain barrier (μBBB). *Lab Chip* **12**, 1784–1792 (2012).
31. Zhang, S. *et al.* Reduced cytotoxicity of silver ions to mammalian cells at high concentration due to the formation of silver chloride. *Toxicology in Vitro* **27**, 739–744 (2013).
32. Yeste, J. *et al.* A perfusion chamber for monitoring transepithelial NaCl transport in an in vitro model of the renal tubule. *Biotechnol Bioeng* **115**, 1604–1613 (2018).
33. Henry, O. Y. F. *et al.* Organs-on-chips with integrated electrodes for trans-epithelial electrical resistance (TEER) measurements of human epithelial barrier function. *Lab Chip* **17**, 2264–2271 (2017).
34. van der Helm, M. W. *et al.* Non-invasive sensing of transepithelial barrier function and tissue differentiation in organs-on-chips using impedance spectroscopy. *Lab Chip* **19**, 452–463 (2019).
35. Mermoud, Y., Felder, M., Stucki, J. D., Stucki, A. O. & Guenat, O. T. Microimpedance tomography system to monitor cell activity and membrane movements in a breathing lung-on-chip. *Sens Actuators B Chem* **255**, 3647–3653 (2018).
36. Yeste, J. *et al.* A perfusion chamber for monitoring transepithelial NaCl transport in an in vitro model of the renal tubule. *Biotechnol Bioeng* **115**, 1604–1613 (2018).

37. Yeste, J., Illa, X., Guimerà, A. & Villa, R. A novel strategy to monitor microfluidic in-vitro blood-brain barrier models using impedance spectroscopy. in *Bio-MEMS and Medical Microdevices II* vol. 9518 95180N (SPIE, 2015).
38. Griep, L. M. *et al.* BBB on CHIP: Microfluidic platform to mechanically and biochemically modulate blood-brain barrier function. *Biomed Microdevices* **15**, 145–150 (2013).
39. van der Helm, M. W. *et al.* Direct quantification of transendothelial electrical resistance in organs-on-chips. *Biosens Bioelectron* **85**, 924–929 (2016).
40. Brown, J. A. *et al.* Recreating blood-brain barrier physiology and structure on chip: A novel neurovascular microfluidic bioreactor. *Biomicrofluidics* **9**, 1–15 (2015).
41. Giampetruzzi, L. *et al.* Advances in Trans-Epithelial Electrical Resistance (TEER) monitoring integration in an Intestinal Barrier-on-Chip (IBoC) platform with microbubbles-tolerant analytical method. *Sens Biosensing Res* **37**, 100512 (2022).
42. Kim, B. S. *et al.* Real-time physiological sensor-based liver-on-chip device for monitoring drug toxicity. *Journal of Micromechanics and Microengineering* **30**, 115013 (2020).
43. Kang, Y. T., Kim, M. J. & Cho, Y. H. A cell impedance measurement device for the cytotoxicity assay dependent on the velocity of supplied toxic fluid. *Journal of Micromechanics and Microengineering* **28**, 045012 (2018).
44. Koutsouras, D. A. *et al.* Probing the Impedance of a Biological Tissue with PEDOT:PSS-Coated Metal Electrodes: Effect of Electrode Size on Sensing Efficiency. *Adv Healthc Mater* **8**, 1901215 (2019).
45. Susloparova, A. *et al.* Low impedance and highly transparent microelectrode arrays (MEA) for in vitro neuron electrical activity probing. *Sens Actuators B Chem* **327**, 128895 (2021).
46. Marrero, D. *et al.* Organ-on-a-chip with integrated semitransparent organic electrodes for barrier function monitoring. *Lab Chip* (2023) doi:10.1039/D2LC01097F.
47. Deosarkar, S. P. *et al.* A Novel Dynamic Neonatal Blood-Brain Barrier on a Chip. *PLoS One* **10**, 142725 (2015).
48. Kim, H. J., Huh, D., Hamilton, G. & Ingber, D. E. Human gut-on-a-chip inhabited by microbial flora that experiences intestinal peristalsis-like motions and flow. *Lab Chip* **12**, 2165–2174 (2012).
49. Odijk, M. *et al.* Measuring direct current trans-epithelial electrical resistance in organ-on-a-chip microsystems. *Lab Chip* **15**, 745–752 (2015).
50. Schmitz, T. *et al.* Nanostructured TiN-Coated Electrodes for High-Sensitivity Noninvasive Characterization of in Vitro Tissue Models. *ACS Appl Nano Mater* **1**, 2284–2293 (2018).
51. Krishnakumar, A. *et al.* Organ-on-a-Chip Platform with an Integrated Screen-Printed Electrode Array for Real-Time Monitoring Trans-Epithelial Barrier and Bubble Formation. *ACS Biomater Sci Eng* **9**, 1620–1628 (2023).
52. Chmayssem, A. *et al.* New Microfluidic System for Electrochemical Impedance Spectroscopy Assessment of Cell Culture Performance: Design and Development of New Electrode Material. *Biosensors (Basel)* **12**, (2022).
53. Brown, B. H., Wilson, A. J. & Bertemes-Filho, P. Bipolar and tetrapolar transfer impedance measurements from volume conductor. *Electron Lett* **36**, 2060–2062 (2000).
54. Bera, T. K. Bioelectrical Impedance Methods for Noninvasive Health Monitoring: A Review. *J Med Eng* **2014**, 1–28 (2014).
55. Grimnes, S. & Martinsen, Ø. G. Sources of error in tetrapolar impedance measurements on biomaterials and other ionic conductors. *J Phys D Appl Phys* **40**, 9–14 (2007).
56. Yeste, J. *et al.* Geometric correction factor for transepithelial electrical resistance measurements in transwell and microfluidic cell cultures. *J Phys D Appl Phys* **49**, (2016).

57. Ferrari, E., Palma, C., Vesentini, S., Occhetta, P. & Rasponi, M. Integrating Biosensors in Organs-on-Chip Devices: A Perspective on Current Strategies to Monitor Microphysiological Systems. *Biosensors (Basel)* **10**, (2020).
58. Zhu, Y. *et al.* State of the art in integrated biosensors for organ-on-a-chip applications. *Curr Opin Biomed Eng* **19**, (2021).
59. Soucy, J. R., Bindas, A. J., Koppes, A. N. & Koppes, R. A. Instrumented Microphysiological Systems for Real-Time Measurement and Manipulation of Cellular Electrochemical Processes. *iScience* **21**, 521–548 (2019).
60. Bossink, E. G. B. M., Zakharova, M., De Bruijn, D. S., Odijk, M. & Segerink, L. I. Measuring barrier function in organ-on-chips with cleanroom-free integration of multiplexable electrodes. *Lab Chip* **21**, 2040–2049 (2021).
61. Wang, Y. I., Abaci, H. E. & Shuler, M. L. Microfluidic blood–brain barrier model provides in vivo-like barrier properties for drug permeability screening. *Biotechnol Bioeng* **114**, 184–194 (2017).
62. Walter, F. R. *et al.* A versatile lab-on-a-chip tool for modeling biological barriers. *Sens Actuators B Chem* **222**, 1209–1219 (2016).
63. Partyka, P. P. *et al.* Mechanical stress regulates transport in a compliant 3D model of the blood-brain barrier. *Biomaterials* **115**, 30–39 (2017).
64. Motallebnejad, P., Thomas, A., Swisher, S. L. & Azarin, S. M. An isogenic hiPSC-derived BBB-on-a-chip. *Biomicrofluidics* **13**, 064119 (2019).
65. Brakeman, P. *et al.* A modular microfluidic bioreactor with improved throughput for evaluation of polarized renal epithelial cells. *Biomicrofluidics* **10**, 064106 (2016).
66. Skardal, A. *et al.* Multi-tissue interactions in an integrated three-tissue organ-on-a-chip platform. *Sci Rep* **7**, (2017).
67. Mermoud, Y., Felder, M., Stucki, J. D., Stucki, A. O. & Guenat, O. T. Microimpedance tomography system to monitor cell activity and membrane movements in a breathing lung-on-chip. *Sens Actuators B Chem* **255**, 3647–3653 (2018).
68. Stucki, J. D. *et al.* Medium throughput breathing human primary cell alveolus-on-chip model. *Scientific Reports 2018 8:1* **8**, 1–13 (2018).
69. Ramadan, Q. & Ting, F. C. W. In vitro micro-physiological immune-competent model of the human skin. *Lab Chip* **16**, 1899–1908 (2016).
70. Alexander, F. A., Eggert, S. & Wiest, J. Skin-on-a-chip: Transepithelial electrical resistance and extracellular acidification measurements through an automated air-liquid interface. *Genes (Basel)* **9**, (2018).
71. Sriram, G. *et al.* Full-thickness human skin-on-chip with enhanced epidermal morphogenesis and barrier function. *Materials Today* **21**, 326–340 (2018).
72. Maoz, B. M. *et al.* Organs-on-Chips with combined multi-electrode array and transepithelial electrical resistance measurement capabilities. *Lab Chip* **17**, 2294–2302 (2017).
73. Marrero, D. *et al.* Gut-on-a-chip: Mimicking and monitoring the human intestine. *Biosens Bioelectron* **181**, 113156 (2021).
74. Kim, H. J., Li, H., Collins, J. J. & Ingber, D. E. Contributions of microbiome and mechanical deformation to intestinal bacterial overgrowth and inflammation in a human gut-on-a-chip. *Proc Natl Acad Sci U S A* **113**, E7–E15 (2016).
75. Maurer, M. *et al.* A three-dimensional immunocompetent intestine-on-chip model as in vitro platform for functional and microbial interaction studies. *Biomaterials* **220**, 119396 (2019).
76. Shah, P. *et al.* A microfluidics-based in vitro model of the gastrointestinal human-microbe interface. *Nat Commun* **7**, (2016).

77. Tan, H. Y. *et al.* A multi-chamber microfluidic intestinal barrier model using Caco-2 cells for drug transport studies. *PLoS One* **13**, e0197101 (2018).
78. Beaurivage, C. *et al.* Development of a gut-on-a-chip model for high throughput disease modeling and drug discovery. *Int J Mol Sci* **20**, (2019).
79. Nicolas, A. *et al.* High throughput transepithelial electrical resistance (TEER) measurements on perfused membrane-free epithelia. *Lab Chip* **21**, 1676–1685 (2021).
80. Gijzen, L. *et al.* An Intestine-on-a-Chip Model of Plug-and-Play Modularity to Study Inflammatory Processes. *SLAS Technol* **25**, 585–597 (2020).

Objectives of the thesis

The main goal of this thesis is to develop a 3D bioprinted hydrogel gut-on-chip model with integrated TEER sensing capabilities. In this model, both the epithelial and stromal compartments of the intestinal mucosa are represented and cultured under flow to faithfully recapitulate the 3D configuration and the dynamic extracellular conditions of *in vivo* gut tissues. A high resolution DLP-SLA bioprinting technique is used to generate hydrogel channels with lateral villi-like shapes in a rapid and precise manner, while allowing their encasement into a tri channel microfluidic chip. The proposed system also allows the integration of electrodes inside the chip for real time TEER quantification of the epithelial barrier formation and integrity using EIS. To achieve this, different objectives are defined:

1. To fabricate hydrogel channels that replicate the dimensions and shape of human intestinal villi using a visible-light DLP-SLA 3D bioprinting technique.

2. To develop a 3D gut-on-chip model of the intestinal mucosa where stromal cells are embedded in the hydrogel to support the growth of epithelial cells and their barrier formation.

3. To numerically validate and integrate an electrode configuration within the gut-on-chip device for EIS-based TEER measurements of an epithelial barrier in real time.

3. Fabrication of a 3D bioprinted hydrogel microfluidic device with villi-like structures

3.1. Design of the 3D hydrogel gut-on-a-chip model

During these last years, advanced 3D intestinal *in vitro* models have been developed using light-based bioprinting techniques to generate hydrogels mimicking key structural elements of the gut epithelium within the physiological range [1–3]. However, despite the progress in the field, current 3D bioprinted intestinal models are based on static conditions, lacking essential mechanical cues from fluid flow present in the *in vivo* gut epithelium.

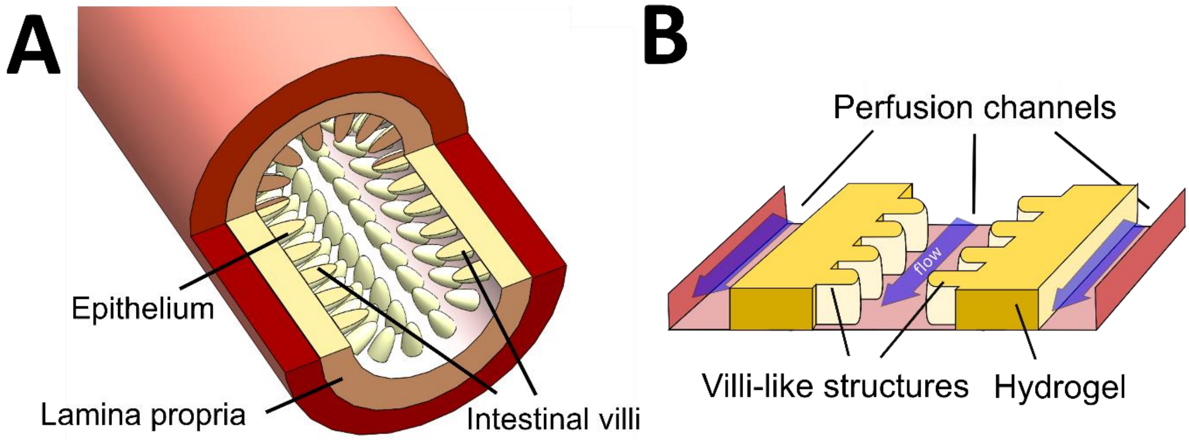

Figure 3.1: *Biomimetic hydrogel channel for a 3D gut-on-chip model. (A) Schematic cross-section of the small intestine. (B) 3D representation of the central part of the chip with the lateral, central channels and the hydrogel.*

To establish a realistic *in vitro* model of the gut mucosa, a perfusable 3D hydrogel channel with villi-shaped structures is presented in this thesis. The designed hydrogel reproduces a cross-section of the intestinal epithelium, with a central channel that mimics the lumen and villi-like structures on the sides to support the formation of an epithelial barrier (Figure 3.1 A, B), while also allowing the encapsulation of stromal cells to represent the lamina propria. The substrate was initially fabricated via DLP-SLA bioprinting. Then, the printed channel was encased within a microfluidic device, where two lateral channels were defined to guarantee the perfusion of the required oxygen and nutrients for long-term dynamic cell co-culture. The fabrication process of the hydrogel microfluidic device is explained in this chapter.

3.2. Materials and methods

3.2.1. GelMA preparation and characterization

3.2.1.1. GelMA synthesis

Extracted from animals, gelatin is a naturally derived polymer obtained from the partial hydrolysis of collagen. It can be physically cross-linked via thermal gelation, but the reaction is not stable above 37ºC. Due to this, gelatin is often chemically modified with methacrylate anhydride (MA) by adding methacryloyl groups to the primary amine and hydroxyl groups to form GelMA (Figure 3.2). The photopolymerization of GelMA, combined with photoinitiators, allows the formation of stable structures at body temperature [4].

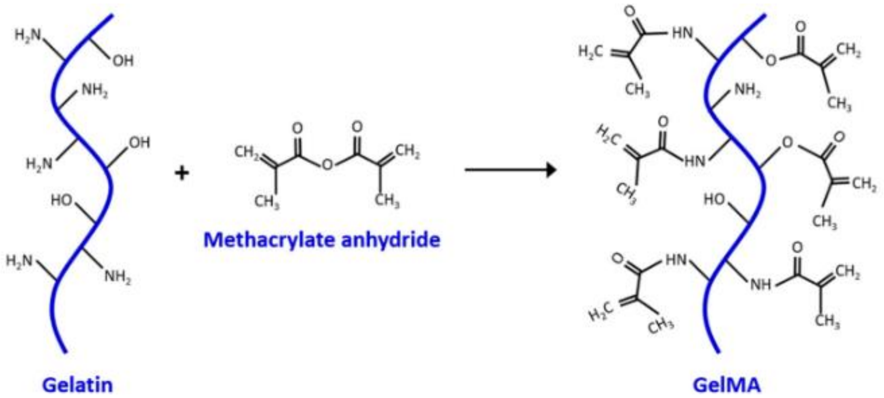

Figure 3.2: *Schematic representation of the chemical reaction of gelatin and methacrylate anhydride to form GelMA. Adapted with permission from MDPI, 2022* [36].

GelMA was synthesized following a previously described procedure (Figure 3.3) [5,6]. Briefly, 10 % (w/v) gelatin was obtained by dissolving gelatin from porcine skin type A (Sigma-Aldrich) in phosphate buffer saline (PBS, Gibco, ThermoFisher Scientific) at 50°C under stirring conditions for approximately 2 h. The methacrylic anhydride (Sigma-Aldrich) was added to the gelatin solution with a syringe pump (NE-1000 Programmable Single Syringe Pump, New Era) with a flow rate of 0.5 mL/min to reach a final concentration of 1.25 % (v/v) MA (Figure 3.3). The solution was left to react under stirring conditions at 50°C for 1 h to avoid phase separation. After this, GelMA solution was transferred to 50 mL Falcon tubes (Eppendorf) and centrifuged at 1200 rpm (rotina 38R, Hettich) for 3 min at room temperature to remove the unreacted MA and other cytotoxic by-products. The reaction was stopped by adding warm PBS to the supernatant. Following this, the solution was dialyzed against milliQ water at 40°C with 6-8 kDa molecular weight cut-off dialysis membranes (Spectra/por 1 Dialysis Membranes, Spectrumlabs) (Figure 3.3). This procedure was performed for three days, changing the water three times a day, to remove all the unreacted MA and by-products. The dialyzed solution was transferred into a glass beaker and the pH of the GelMA solution was adjusted to 7.4 with a pH meter (GLP21). Finally, the samples were frozen overnight at -80°C in 50 mL Falcon tubes covered with Parafilm, lyophilized for 3 or 4 days (Freeze Dryer Alpha 1-4 LD Christ) and stored in the freezer at -20°C for later use.

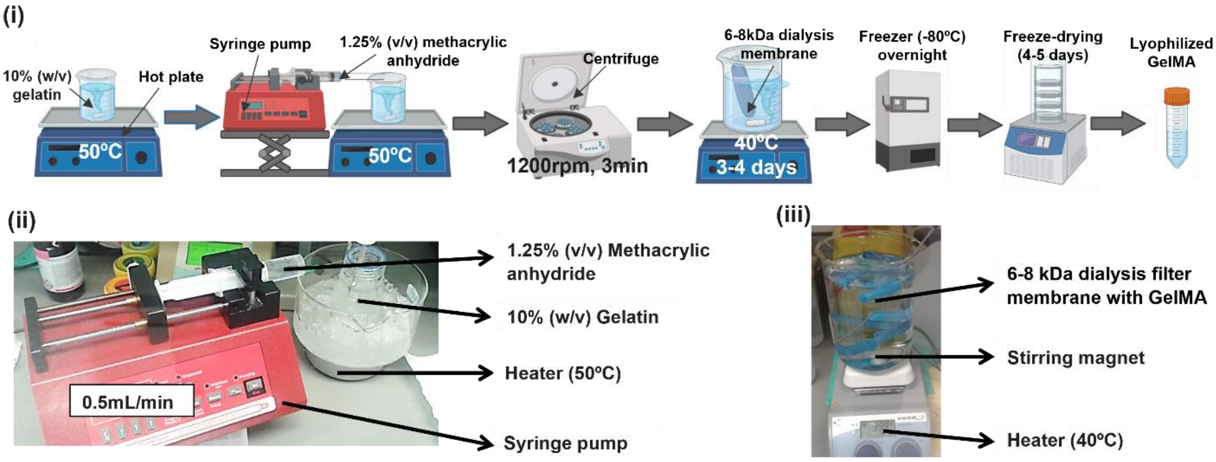

Figure 3.3: *Synthesis of GelMA. (i) Schematic of the preparation process of GelMA. (ii) Image of MA adding to the gelatin solution with a syringe pump. (ii) Image of the dialysis of unreacted MA in GelMA solution in filter membranes.*

3.2.1.2. *Characterization of GelMA via TNBSA assay*

As the concentration of MA increases, more amino and hydroxyl groups are chemically modified. The total percentage of methacryloyl groups added to gelatin is known as the degree of methacrylation. The mechanical and structural properties of the hydrogel, including porosity, pore size and swelling, are influenced by this parameter. A TNBSA assay was performed to characterize the degree of methacrylation of the prepared GelMA (Figure 3.4) [7,8]. In this assay, trinitrobenzene sulfonic acid (TNBSA) reacts with the primary amino groups of the gelatin to form orange-coloured trinitrophenyl (TNP) derivate that can be measured by absorbance. Gelatin, as a control, and two different GelMA (known and unknown degree of methacrylation) were dissolved under stirring conditions at 40ºC in a sodium carbonate buffer ($NaHCO_3$, pH 8.4, 0.1M in Milli-Q water, Sigma-Aldrich) at a concentration of 0.5 mg/mL. To generate a standard curve, a serial dilution of 100 µL of gelatin and GelMA solutions in $NaHCO_3$ from 0.5 to 0 mg/mL were placed in a 96-well plate (Nunc^{TM}, ThermoFisher Scientific). Wells with only carbonate buffer were also added as blank. Next, 50 µL of working solution (TNBSA 0.01% v/v in carbonate buffer, Sigma-Aldrich) were added and the plate was incubated at 37ºC for 2 h in complete darkness. After this, the reaction was stopped and stabilized by adding 50 µL of sodium dodecyl sulfate (SDS, Sigma-Aldrich) at 10% (v/v) and 25 µL of HCl (Panreac Applichem) 1M in Milli-Q water to each well. Gelatin and GelMA samples are solubilized by SDS, preventing precipitation of the samples after addition of HCl. Absorbance was measured at a wavelength of 335 nm with a microplate reader (Infinite M200 PRO Multimode Microplate Reader, Tecan). The resulting values were used to calculate the degree of methacrylation of the new batch of GelMA, comparing the calibration curve of the raw gelatin solution (total of free amines available) to the calibration curve of the GelMA solutions. Using this curve, the percentage of non-modified Lys can be determined from the absorbance. The degree of methacrylation was obtained from the subtraction of the remaining free amino groups to the total amount of amino groups.

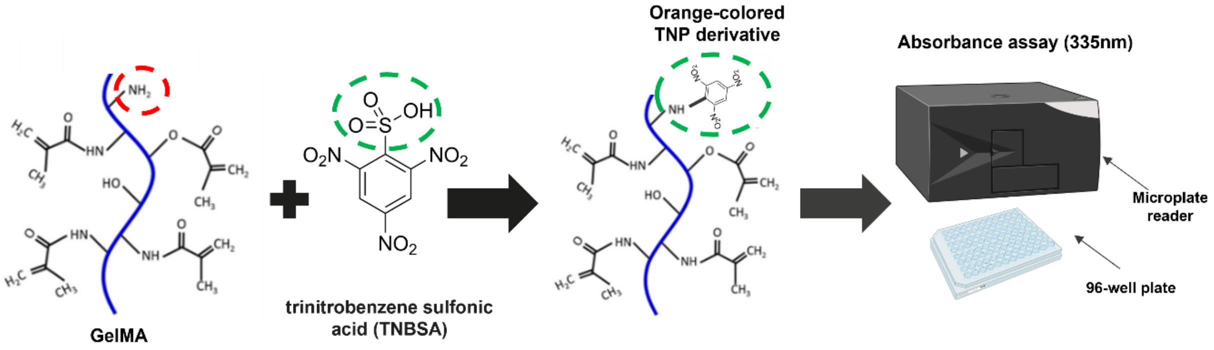

Figure 3.4: *Characterization of the methacrylation degree of GelMA via TNBSA assay.*

3.2.2. *Bioink composition*

A GelMA-PEGDA pre-polymer solution was prepared as a bioink for 3D bioprinting of hydrogels. PEGDA is a synthetic polymer obtained from the chemical modification of PEG molecules with acrylate groups at each end of the chain for chemical cross-linking. Hydrogels were generated via free radical photopolymerization with visible light exposure (Figure 3.5 A). To achieve this, the type-I photoinitiator LAP was added to the pre-polymer solution. LAP has a local absorbance maximum at around 375 nm but it is also photosensitive in the visible light range between 400 nm and 420 nm (Figure 3.5 B). To increase the resolution of the defined structures, tartrazine, a synthetic azo dye, was also added to the mix [9]. Its absorbance spectrum overlaps with the one of the light sources and it is close to the absorption peak of LAP, allowing a precise tuning of the curing depth during 3D printing (Figure 3.5 B).

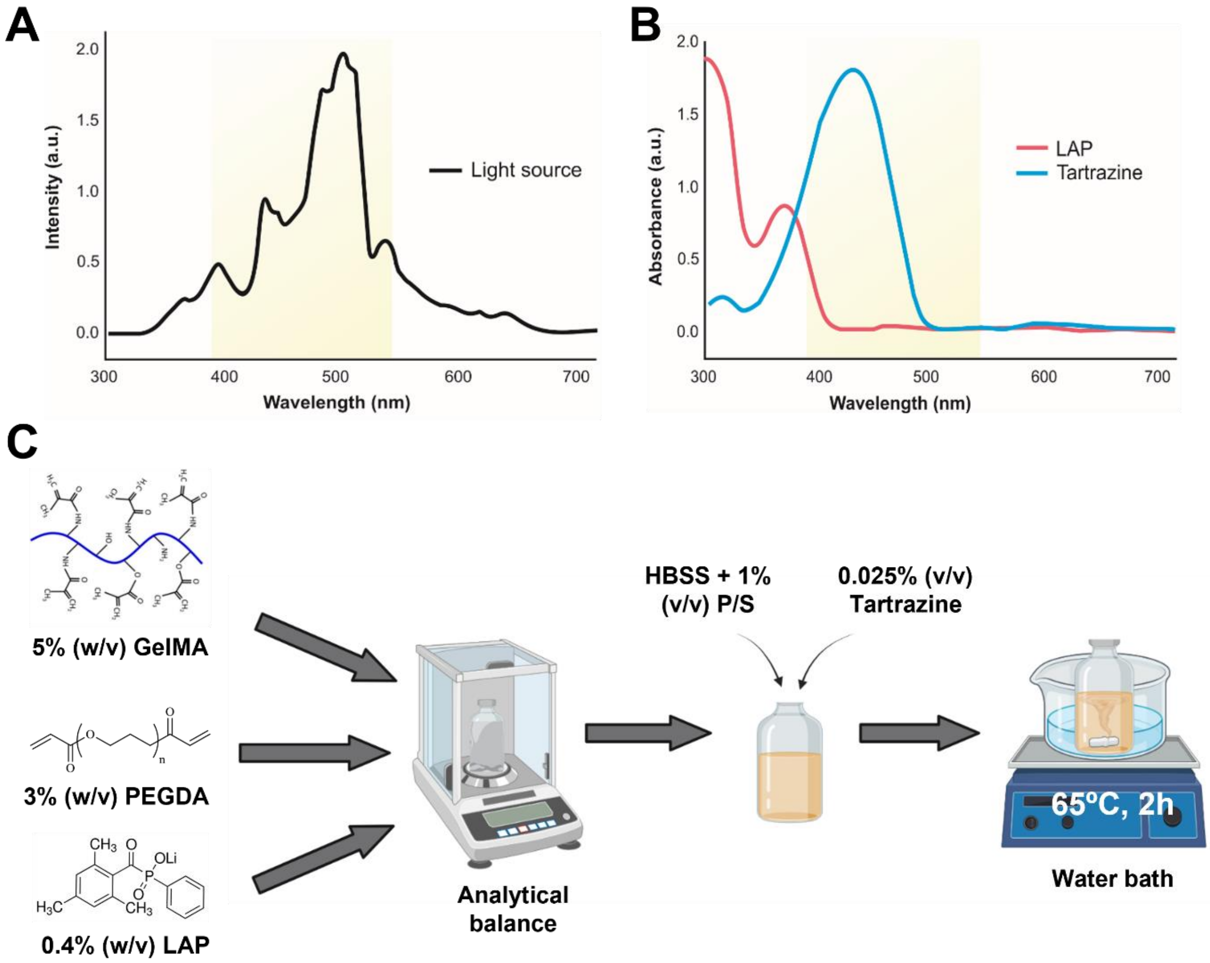

Figure 3.5: *Bioink composition. (A) Emission spectrum of the light projector and (B) absorption spectra of LAP and tartrazine. Adapted with permission from Elsevier, 2023 [3]. (C) Schematic illustration of the preparation of PEGDA-GelMA pre-polymer solution.*

The prepared bioink was characterized in a previous study, with the following composition: 3 % (w/v) PEGDA, with a molecular weight of 4000 Da (Sigma-Aldrich), 5 % (w/v) GelMA, 0.4 % (w/v) LAP (TCI chemicals) and 0.025 % (v/v) tartrazine (Acid Yellow 23, Sigma-Aldrich) [3]. The selected concentrations for both LAP and tartrazine were below the cytotoxic range [10,11]. PEGDA, GelMA and LAP were first added in a small glass vial wrapped in aluminum paper to avoid light exposure, weighted with an analytical balance, and dissolved in Hank's Balanced Salt Solution (HBSS; Gibco, ThermoFisher Scientific) supplemented with 1% (v/v) P/S and tartrazine solution (0.2 mg/mL diluted in HBSS) at 65ºC in a water bath under stirring conditions for 2 h (Figure 3.5 C). Once dissolved, the solution was stored in the fridge for later use. Before the printing, the bioink was kept at 37°C in a water bath for at least 30 min to avoid thermal gelation. For cell-laden hydrogel fabrication, cells were directly mixed with the pre-polymer solution at 37ºC before printing.

3.2.3. 3D bioprinting of PEGDA-GelMA hydrogel channels

3.2.3.1. DLP-SLA bioprinting setup

To fabricate the hydrogel channels, a customized commercial SLA 3D printer (SOLUS; Junction3D) was used [3]. The system consists of three main components: a printing support coupled to a Z-axis motor, a resin vat and a light beam projector (Vivitek) (Figure 3.6 A). The printing support (diameter: 12 mm) and the circular resin vat (inner diameter: 20 mm), made of aluminum, were customized to print hydrogels with reduced sizes (less than 10 mm in diameter) using small volumes of pre-polymer solution (less than 2 mL), while keeping the bioink at 37ºC using a built-in heater with a thermostat (TUTCO) to allow cell-laden hydrogel printing and prevent thermal gelation. The choice of aluminum as a material substrate was based on its good thermal conductivity and its low oxygen permeability. A 150 µm-thick fluorinated ethylene propylene (FEP) plastic film was attached to the bottom of the vat to create a gas permeable transparent window for the patterned light to reach the pre-polymer solution. This created an oxygen gradient within the pre-polymer solution, inhibiting the cross-linking reaction at the liquid-film interface, and preventing the hydrogel from sticking to the bottom of the vat. The full high definition 1080p light projector was used to project light from the bottom of the vat for patterned hydrogel polymerization (Figure 3.6 B). To prevent cell damage due to infrared (IR) radiation exposure, a short pass heat protection filter (KG3 SCHOTT, Edmund Optics) was attached to the 3D printer. The optical power density of the projector was set to 12.3 W/cm^2 in the 320 nm to 640 nm wavelength spectral range.

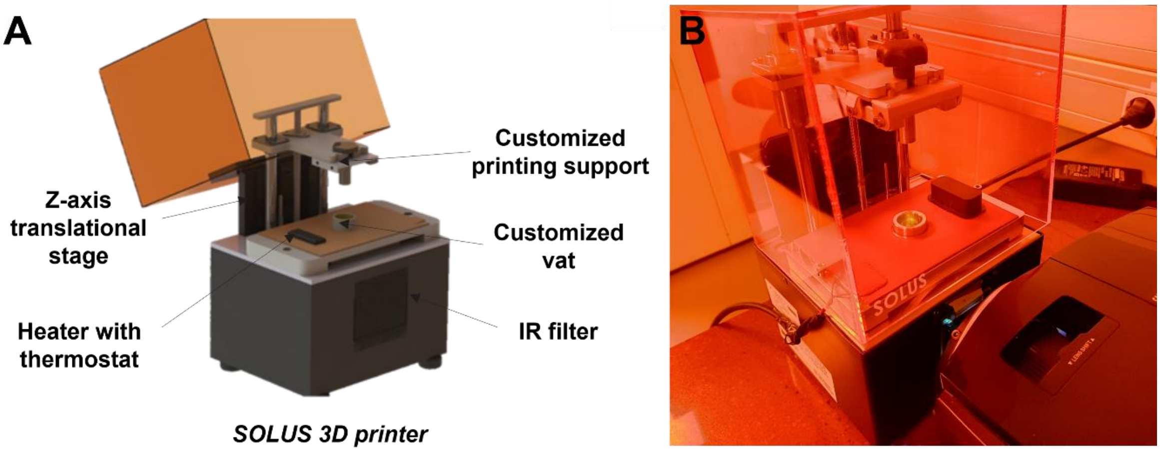

Figure 3.6: *DLP-SLA bioprinting setup. (A) Schematic of the 3D SLA printer with the customized vat and printing support. (B) Image of the printing setup, including the 3D printer and the light projector.*

3.2.3.2. Silanization of PET substrates

PET substrates were silanized to ensure a better attachment of the printed hydrogels. Non-porous PET foil sheets (125 µm; Dupont Melinex ST504) were cut with a cutting plotter (Silhouette Cameo 4) to generate 12 mm diameter circular substrates. After cleaning them with isopropanol (IPA), the samples were placed in a glass petri dish and their top surface was treated with a UV ozone cleaner (ProCleaner; Bioforce Technologies) for 15 min. During this step, the substrate surface is activated due to the formation of hydroxyl groups produced by the radicals from the oxygen plasma treatment. Immediately after, the substrates were incubated with a solution containing 95 % (v/v) absolute ethanol, 3 % (v/v) acetic acid (1:10 dilution) and 2 % (v/v) (trimethoxysilyl)propyl methacrylate (TMSPMA; Sigma-Aldrich) for 2h on the rocker at room temperature. During this time, the silane molecules react with the hydroxyl groups of the PET substrate to form stable siloxane bonds, coating the surface with a silane monolayer (Figure 3.7 A). TMSPMA was chosen because it has methacrylate groups that react with the methacryloyl groups of GelMA and the acrylate groups of PEGDA, ensuring good adhesion of the hydrogels to the PET substrate and avoiding detachment in aqueous solutions [12]. After the incubation time, the substrates were thoroughly rinsed with 96 % (v/v) ethanol and placed in an oven at 65°C for 1 h to dry. The silanized substrates were then placed in a plastic petri dish and stored under oxygen-free and low humidity vacuum conditions in a desiccator, preventing degradation of the surface functionalization before its use (Figure 3.7 B).

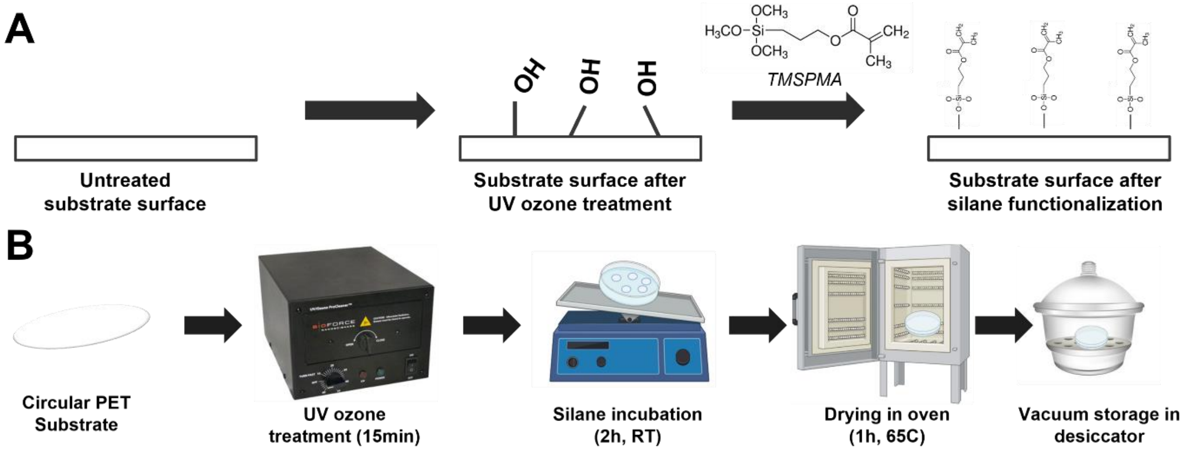

Figure 3.7: *Silanization of PET substrates for hydrogel bioprinting. (A) Illustration of the surface functionalization of PET substrates with TMSPMA silane. (B) Schematic of the silanization process.*

3.2.3.3. 3D CAD design of the hydrogel channels

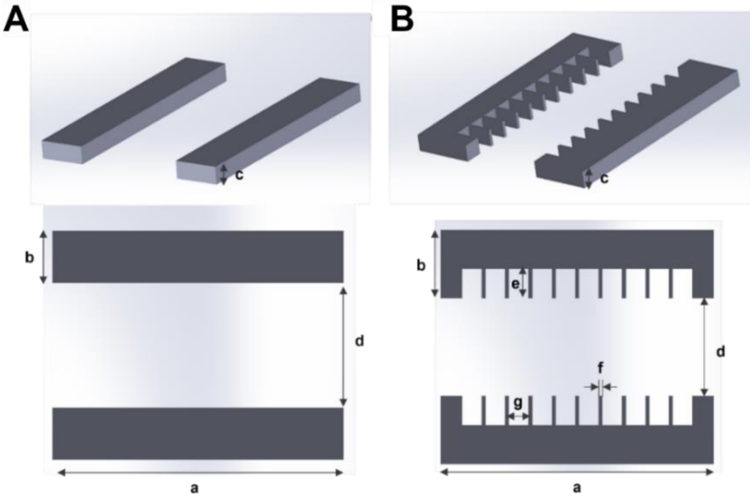

Figure 3.8: *3D CAD designs of hydrogel channels. (A) Rectangular-shaped hydrogels. (B) Hydrogels with lateral pillars. a: hydrogel length; b: hydrogel width; c: hydrogel thickness; d: central channel width; e: pillar length; f: pillar width; g: pillar inter-spacing.*

Two main designs of 3D hydrogel channels were created for printing on SolidWorks 2018 (Dassault Systems). On one hand, two rectangular-shaped hydrogels with vertical flat walls separated by a central channel were designed (Figure 3.8 A). On the other hand, a design with two hydrogels with lateral pillars on the vertical walls facing the central channel was defined to mimic the shape of the intestinal villi found *in vivo* (Figure 3.8 B). Different geometries were tested to obtain optimal encasing of the hydrogel within the chip while preserving the shape of the designed hydrogel channels. The tested dimensions of hydrogel width, length, thickness, along with channel width and pillar dimensions are summarized in table 3.1.

Dimensions	**Rectangular channel**	**Villi-like channel**
Hydrogel length (mm)	6 - 7	6 - 7
Hydrogel width (mm)	0.5 - 2.5	1 - 2.5
Hydrogel thickness (µm)	250 - 750	250 - 750
Central channel width (mm)	1 - 3	1 - 3
Pillar length (mm)	-	0.5 - 1
Pillar width (µm)	-	75 - 100
Pillar inter-spacing (mm)	-	0.5 - 0.75

Table 3.1: *Design dimensions of the printed hydrogel channels.*

3.2.3.4. 3D bioprinting process

The procedure to print the hydrogels followed several steps. First, the CAD file containing the 3D design was uploaded to a laptop connected to the printer and the printing parameters were defined on the dedicated software. The tested printing parameters were set up as following: layer thickness between 10 and 20 µm and normal layer exposure time between 1 and 10 s. Second, a silanized PET substrate was attached to the bottom side of the printing support with a circular pressure sensitive adhesive (PSA) (ArCare 92712, Adhesive Research). The pre-polymer solution was then loaded into the vat at 37ºC before the printing started. During the printing process, the hydrogel was photopolymerized in a layer-by-layer procedure: the printing support initially submerged in the vat filled with the pre-polymer solution, then white and black patterns generated from the z-sliced version of the 3D CAD design were projected from the light source to the bioink, triggering the photo cross-linking of a thin hydrogel layer on the substrate surface. After that, the printing support moved upwards, and the process was repeated in a sequential manner (Figure 3.9). Once the printing was completed, the substrate with the attached hydrogel was rinsed with warm PBS supplemented with 1 % v/v P/S, gently dried with clean room wipes to remove unreacted bioink residues, and finally detached from the platform to be placed in a 24-well plate (Nunclon^{TM}, ThermoFisher) with PBS or media (when cells were encapsulated) to avoid hydrogel drying. All hydrogel printings were performed under controlled environmental conditions in the Microfab space of IBEC. Visual characterization of the hydrogels was performed with a stereomicroscope (Olympus, SZX2-ILLB) and images were analyzed with ImageJ software (http://imagej.nih.gov/ij, NIH).

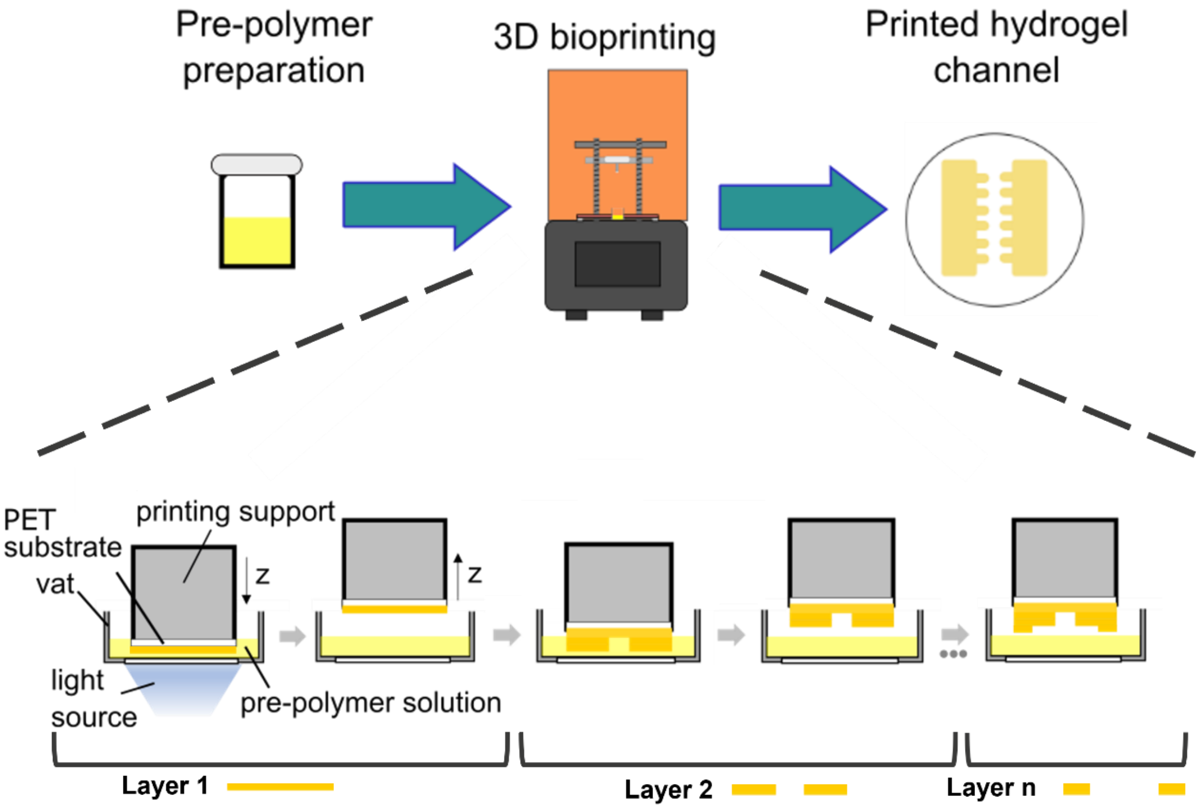

Figure 3.9: *3D Bioprinting process of hydrogels. The patterned light beam from the projector reaches the pre-polymer solution, triggering the photo cross-linking of the bioink on the plastic substrate attached to the printing support and creating a new hydrogel layer.*

3.2.4. Design and fabrication of the microfluidic chip

A multi-layer microfluidic device with three independent channels was designed to encase the printed hydrogel channel within a central chamber for dynamic cell culture. The device (width: 25 mm, length: 40 mm) consists of two top and bottom plates and a middle piece with three parallel channels to support the perfusion of media along the hydrogel. The upper and lower plates were made of cyclo-olefin polymer (COP, 2 mm, Zeonor; Microfluidic ChipShop) (Figure 3.10 A). COP was chosen as a substrate material due to its chemical resistance to solvents, its optical transparency, and its high glass transition temperature (above 130ºC), allowing autoclaving of the pieces for biomedical applications [13]. The top and bottom plates were fabricated with inlet holes and screw holes respectively using a computer numerically controlled milling machine (MDX-40A; Roland Digital) (Figure 3.10 B) [14,15]. Male mini-luer connectors (Microfluidic ChipShop) were bonded to the top plate inlet holes with a photocurable silicone adhesive (Loctite 3104, Henkel) by placing them under a UV lamp (70 mW/cm^2) for 2 min. The middle part (COP, 1 mm, Zeonor; Microfluidic ChipShop) was also milled to reduce the height of the substrate according to the thickness of the encased hydrogel (between 300 and 800 µm) and to define the channels and central chamber. All milled pieces were designed on VCarve v7.012 software (Vectric). To enclose the channels at the top and bottom, double-sided PSA (ArCare 92712, Adhesives Research) (Epilog Mini 24 - 30W, EpilogLaser) (Figure 3.10 C) was laser-cut and patterned COP foils (125 µm, Topas; Microfluidic ChipShop) were designed (CorelDraw 2018 Graphic), cut with a cutting plotter (CAMM-1 Servo GX24, Roland DG Corporation) (Figure 3.10 D) and bonded to the middle piece. A circular open adhesive side was left to attach the substrate with the hydrogel channel. Two silicone sheets of 1 mm (platinum cured sheet, Silex) were also cut with the cutting plotter.

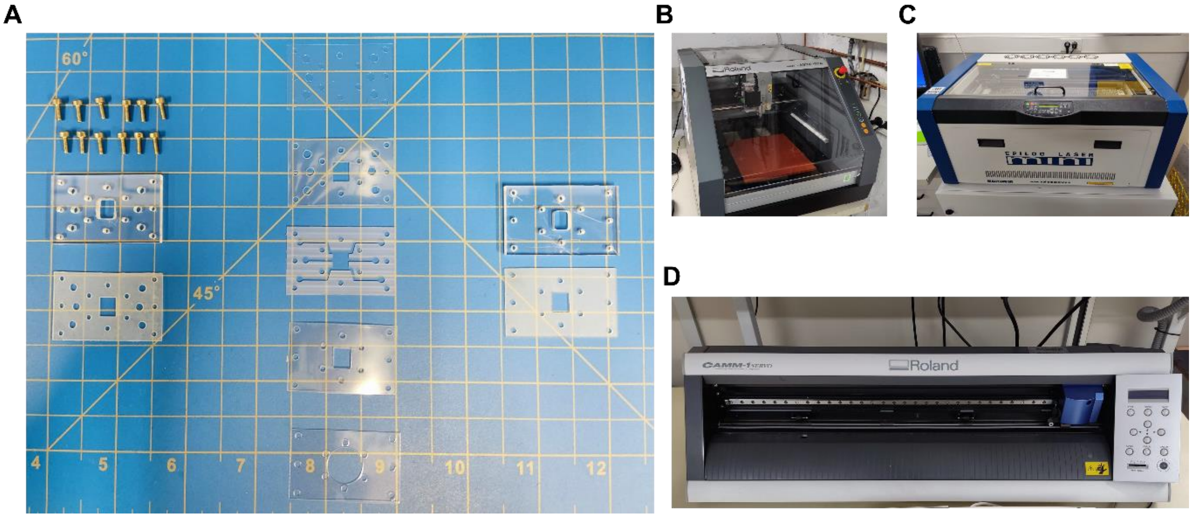

Figure 3.10: *Fabrication of the microfluidic device. (A) Image of the different components of the chip. Images of the (B) CNC milling machine, (C) the laser cutting machine and (D) the cutting plotter.*

After the printing, the circular PET substrate with the hydrogel channel was attached to the bottom side of the middle piece to encase the polymeric scaffold in the central chamber, acting as a separator between the three channels (Figure 3.11). After this, the device was assembled with a clamping system where the middle piece containing the hydrogel was sandwiched between the top and bottom silicone sheets and COP plates (Figure 3.11 A). The silicone sheets acted as gaskets to prevent leakage in the chip during the experiments. Screws were placed close to the hydrogel channel and inlet ports to ensure a tight sealing of the chip. The mini-luer connectors of the top plate were directly inserted into the external tubing to allow active fluid perfusion (Figure 3.11 B). For cell-laden hydrogels, the assembly of the device was performed in a laminar cabinet to prevent potential contamination issues during manipulation.

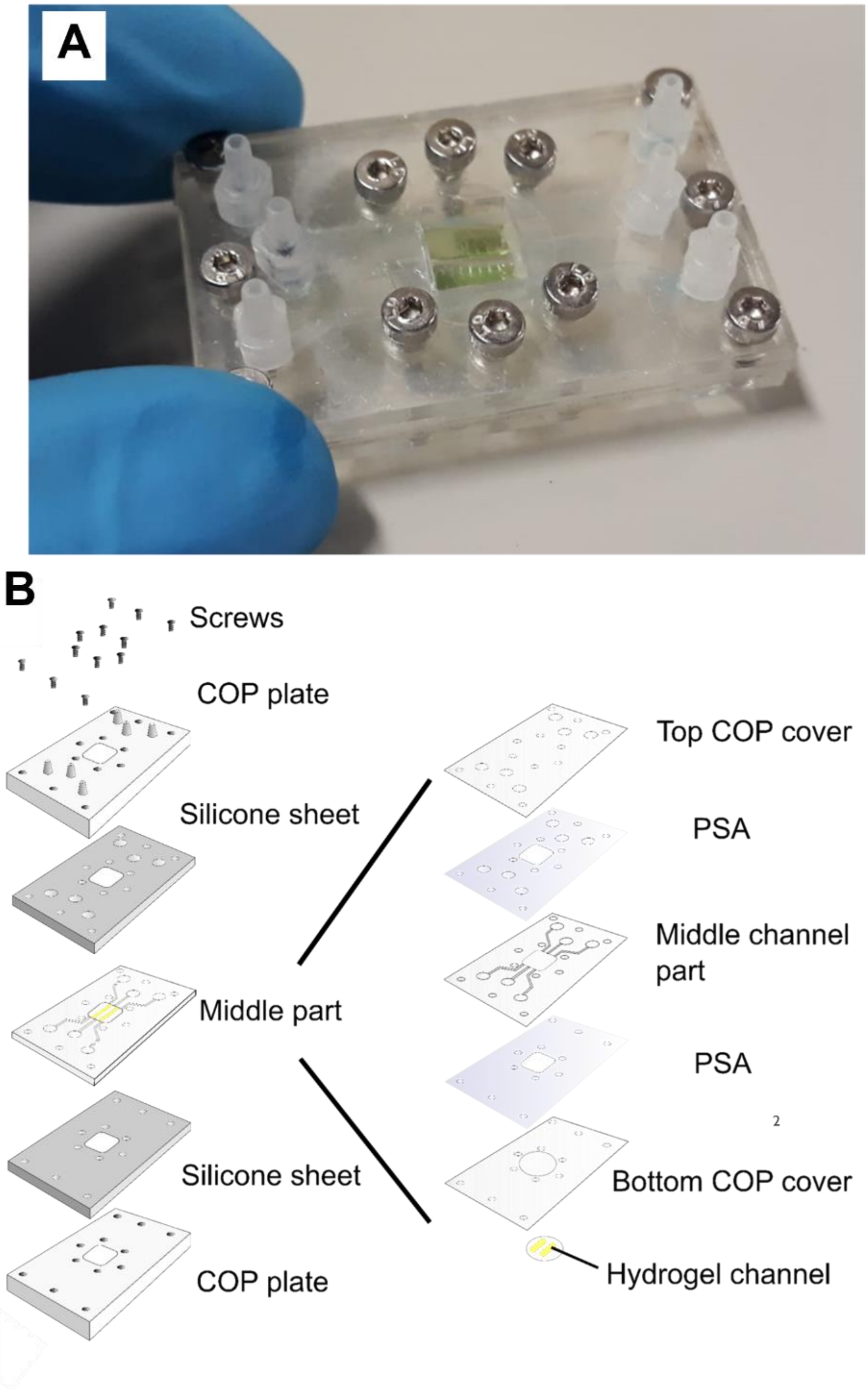

Figure 3.11: *Assembly of the hydrogel microfluidic device. (A) Image of the chip with the encased hydrogel channel. (B) Exploded view of the different components of the microfluidic chip.*

3.3. Results

3.3.1. Optimization of the main printing parameters for 3D hydrogel channels with villi-like structures

DLP-SLA is a microfabrication technique that has been adapted for the bioprinting of hydrogels due to its simplicity and high versatility [16–18]. As a first step, the parameters to print the hydrogel channel were optimized to obtain lateral villi-like structures with dimensions close to the designed ones. To do this, a 6 mm long, 3.5 mm wide and 500 µm thick hydrogel channel with lateral pillars 500 µm long and 100 µm wide, spaced 500 µm was defined and printed (Figure 3.12 A). We used a bioink containing 5 % (w/v) of GelMA, 3 % (w/v) PEGDA and 0.4 % (w/v) of photoinitiator LAP, mixed with the azo dye tartrazine, used as a photoabsorber, with a concentration of 0.025 % (w/v). Previous work on DLP bioprinting has shown the suitability of this pre-polymer solution to generate 3D hydrogel scaffolds with free-standing villi-like pillars for advanced intestinal *in vitro* models [3]. PEGDA offers long-term mechanical stability while GelMA can support cell encapsulation and attachment for cell co-culture [19,20]. Once prepared, the bioink solution was loaded into the custom vat and the projector generated sliced light patterns of the 3D CAD design to fabricate the hydrogel in a layer-by-layer manner.

	Printing parameters
Bottom layer exposure time	15 s
Normal layer exposure time	1 s - 5 s - 10 s
Layer thickness	10 µm - 13 µm - 20 µm
Number of initial layers	2

Table 3.2: *Tested printing parameters to fabricate hydrogel channels via DLP SLA printing.*

The layer thickness and the layer exposure time are the main printing parameters that can modulate the polymerization of the scaffolds (Figure 3.12 B). Also, a defined number of initial layers is generally set with a higher exposure time than the rest of the layers to ensure good attachment of the hydrogel to the substrate. The tested printing parameters for the fabrication of the PEGDA-GelMA hydrogel channels are summarized in Table 3.2.

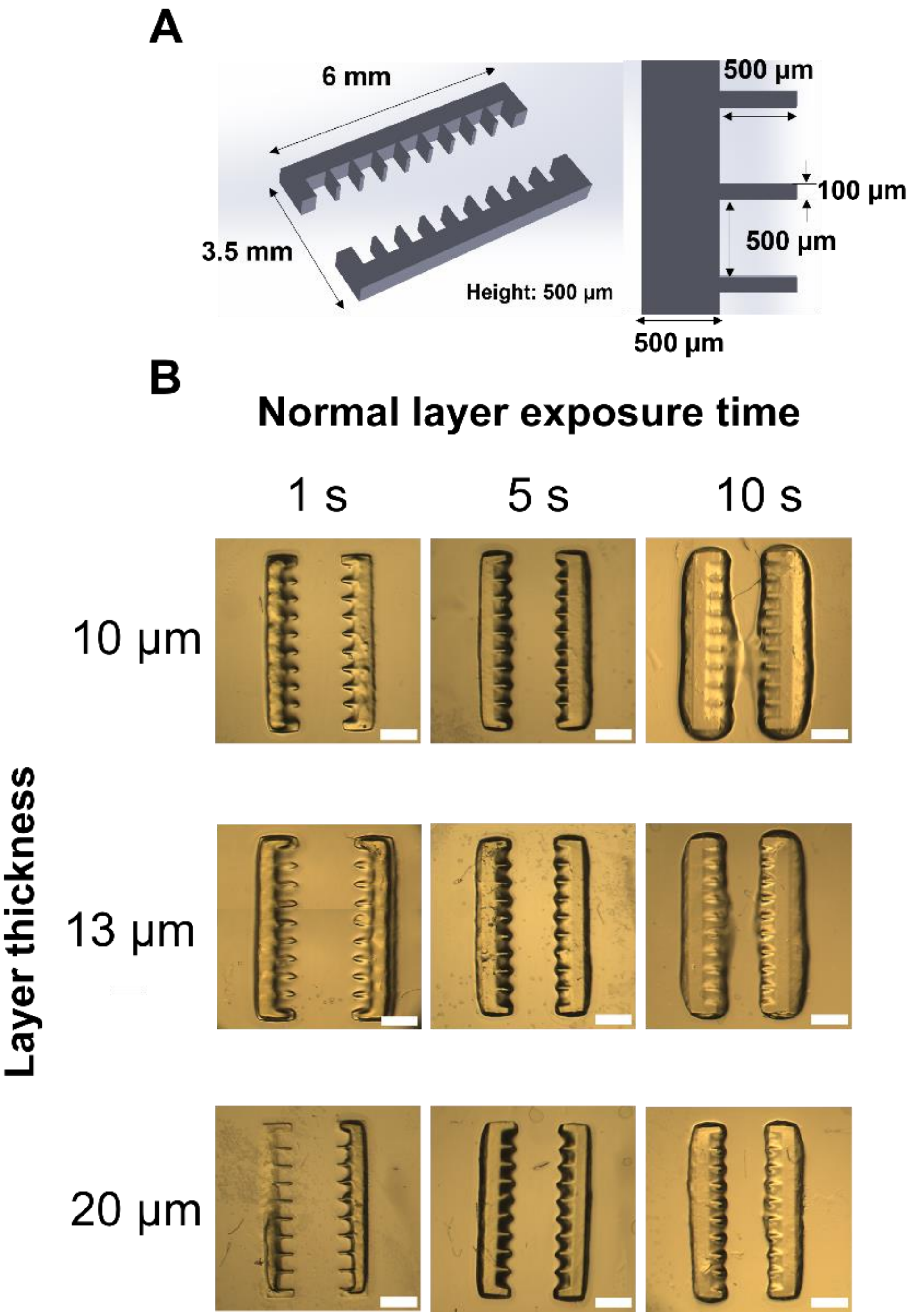

Figure 3.12: *Effect of printing parameters on the morphology of hydrogel channels with lateral villi-like features. (A) 3D CAD model of the printed hydrogel channel. (B) Top images of the hydrogel channel with different layer thicknesses and layer exposure times. Scale bar: 1 mm.*

The impact of the normal layer exposure time on the fidelity of the printed lateral pillar structures was first assessed, with varying exposure times ranging from 1 s to 10 s, for a fixed layer thickness of 13 µm (Figure 3.12 B, central row). This parameter controls the energy dosage applied to the pre-polymer solution from the light source, tuning the curing depth during the printing process [21]. For 1 s of single layer exposure time, the hydrogel was under-polymerized and poorly defined, as the energy dose did not reach the threshold to fully cross-link the polymeric solution (Figure 3.13 A, left). The total height of the polymeric scaffold was less than 300 µm, considerably smaller than the one of the channel design (Figure 3.13 D). Increasing to 5s of exposure time significantly improved the shape of the hydrogel (Figure 3.13 A, center). The villi-like pillars approached the dimensions of the CAD design, with a length around 400 µm (Figure 3.13 B) and a width of around 100 µm (Figure 3.13 C). Lateral images of the printed hydrogels showed a total height of 540 µm approximately, with some over-polymerization at the base between the pillars (Figure 3.13 D). However, a further increase of the layer exposure time to 10 s resulted in light overexposure of the solution and the polymerization of areas outside the printed layer (Figure 3.13 A, right). In this case, the inter-space between the lateral pillar structures was filled with cross-linked solution, significantly reducing the length of well-defined lateral pillars. Overall, these results highlighted the importance of setting an optimal exposure time to finely control the morphology of the lateral pillars when printing the hydrogel channel design.

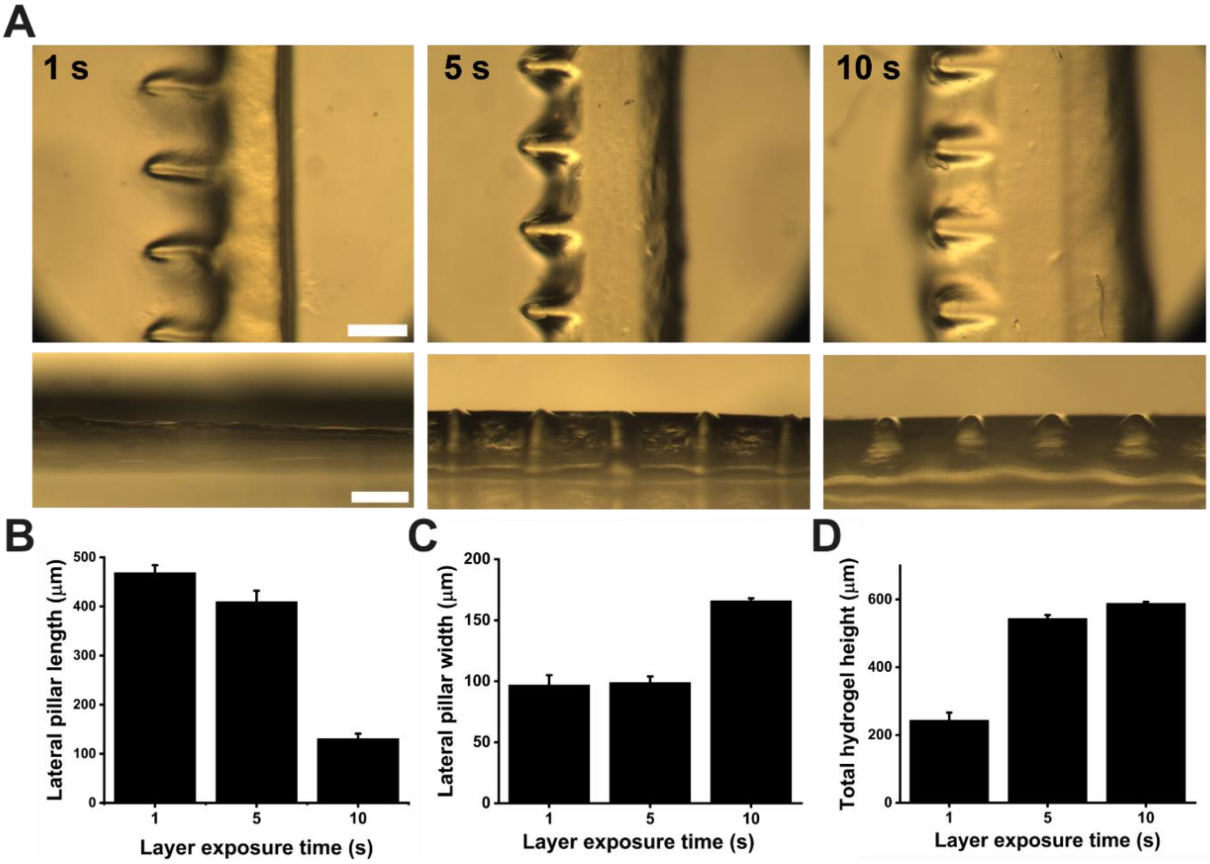

Figure 3.13: *Effect of normal layer exposure time on hydrogel channels. (A) Top and lateral images of the printed scaffolds with lateral villi-like pillars printed with different layer exposure times. Scale bar: 500 µm. (B) Lateral pillar length (C) lateral pillar width and (D) total hydrogel height quantification as a function of layer exposure time. Values are displayed as mean ± S.D. (N=3).*

The layer thickness, also referred as the slicing thickness, was the second studied parameter to assess its effect on the printing of hydrogel channels, as it determines the total number of layers and the z resolution of the printed structures [22]. For a fixed layer exposure time of 5s, the impact of the layer thickness on the morphology of the lateral pillars was quantified within a range between 10 µm and 20 µm (Figure 3.12, central column). For 10 and 13 µm, it was observed that the villi-like structures had dimensions close to the ones of the CAD design, with some over-polymerization at the inter-space between the villi (Figure 3.14 A, left and center; Figure 3.14 B, C, D). However, for thicker layers (20 µm), the hydrogel lateral shapes were slightly less defined in height, due to a reduced resolution along the z axis (Figure 3.14 A, right). Also, the hydrogels obtained with this layer thickness were much softer and prone to break apart than with shorter layer thicknesses.

As a result of these printing tests, we selected 5 s of single layer exposure time and 13 µm of layer thickness as the main parameters for the optimal printing of 3D hydrogel channels, resulting in total printing times of around 6 min for 500 µm-thick hydrogel designs.

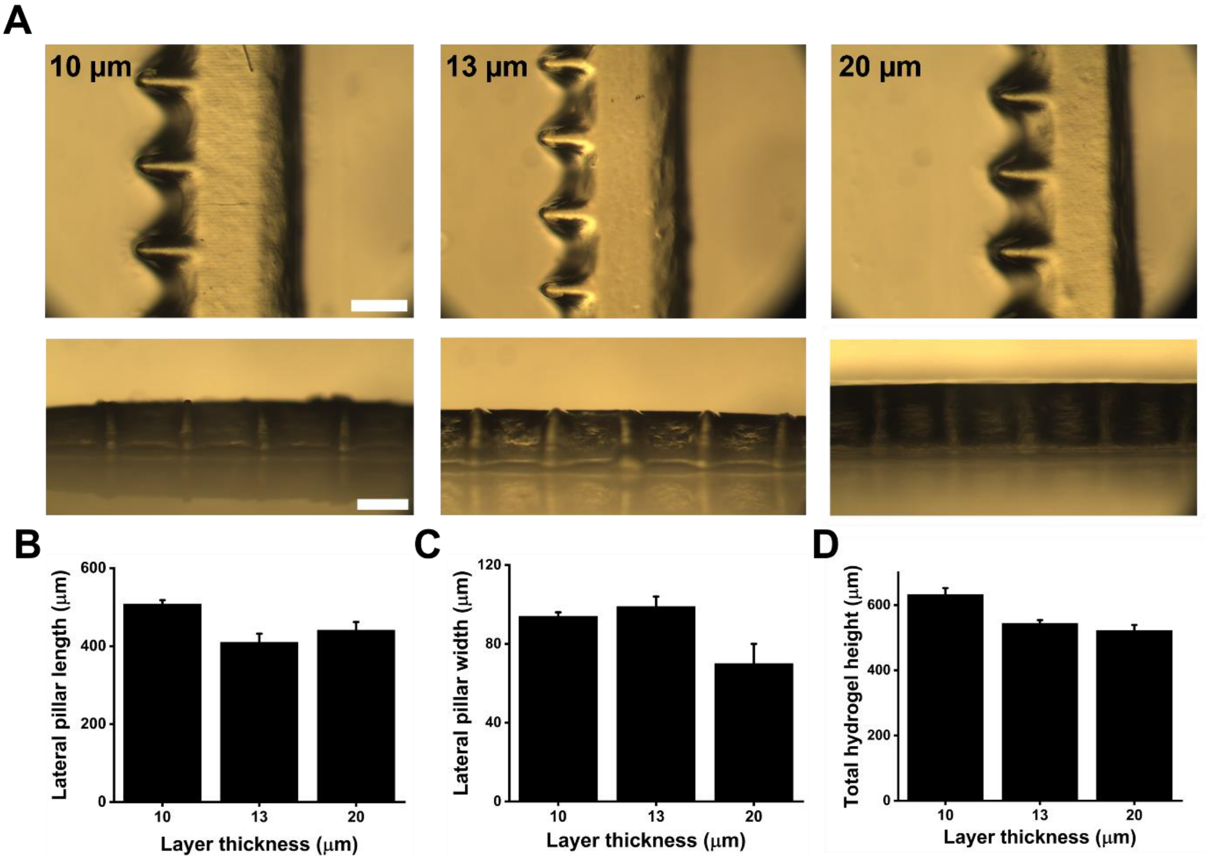

Figure 3.14: *Effect of design layer thickness on printed hydrogel channels. (A) Top and lateral images of the printed scaffolds with lateral villi-like pillars printed with different layer thicknesses. Scale bar: 500 µm. (B) Lateral pillar length (C) lateral pillar width and (D) total hydrogel height quantification as a function of layer thickness. Values are displayed as mean ± S.D. (N=3).*

Once the printing parameters were selected, the effect of the channel design on the printed dimensions of the hydrogels was evaluated. As the scaffolds had to be spatially encased within a microfluidic device, it was critical to compare the printed sizes of the channels with the design dimensions. For this, 3D CAD designs of 6 mm long and 1mm wide rectangular shaped hydrogels spaced 1.5 mm were generated with total heights ranging from 250 µm to 750 µm (Figure 3.15 A). After printing, the height and length of the hydrogel channels were quantified for the different designs. For all tested heights, it was observed that the printed hydrogels were taller than the CAD design (Figure 3.15 B). The difference between the designed and printed hydrogels was more pronounced for smaller heights (250 µm), with printed scaffolds being more than 27 % taller compared to the designed scaffolds, than for increased heights (500 µm and 750 µm), for which the difference was between 10 % and 15 % (Figure 3.15 C). This is due to the longer exposure times of the first bottom layers, resulting in over polymerized thicker layers than the rest. The effect of overexposure reaction can also be observed when assessing the length of the hydrogel at different z levels, with longer layers at the bottom than at the top (Figure 3.15 D). For 250 µm thick scaffolds, the difference in length was 240 µm (top/bottom variation: 4.2%) while for 500 and 750 µm thick ones, the difference increased to 420 µm (top/bottom variation: 7.2%) and 450 µm (top/bottom variation: 7.6%) respectively. From these results, we could finely adjust the designs of the hydrogel channels to correctly encase them within the microfluidic device.

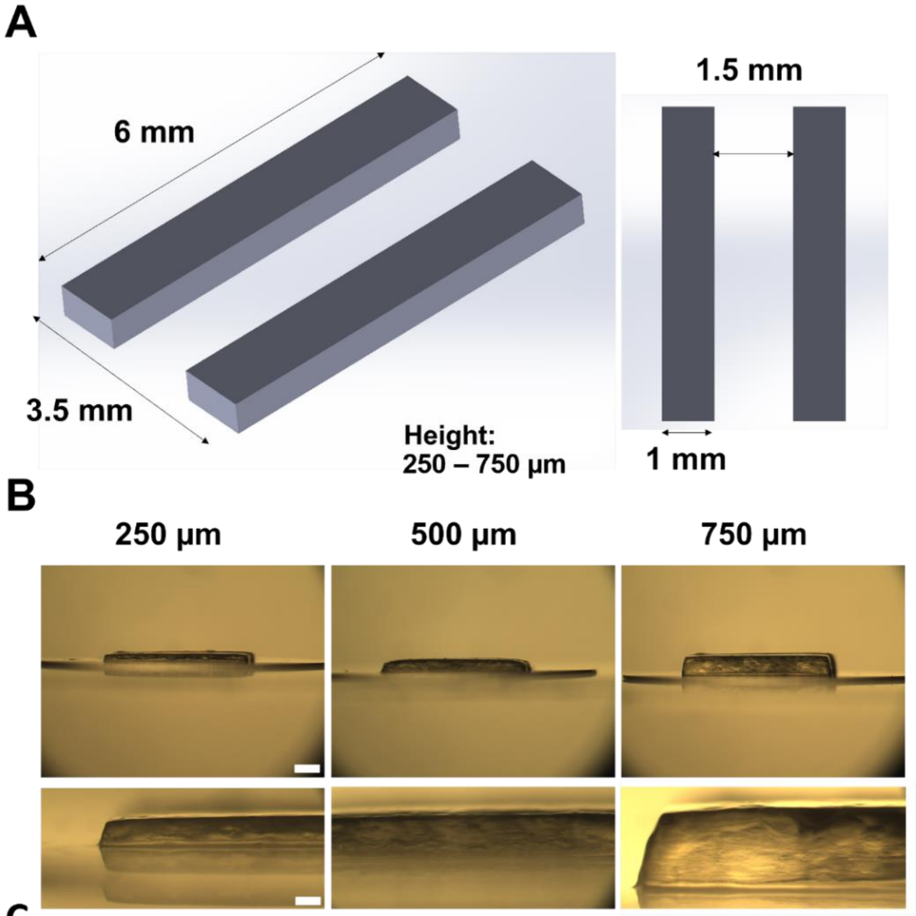

C

Design height (µm)	Printed height (µm)	% variation
250	319±7	27.6
500	569±10	13.8
750	836±14	11.5

D

Design height (µm)	Length bottom layer (mm)	Length top layer (mm)	Difference top/bottom (mm)
250	5.77±0.03	5.53±0.02	0.24
500	5.83±0.03	5.41±0.08	0.42
750	5.96±0.05	5.51±0.02	0.45

Figure 3.15: *Effect of CAD design on the dimensions of hydrogel channels. (A) 3D CAD model of the tested rectangular-shaped hydrogel channel. (B) Lateral images of the printed channels with different designed heights. Scale bar (top): 500 µm. Scale bar (bottom): 250 µm. (C) Quantification of the printed*

hydrogel heights and comparison with the design ones. (D) Quantification of the total length at the top and bottom level of the hydrogel channel for different design heights. Values are displayed as mean ± S.D. (N=3).

3.3.2. Assembly of the 3D hydrogel channels within a microfluidic chip

A tri-channel microfluidic device was designed to place the hydrogel channel inside for dynamic cell culture (Figure 3.16 A). The chip was made out of plastic COP using low-cost rapid prototyping techniques. After printing, the 3D hydrogel channel was encased in the central part of the chip, acting as a physical separator between the three independent channels (Figure 3.16 B, C). The lateral channels were designed to provide continuous nutrient and oxygen transport to the embedded cells across the hydrogel, while the central one served for both media perfusion and the seeding of intestinal epithelial cells. To ensure no leakage in between the channels, the PET substrate with the attached hydrogel was bonded to the middle piece of the chip using a double-sided PSA. Once allocated in the central chamber, a clamping system composed of two silicone sheets, two plastic COP plates and screws ensured a tight seal of the entire system (Figure 3.16 D).

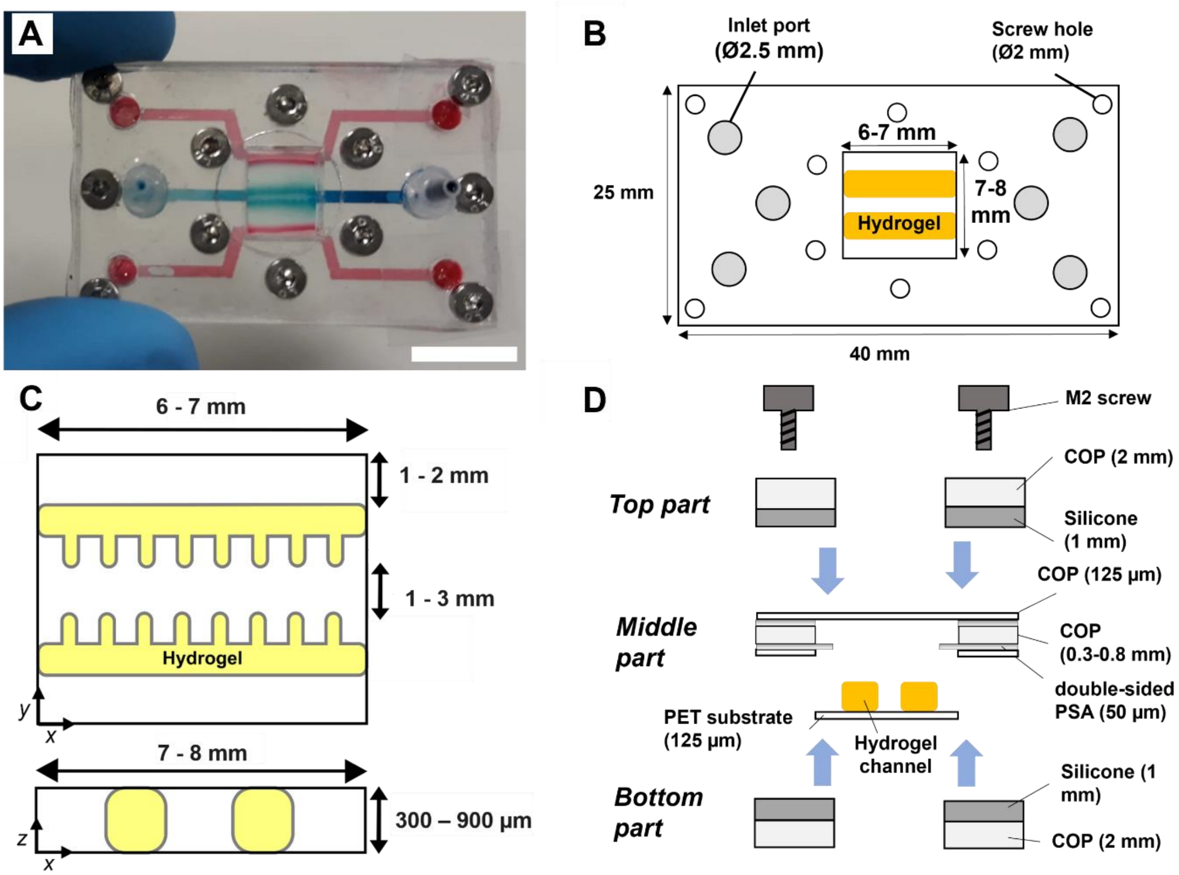

Figure 3.16: *Dimensions and assembly of the hydrogel microfluidic device. (A) Image of the chip with color dyes perfused in the three independent channels. (B) Dimensions of the central chamber where the hydrogel channel is placed. (C) Top schematic of the chip. (D) Lateral representation of the assembly process in which the hydrogel channel is bonded to a bottom PSA and encased within the central area of the device.*

The swelling properties of a hydrogel are directly linked to the capacity of the polymeric mesh to absorb water [23,24]. Their effect on the spatial architecture of the scaffold is relevant to consider as it is dependent on the composition of the bioink and the cross-linking reaction. Previous studies with the used GelMA-PEGDA mix on printed hydrogel disks showed that the volumetric swelling rate (change of hydrogel volume over time) at equilibrium after 24 h was 11.6 ± 2 % [3], lower than other similar pre-polymer solutions reported in the literature [19]. However, spatial confinement of the hydrogels can also affect the swelling properties, as the polymeric mesh cannot expand evenly in all directions. Following this, the effect of swelling on the dimensions of the lateral villi when placed in the microfluidic chip was evaluated (Figure 3.17 A). After printing the hydrogel channels, they were encased in the microfluidic chip and the channels were filled with PBS to prevent hydrogel dehydration. The tested devices were placed in an incubator at 37ºC for 1 day to let the hydrogels reach their swelling equilibrium. Measurements of the width and length of the lateral pillars, along with the pillar interspace and channel width were performed before encasement of the hydrogel channel, inside the chip at time 0 and 24 h after encasement on-chip (Figure 3.17 B). The encasement of the polymeric scaffold had a significant impact on the dimensions of the lateral villi, as the applied pressure from the assembly of the chip induced a spatial deformation of the hydrogels. This effect could be observed for the pillar width, increased from 123 ± 5 μm to 295 ± 13 μm, and the pillar interspace, reduced from 716 ± 15 μm to 428 ± 32 μm (Figure 3.17 D, E). Also, due to this, the length of the villi slightly increased, causing a decrease of the central channel width (Figure 3.17 C, F). After reaching swelling equilibrium at 24h, both the width and length of the lateral villi were increased by 5.3% and 8.3% respectively (Figure 3.17 C, D). These results showed relatively low levels of swelling for the hydrogels when confined in the chip, in accordance with previous studies based on the same bioink solution. Despite the increase on size of the villi-like features due to the encasement within the chip, the resulting dimensions were still in the target physiological range.

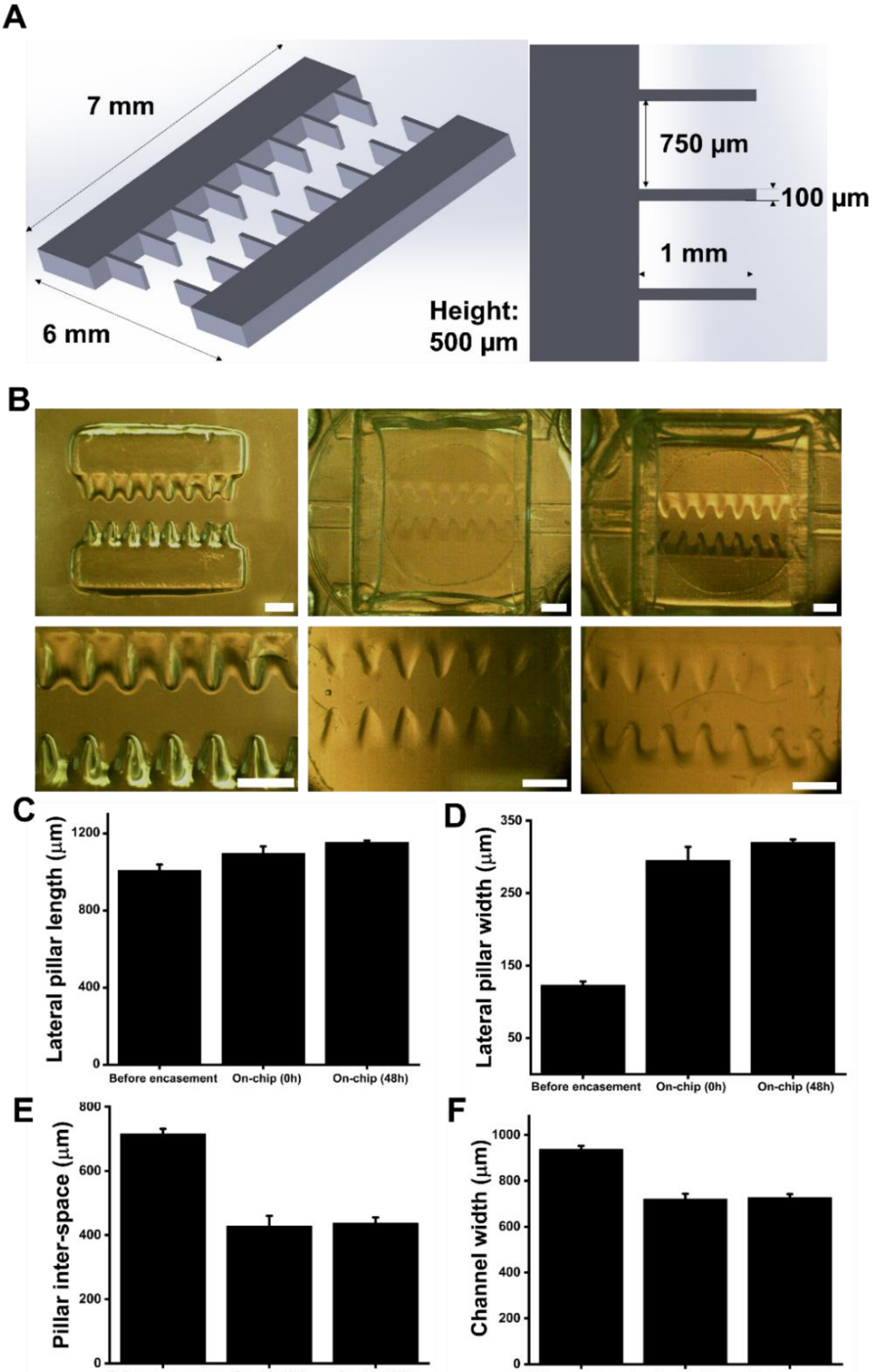

Figure 3.17: *On-chip swelling of hydrogel channels with villi-like features. (A) 3D CAD design of the hydrogel channel. (B) Top images of the hydrogel channels with lateral pillars after printing (left), at time 0 after encasement in the chip (center), and 24h inside the chip (right). Scale bar (top): 1 mm; (bottom): 750 µm. Plots of (C) the lateral pillar length, (D) width, (E) pillar inter-space and (F) channel width before encasement, on-chip at time 0 and 24h on-chip after swelling. Values are displayed as mean ± S.D. (N=2).*

The total length of the hydrogel channel was a key parameter to make sure there was no leakage between the lateral and the central channels. The effect of the design length on the printed hydrogel was assessed to ensure the good allocation of the hydrogel channel within the chip. The tested designed lengths were in the range between 5.7 and 6.3 mm, and the rectangular-shaped hydrogels were encased in a central chamber 6 mm long, 7 mm wide and 500 µm high (Figure 3.18 A). After 24 h post-printing, the hydrogels were placed inside the chip. It could be observed that for a design length of 5.9 mm, the scaffold could fit within the central chamber of the chip while preventing leakage between adjacent channels (Figure 3.18 B). For shorter lengths, the hydrogel channel would not reach the plastic piece, or the sealing would not be good enough to avoid leakages. For longer ones, the hydrogel would not fit within the allocation space and the bottom layers of the scaffold would superpose with the plastic edges, also inducing leakages between channels (Figure 3.18 B). A critical aspect of the allocation of the hydrogel channels within the device was the centering of the scaffold over the substrate. Some preliminary printing tests were always performed before the printing of the hydrogel channel to make sure it was spatially aligned with the chip channels by adjusting the XY coordinates of the design on the printer software.

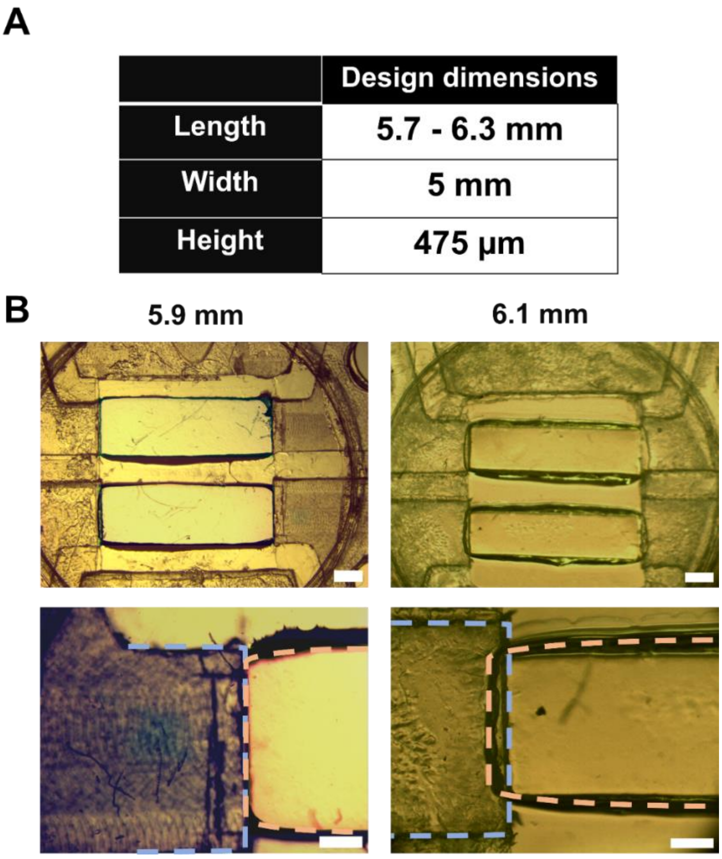

	Design dimensions
Length	5.7 - 6.3 mm
Width	5 mm
Height	475 µm

Figure 3.18: *Effect of the design length on the encasement of the hydrogel channel within the microfluidic chip. (A) Design dimensions of the tested hydrogels. (B) Top images of the encased hydrogel channels for different design lengths. The blue dotted lines show the edges of the plastic piece, while the red ones show the boundaries of the hydrogel. Scale bar (top): 1mm; (bottom): 500 µm.*

To assess potential leakage between the channels and in other parts of the chip, different tests were performed in static and dynamic conditions. First, a blue ink was perfused in the central channel to follow up the diffusion across the hydrogel at different time points for one hour (Figure 3.19 A). The images were then analyzed to extract the normalized intensity plots along the width of the hydrogel channel. At time 0, the intensity peak could be observed at the center, corresponding to the perfusion of the dye in the central channel. Over time, two new peaks emerged as the color dye diffuses through both sides of the scaffold (Figure 3.19 A). During the experiment, no ink was observed leaking in between the plastic piece and the scaffold, demonstrating the hydrogel channels were closing the gaps. As a second step, microfluidic chips with encased hydrogel channels were connected to a peristaltic pump (Reglo Digital 2 channels, Ismatec) to continuously flow a diluted blue ink solution at room temperature through the lateral channels for 5 days (Figure 3.19 B). While the solution could not be perfused in the central channel due to the technical limitations of the pump, we could not observe any leakage in any part of the system during the experiment, indicating a tight sealing of the microfluidic device. These preliminary tests showed that the hydrogels could act as an effective physical separator of the three channels and that the proposed chip was leakage-proof under fluid flow, proving its use for long-term dynamic cell culture.

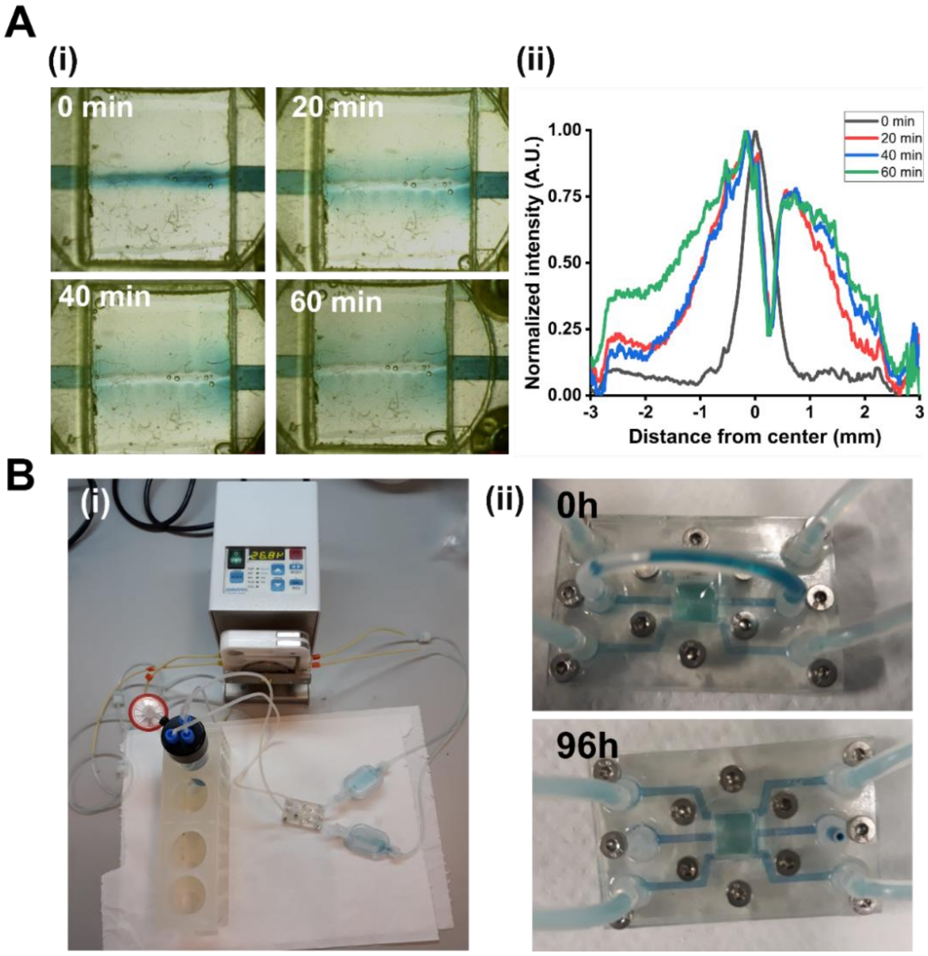

Figure 3.19: *Leakage tests of the hydrogel-encased microfluidic devices. (A) (i) Top images of the hydrogel channel on-chip after perfusion of the blue ink in the central channel at different time points. Scale bar: 1 mm. (ii) Normalized intensity plots across the hydrogel channel at different time points. (B) (i) Image of the microfluidic setup to assess potential leakage in the chip under perfusion. (ii) Images of the chip at time 0 and 96h after perfusion of a diluted blue ink solution.*

3.4. Discussion

DLP-SLA 3D bioprinting has been increasingly adopted as a suitable technique for hydrogel fabrication in *in vitro* gut models. While others such as soft lithography and laser photopatterning have also been proposed, these techniques generally require longer preparation times or more expensive equipment [25,26]. By using a layer-by-layer approach, DLP-SLA bioprinting can yield high-resolution structures with low printing times, generating hydrogels that can faithfully replicate the 3D architecture of the epithelial barrier [18,27], essential for its development and function[28,29]. Here, we used a custom bioprinting setup based on visible-light photopolymerization using a previously characterized PEGDA-GelMA bioink to better control the printing conditions [3]. Selecting optimal printing parameters is critical to obtain mechanically stable 3D hydrogels that closely mimic the desired tissue architecture. As these parameters are linked, changing one of them can have a large impact on the curing depth. In our case, different combinations of layer exposure time and layer thickness were tested and finely adjusted to generate hydrogel channels with lateral villi-like shapes that resembled the *in vivo* dimensions of the intestinal epithelium.

Once the printing parameters were selected, the printed hydrogels had to be placed inside the microfluidic chip to establish the gut-on-chip model. A tri-channel configuration was designed and fabricated for the device to allocate the hydrogel channel in the central area and to support long term cell co-culture. It is important to mention that hydrogels have generally been integrated in gut-on-chip systems by initially loading a pre-polymer solution within the chip to be polymerized later [25,30,31]. Due to the configuration of our bioprinting setup, the hydrogels channels had to be encased within the chip after polymerization. Because of this, we adjusted the CAD dimensions of the design to properly encase the polymeric substrates within the chip while ensuring the sealing between the microfluidic channels. Also, the swelling effect of the hydrogel was considered in the designs to preserve the correct dimensions of the lateral villi and ensure proper allocation of the scaffold. After assembly, the hydrogel microfluidic device was tested for long-term perfusion, showing no signs of leakage, and proving its ability to be used as a platform for gut-on-chip applications.

3.5. References

1. Creff, J. *et al.* Fabrication of 3D scaffolds reproducing intestinal epithelium topography by high-resolution 3D stereolithography. *Biomaterials* **221**, (2019).
2. Taebnia, N. *et al.* Dual-Material 3D-Printed Intestinal Model Devices with Integrated Villi-like Scaffolds. *ACS Appl Mater Interfaces* **13**, 58434–58446 (2021).
3. Torras, N. *et al.* A bioprinted 3D gut model with crypt-villus structures to mimic the intestinal epithelial-stromal microenvironment. *Biomaterials Advances* **153**, 213534 (2023).
4. Yue, K. *et al.* Synthesis, properties, and biomedical applications of gelatin methacryloyl (GelMA) hydrogels. *Biomaterials* **73**, 254 (2015).
5. Loessner, D. *et al.* Functionalization, preparation and use of cell-laden gelatin methacryloyl-based hydrogels as modular tissue culture platforms. *Nat Protoc* **11**, 727–746 (2016).
6. Nichol, J. W. *et al.* Cell-laden microengineered gelatin methacrylate hydrogels. *Biomaterials* **31**, 5536 (2010).
7. Habeeb, A. F. S. A. Determination of free amino groups in proteins by trinitrobenzenesulfonic acid. *Anal Biochem* **14**, 328–336 (1966).
8. Claaßen, C. *et al.* Quantification of Substitution of Gelatin Methacryloyl: Best Practice and Current Pitfalls. *Biomacromolecules* **19**, 42–52 (2018).

9. Leulescu, M. *et al.* Tartrazine: physical, thermal and biophysical properties of the most widely employed synthetic yellow food-colouring azo dye. *J Therm Anal Calorim* **134**, 209–231 (2018).
10. Mpountoukas, P. *et al.* Cytogenetic evaluation and DNA interaction studies of the food colorants amaranth, erythrosine and tartrazine. *Food and Chemical Toxicology* **48**, 2934–2944 (2010).
11. Nguyen, A. K., Goering, P. L., Reipa, V. & Narayan, R. J. Toxicity and photosensitizing assessment of gelatin methacryloyl-based hydrogels photoinitiated with lithium phenyl-2,4,6-trimethylbenzoylphosphinate in human primary renal proximal tubule epithelial cells. *Biointerphases* **14**, 021007 (2019).
12. Yuk, H., Zhang, T., Lin, S., Parada, G. A. & Zhao, X. Tough bonding of hydrogels to diverse non-porous surfaces. *Nature Materials 2015 15:2* **15**, 190–196 (2015).
13. Agha, A. *et al.* A Review of Cyclic Olefin Copolymer Applications in Microfluidics and Microdevices. *Macromol Mater Eng* **307**, 2200053 (2022).
14. Yeste, J., Illa, X., Guimerà, A. & Villa, R. A novel strategy to monitor microfluidic in-vitro blood-brain barrier models using impedance spectroscopy. in *Bio-MEMS and Medical Microdevices II* vol. 9518 95180N (SPIE, 2015).
15. Yeste, J. *et al.* A perfusion chamber for monitoring transepithelial NaCl transport in an in vitro model of the renal tubule. *Biotechnol Bioeng* **115**, 1604–1613 (2018).
16. Soman, P., Chung, P. H., Zhang, A. P. & Chen, S. Digital Microfabrication of User-Defined 3D Microstructures in Cell-Laden Hydrogels. *Biotechnol. Bioeng* **110**, 3038–3049 (2013).
17. Bhusal, A. *et al.* Multi-material digital light processing bioprinting of hydrogel-based microfluidic chips. *Biofabrication* **14**, 014103 (2021).
18. Grigoryan, B. *et al.* Multivascular networks and functional intravascular topologies within biocompatible hydrogels. *Science (1979)* **364**, 458–464 (2019).
19. Vila, A. *et al.* Hydrogel co-networks of gelatine methacrylate and poly(ethylene glycol) diacrylate sustain 3D functional in vitro models of intestinal mucosa. *Biofabrication* **12**, (2020).
20. Wang, Z. *et al.* A simple and high-resolution stereolithography-based 3D bioprinting system using visible light crosslinkable bioinks. *Biofabrication* **7**, 045009 (2015).
21. Ng, W. L. *et al.* Vat polymerization-based bioprinting—process, materials, applications and regulatory challenges. *Biofabrication* **12**, 022001 (2020).
22. Gong, H., Bickham, B. P., Woolley, A. T. & Nordin, G. P. Custom 3D printer and resin for 18 µm × 20 µm microfluidic flow channels. *Lab Chip* **17**, 2899–2909 (2017).
23. Flory, P. J. & Rehner, J. Statistical Mechanics of Cross-Linked Polymer Networks I. Rubberlike Elasticity. *J Chem Phys* **11**, 512–520 (1943).
24. Peppas, N. A., Hilt, J. Z., Khademhosseini, A. & Langer, R. Hydrogels in biology and medicine: From molecular principles to bionanotechnology. *Advanced Materials* **18**, 1345–1360 (2006).
25. Nikolaev, M. *et al.* Homeostatic mini-intestines through scaffold-guided organoid morphogenesis. *Nature* **585**, 574–578 (2020).
26. Shim, K. Y. *et al.* Microfluidic gut-on-a-chip with three-dimensional villi structure. *Biomed Microdevices* **19**, (2017).
27. Zhang, R. & Larsen, N. B. Stereolithographic hydrogel printing of 3D culture chips with biofunctionalized complex 3D perfusion networks. *Lab Chip* **17**, 4273–4282 (2017).
28. Yanagawa, F., Sugiura, S. & Kanamori, T. Hydrogel microfabrication technology toward three dimensional tissue engineering. *Regen Ther* **3**, 45–57 (2016).

29. Wang, Y. *et al.* A microengineered collagen scaffold for generating a polarized crypt-villus architecture of human small intestinal epithelium. *Biomaterials* **128**, 44–55 (2017).
30. Trietsch, S. J. *et al.* Membrane-free culture and real-time barrier integrity assessment of perfused intestinal epithelium tubes. *Nat Commun* **8**, (2017).
31. Beaurivage, C. *et al.* Development of a gut-on-a-chip model for high throughput disease modeling and drug discovery. *Int J Mol Sci* **20**, (2019).

4. Generation of a 3D bioprinted *in vitro* model of the intestinal mucosa in a hydrogel gut-on-chip

Current hydrogel gut-on-chips are established using complicated microfabrication techniques that limit their potential reach within the field. Alternatively, DLP-SLA 3D bioprinting is a versatile and simple technique that can generate high-resolution hydrogel structures for advanced *in vitro* models. As presented in chapter 4, this technique was used to fabricate hydrogel channels that mimic the intestinal villi to better recapitulate the morphology of the gut epithelial layer, crucial for barrier development and function. In this chapter, we present a 3D bioprinted gut-on-chip that reproduces this key spatial architecture along with the compartmentalized structure of the intestinal mucosa. To establish this advanced *in vitro* model, stromal cells were embedded in the bioprinted hydrogel and co-cultured with epithelial cells to support the formation of an epithelial barrier under continuous flow for several weeks.

4.1. Materials and methods

4.1.1. *Cell culture*

4.1.1.1. NIH-3T3 fibroblast cell culture

NIH-3T3 cells (ATCC® CRL-1658™) were purchased from American Type Culture Collection (ATCC, USA). The cells were derived from Swiss mouse embryonic fibroblast stem cells, following a method developed by Howard Green and George Todaro in 1962. In our model, NIH-3T3 cells were used to mimic the fibroblasts present in the stromal compartment of the intestinal mucosa. As they are easy to culture, NIH-3T3 cells have become a popular choice in cell co-culture studies, such as intestinal models [1].

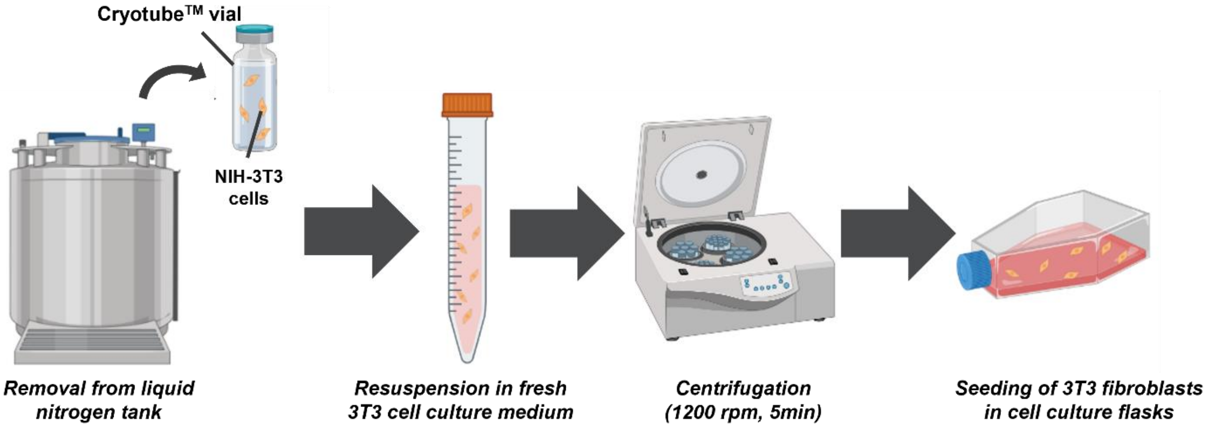

Figure 4.1: *Representation of the thawing process of NIH-3T3 cells.*

Initially, NIH-3T3 fibroblasts were thawed and expanded from a frozen Cryotube™ vial (ThermoFisher Scientific) containing the cells, located in the liquid nitrogen tank (Figure 4.1). Cell culture medium was first added at room temperature into the vial and pipetted up and down to favor defrosting of the freezing medium. The cell suspension was then transferred to a 15 mL Falcon tube (ThermoFisher Scientific) with fresh medium for dilution. Frozen medium contains 10 % (v/v) dimethyl sulfoxide (DMSO) (Sigma-Aldrich). It is added to reduce cell damage from ice crystal formation during the freezing procedure. However, DMSO is also toxic to cells, so their exposure to it must be minimized in terms of time by quickly diluting the freezing medium with fresh cell culture medium for NIH-3T3 cells. Cell culture medium for NIH-3T3 cells contained high-glucose Dulbecco's modified eagle medium (DMEM) with Phenol red and Glutamax (Gibco; ThermoFisher Scientific), supplemented with 10 % (v/v) fetal bovine serum (FBS, Gibco; ThermoFisher Scientific), 1 % (v/v) P/S (Sigma-Aldrich). FBS is often added in cell culture medium to promote cell growth, while P/S is an antibiotic mix used to prevent bacterial contamination. The Falcon tube with the cell suspension was then centrifuged for 5 min at 1200 rpm. The supernatant was discarded, and the pellet was resuspended in 3T3 fibroblast medium at 37ºC. Cells were seeded in 175 cm^2 cell culture treated flasks (Nunc^{TM}, ThermoFisher Scientific) and grown in an incubator (New Brunswick and Binder) at 37ºC, 5 % CO_2. 3T3 fibroblast medium was exchanged every 2-3 days until cells reached around 90 % confluence.

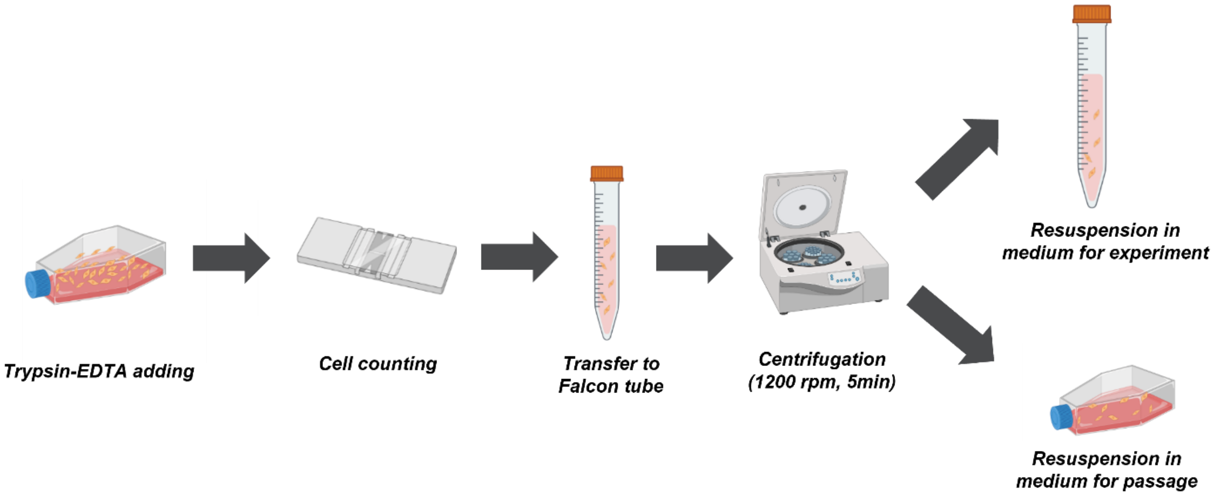

Figure 4.2: *Main steps of the cell passage of NIH-3T3 cells.*

When confluence was reached, cells were passaged to a new flask to maintain them in cell culture (Figure 4.2). For passages, 3T3 fibroblast cell medium was first removed, and cells were washed once with PBS at 37ºC. 0.25 % (v/v) Trypsin-EDTA (Gibco, ThermoFisher) at 37ºC was then added in the flask to detach the cells for 3 - 5 min. After this, the resuspended fibroblasts were pipetted up and down to disrupt formation of cell aggregates and transferred into a 50 mL conical Falcon tube (ThermoFisher Scientific) with fibroblast cell medium. Cells were counted with a Neubauer chamber (Sigma-Aldrich) and a volume with the desired number of cells was placed in a 15 mL Falcon tube. Cells were centrifuged at 1200 rpm for 5 min. Supernatant was removed and NIH-3T3 cells were resuspended in a specific volume with fresh fibroblast cell culture medium to obtain the desired cell density for the passage or an experiment.

4.1.1.2. Human epithelial Caco-2 cell culture

Caco-2 cells (ATCC® HTB-37^{TM}) were used to reproduce the intestinal epithelium in our model. Caco-2 cells were derived from colorectal adenocarcinoma cells, in a protocol initially established by Jorgen Fogh. Caco-2 cells are commonly used from drug permeability studies as they can represent the epithelial compartment of the gut [2,3].

Caco-2 cells were thawed from a cryotube^{TM} vial containing the cells, located in the liquid nitrogen tank, following the previously mentioned protocol. Cells were expanded in 75 cm^2 cell culture treated flasks in high-glucose DMEM with phenol red (Glutamax supplement, Gibco;

ThermoFisher Scientific), supplemented with 10 % (v/v) fetal bovine serum (FBS, Gibco; ThermoFisher Scientific), 1 % (v/v) non-essential amino acids (NEAA, Gibco; ThermoFisher Scientific), 1 % (v/v) P/S (Sigma-Aldrich) and harvested for cell culture experiments. Caco-2 cells were passaged when the confluence reached between 80 % - 90 %. Cells were cultured at 37°C, 5 % CO_2, medium was refreshed every 2 - 3 days and cell passage was done once a week.

4.1.2. *Microfluidic perfusion for intestinal cell culture on-chip*

4.1.2.1. *Shear stress simulations*

Epithelial cells are subjected to dynamic mechanical forces from the peristaltic intestinal flow [4]. Among them, fluid shear stress (FSS) represents the frictional parallel force per unit of area applied to the cell walls. This force can significantly alter the structure and function of cell barriers. Based on the Navier-Stokes equation, an evaluation of shear stress in dynamic cell culture can be performed numerically with computational simulations or analytically with geometry-dependent formula. In the case of channels with a rectangular cross-section where Newtonian fluids are perfused in a steady laminar flow, shear stress τ (in Pa or dyn/cm^2) can be described with the following equation:

$$\textbf{\textit{(eq. 4.1)}}\quad \tau = \frac{6\mu Q}{h^2 w}$$

Where μ is the fluid viscosity (in Pa.s), Q is the flow rate (in m^3/s), h is the height of the channel (in m) and w, the width of the channel (in m). This equation can be applied when h«w.

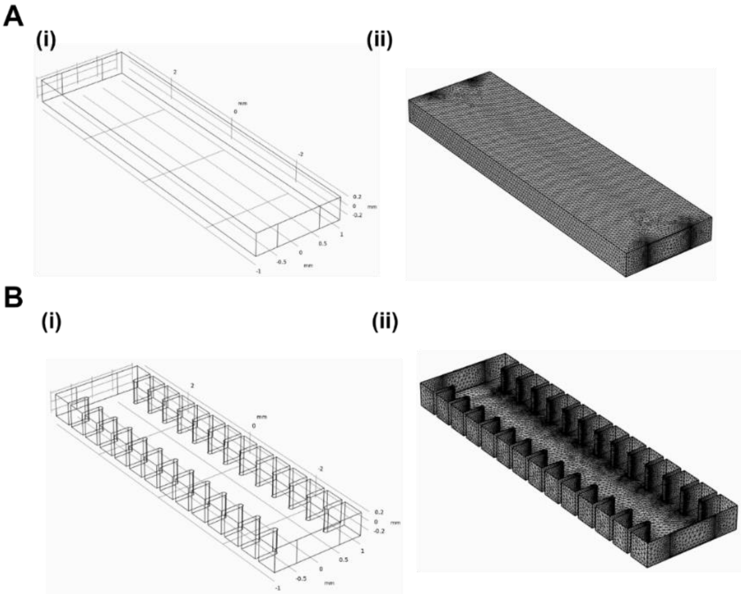

Figure 4.3: *Hydrogel channel geometries defined for shear stress simulations. (A) Rectangular shaped channel. (i) 3D Schematic drawing and (ii) tetrahedral mesh of the channel. (B) Channel with lateral villi structures. 3D Schematic drawing and (ii) tetrahedral mesh of the channel.*

3D finite element method (FEM) simulations of the central channel were performed to assess the range of shear stress exerted on the epithelial cells grown on the hydrogel under different fluid flows. 3D designs of the rectangular-shaped (Figure 4.3 A) and lateral pillar-sided hydrogel channels (Figure 4.3 B) were used to quantify the dynamic mechanical forces with COMSOL (COMSOL Multiphysics v5.6). Using the "laminar flow" (spf) interface within the CFD module, flow velocity profiles were modelled along the central channel, where epithelial cells are present. Shear stress was computed as the product of shear rate (unit: s^{-1}) and fluid viscosity (unit: Pa.s). Also, fluid properties of DMEM +10% FBS cell medium were defined in the model. Moreover, the lateral walls of the hydrogel were defined as no-slip boundaries for the computation. Simulations parameters are summarized in Table 5.1.

Parameters	**Values**
Fluid viscosity μ (Pa.s)	$9.4*10^{-4}$
Fluid density (kg/m^3)	1013
Fluid flow Q (μL.min^{-1})	5 - 25
Rectangular channel	
Channel width w (mm)	1 - 3
Channel length l (mm)	7
Channel height h (mm)	0.5
Lateral villi channel	
Channel width w (mm)	2 - 3
Channel length l (mm)	7
Channel height h (mm)	0.5
Pillar width (μm)	100
Pillar length (μm)	500
Pillar height (μm)	500
Pillar interspace (μm)	500

Table 4.1: *Parameters used for the shear stress simulations on COMSOL.*

4.1.2.2. Microfluidic setup

To support cell culture under dynamic conditions, the chip was connected to a closed-loop microfluidic setup where each channel was perfused independently (Figure 4.4 A). Two peristaltic pumps (Reglo Digital 2 channels and Reglo ICC 4 channels; Ismatec, Cole-Parmer) were used to generate a continuous flow within the microfluidic devices. 3-stop BPT tubing, with an inner diameter (ID) of 0.51 mm (PharMed, Saint-Gobain) were connected to the peristaltic pumps with MS-CA cassettes. Silicone extension tubing (ID 0.51 mm, Freudenberg Medical) was used to connect the pump system to the chips placed inside the incubator. The connection between the silicone and BPT tubes was done with polypropylene (PP) male/female luer adapters (1/16" hose barb, Avantor VWR). 50 mL Falcon tubes (ThermoFisher Scientific) filled with cell culture medium were connected to the external microfluidic setup via 4-port microfluidic adaptors (Elveflow) in which polytetrafluoroethylene (PTFE) tubing sleeves (OD 1/16", Avantor VWR) were directly inserted in the silicone tubing and tightly sealed with 1/4"-28 to 1/16" OD fittings and 1/16" OD ferrules (Elveflow) to perfuse the medium. Sterile passive bubble filters (Speedflow Kids; Gvs) were also added in-line at the chip inlets to reduce the risk of bubble formation (Figure 4.4 B). Before starting experiments with cells, all components (tubing and adapters) of the microfluidic setup and the chip were placed in tip boxes to sterilize them via autoclaving (high-pressure saturated steam). Tubing was autoclaved at 110ºC to prevent the melting of the glued stops, while the rest of the components were autoclaved at 121ºC.

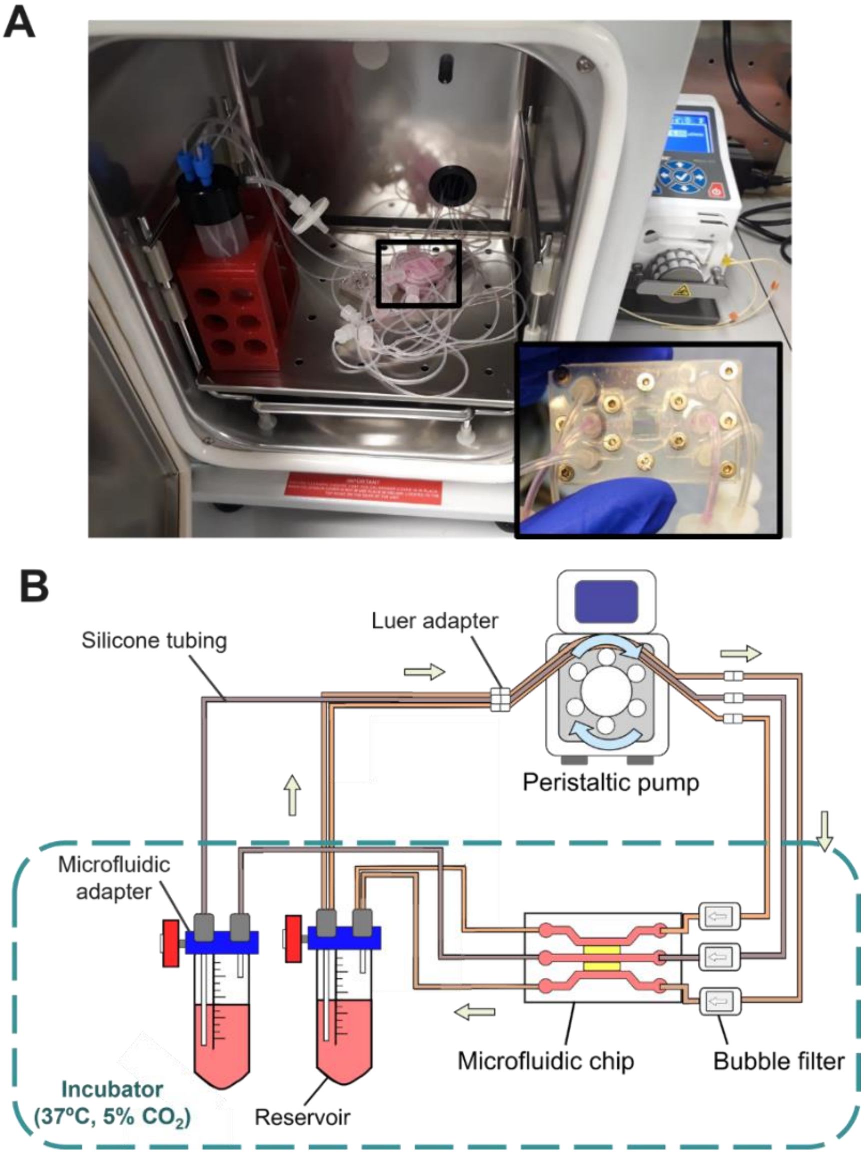

Figure 4.4: *Microfluidic setup for cell culture. (A) Image of the setup inside the incubator with a zoom-in image of the chip (bottom right corner). (B) Schematic representation of the closed-loop recirculating perfusion system.*

4.1.3. Fabrication of the 3D bioprinted gut-on-chip model

4.1.3.1. Fabrication of the bioprinted intestinal stromal compartment

To mimic the stromal compartment of the intestinal mucosa in our gut-on-chip model, NIH-3T3 fibroblasts were encapsulated in the bioprinted hydrogel channels for dynamic cell culture in the chip. The composition of the bioink was the same one characterized in chapter 3: 5 %

(w/v) GelMA, 3 % (w/v) PEGDA, 0.4 % (w/v) LAP and 0.025 % (v/v) Tartrazine. Following the previously mentioned method, NIH-3T3 cells cultured in flasks were first trypsinized, transferred to a 1.5 mL Eppendorf tube and centrifuged at 1200 rpm for 5 min. After the supernatant was removed, the pellet was resuspended in 1.5 mL of GelMA-PEGDA pre-polymer solution at 37°C to obtain a cell density of $7.5*10^6$ cells/mL. Following this, the cell-laden bioink was loaded into the vat and hydrogel channels were bioprinted on silanized PET substrates in a layer-by-layer manner using the printing parameters described in chapter 3 (layer exposure time: 5 s; layer thickness: 13 µm) (Figure 4.5). Once the NIH-3T3 cell-laden hydrogel channels were printed, samples were cleaned with PBS supplemented with 1 % (v/v) P/S, gently dried with clean room wipes to remove unreacted residues and finally detached from the printing support with a surgical blade to be placed into a sterile 24 well-plate (Nunclon^{TM}, ThermoFisher) with cell culture medium. 0.3 % (v/v) Normocin^{TM} (Invitrogen) was added to the 3T3 fibroblast medium to reduce the risks of biological contamination in a non-sterile working setup. Normocin^{TM} is a formulation containing three antibiotic compounds that prevent bacterial, mycoplasma and fungal contaminations. The bioprinted samples were then kept in an incubator at 37ºC, 5 % CO_2 for 2 - 3 h before chip assembly.

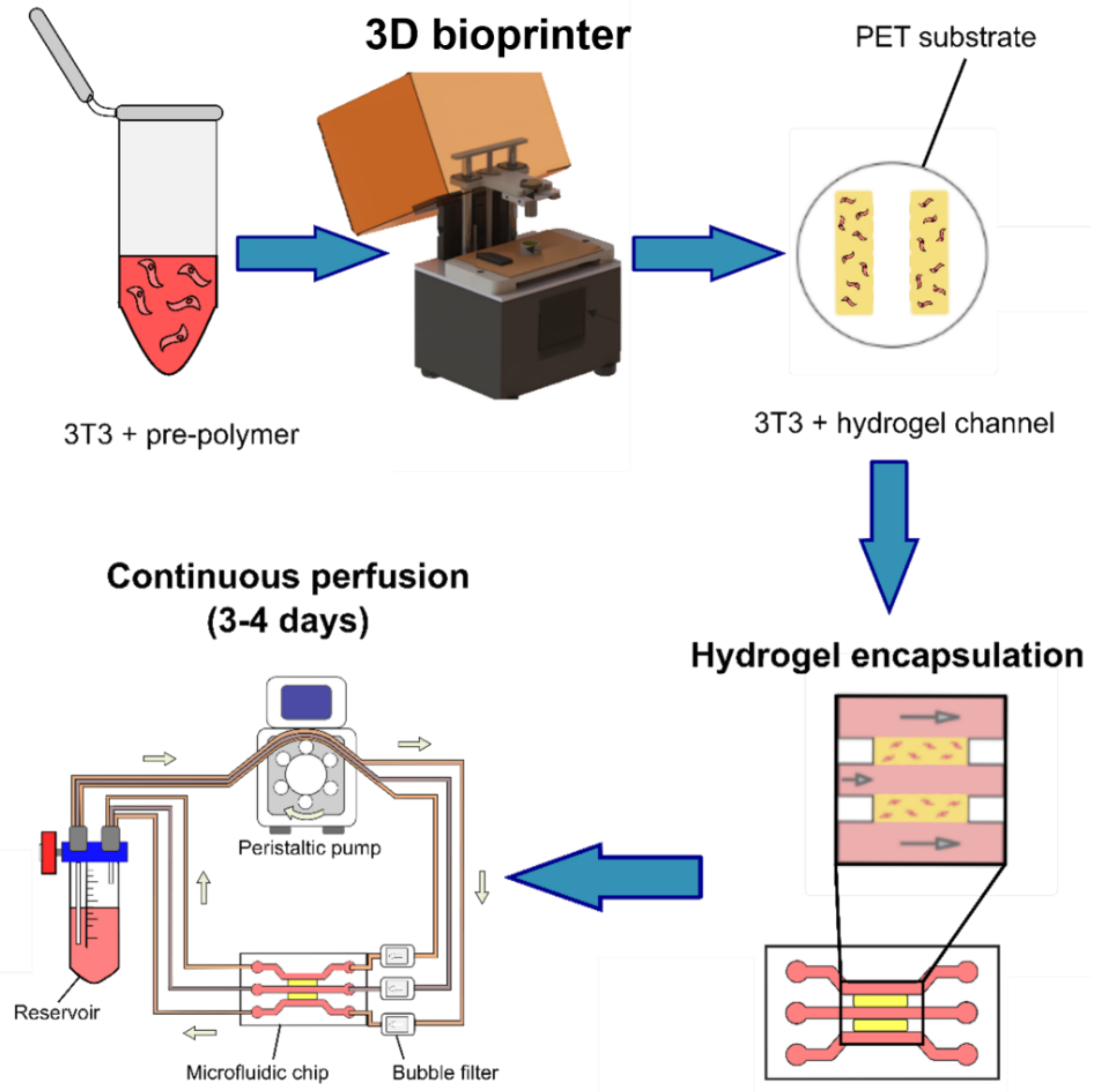

Figure 4.5: *Fabrication process of the intestinal stromal compartment for the gut-on-chip model.*

After this time, all the autoclaved components of the microfluidic setup and the chip were placed in the laminar hood. The sterile tubes were connected to the reservoirs containing 3T3 fibroblast medium, and to the peristaltic pump to fill up the channels with it. Afterwards, cell-laden hydrogel channels were encased in the central chamber of the microfluidic chip by attaching the substrate to the bottom PSA layer of the middle piece (Figure 4.5). The chip was then assembled by sandwiching the middle piece between the silicone and plastic COP plates and sealing the device with screws. Shortly after, warm cell culture medium was manually loaded into the three channels to avoid cell death, prevent hydrogel dehydration, and check potential leakage between channels. Finally, the chip was connected to the microfluidic setup by inserting the mini-luer connectors inside the silicone tubing and all the components except the pump were placed inside the incubator at 37ºC. Recirculating medium was perfused continuously along the channels from two different reservoirs, one for the lateral channels and another one for the central channel, with a flow rate of 5 µL/min to support the cell culture of the hydrogel-embedded NIH-3T3 cells for 3 or 4 days (Figure 4.5).

4.1.3.2. Intestinal epithelial cell seeding

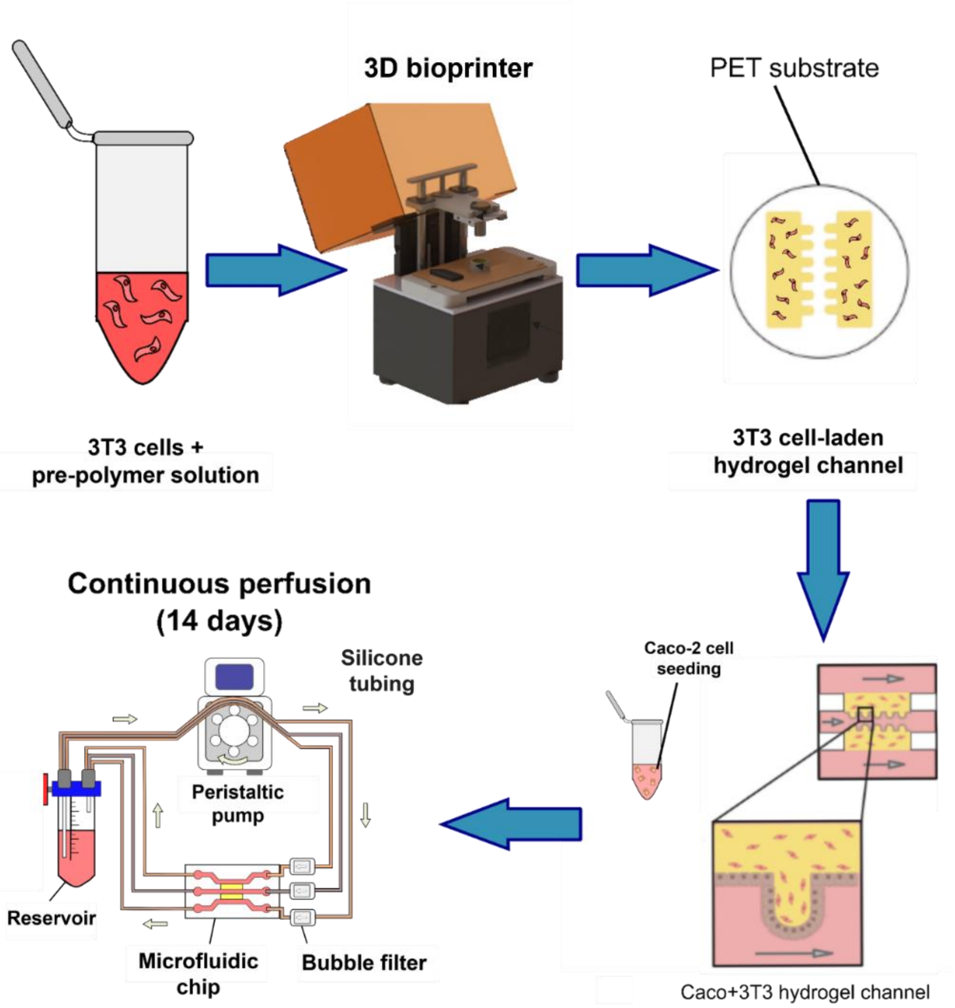

Figure 4.6: *Fabrication process of the 3D bioprinted intestinal mucosa for the gut-on-chip model.*

To represent the epithelial compartment of the intestinal mucosa in our 3D gut-on-chip model, Caco-2 cells were seeded in the central channel with a cell density of $7.5*10^5$ cells/cm^2 (10^7 cells/mL) after 3 or 4 days of culturing hydrogel-embedded NIH-3T3 cells under continuous flow. The cell density was selected based on previous studies in which Caco-2 cells were grown on similar PEGDA-GelMA hydrogels [5]. For the seeding procedure, the peristaltic pump was first stopped, and the chips were disconnected from the microfluidic setup inside the laminar cabinet. Medium from the central channel was removed and 150 µL of Caco-2 cell culture medium with the resuspended cells were loaded manually inside. To allow the cells to sediment on the hydrogel walls, the chips were placed vertically on each side in the incubator at 37ºC for 2h each time. After this, the chips were inspected under a brightfield optical microscope (ECLIPSE Ts2 Optical Microscope, Nikon) to check cell attachment. Finally, the chips were connected back to the peristaltic pump and medium perfusion was re-started afterwards with a flow rate of 5-10 µL/min in all channels for 14 days (Figure 4.6). Cells inside the chip were inspected under the optical microscope every 2 days to assess formation of an epithelial barrier, and medium from the reservoirs was replaced every 5 - 6 days.

4.1.4. Characterization of the 3D bioprinted gut-on-chip model

4.1.4.1. Cell viability assay

The cell viability of hydrogel-embedded NIH-3T3 fibroblasts grown on-chip was assessed with a Live/Dead^{TM} cytotoxicity kit assay (Invitrogen) 1 and 4 days after cell encapsulation. The kit is a quick and easy two-based assay that discriminates between live and dead cells based on plasma membrane integrity and esterase activity. It has two fluorescent dyes, calcein AM and ethidium homodimer-1 (EthD-1). On one hand, calcein AM labels viable cells green in a process in which the non-fluorescent molecules permeate inside the cell and ubiquitous intracellular esterase enzymes remove ester groups to render them fluorescent (Figure 4.7). The excitation and emission wavelengths of calcein AM are 495 nm and 515 nm respectively. On the other hand, EthD-1 labels dead cells red by penetrating the ones with compromised plasma membranes and binding to their DNA with high affinity, inducing conformational changes of the molecule that increase its fluorescence (Figure 4.7). The excitation and emission wavelengths of EthD-1 are 495 nm and 635 nm respectively.

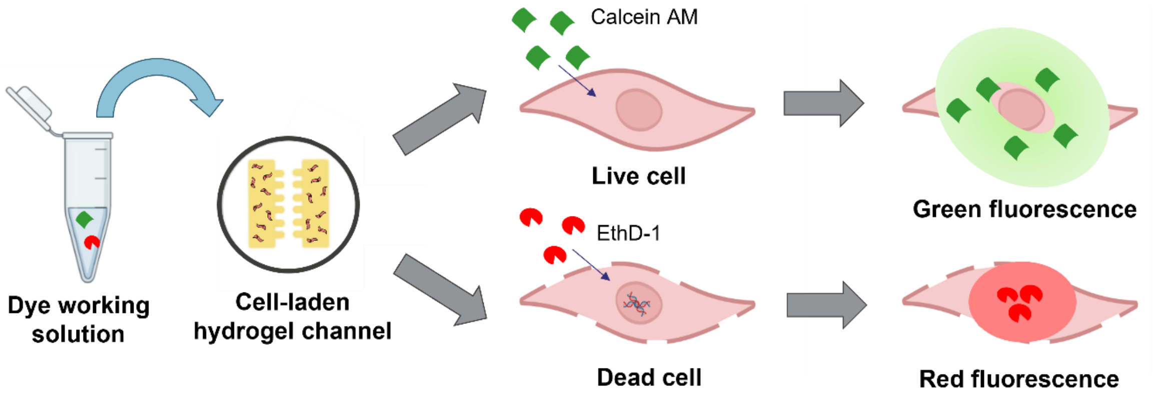

Figure 4.7: *Working principle of a Live/Dead^{TM} assay. Non-fluorescent calcein AM molecules permeate the membrane of live cells, where esterase enzymes render them fluorescent green. When cells are dead, ethidium homodimer-1 (EthD-1) enters through the damaged plasma membrane and binds their DNA, generating a red fluorescent signal.*

To evaluate the viability of the encapsulated cells, the chips were first taken out from the incubator and disassembled in the laminar cabinet. The substrates with the attached cell-laden hydrogels were carefully retrieved from the device by detaching them from the PSA with a surgical blade. After this, the samples were placed in a sterile 24 well-plate (Nunclon^{TM}, ThermoFisher) with PBS at 37ºC inside the wells to remove esterases present in the cell culture medium that can generate false positives. During the washes, the dye solution was prepared without light in the laminar hood. 4 µL of 2 mM EthD-1 (Invitrogen) were diluted in 2 mL of sterile PBS to obtain a 4 µM EthD-1 solution. 1 µL of 4 mM calcein AM (Invitrogen) was diluted in the PBS solution containing EthD-1 solution to obtain a final concentration of 2 mM calcein AM. Finally, 2 µL of Hoeschst Reagent (H3570, Invitrogen) were added to 1 mL of dye working solution in a 1/10 dilution to stain cell nuclei. Once all the reagents were added, the working solution was vortexed to ensure their proper mixing. After completing the washing step, 250 µL of working solution were directly added to each hydrogel and samples were placed inside the incubator at 37ºC for 20 min protected from light with aluminum foil. Following this, hydrogels were washed for 8 minutes two times with sterile PBS. Finally, the samples were mounted on glass coverslips with a drop of PBS for confocal imaging. Cell-laden hydrogels were analyzed with a confocal laser-scanning microscope (LSM800; Zeiss) located in the IBEC MicroFabSpace facilities. Images were acquired with 10x and 20x dry objectives and a set of 3D stack images was generated to image the cells inside the thick hydrogel channels. The files were post-processed on ImageJ 1.53t software (NIH; open source). The quantification of live and dead cells was done by counting the number of total, dead and live cells. Cell viability rates were then plotted as a percentage of the total number of cells for each condition.

4.1.4.2. Immunofluorescence assay

Cells were immunostained after 14 days of cell culture in the chip to assess the distribution of hydrogel-embedded NIH-3T3 fibroblasts and the presence of tight junction markers for epithelial Caco-2 cells. This assay relies on the use of antibodies to label specific target proteins with a fluorescent dye, also referred to as fluorophore. Two types of immunofluorescence assays (IFA) can be distinguished, direct and indirect ones [6]. Direct IFA is based on a single antibody conjugated to a fluorophore for the detection of the target protein. Indirect IFA uses two antibodies: the primary antibody binds to the protein of interest while a fluorophore-conjugated secondary antibody specifically binds to the primary one for fluorescence imaging. In these assays, several proteins can be imaged simultaneously for one sample by adding specific primary antibodies and secondary antibodies with different fluorophores. To prevent non-specific binding, primary antibodies are generally selected from different animal sources such as mice, goats, or rabbits. Also, choosing the right secondary antibodies is important as they are designed to bind primary ones with a specific animal source.

To preserve the integrity of the epithelial cell barrier on the hydrogel channel, the immunostaining assay was performed inside the chip (Figure 4.8). First, the cell culture medium was washed out from the hydrogels by replacing it with filtered PBS at 37ºC using the peristaltic pump. This step was performed inside the incubator for 1h and PBS was perfused with similar flow rates as for cell culture (5-10 µL/min) to ensure no mechanical disruption of the attached epithelial cells. After this, the chips were disconnected from the microfluidic setup and re-connected to a syringe pump (NE-1000 Programmable Single Syringe Pump, New Era) with silicone tubing (OD 0.76 mm, Freudenberg Medical) and luer adaptors (Avantor, VWR) outside the incubator to remove the PBS from the channels. Once empty, both the syringe pump and the chip were placed under a chemical hood and 300 µL of 10 % buffered formalin solution (Sigma-Aldrich) were loaded in all three channels. After the filling was completed, the chip ports were closed with plastic plugs and the hydrogels were incubated with the formalin solution for 1 h at room temperature under shaking conditions to fix the cells. The solution was then washed out by perfusing filtered PBS overnight with a flow rate of 5 µL/min. The next step after fixation was the permeabilization of the cells. To do this, a buffer solution containing 0.5 % (v/v) TritonX (Sigma-Aldrich) diluted in filtered PBS was prepared. PBS was removed from the channels of the chips and the buffer was loaded using the syringe pump with a flow rate of 5 - 10 µL/min for static incubation during 2 h. After the permeabilization step, the buffer solution was removed from the chips and the channels were washed out with filtered PBS for 1 h with the syringe pump. A blocking solution containing 1 % (w/v) bovine serum albumin (BSA, Sigma-Aldrich), 3 % (v/v) donkey serum (Milipore) and 0.3 % (v/v) TritonX (Sigma-Aldrich) diluted in filtered PBS was then loaded in all channels (flow rate: 5-10 µL/min) and left for incubation under shaking conditions overnight in the cold room (4ºC). Once the blocking step was completed, the buffer solution was removed with the syringe pump. The working buffer containing the primary antibodies was then prepared. Primary antibodies anti-rabbit Zonula-Occludens-1 (2.5 µg/mL) (ZO-1, ThermoFisher) in a 1:100 dilution, anti-mouse β-Catenin (1 µg/mL) (Abcam) in a 1:200 dilution or anti-goat collagen IV (Biorad) in a 1:250 dilution were added to 1mL of the buffer solution with 0.1 % (w/v) BSA, 0.3 % (v/v) donkey serum and 0.2 % (v/v) TritonX diluted in filtered PBS. ZO-1 is a tight junction-associated protein present in polarized epithelial cells [7]. β-Catenin is a protein that belongs to the adherens junction complex. It is a marker of cell-cell junction for epithelial cells [8]. Collagen IV is an ECM protein located in the basement membrane and stromal compartment of the intestinal mucosa. It is often used as a marker to assess the functionality of stromal cells to secrete collagen proteins and remodel the surrounding matrix [9]. The primary antibody working buffer was then loaded into all channels of the chips with a flow rate of 5 - 10 µL/min and, once they were all filled, the device was placed back in the cold room under shaking conditions overnight. For the final step of the immunofluorescence assay, secondary antibodies anti-mouse Alexa A488 (4 µg/mL) in a 1:500 dilution (Invitrogen; ThermoFisher Scientific) and anti-rabbit Alexa A647 (4 µg/mL) in a 1:500 dilution (Invitrogen; ThermoFisher Scientific), along with DAPI (5 µg/mL) in a 1:1000 dilution (ThermoFisher Scientific) and Rhodamine-phalloidin (0.07 µM) in a 1:140 dilution (Cytoskeleton), were added to a secondary working buffer solution containing 0.1 % (w/v) BSA and 0.3 % (v/v) donkey serum in filtered PBS. DAPI is a blue-fluorescent stain that strongly binds to adenine-thymine rich areas of DNA [10]. It is generally used to stain cell nuclei. Phalloidin is a peptide that selectively labels actin filaments of the cell cytoskeleton [11]. Before adding the buffer solution, the chips were washed out with PBS for 3 - 4 h under perfusion to remove unbounded primary antibodies from the hydrogel. After this, the secondary antibody working buffer was loaded into the chip (flow rate: 5 - 10 µL/min) protected from light with aluminum foil and left for incubation 2 h under shaking conditions at 4ºC. Finally, the buffer was washed out with filtered PBS for 2 – 3 h using the syringe pump. PBS was left in the channels after the wash to prevent hydrogel dehydration.

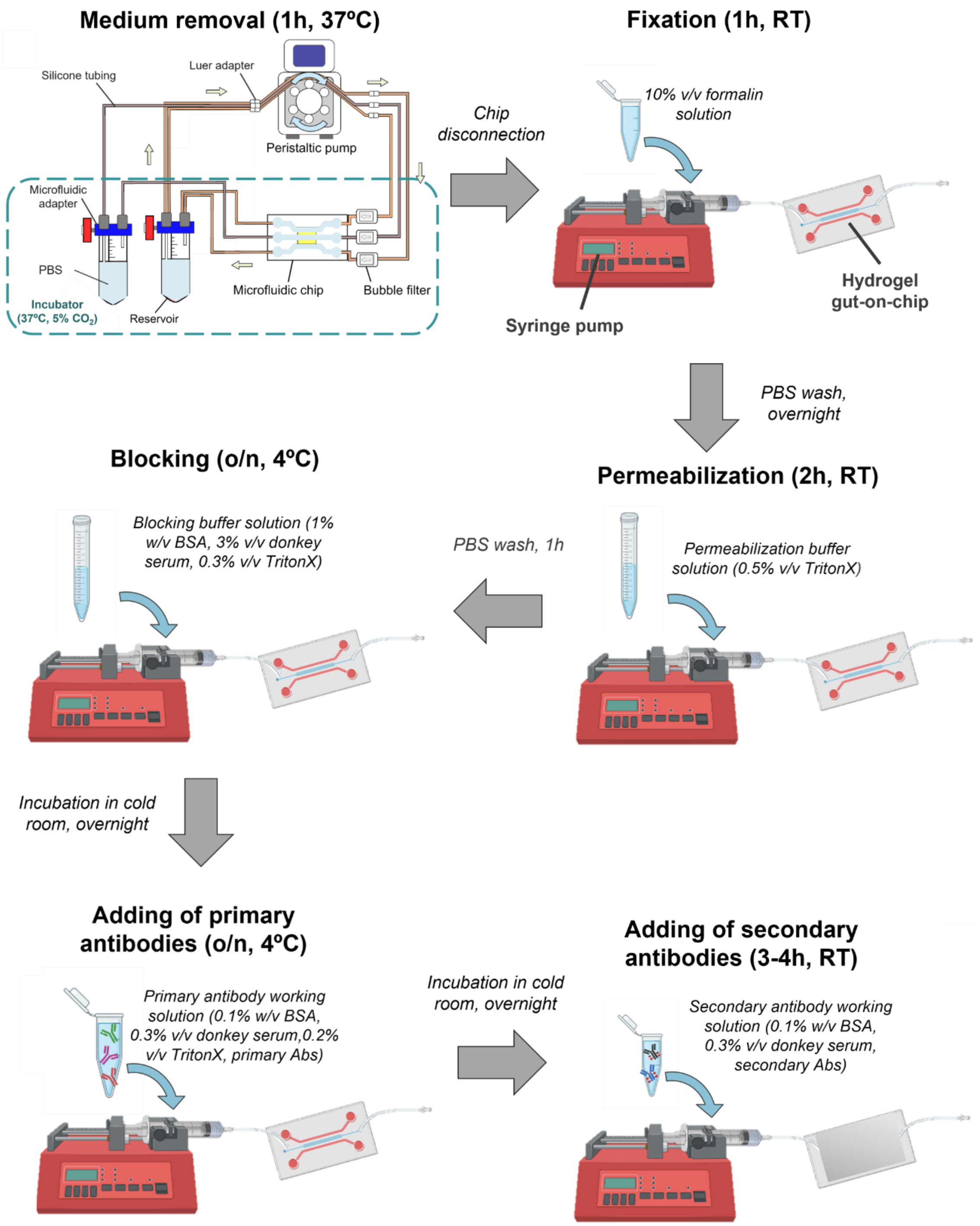

Figure 4.8: *Main steps of the immunostaining process on-chip.*

Immunostained samples were first imaged inside the chip with a fluorescence inverted microscope (Leica Thunder). 5x and 10x dry objectives were used to generate tile images of the full hydrogel channel. Later, the chip was disassembled and the substrate with the hydrogels was carefully removed with a surgical blade inside the laminar cabinet without light. The sample was placed inside a 24 well-plate (Nunclon^{TM}, ThermoFisher Scientific) with PBS and then analyzed via confocal imaging (LSM 800; Zeiss) to obtain better image resolution of the Z-stacks. The acquired images were treated on ImageJ 1.53t software (NIH; open source).

4.1.4.3. Permeability assay

Paracellular permeability assays are commonly used in *in vitro* intestinal studies to assess epithelial barrier integrity and predict drug oral absorption [12]. In conventional Transwell®-based models, a labelled tracer, usually a fluorescent dye, is added in the apical compartment of the system to measure its diffusion to the basolateral compartment through the cell monolayer. Measurements of fluorescent intensity from the diffused compound in the bottom compartment are recorded periodically with a microplate reader to monitor the evolution over time. A calibration curve is also defined to correlate the tracer concentration with the measured fluorescence intensity. From these data, the apparent permeability $P_{app,}$ defined by the amount of tracer transported through the membrane per time, can be calculated [13]:

(eq. 4.2) $$P_{app} = \frac{\Delta C_{receiver} * V_{receiver}}{\Delta t * A_{barrier} * C_{donor}} \text{ (in cm/s)}$$

Where $\Delta C_{receiver}$ is the difference of tracer concentration at the basolateral compartment over the measured time (in µmol), $V_{receiver}$ is the total volume in the basolateral compartment (in cm^3), Δt is the time difference (in s), $A_{barrier}$ is the membrane area (in cm^2) and C_{donor}, the concentration at the apical compartment (in µmol). The linearity of the formula is generally valid when $C_{receiver}$ remains below 10% of C_{donor}, as, in this range, the concentration gradient and resulting flux is not significantly influenced by the increasing concentration in the basolateral compartment.

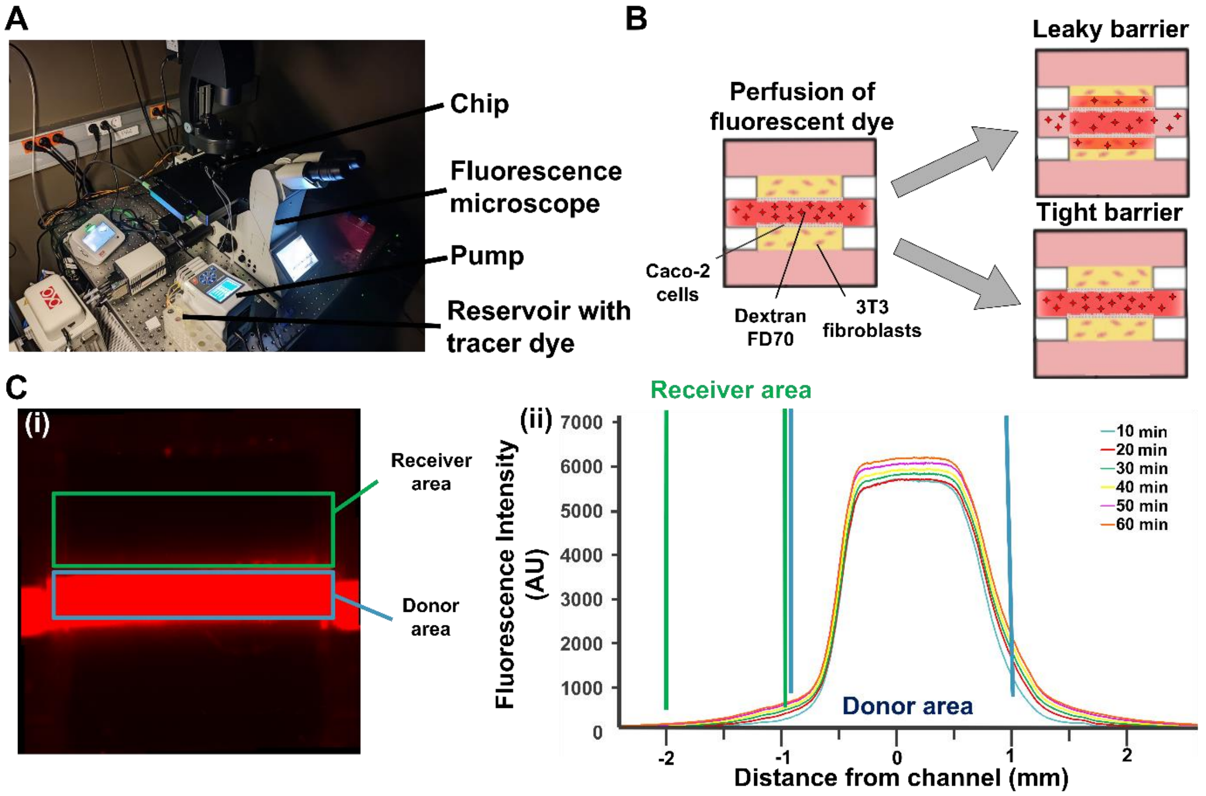

Figure 4.9: *Permeability assay to characterize barrier integrity in the 3D hydrogel gut-on-chip. (A) Setup to perform the permeability assay on-chip under a high-resolution fluorescence microscope. (B) Schematic of the barrier integrity assay, where the perfused fluorescent dextran diffuses through the hydrogel when the barrier is leaky while it remains in the central channel when it is tight. (C) Methodology to measure the apparent permeability P_{app} of the epithelial barrier on the hydrogel channel.*

(i) A donor region is selected in the central channel where the dextran dye is perfused. A receiver region in the hydrogel is selected to quantify tracer diffusion over time. (ii) At each time point, the average fluorescent intensity in the receiver area is extracted using the Fiji software and divided by the average intensity in the donor area to quantify P_{app}.

For our 3D gut-on-chip model, permeability assays were performed inside the device after 14 days of microfluidic cell culture since epithelial cell seeding (Figure 4.9 A). Rhodamine-dextran with a molecular weight of 70 kDa (FD70, Sigma-Aldrich) was selected as the labelled tracer to perform the assay, as its size is close to the one of albumin (58 kDa), one of the most common proteins found in cell culture medium. Previous studies with the same bioink showed that the molecular weight exclusion limit was 360 kDa, thus allowing the transport of smaller molecules like FD70 through the hydrogel [14]. The dye solution was initially prepared by diluting the dextran in HBSS supplemented with 1 % (v/v) P/S (2 mg/mL). The solution was sterilized with 0.22 µm PET filters and then transferred to a 15 mL Falcon tube protected from light. The device was disconnected from the microfluidic setup and placed under the fluorescence microscope (Leica Thunder) within an incubator system at 37ºC, 5 % CO_2. The chip was then connected to a pump (syringe or peristaltic) and the reservoir containing the dextran solution using flexible silicone tubing (Freudenberg Medical). Once the system was set up, the fluorescent tracer was perfused along the central channel at a flow rate of 5 µL/min for 90 min. The lateral diffusion of the dye across the two adjacent hydrogels was recorded within the central area of the chip every 10 min with a 10x dry objective. Leaky barriers displayed increasing fluorescence signals in the hydrogel areas over time than tight ones, as, for the latter, the paracellular transport of the tracers was more restricted by the tight junctions of the epithelial barrier (Figure 4.9 B).

The recorded images of the hydrogel channel were then analyzed to extract the fluorescence intensity profiles at different areas of interest with Fiji software, and to calculate the apparent permeability of the cell barrier (Figure 4.9 C) [15,16]. To do this, the average fluorescence intensity of the considered hydrogel region was divided by the average fluorescence intensity of the selected region of the central channel. Assuming a proportional relationship between the dextran concentration and the fluorescence intensity, P_{app} could be determined:

$$\textbf{(eq. 4.3)}\ P_{app} = \frac{\Delta I_{f,gel} * V_{gel}}{\Delta t * A_{barrier} * I_{f,channel}}$$

Where $\Delta I_{f,gel}$ is the difference of average fluorescence intensity in the hydrogel channel between t=0 and t=90 min. V_{gel} is the volume of the hydrogel region where fluorescence is quantified. Δt is the time of the experiment. $A_{barrier}$ is the area of the hydrogel channel lateral edge. $I_{f,channel}$ is the average fluorescence intensity of the central channel where the dextran is perfused. The apparent permeability was calculated for cell-free hydrogels, defined as controls, and hydrogel channels with co-cultured 3T3 fibroblasts and Caco-2 cells to evaluate the transport of the dextran through the epithelial barrier.

4.1.5. Data representation and analysis

Plot values are displayed as the mean ± standard deviation (S.D.). OriginPro 9.60 (OriginLab) was used to generate the graphs. Student's paired t-tests were run to compare groups of data to determine their difference. $p<0.05$ was used as a threshold to confirm the statistical significance of datasets.

4.2. Results

4.2.1. Evaluating fluid shear stress in the hydrogel gut-on-chip

Shear stress simulations were initially performed to estimate the optimal flow rate in the central channel for epithelial cell culture in our 3D gut-on-chip. To do this, a range of flow rates between 5 and 25 µL/min was set to calculate the corresponding wall shear stress on the hydrogel surfaces. Based in previous studies with Caco-2 cells cultured in microfluidic devices, a shear stress in the range of 0.01 and 0.025 dyn/cm^2 was considered suitable for cell medium perfusion [4]. Two main geometries were considered for the computational study: a channel with a rectangular cross-section and another one with lateral villi-like structures (channel height: 500 µm). For the first one, different channel widths ranging from 1 to 3 mm were considered to model the flow rate (Figure 4.10 A). It was observed that shear stress values were relatively uniform on the hydrogel walls, with lower values on the areas closer to the inlet and outlet due to their narrower size (1 mm wide) (Figure 4.10 B and C).

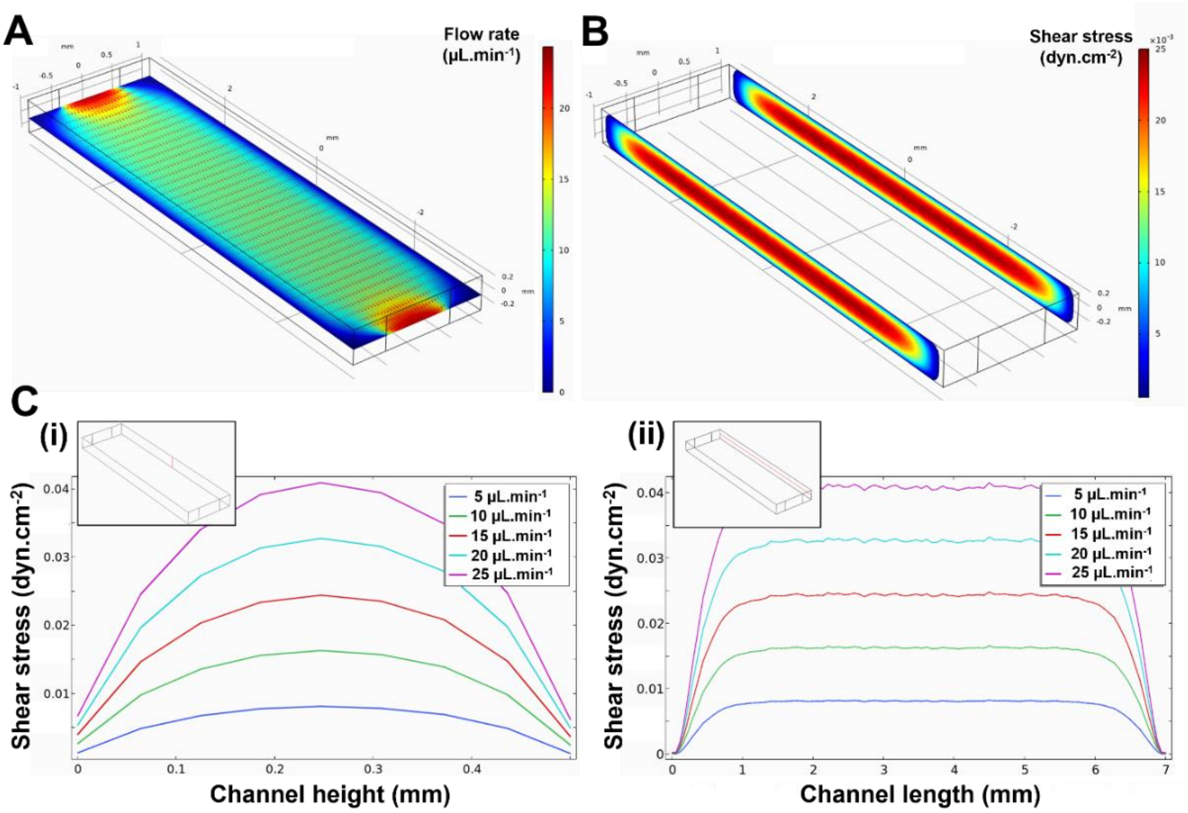

Figure 4.10: *Shear stress simulations on hydrogel channels with rectangular cross-sections. (A) 3D view of the flow rate within the central channel. Flow rate of the channel was set to 15 µL/min and the channel width, to 2mm. Red arrows represent the flow velocity vectors in the XY plane. (B) 3D representation of shear stress on the lateral walls of the hydrogels. (C) Shear stress plots for flow rates ranging from 5 to 25 µL/min. (i) Shear stress plot along the hydrogel height. (ii) Shear stress plot along the channel length. For both plots, the cut line used to display the shear stress is shown in the upper left 3D drawing.*

Average shear stress values were also calculated for each channel width and flow rate (Table 4.2). For narrow central channels (width: 1 mm), flow rates between 5 - 10 µL/min resulted in FSS within the optimal range, between 0.014 and 0.03 dyn/cm^2. In the case of intermediate (width: 2 mm) and wide channels (width: 3 mm), flow rate ranges of 10 - 20 µL/min (between 0.011 and 0.021 dyn/cm^2) and 20 - 25 µL/min (between 0.012 and 0.015 dyn/cm^2) respectively were considered appropriate for Caco-2 cell culture inside the chip. Moreover, the average FSS had similar values to the analytical solutions for microfluidic channels with rectangular cross-sections.

Flow rate (μL.min^{-1})	**Shear stress - 1 mm** (dyn.cm^{-2})	**Shear stress - 2 mm** (dyn.cm^{-2})	**Shear stress - 3 mm** (dyn.cm^{-2})
5	0.014	0.005	0.003
10	0.030	0.011	0.006
15	0.044	0.016	0.009
20	0.060	0.021	0.012
25	0.074	0.026	0.015

Table 4.2: *Average surface shear stress for different channel widths (from 1 mm to 3 mm) and flows.*

In the case of the central channel with lateral villi-like structures, flow profiles were less uniform than for the rectangular channel design, with high flow rates in the central parts of the channel and low ones in between the pillars (Figure 4.11 A). This distribution translated into a spatial gradient of shear stress along the villus axis, with higher frictional forces at the tip of the lateral pillars than at their sides and bottom regions (Figure 4.11 B and C).

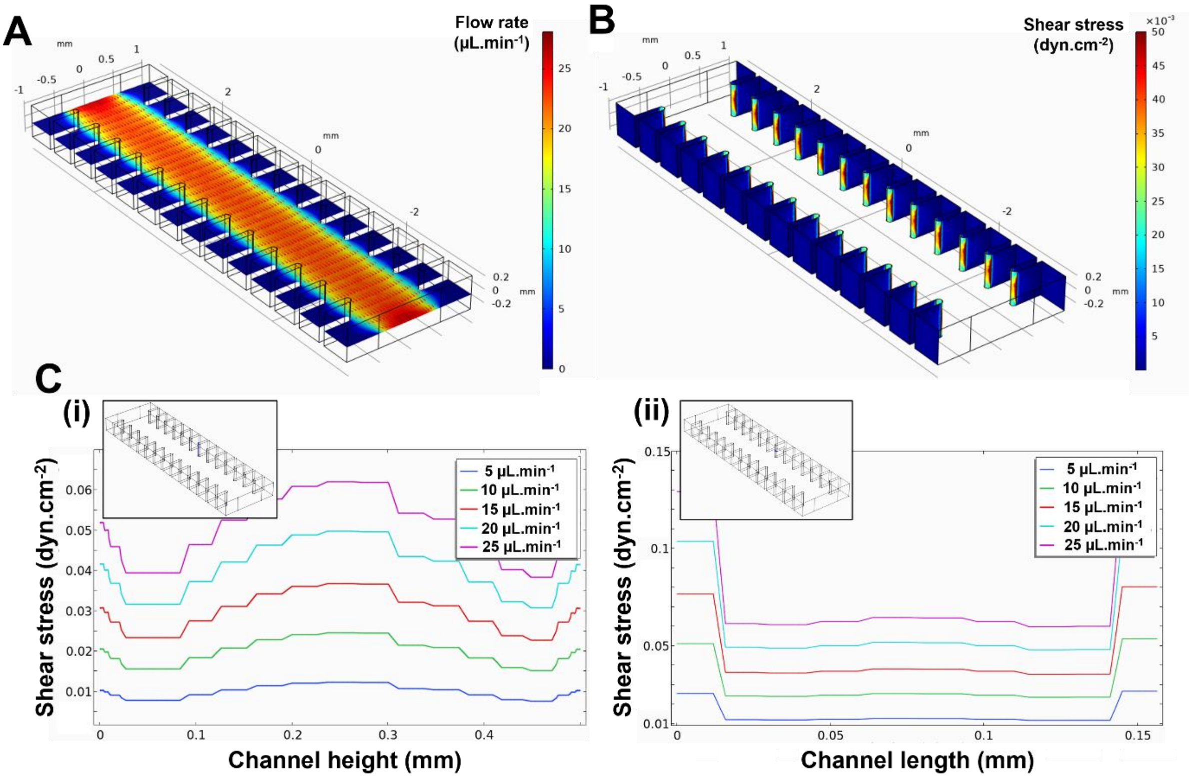

Figure 4.11: *Shear stress simulations on hydrogel channels with lateral villi-like structures. (A) 3D view of the flow rate within the central channel. Flow rate of the channel was set to 15 µL/min and the channel*

width, to 2 mm (1 mm + 0.5 mm x2 villi). Red arrows represent the flow velocity vectors in the XY plane. (B) 3D representation of shear stress on the lateral walls of the hydrogels. (C) Shear stress plots for flow rates ranging from 5 to 25 µL/min. (i) Shear stress plot along the hydrogel height. (ii) Shear stress plot along the channel length. For both plots, the cut line used to display the shear stress is shown in the upper left 3D drawing.

Average shear stress values were computed for each region of the pillar structures (Table 4.3). As observed in the plots, shear stress at the tip of the villi were orders of magnitude higher than at the sides and bottom parts of the lateral structures. Based on these computed values, we selected flow rates between 5 and 10 µL/min as suitable for microfluidic cell culture, as higher ones could have a negative impact on the epithelial cells located at the pillar tips. The observed spatial differences in FSS values are in accordance with previous 3D simulations based on biomimetic intestinal scaffolds on-chip [17] and *in vivo* observations, where the bottom regions of the villi and crypts are shielded from mechanical forces while the lateral walls and tip of the villi are exposed to the mechanical forces of peristaltic flow.

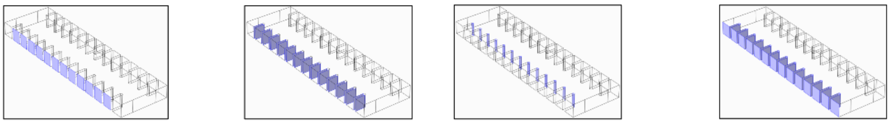

Flow rate (μL.min^{-1})	Shear stress – bottom (dyn.cm^{-2})	Shear stress - lateral (dyn.cm^{-2})	Shear stress - tip (dyn.cm^{-2})	Average shear stress (dyn.cm^{-2})
5	0.0001	0.0007	0.0114	0.0017
10	0.0003	0.0015	0.0229	0.0035
15	0.0004	0.0022	0.0343	0.0052
20	0.0005	0.0029	0.0464	0.0070
25	0.0007	0.0037	0.0579	0.0088

Table 4.3: *Average shear stress at different regions of the hydrogel channel: bottom part, lateral walls of the villi and tip of the pillars. The average shear stress of the total surface is also displayed.*

In summary, for a chosen channel geometry and based on the simulation results, we selected a specific flow range (5-10 µL/min) to optimize the cell culture and barrier formation of Caco-2 cells within the hydrogel gut-on-chip device.

4.2.2. 3D PEGDA-GelMA hydrogel channels support 3T3 fibroblast embedding under perfusion

NIH-3T3 fibroblasts were selected to represent the stromal compartment of our gut-on-chip model. 3T3 cells were added to the 5 % (w/v) GelMA – 3 % (w/v) PEGDA - 0.4 % (w/v) LAP – 0.025 % (v/v) tartrazine pre-polymer solution with a density of 7.5x10^6 cells/mL before the printing process. The bioink was then loaded into the vat and hydrogel channels with rectangular cross-sections were printed with the optimal printing parameters previously described (layer exposure time: 5 s, layer thickness: 13 µm). After the printing, the PET substrate with the hydrogel channel was detached from the printing support and, later on, allocated in the central chamber of the microfluidic chip. Once encased, the device was connected to the peristaltic pump and the cell-laden hydrogel channel was continuously perfused with cell medium with a fluid flow of 5 µL/min along the three independent channels. Cell viability of the 3T3 fibroblasts was assessed with Live/Dead$^{\mathrm{TM}}$ assays and confocal imaging 1 and 4 days after cell embedding. To perform the assays, the device was disconnected from the microfluidic setup and the substrate with the cell-laden hydrogel was carefully retrieved from the chip.

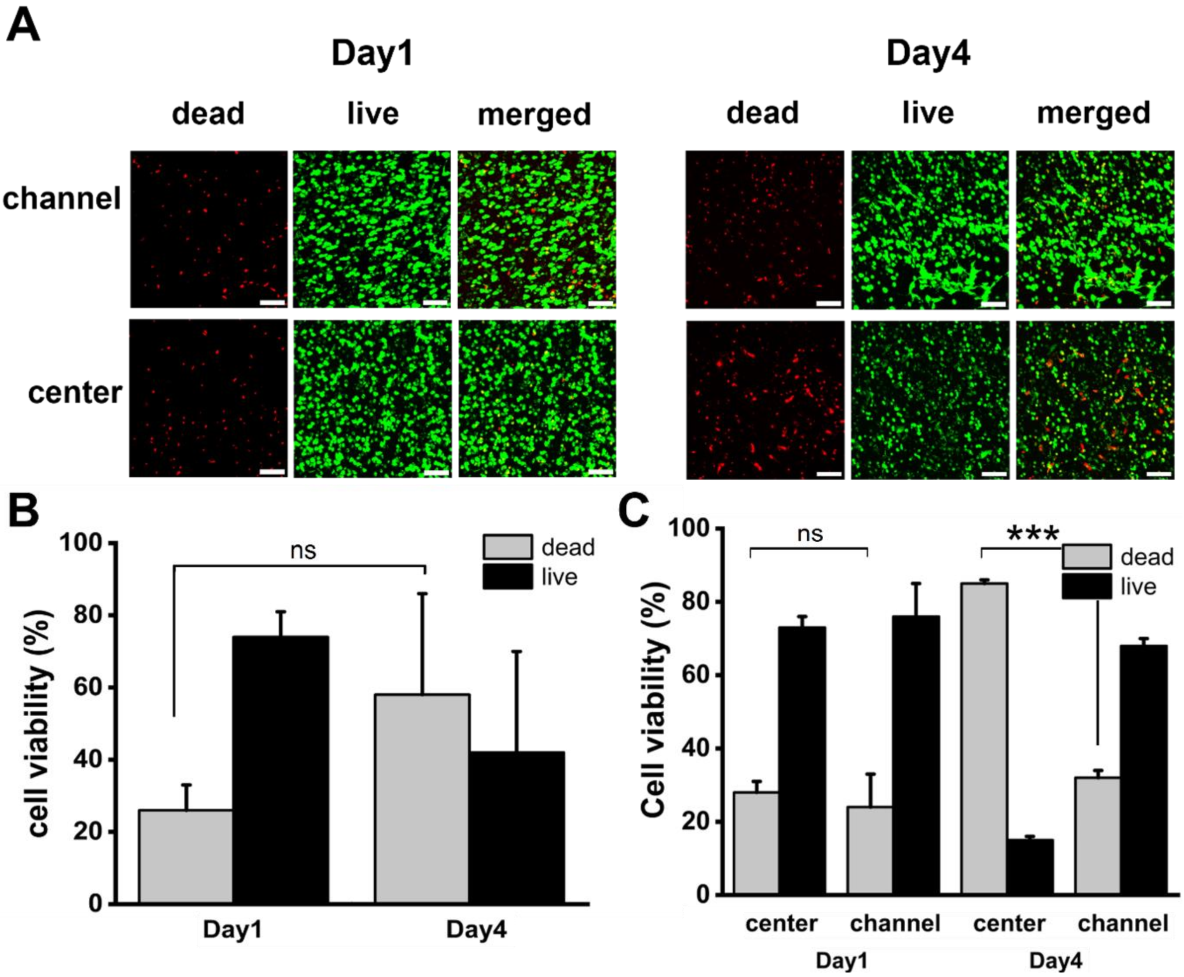

Figure 4.12: *Cell viability in cell-laden hydrogel channels under flow. (A) Maximum intensity projections of encapsulated 3T3 fibroblasts in regions close to the edges and center of the hydrogel at day 1 and 4 after cell culture on-chip obtained from Live/Dead™ assays. Scale bar: 100 µm. (B) Quantification of cell viability after days 1 and 4 under dynamic cell culture conditions. (C) Quantification of cell viability after days 1 and 4 at the central regions and edges of the hydrogel under dynamic cell culture conditions. Values are the mean percentage of cell viability ±SD (n≥2) *** indicates a statistical significance where p<0.0001.*

First assays were performed with hydrogel channels 500 µm thick and 2 mm wide for each side (total width: 5 mm). Central parts of the hydrogel, along with areas close to the channels, were imaged to compute the cell viability as the rate of live cells over the total number of cells. On day 1, low numbers of dead cells (red) could be observed both in the inner regions and edges of the hydrogel channels, where most cells were alive (green), resulting in cell viabilities of around 75 % (Figure 4.12 A (left) and 4.12 B). However, after 4 days under dynamic cell culture, most of the 3T3 fibroblasts embedded in the central parts of the hydrogel were dead, with cell viability around 15 % (Figure 4.12 A (right) and 4.12 C). Even though the proportion of viable cells in the areas near the channels was still high, total cell viability for the analyzed samples was below 45 % (Figure 4.12 B). This low rate of live cells in the inner regions of the gel could be explained by insufficient supply of oxygen and nutrients within the printed scaffolds. Even though medium was perfused continuously through all channels during the experiment, limitations of diffusive transport across the cell-laden hydrogel due to the geometry of the channels, with only two hydrogel lateral surfaces allowing nutrient and waste exchange, could explain the increased cell death in the most inner areas of the scaffold.

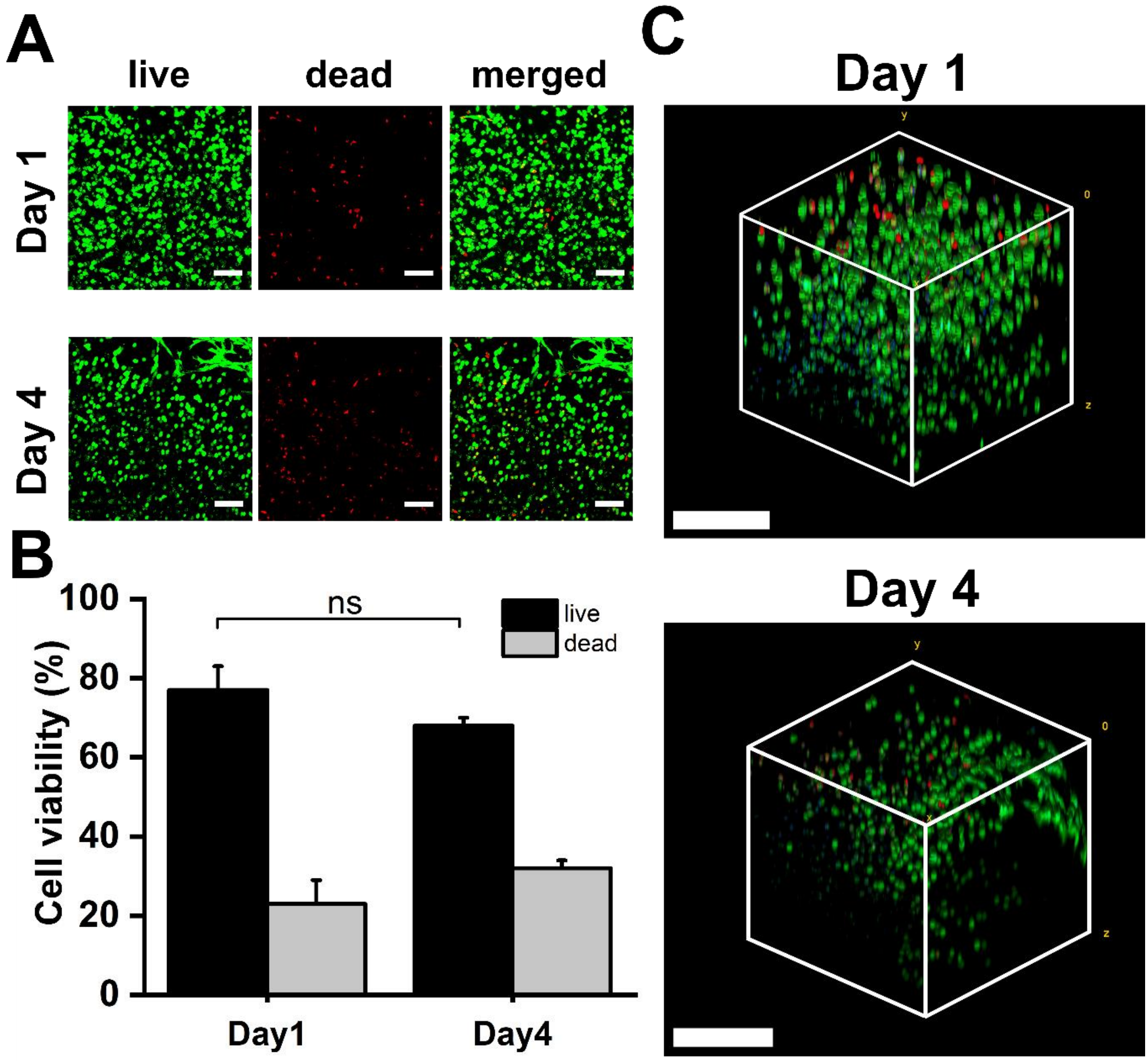

Figure 4.13: Cell viability in cell-laden hydrogel channels under flow with smaller widths. (A) Maximum intensity projections of encapsulated 3T3 fibroblasts at day 1 and 4 after cell culture on-chip obtained from Live/Dead™ assays. Scale bar: 100 µm. (B) Quantification of cell viability after days 1 and 4 under dynamic cell culture conditions. (C) 3D volume reconstruction of the 3T3 cell-laden hydrogels shown in (A). Scale bar: 250 µm. Values are the mean percentage of cell viability ±SD (n=3).

To improve the transport of oxygen and nutrients within the cell-laden hydrogels, the width of the rectangular-shaped scaffolds was reduced from 2 mm to 1 mm. After 24 hours under cell medium perfusion, most of the 3T3 cells were homogenously distributed and still alive, with cell viability rates close to 80 % (Figure 4.13 A and B). Also, some cells started to spread on the surface and edges of the hydrogel channel (Figure 4.13 C, top), in accordance with previous observations in static conditions [5,14]. After 4 days in dynamic cell culture, a slight decrease of viable cells compared to day 1 was observed, but this difference had no statistical significance and the cell viability rate was still very high, reaching 70 % (Figure 4.13 B). Also, 3T3 fibroblasts migrated towards the surfaces of the hydrogel lateral walls and most of them were spread (Figure 4.13 C, bottom). This migration could be explained by mass transport dynamics across the hydrogel walls, generating spatial gradients of oxygen and medium concentration that induced cell movement towards the edges. Nevertheless, cells in the inner regions also showed higher cell viability rates than with the previous design, demonstrating the positive effect of reducing the width of the hydrogels. Moreover, it is important to point out that, while the cell viability was high for on-chip cell culture, this was slightly lower when compared to previous 3D *in vitro* models with the same cell-laden bioinks in static conditions. In this case, cell viability rates were 93 % on day 1 and 86 % on day 7 [14]. This difference could be attributed to the mechanical stress induced on the cell-laden hydrogel channels during the chip assembly. As the printed scaffolds are slightly compressed by the clamping system, the encapsulated cells are subjected to these forces, thus negatively affecting their viability.

Overall, these results showed that our 3D hydrogel channels can support the cell culture of embedded stromal cells under fluid flow in the microfluidic device, proving their suitability for 3D gut-on-chip models.

4.2.3. Caco2 cell attachment and epithelial barrier formation on cell-laden hydrogel channel under dynamic conditions

After assessing the cell viability of stromal cells in the hydrogel channel under dynamic conditions, we combined the cell encapsulation of 3T3 fibroblasts with the cell co-culture of Caco-2 cells on the hydrogel to recapitulate the compartmentalized structure of the intestinal mucosa in our 3D gut-on-chip model. NIH-3T3 fibroblasts were mixed with the previously mentioned PEGDA-GelMA bioink at a density of $7.5x10^6$ cells/mL, and hydrogel channels with lateral villi-like structures were bioprinted using the optimized printing parameters. After the printing process, the cell-laden hydrogel channel was allocated in the chip and the embedded fibroblasts were cultured under flow (5 µL/min) with a peristaltic pump system for 3 - 4 days. During this time, 3T3 cells could migrate towards the hydrogel lateral walls to better support the formation of an epithelial barrier by secretion of ECM proteins, as observed in previous studies [5,14]. Following this, the device was disconnected from the microfluidic setup and Caco-2 cells were seeded on the central channel with a density of 10^7 cells/mL ($7.5*10^5$ cells/cm^2). To improve cell attachment to the hydrogel walls, the chip was placed vertically and kept in static conditions for 2 h on each side. Once seeding was completed, the chip was repositioned horizontally and reconnected to the pump setup. Caco-2 cells were cultured under continuous perfusion for 14 days. The flow rate of lateral channels was kept to 5 µL/min to support the cell culture of hydrogel-embedded 3T3 cells while the fluid flow in the central channel was set to 5 - 10 µL/min to obtain optimal shear stress values for epithelial cell growth on-chip (0.01 - 0.025 dyn/cm^2).

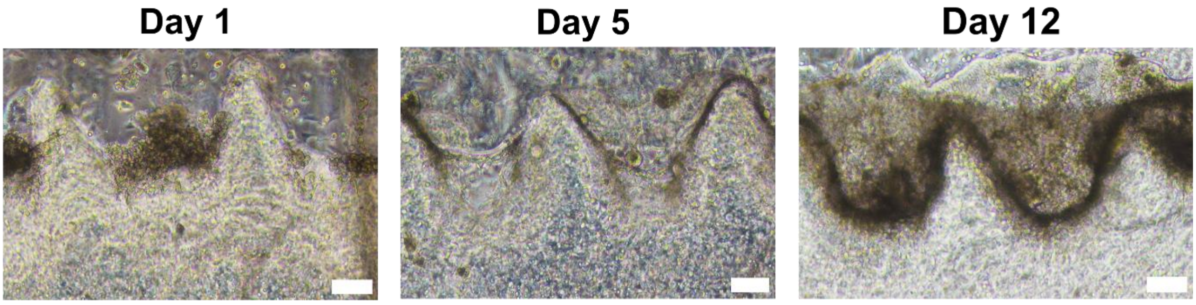

Figure 4.14: *Epithelial barrier formation in the bioprinted 3D gut-on-chip. Brightfield images of Caco-2 cells forming a cell barrier on a section of the villi-shaped lateral wall from day 1 to day 12 post-seeding. Scale bar: 200 µm.*

In Figure 4.14, top brightfield images of the cell-laden hydrogel channel show Caco-2 cells growing on the villi-shaped walls with the encapsulated 3T3 fibroblasts under perfusion at different days. On day 1 after epithelial cell seeding, most of the epithelial cells remained clustered in between the villi structures. From day 5, Caco2 cells started to partially cover the hydrogel walls, and after 12 days of cell co-culture in the chip, the epithelial cells fully covered the surface of the hydrogel walls along the central channel. Remarkably, epithelial cells could not form uniform barriers in the regions where the 3T3 fibroblasts were not present on the edges of the hydrogel walls, highlighting the importance of the stromal-epithelial cross-talk for the barrier formation.

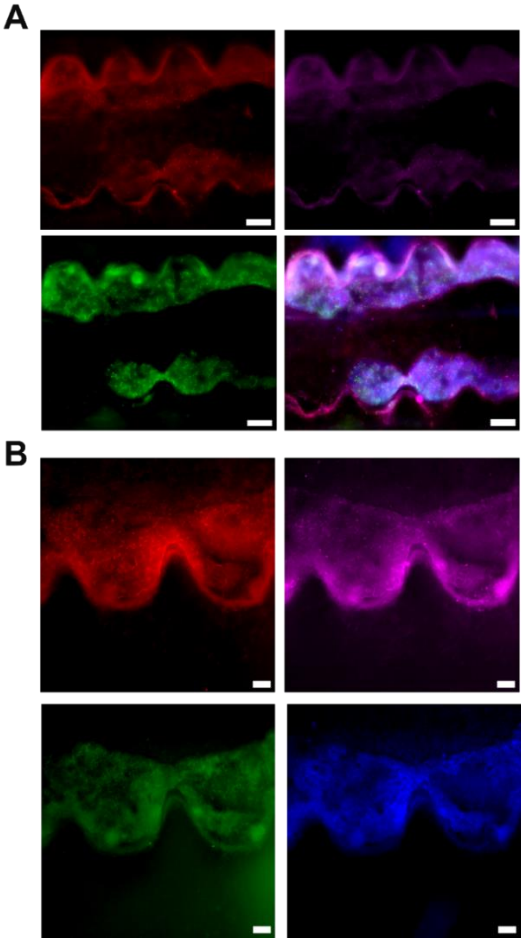

Figure 4.15: *Fluorescence imaging of the stromal and epithelial compartments in the 3D bioprinted gut-on-chip model. (A) Maximum projections from fluorescence microscopy images of the central channel*

with the formed epithelial barrier in the chip after 14 days in cell culture. F-actin is stained in red, ZO-1 in green, β-catenin, in magenta and nuclei, in blue. A merged composition of all markers is shown in the bottom right image. Due to the cell growth of the 3T3 fibroblasts on the bottom PET substrate before epithelial cell seeding, Caco2 cells could not fully cover the plastic substrate. Scale bar: 500 µm. (B) Fluorescence images of the epithelial cells and hydrogel-embedded fibroblasts on a section of the channel. Scale bar: 100 µm.

To assess the presence of an intestinal epithelial barrier covering the 3D cell-laden hydrogel channel, immunostainings were performed inside the chip. After 14 days of dynamic cell culture, the device was disconnected from the microfluidic setup and a syringe pump was used to perform the immunofluorescence assay, perfusing the different buffers through the microfluidic channels of the chip. Once completed, the chip was imaged first with a fluorescence microscope. Tile imaging of the full hydrogel channel showed expression of tight junction and adherens junction markers ZO-1 and β-catenin along the lateral villi-shaped walls and in certain areas of the bottom substrate (Figure 4.15 A and B), indicating the presence of an epithelial barrier on-chip. Following this, the substrate with the stained hydrogel channel was carefully retrieved for confocal imaging for higher resolution. With respect to the embedded fibroblasts, accumulation of F-actin marker on the hydrogel wall showed that most 3T3 fibroblasts were localized and spread on the boundaries of the hydrogel, in direct contact with the Caco2 cells, with much fewer fibroblasts inside the hydrogel than in the first days after printing. Top confocal stacked images of Caco2 cells also showed expression of β-Catenin and ZO-1, with strong staining signals lining the villi-shaped lateral surfaces of the hydrogel (Figure 4.16 A). A 3D volume reconstruction of the imaged sample confirmed the presence of these cell-cell junction markers along the vertical wall of the hydrogel channel (Figure 4.16 B). Also, it was also observed that collagen IV, a functional marker of the fibroblasts, was expressed by the 3T3 cells and found in surrounding areas close to the channel, suggesting stromal cells were capable to secrete these proteins, thus contributing to ECM remodeling and improving epithelial cell attachment (Figure 4.16 C).

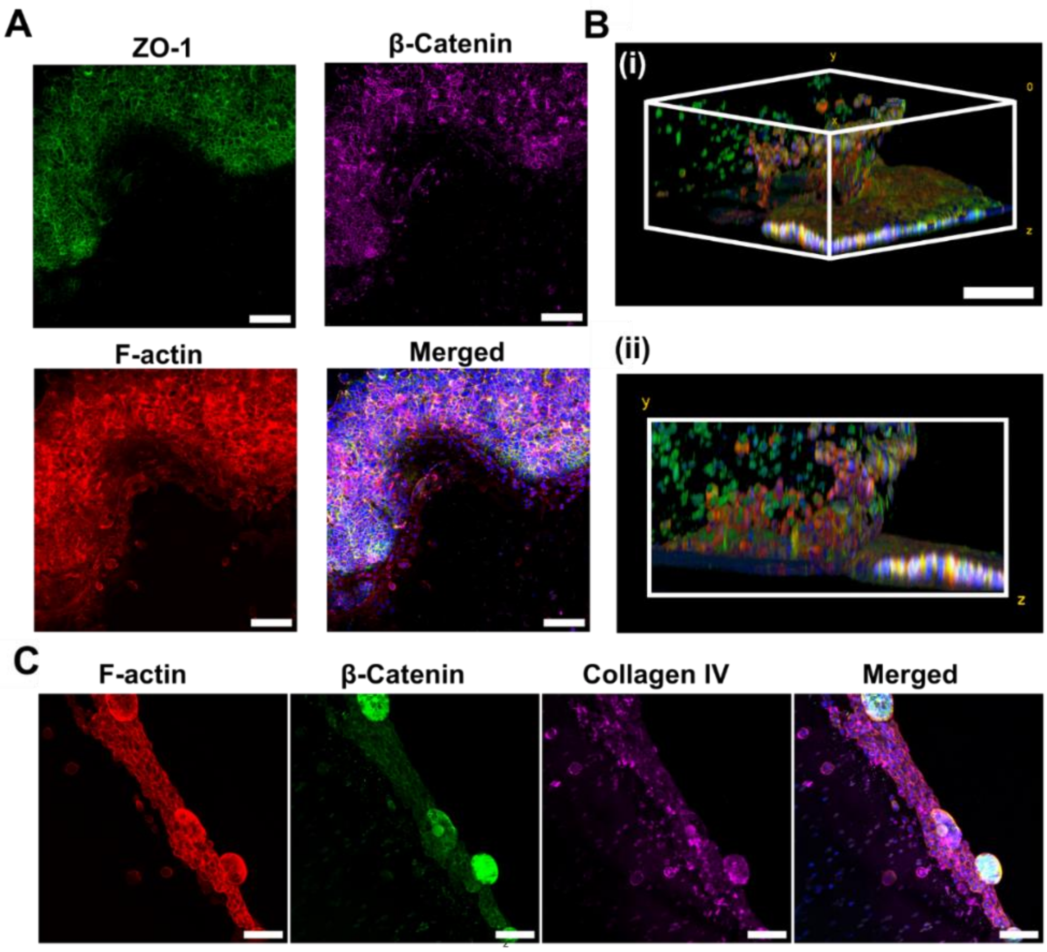

Figure 4.16: *Confocal imaging of the stromal and epithelial compartments in the 3D bioprinted gut-on-chip model. (A) Maximum intensity confocal projections of immunostainings for ZO-1 (green), β-Catenin (magenta) and F-actin (red) of the co-cultured fibroblasts and epithelial cells on a villi-like shaped section of the hydrogel channel. DAPI was used to stain the nuclei. The image on the bottom right shows a merged display of all the markers. All simples were stained after 14 days of cell culture. Scale bar: 100 µm. (B) Confocal 3D reconstructions of the stained sample (β-Catenin in green, F-actin in red) with (i) a perspective view (top image) and (ii) a lateral view (bottom image). Scale bar: 200 µm. (C) Expression of collagen IV (magenta) by 3T3 fibroblasts and β-catenin (green) by Caco2 epithelial cells on the hydrogel central channel. Actin filaments are stained in red and nuclei, in blue. Maximum intensity projections are shown for all markers. The image on the right shows a merged display of all the markers. Scale bar: 100 µm.*

From these results, we proved the ability of our hydrogel 3D gut-on-chip system to support the dynamic cell co-culture of stromal and epithelial cells within a compartmentalized structure that mimics key spatial features of the *in vivo* intestinal mucosa.

4.2.4. Permeability characterization of the Caco2 cell barrier

To assess the integrity of the epithelial cell barrier in the 3D bioprinted gut-on-chip, we first quantified the apparent permeability P_{app} of the Caco2 cell barrier with 3T3 fibroblasts encapsulated in rectangular-shaped hydrogel channels. After 14 days of cell co-culture under dynamic conditions, the central channel of the microfluidic chip was perfused continuously (10 µL/min) with a red fluorescent 70 kDa rhodamine-dextran solution for 90 min under a high-resolution fluorescence microscope, where images were taken at the central region of the chip to observe the radial diffusion gradient across the hydrogel (Figure 4.17 A). Permeability experiments with hydrogels without cells were also performed as controls.

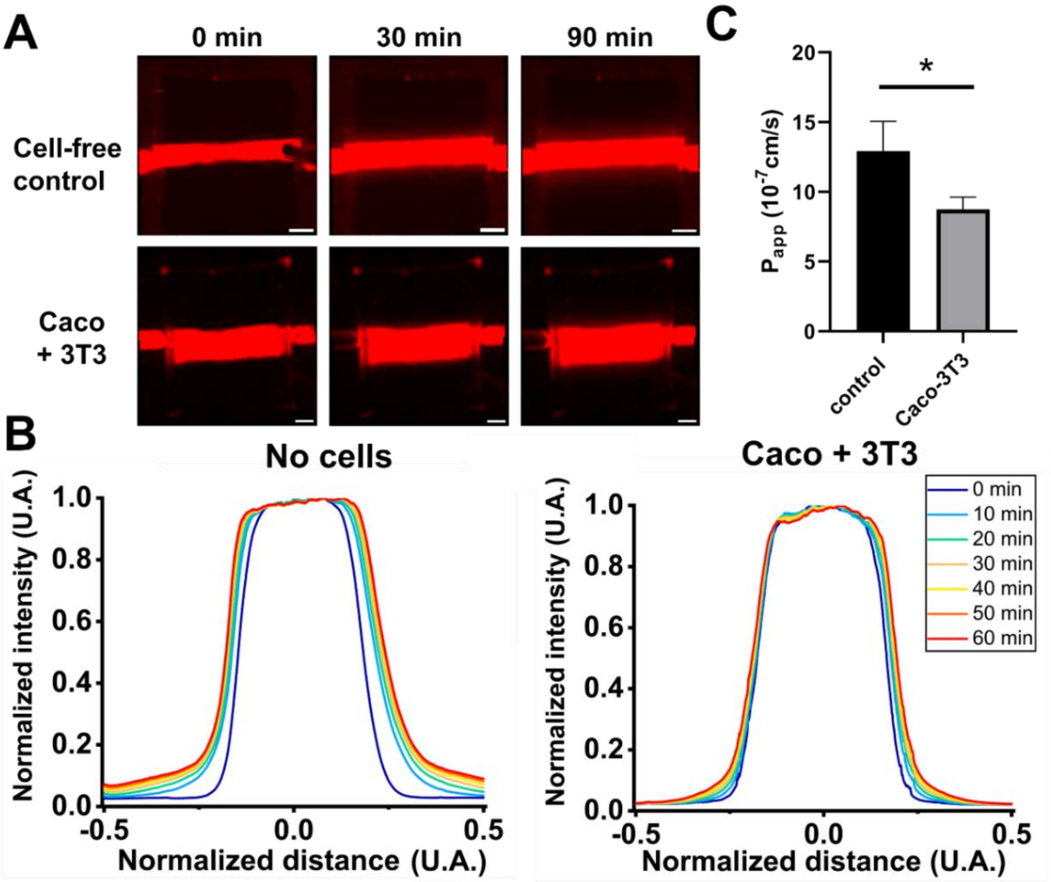

Figure 4.17: *Apparent permeability of the epithelial barrier formed on the stromal cell-laden hydrogel channel in the 3D gut-on-chip. (A) Fluorescent images of the central channel perfused with Rhodamine-Dextran 70 kDa (FD70) with an epithelial barrier (Caco-3T3) and hydrogel only (control) at time 0, 30 min and 90 min. Scale bar: 1 mm. (B) Fluorescence intensity profiles across the central channel with and without a Caco-2 cell barrier. The displayed graphs represent different time points up to 1h. (C) Apparent permeability* P_{app} *of FD70 for epithelial barriers grown on the hydrogel channels with encapsulated fibroblasts under flow (Caco-3T3) and for cell-free hydrogel channels (control). Values are mean ± SD (n=3) * indicates a statistical significance where* $p<0.05$.

Figure 4.17 B shows the normalized fluorescence intensity profiles across the central perfusion channel and the hydrogel at different time points for both the control and the 3D multicellular intestinal model. In the regions of the hydrogel closer to the central channel, a significant increase of fluorescence intensity can be observed for the cell-free control while this increase appears slower and more moderate for the gut-on-chip. From these plots, apparent permeability values were extracted by computing the average fluorescence values in the regions of interest, showing a lower permeability for the Caco2 epithelial barriers formed on the 3T3 cell-laden hydrogels compared to the control samples (Figure 4.17 C). These lower P_{app} values are associated to a higher restriction of the paracellular transport of fluorescent markers through the tight junctions, in accordance with previous studies of *in vitro* intestinal permeability on PEGDA-GelMA hydrogel constructs [5]. Overall, these results suggest the presence of an epithelial barrier formed on the fibroblast-laden hydrogel channel within the 3D gut-on-chip model.

4.3. Discussion

Several studies have highlighted the important role of the stromal-epithelial cell cross-talk in the integrity and function of the intestinal barrier [18,19]. With the combination of cell-laden hydrogels with gut-on-chip devices, some groups have successfully recapitulated the compartmentalized architecture of the intestinal mucosa by co-culturing mesenchymal and epithelial cells on scaffolds that mimic the intestinal villi and crypts [20,21]. However, the required fabrication techniques to generate these 3D hydrogels are often time-consuming, expensive, and unsuitable for high-throughput applications. With our approach based on DLP-SLA bioprinting, we could generate cell-laden hydrogel channels with villi-like features in a fast and reliable manner. Using a biocompatible GelMA-PEGDA bioink, fibroblasts representing the stromal compartment were encapsulated in the hydrogel channel for cell culture on-chip, resulting in high cell viability rates under flow conditions. As observed before with this bioink [14], the hydrogel-embedded stromal cells migrated towards the surface of the scaffold, promoting the attachment of the intestinal epithelial cells by secreting ECM proteins, and boosting the formation of a continuous epithelial cell barrier for two weeks under continuous perfusion.

The presented 3D bioprinted hydrogel gut-on-chip system is also compatible with standard barrier characterization assays. By performing permeability assays in our hydrogel gut-on-chip model, we could validate the presence of a full barrier, in accordance with previous studies in static conditions [5]. As conventional drug screening studies based on *in vitro* models rely on this type of assays, our gut-on-chip could be easily used as a suitable platform to test the effect of compounds on the integrity of the intestinal epithelial barrier [22].

4.4. References

1. Hynds, R. E., Bonfanti, P. & Janes, S. M. Regenerating human epithelia with cultured stem cells: feeder cells, organoids and beyond. *EMBO Mol Med* **10**, 139–150 (2018).
2. Artursson, P., Palm, K. & Luthman, K. Caco-2 monolayers in experimental and theoretical predictions of drug transport. *Adv Drug Deliv Rev* **46**, 27–43 (2001).
3. Hubatsch, I., Ragnarsson, E. G. E. & Artursson, P. Determination of drug permeability and prediction of drug absorption in Caco-2 monolayers. *Nat Protoc* **2**, 2111–2119 (2007).
4. Delon, L. C. *et al.* A systematic investigation of the effect of the fluid shear stress on Caco-2 cells towards the optimization of epithelial organ-on-chip models. *Biomaterials* **225**, (2019).
5. Vila, A. *et al.* Hydrogel co-networks of gelatine methacrylate and poly(ethylene glycol) diacrylate sustain 3D functional in vitro models of intestinal mucosa. *Biofabrication* **12**, (2020).
6. Immunofluorescence Assays | Principle | ibidi. https://ibidi.com/content/364-the-principle-of-immunofluorescence-assays.
7. Rodgers, L. S., Tanner Beam, M., Anderson, J. M. & Fanning, A. S. Epithelial barrier assembly requires coordinated activity of multiple domains of the tight junction protein ZO-1. *J Cell Sci* **126**, 1565–1575 (2013).
8. Tian, X. *et al.* E-Cadherin/β-catenin complex and the epithelial barrier. *J Biomed Biotechnol* **2011**, (2011).
9. Tentaku, A. *et al.* Proximal deposition of collagen IV by fibroblasts contributes to basement membrane formation by colon epithelial cells in vitro. *FEBS J* **289**, 7466–7485 (2022).

10. Chazotte, B. Labeling nuclear DNA using DAPI. *Cold Spring Harb Protoc* **2011**, (2011).
11. Mahaffy, R. E. & Pollard, T. D. Influence of Phalloidin on the Formation of Actin Filament Branches by Arp2/3 Complex. *Biochemistry* **47**, 6460 (2008).
12. Brodin, B., Steffansen, B. & Nielsen, C. Passive diffusion of drug substances: The concepts of flux and permeability. in 135–151 (2010).
13. Palumbo, P. *et al.* A general approach to the apparent permeability index. *J Pharmacokinet Pharmacodyn* **35**, 235–248 (2008).
14. Torras, N. *et al.* A bioprinted 3D gut model with crypt-villus structures to mimic the intestinal epithelial-stromal microenvironment. *Biomaterials Advances* **153**, 213534 (2023).
15. Nicolas, A. *et al.* High throughput transepithelial electrical resistance (TEER) measurements on perfused membrane-free epithelia. *Lab Chip* **21**, 1676–1685 (2021).
16. Trietsch, S. J. *et al.* Membrane-free culture and real-time barrier integrity assessment of perfused intestinal epithelium tubes. *Nat Commun* **8**, (2017).
17. Costello, C. M. *et al.* Microscale Bioreactors for in situ characterization of GI epithelial cell physiology. *Sci Rep* **7**, 1–10 (2017).
18. Rowart, P., Erpicum, P., Krzesinski, J. M., Sebbagh, M. & Jouret, F. Mesenchymal Stromal Cells Accelerate Epithelial Tight Junction Assembly via the AMP-Activated Protein Kinase Pathway, Independently of Liver Kinase B1. *Stem Cells Int* **2017**, (2017).
19. Powell, D. W., Pinchuk, I. V., Saada, J. I., Chen, X. & Mifflin, R. C. Mesenchymal Cells of the Intestinal Lamina Propria. *Annu Rev Physiol* **73**, 213 (2011).
20. Verhulsel, M. *et al.* Developing an advanced gut on chip model enabling the study of epithelial cell/fibroblast interactions. *Lab Chip* **21**, 365–377 (2021).
21. Nikolaev, M. *et al.* Homeostatic mini-intestines through scaffold-guided organoid morphogenesis. *Nature* **585**, 574–578 (2020).
22. Almeida, H. *et al.* Cell-Based Intestinal In Vitro Models for Drug Absorption Screening. *Drug Discovery and Evaluation: Safety and Pharmacokinetic Assays* 1–22 (2022) doi:10.1007/978-3-030-73317-9_94-1.

5. A 3D bioprinted hydrogel gut-on-chip with integrated TEER sensing capabilities

As explained in chapter 2, electrodes have been integrated within conventional gut-on-chip devices via thin film deposition for real time TEER quantification during cell culture [1–3]. By placing them near the cell culture membrane, more uniform current densities can be obtained, thus ensuring reliable TEER readouts over the full epithelial monolayer. However, this approach has only been implemented for membrane-based microfluidic chips. To this day and to the best of our knowledge, no 3D hydrogel organ-on-chips have been developed to integrate electrodes for real time TEER quantification. In this chapter, we present a proof of concept of a bioprinted 3D gut-on-chip with integrated TEER sensors to assess in real time the formation of an intestinal epithelial barrier under perfusion. By placing the electrodes in close proximity to the cell culture area, the formation of the intestinal epithelial barrier inside the chip could be monitored under dynamic flow conditions for two weeks.

5.1. Materials and methods

5.1.1. Electrical sensitivity analysis

The spatial configuration of the electrodes within a microfluidic device plays a critical role in TEER quantification. Different groups have proposed various methods to quantify the electrical resistance of cell barriers on-chip, resulting in large discrepancies over the reported values [4,5]. These differences are often explained by the geometry and position of the electrodes, that determine the current density distribution across the cell monolayer. Depending on the chosen disposition, some areas of the cell barrier have a higher effect over the total impedance than others. To quantify the contribution of each to TEER, the electrical sensitivity s can be determined (see chapter 2) [6]. For a two-point measurement system, this variable is proportional to the current density between the two electrodes. Ideally, this value should be uniform and equal to 1 when normalized by the cell barrier area.

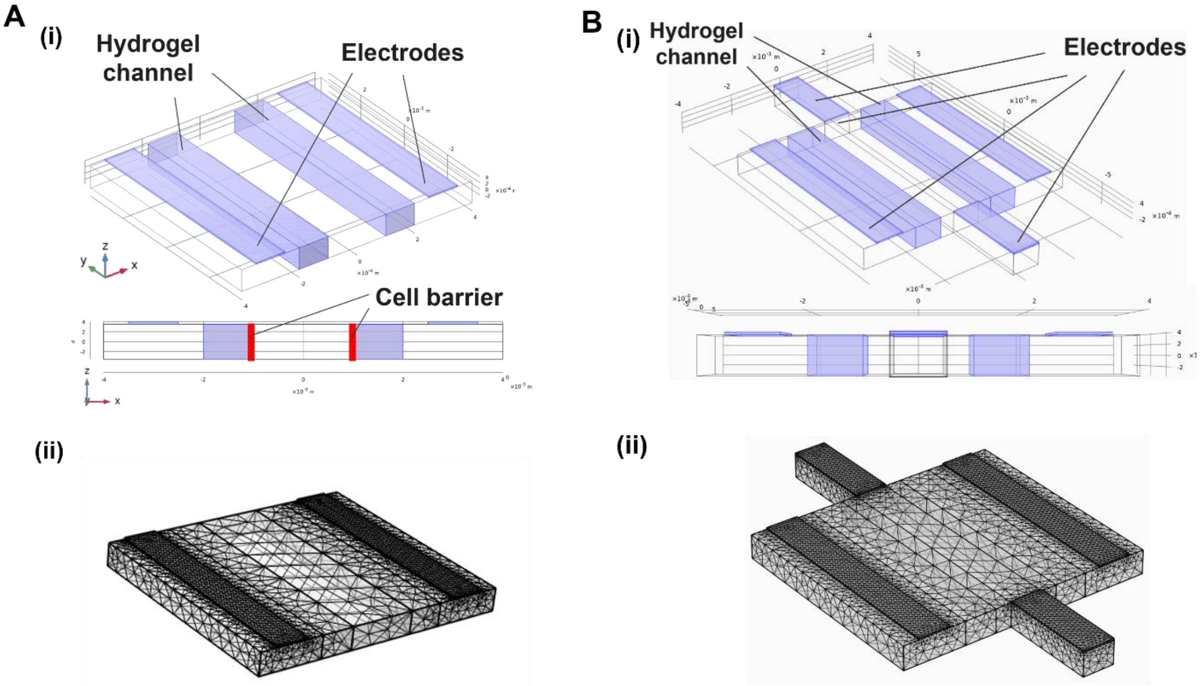

Figure 5.1: *Simulated electrode configurations for TEER quantification in the 3D hydrogel gut-on-chip. (A) (i) 3D drawing (top) and side view (bottom) of the chip with two electrodes placed at the lateral*

channels. (ii) Tetrahedral mesh of the two-electrode configuration. (B) (i) 3D drawing (top) and side view (bottom) of the chip with two electrodes placed at the lateral channels and two others at the inlet and outlet of the central channel. (ii) Tetrahedral mesh of the four-electrode configuration.

To evaluate the current density distribution across the central cell culture chamber with the integrated electrodes and identify potential TEER measurement errors, a 3D finite element method (FEM) study was performed on COMSOL Multiphysics 5.6 with the "Electric currents" interface within the AC/DC module. Two main coplanar electrode designs were simulated: a two-electrode configuration with each electrode covering the top part of each lateral channel (Figure 5.1 A), and a four-electrode configuration where two large electrodes were placed at the lateral channels and two smaller ones, at the inlet and outlet of the central channel (Figure 5.1 B). For the first design, each electrode worked either as a WE or CE and current flowed through the hydrogel channel, measuring the total TEER of cell barriers located on both walls of the central channel. In the second design, each lateral electrode acted as a WE while the two placed on the central channel worked as CE, allowing TEER quantification of the epithelial barrier on each side of the hydrogel channel. A rectangular hydrogel channel (width: 1 mm; length: 7 mm; height: 0.5 mm) was considered for the computations, and the cell barrier was modelled as a contact impedance with a given conductivity on each lateral wall of the central channel. Different TEER values were attributed to the cell barrier in the simulations, ranging from 10^0 to 10^3 Ω.cm^2 and covering the range of reported values in the literature. In the model, a constant DC current signal of 1A was injected through one of the electrodes while the other one was set as ground. The rest of the outer boundaries were defined as electrical insulators. All relevant parameters of the simulation are summarized in Table 5.1. The electrical sensitivity was calculated from the computed current densities across the hydrogel channel using the previously described equation (see chapter 2) to determine which areas of the cell barrier contribute the most and the least for each TEER value. These values were normalized by the cell barrier area. When the normalized sensitivity was close to 1 and uniform over the cell barrier area, the electrode configuration would ensure a homogenous current density distribution and an accurate TEER measurement within the device.

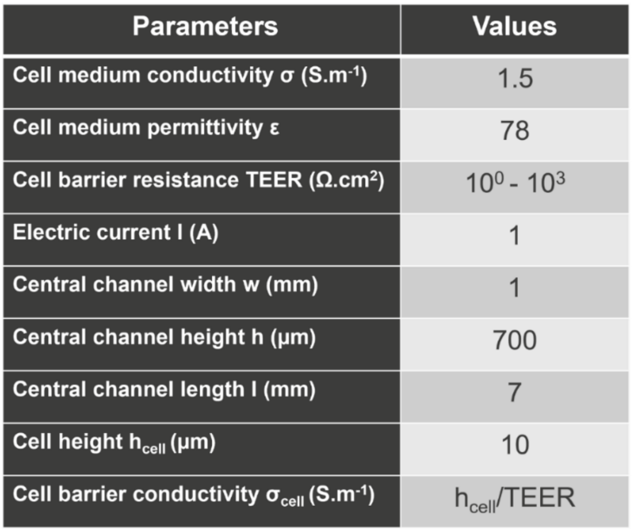

Parameters	Values
Cell medium conductivity σ (S.m^{-1})	1.5
Cell medium permittivity ε	78
Cell barrier resistance TEER (Ω.cm^2)	10^0 - 10^3
Electric current I (A)	1
Central channel width w (mm)	1
Central channel height h (µm)	700
Central channel length l (mm)	7
Cell height h_{cell} (µm)	10
Cell barrier conductivity σ_{cell} (S.m^{-1})	h_{cell}/TEER

Table 5.1: *Parameters used for the electrical sensitivity simulations.*

5.1.2. Fabrication of platinized Au electrodes for on-chip TEER monitoring

5.1.2.1. *Ti-Au electrode fabrication*

To integrate the coplanar electrodes in our microfluidic chip, a 180 mm diameter plastic COP foil (125 µm, Topas; ChipShop) was initially cut with a cutting plotter (CAMM-1 Servo GX-24; Roland) and used as a substrate. An adhesive vinyl shadow mask with electrode patterns was also cut with the plotter and attached to the COP foil (Figure 5.2 A). Following this, a 20/200 nm Ti/Au bi-layer was deposited on the plastic substrate by e-beam evaporation (Figure 5.2 B) [7,8]. The Ti layer was used to improve the bonding between Au and the plastic substrate. The COP foil was then cut into 40 x 25 mm rectangles matching the dimensions of the chip with all the inlets and outlet holes, and the shadow mask was then removed (Figure 5.2 A). A double-sided PSA (ArCare® 92712, Adhesives Research) was then bonded and used as a passivation layer for the electrodes. Later, electric wires and pin connectors were soldered with tin-lead to connect the chip to the electrical equipment. Silver paste was added to ensure a good connection at the bond pad area by thermally curing it at 80ºC for 30 min. Finally, the silver layer was covered with an epoxy resin that was cured with a UV lamp (70 mW/cm^2) for 30 s to prevent chemical oxidation in the incubator.

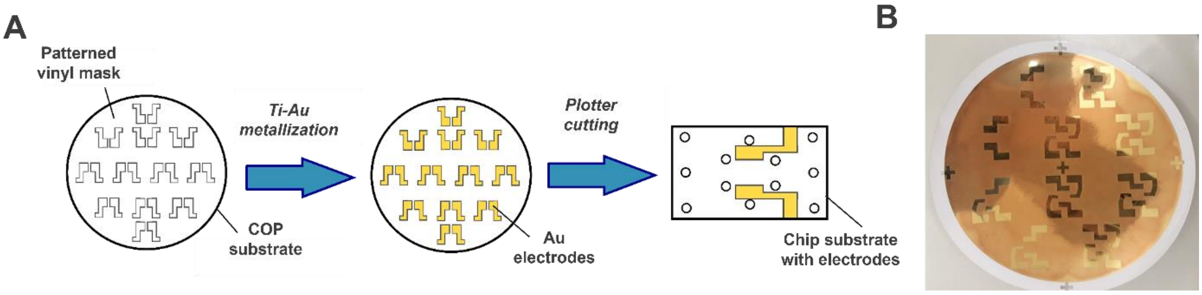

Figure 5.2: *Metallization of patterned electrodes on the chip substrate. (A) Schematic of the Au electrode fabrication and cutting of the chip substrate. (B) Image of the plastic COP wafer with the deposited Ti and Au layers defined by the vinyl shadow mask.*

5.1.2.2. *Platinization of Au electrodes*

Au is one of the most popular materials for the fabrication of electrodes due to its high electrical conductivity, biocompatibility, and high chemical stability. Within the organ-on-chip field, several groups have integrated Au electrodes within their microfluidic devices via thin film deposition for real-time TEER monitoring of cell barriers [1,9]. However, Au has a relatively high polarization impedance, which can have a negative effect on the measurements for two-point configurations. Due to this, several approaches have been proposed to reduce the polarization impedance of the electrode. One of them consists in generating porous or granulated Au thin layers that can increase the total surface area, thus reducing the capacitive effect at the interface between the electrode and the electrolyte [10,11]. Another approach is based on the coating of the surface of Au electrodes with black Pt. In this case, Pt is deposited on the surface of the WE with an electrochemical reaction, generating a rough surface. With this technique, the polarization impedance of Au electrodes can be highly reduced in the lower frequencies, improving their sensitivity and the accuracy of the cell barrier resistance measurements [8].

Following a previously described protocol in our group [12], electrochemical deposition on the patterned Au electrodes with black Pt was performed to reduce their polarization impedance

(Figure 5.3 A). A black platinum chloride solution containing hydrochloric acid 0.1 M, 2.3 % platinum (IV) chloride, and 0.023 % lead (IV) 99 % acetate was first sonicated for 30 min in a water bath at room temperature. After this, the solution was placed on top of the electrodes surface. An Ag/AgCl reference electrode (RE) and a Pt CE (Radiometer Analytics) were immersed in the platinum chloride solution with the Au electrodes (WE) (Figure 5.3 B). The three electrodes were connected to a potentiostat (Solartron SI 1287) and a potential of -0.2 V was applied during 30 s (CorrWare software) to generate the electrochemical reaction. Finally, the Pt black solution was removed, and the electrodes were rinsed with PBS to remove unreacted Pt residues.

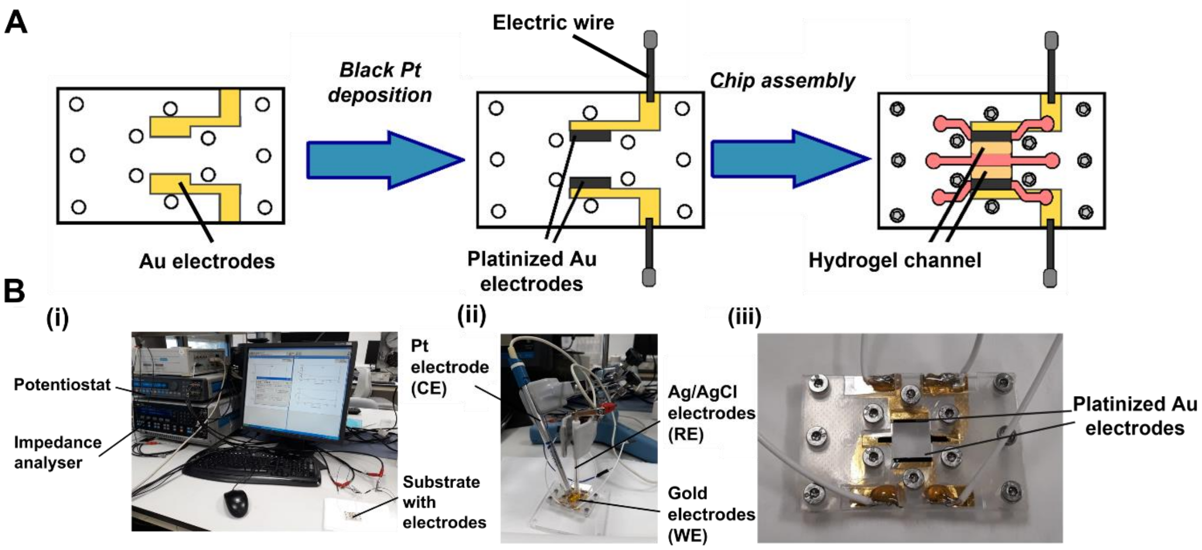

Figure 5.3: *Black Pt coating of the Au electrodes. (A) Schematic of the platinization and chip assembly process. (B) Platinization setup. (i) Image of the electrical setup with the potentiostat. (ii) Image of the electrochemical setup for black Pt deposition. (iii) Image of the black Pt-coated Au electrodes on the chip substrate.*

5.1.2.3. Electrode characterization and integration on-chip

Different types of impedance-based tests were performed on the electrodes after fabrication. The polarization impedance of the Au electrodes was first characterized before and after black Pt deposition via EIS. To do that, a drop of PBS 10 mM (ThermoFisher) was first pipetted on top of the coplanar electrodes. The pair was connected to an impedance analyzer (Solartron SI 1260) as working and counter electrodes. An AC voltage signal of 10 mV was then applied at selected frequencies in the range between 10^0 Hz and 10^6 Hz to obtain the impedance spectra using the ZPlot software. Once the measurements were completed, the resulting curves were compared to evaluate the effect of the platinization on the properties of the electrodes.

Moreover, the responsivity of the electrodes to solutions with different electrical conductivities was assessed by calculating the cell constant K_{cell}. This parameter can be determined by measuring the electrical resistance of an electrolyte solution:

(eq. 5.1) $K_{cell} = R_{meas} * \sigma$ (in m^{-1})

Where R_{meas} is the measured electrical resistance of the electrolyte (in Ω) and σ, the electrical conductivity of the solution (in S/m). First, a PBS 10 mM solution was serially diluted up to a concentration of 0.625 mM. A conductivity meter (EC-Meter GLP31, Crison Instruments) was then used to measure the conductivity of each diluted sample. Following this, a drop of each solution with different molarities was placed on top of the platinized Au electrodes and the impedance of the solutions was quantified via EIS from 10^0 Hz to10^6 Hz (Solartron SI 1260). The respective conductivity and measured resistance of each sample were plotted, and the cell constant of the electrode pair was extracted via linear regression analysis (Microsoft Excel). Moreover, a theoretical $K_{cell,th}$ can be described by the following formula:

$$\textbf{\textit{(eq. 5.2)}}\ K_{cell,th} = \frac{l}{A}\ \text{(in m}^{-1}\text{)}$$

Where A is the surface area of the electrodes (in m^2), and l is the distance between the electrodes (in m). The measured K_{cell} was compared to the theoretical value to assess the uniformity of the current density for the studied electrode configuration.

Once the electrodes were validated, the patterned chip substrate was bonded to the rest of the middle component of the chip with the same double-sided PSA used for their passivation. The plastic COP piece with the defined channels was slightly modified to accommodate the bond pad regions where the wires were soldered. The chip pieces with the integrated electrodes were stored in protective boxes to prevent their scratching before the experiments.

5.1.3. Characterization of the epithelial barrier integrity via TEER measurements in the 3D bioprinted gut-on-chip

5.1.3.1. Experimental setup

Prior to the experiment, the middle piece with the integrated electrodes was sterilized by UV light exposure for 30 min in the laminar hood. The rest of the components of the chip and the microfluidic setup were placed in tip boxes and autoclaved at 110ºC or 121ºC. Following the procedure previously described in chapter 4, PEGDA-GelMA hydrogel channels with rectangular shapes were initially bioprinted with encapsulated NIH-3T3 fibroblasts at a cell density of $7.5*10^6$ cells/mL. Afterwards, the cell-laden hydrogels were encased in the central chamber of the microfluidic chips and the devices were connected to the microfluidic setup for continuous medium perfusion at a flow rate of 5 µL/min for dynamic cell culture during 3 or 4 days (Figure 5.4 A). After this time, Caco-2 cells were seeded in the central channel with a cell density of $7.5*10^5$ cells/cm^2 (10^7 cells/mL) and the chips were placed vertically on each side in the incubator for 2 h each time to facilitate cell attachment to the hydrogels. Once the seeding was completed, the chips were connected both to the peristaltic pump for medium perfusion and to the impedance analyzer (PalmSens 4) to start the EIS-based TEER monitoring of the forming epithelial barrier (Figure 5.4 B and C). The device was connected via Bluetooth to a desktop computer for real time visualization of the impedance measurements. Cells inside the chip were cultured with a flow rate of 5-10 µL/min for 14 days, during which electrical impedance was measured periodically. Visual inspection of the cells was performed every 2 - 3 days with an optical microscope and medium from the reservoirs was replaced every 5 - 6 days.

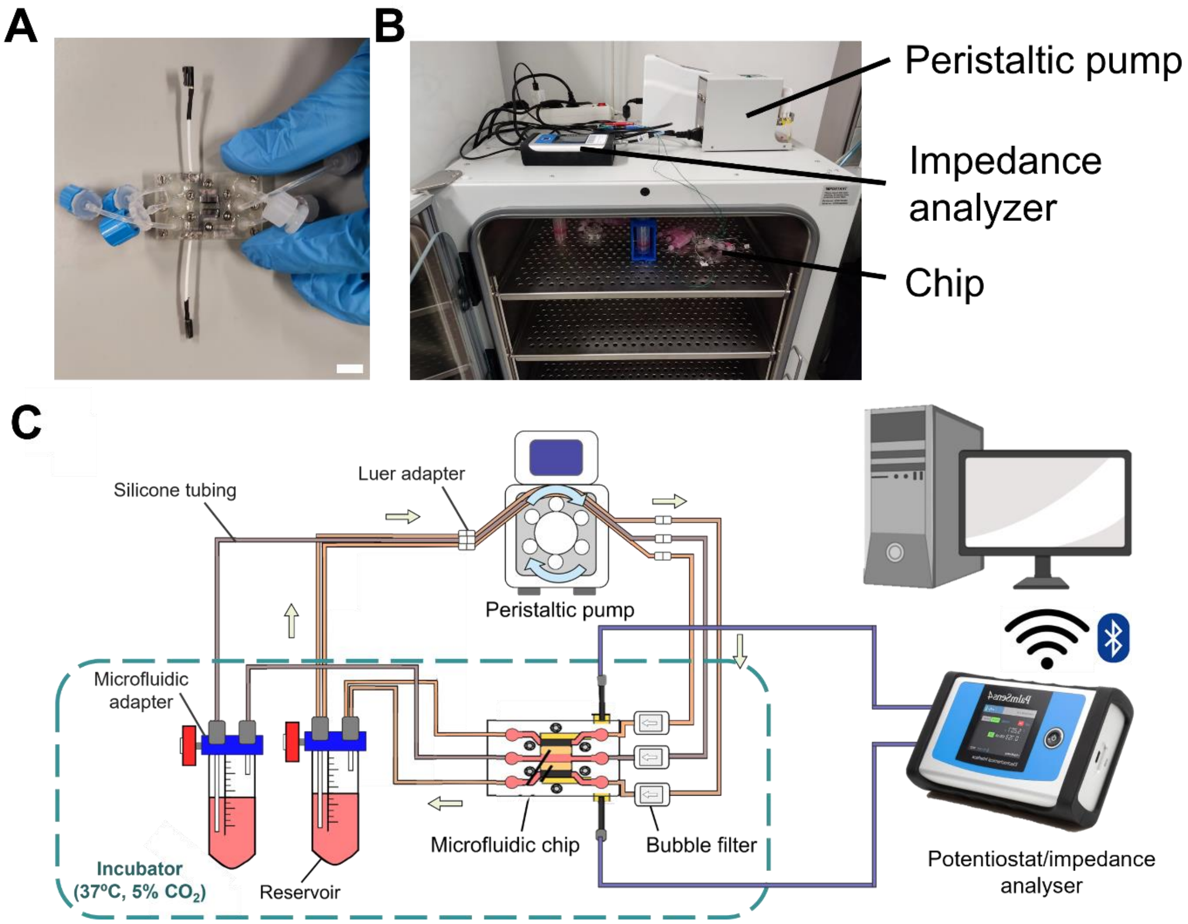

Figure 5.4: *Experimental setup for TEER monitoring in the 3D bioprinted gut-on-chip. (A) Image of the microfluidic device with the integrated electrodes. (B) Image of the complete setup, where chips, tubing and reservoirs are placed inside of the incubator, while the peristaltic pump and the potentiostat/impedance analyzer are placed outside for medium perfusion and TEER quantification respectively. (C) Schematic view of the experimental setup. Impedance data were transferred in real time to a dedicated desktop computer.*

5.1.3.2. TEER quantification of the epithelial barrier

To quantify the integrity of the epithelial cell barrier, TEER measurements were performed in real time during cell culture on-chip. The integrated platinized Au electrodes were connected to a commercial potentiostat (PalmSens 4) in a two-point configuration. An AC voltage excitation signal of 10 mV was applied to measure the total impedance. Impedance spectra were recorded in the frequency range between 10 Hz to 1 MHz via EIS in time intervals of 15 or 30 min. To visualize the evolution of the impedance, Bode plots of the impedance magnitude and phase were plotted by the software.

The measured data were then analyzed to extract the main electrical parameters of the cell barrier, the trans-epithelial electrical resistance TEER and the cell layer capacitance C_{cl}. To do that, an equivalent electrical circuit was used to fit the data to a theoretical model. In this model, a resistance representing TEER is placed in parallel with a CPE representing the cell layer capacitance, both in series with the cell medium resistance R_s (Figure 5.5 A) [13,14]. The electrical equivalent model fitting was performed in the range between 10^2 and 10^5 Hz using a least-squares regression method (PSTrace software). Within these frequencies, the resistive and capacitive behavior of the cell barrier dominates over the electrode impedance and the resistance of the cell medium (Figure 5.5 B). After fitting, the cell layer capacitance was determined as follows:

$$\textbf{\textit{(eq. 5.3)}}\ C_{cl} = \frac{(K*TEER)^{\frac{1}{\alpha}}}{TEER}\ \text{(in µF)}$$

Where K is the admittance of the CPE and α is the exponent of the CPE. Both TEER and C_{cl} were normalized by the area of the cell barrier to compare them to other values reported in the literature.

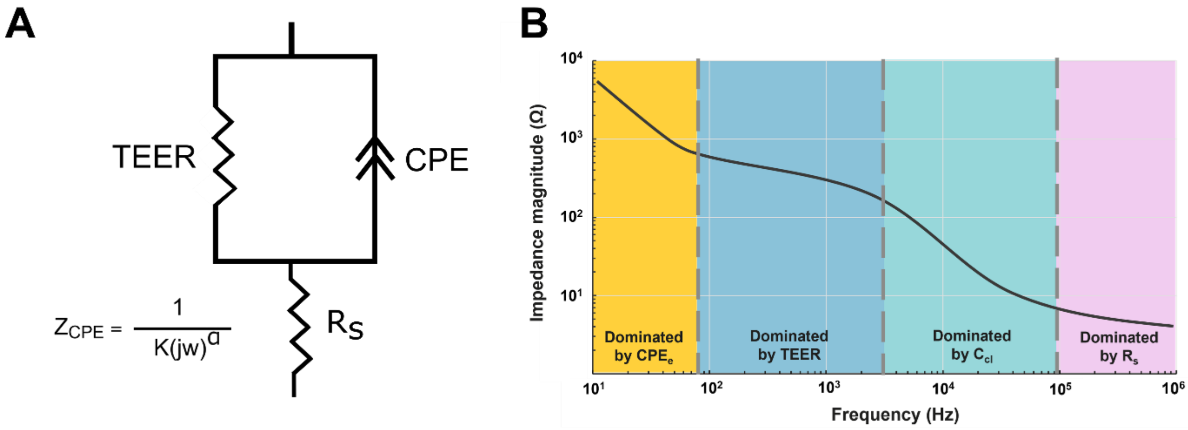

Figure 5.5: *TEER quantification via equivalent electrical model fitting. (A) Schematic of the used equivalent electrical circuit for the fitting of impedance data. (B) Example of Bode impedance magnitude spectrum where each area of the plot is linked to the dominating electrical element of the model.*

5.1.3.3. Barrier disruption assay

The recovery of the epithelial barrier upon chemical disruption was assessed with ethylenediaminetetraacetic acid (EDTA). EDTA acts as a chelating agent that removes extracellular calcium Ca^{2+} ions from the cell medium, inducing the disruption of intercellular junctions and increasing the permeability of the barrier [15,16]. This effect on the epithelial cell barrier can be observed via TEER monitoring, with a rapid decrease of the resistance due to the breakdown of the tight junctions [17]. Upon removal of EDTA, the rupture of the tight junctions is reversed, and the barrier can be recovered, which translates into a new increase of TEER over time [18].

To perform the barrier disruption assay, 10 mM EDTA (Sigma-Aldrich) diluted in DMEM cell medium was perfused in the central channel where the epithelial barrier was formed after 14 days of dynamic cell culture in the gut-on-chip. A dedicated in-line luer injection port (Ibidi) was connected to the inlet port and the Ca^{2+} chelating agent was loaded with a 1 mL syringe into the flowing cell medium. EDTA was then perfused through the channel for 5 min. During this time, TEER values were recorded every 30 s to closely follow-up the rapid decrease. Following this, TEER monitoring continued to periodically evaluate the recovery of the epithelial cell barrier for 24h. During the recovery phase, the chips were kept under continuous cell medium flow inside the incubator at 37ºC.

5.2. Results

5.2.1. Electrical sensitivity distribution with a coplanar electrode configuration in the 3D gut-on-chip

Different configurations of coplanar electrodes were designed to perform TEER quantification in the gut-on-chip device. In conventional configurations within organ-on-chips, integrated electrodes are generally placed at the top and bottom of the cell culture chamber, fully or partially hindering optical inspection of the cells during the experiment. As an alternative, placing the electrodes on the same substrate facilitates the fabrication process while also allowing real time optical imaging of the whole cell culture inside the chip [19]. Since this electrode disposition has not been previously used in hydrogel organ-on-chips, we decided to perform a preliminary validation step with a 3D finite element method (FEM) electrical simulation study. The main goal of these simulations was to assess the uniformity of the current density over the cell barrier area and to identify potential TEER measurement errors. Considering a two-point measurement system, the current density distribution was computed between the electrodes for different TEER values of the cell barrier ranging from 10^0 to 10^3 $\Omega.cm^2$. The electrical sensitivity was then calculated to quantify higher or lower contributions to the total TEER on the different regions of the barrier, as reported in previous studies [8].

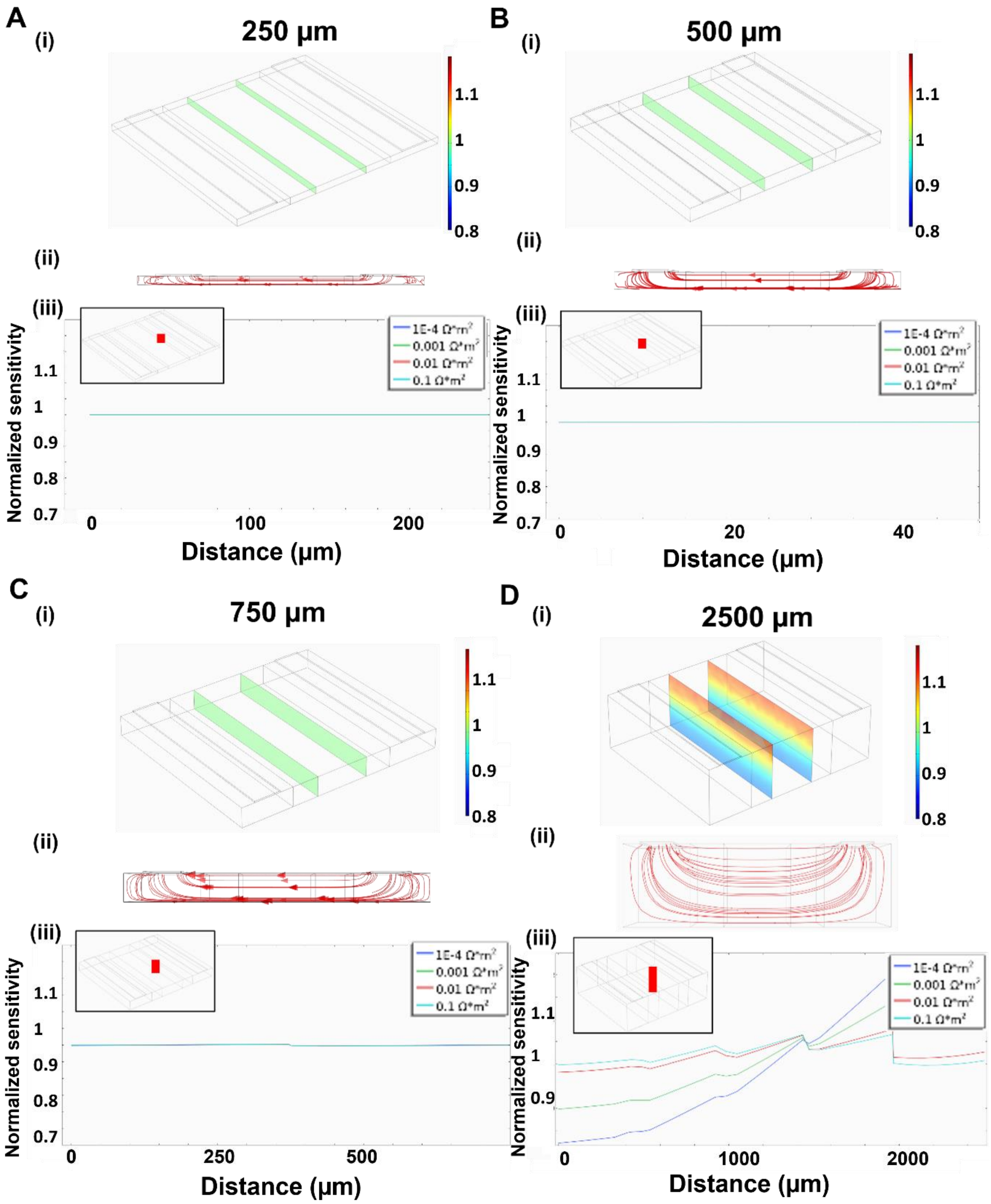

Figure 5.6: *Electrical sensitivity distribution in the central channel for a 2-electrode coplanar configuration. Simulation results for a channel height of (A) 250, (B) 500, (C) 750 and (D) 2500 µm. (i) 3D surface plot of the normalized sensitivity of the cell barriers on each side of the hydrogel channel. (ii) Side view of the current density lines across the hydrogel channel between the two electrodes. (iii) Graphs of the electrical sensitivity along the XZ plane for different TEER between 10^0 and 10^3 Ω.cm^2. The cutline used to display the values is represented in the upper left 3D drawing. All the plots and graphs were generated in COMSOL 5.6.*

A design with two coplanar electrodes placed at the lateral channels was first considered. Simulations were performed with different channel heights comprised between 250 to 750 µm to represent the dimensions of the bioprinted hydrogel channels. Within this range, the computational results showed that the normalized sensitivity was uniform and equal to 1 over the full cell barrier area for all TEER values (Figure 5.6 A, B and C). For larger hydrogel heights (> 2mm), non-uniform current distributions were observed at the hydrogel channel for TEER values below 100 $\Omega.cm^2$, with larger electrical sensitivities in the areas closer to the coplanar electrodes than the ones at the bottom (Figure 5.6 D). But these simulated heights were outside our usual range of hydrogel bioprinting sizes, thus not having a negative impact for the considered design in our applications.

As a second design, we considered a four-electrode coplanar configuration in which two small electrodes at the inlet and outlet parts of the central channel were added to the two electrodes at the lateral channels. With this configuration, it would be possible to measure the cell barrier on each side of the hydrogel channel independently. However, the computed electrical sensitivity results showed a non-uniform current distribution along the central channel length for all channel heights (Figure 5.7). Regions of the cell barrier closer to the electrodes in the central channel had a higher contribution to the overall electrical resistance than the ones in the central parts. This effect was dependent on the considered TEER: the lower the cell layer resistance, the less uniform the current density distribution was. Due to these spatial differences in electrical sensitivity, this configuration was deemed not fit to obtain accurate TEER measurements of the full cell barrier in the device. One possible solution would be to pattern an Au electrode over the full length of the central channel, but this would significantly reduce the optical access to the forming epithelial cell barrier during cell culture. Another option would be to use a semi-transparent electrode material such as PEDOT:PSS to allow independent measurements of each cell barrier in the hydrogel central channel while allowing cell visualization [20].

Overall, with these electrical simulations, we numerically validated the two-electrode configuration to obtain a uniform current density over the entire cell barrier area and to quantify accurately the TEER of the epithelial cell barrier.

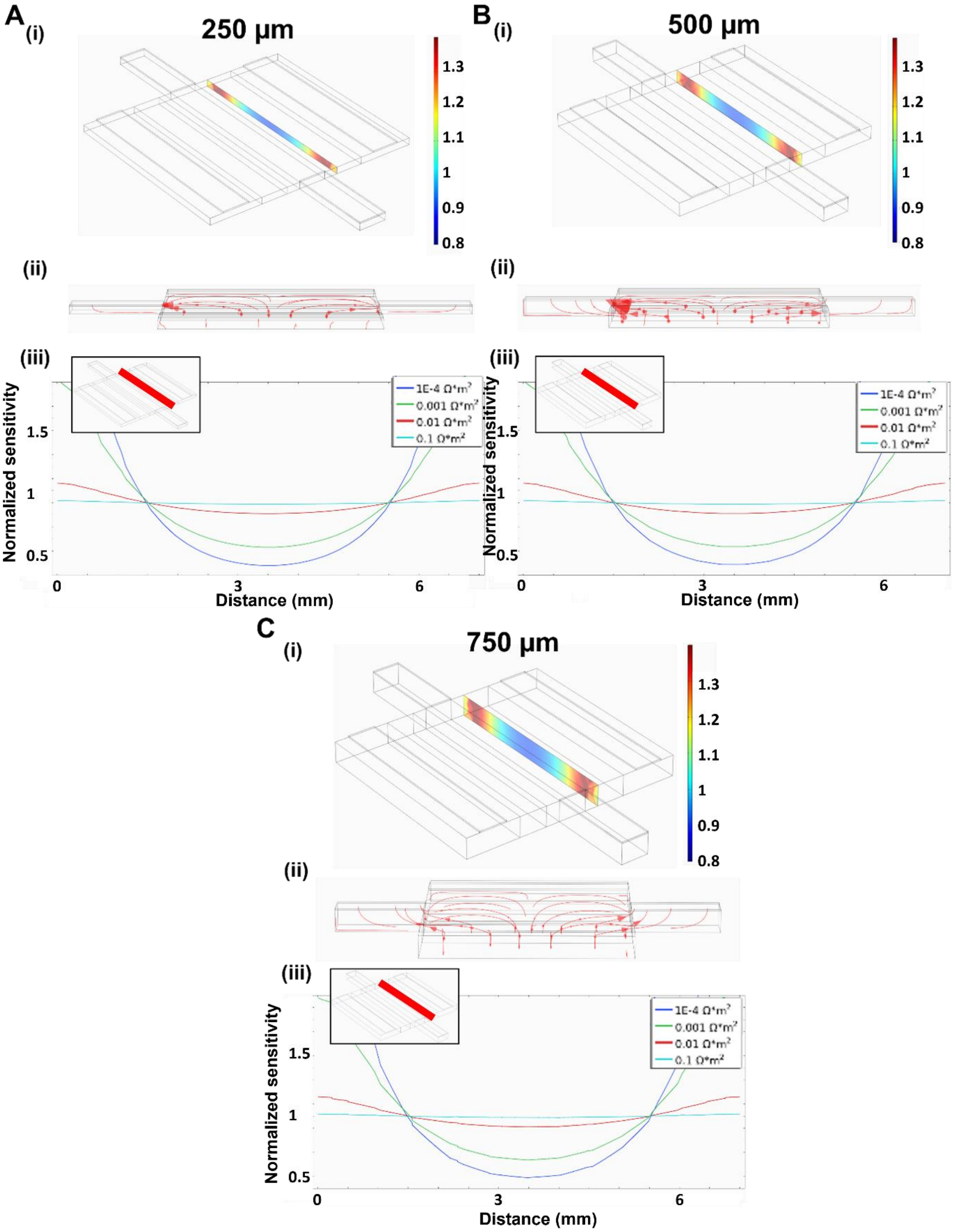

Figure 5.7: *Electrical sensitivity distribution in the central channel with a four-electrode coplanar configuration. Simulation results for a channel height of (A) 250, (B) 500, (C) 750 µm. (i) 3D surface plot of the normalized sensitivity of the cell barriers on each side of the hydrogel channel. (ii) Side view of the current density lines across the hydrogel channel between the two electrodes. (iii) Graphs of the electrical sensitivity along the XZ plane for different TEER between* 10^0 *and* 10^3 *Ω.cm*^{2}*. The cutline used to display the values is represented in the upper left 3D drawing. All the plots and graphs were generated in COMSOL 5.6.*

5.2.2. *Electrical characterization of the integrated electrodes*

After assessing their electrical sensitivity for different spatial configurations, the Au electrodes were integrated in the chip via thin film deposition, followed by a platinization of the electrodes. The effect of the platinization was evaluated by measuring the impedance of a PBS 10 mM solution via EIS and determining the cutoff frequency separating the linear regime related to the electrolyte conductivity and the non-linear regime linked to the electrode polarization impedance. As observed in Figure 5.8 A, bare Au electrodes had a significant capacitive effect in a large section of the spectrum, with a cutoff frequency close to 1 kHz. By coating the electrodes with black Pt, the polarization impedance of the Au surfaces was highly reduced, with a cutoff frequency below 10 Hz. With this approach, TEER quantification could be performed in the frequency range of interest ($10^2 – 10^5$ Hz) without the effect of electrical polarization of the electrodes.

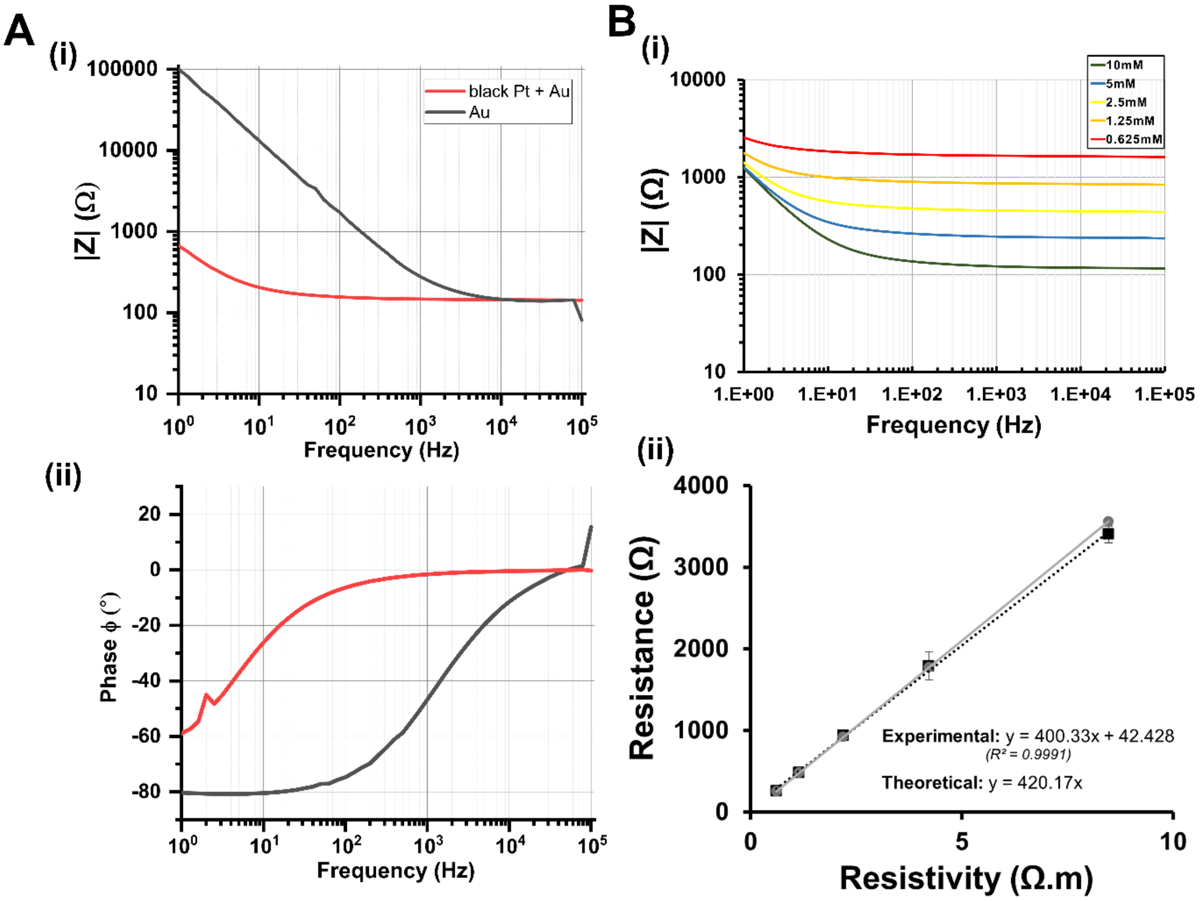

Figure 5.8: *Characterization of platinized Au electrodes. (A) Bode impedance (i) magnitude and (ii) phase plots before and after black Pt deposition. (B) Determination of the cell constant of the electrodes. (i) Bode magnitude plot for different molarities of PBS. (ii) Measured resistance vs resistivity graph to extract the cell constant as the slope of the linear curve (black dashed line) and compare it to the theoretical one (gray straight line). Values are represented as mean ± S.D. (N=3).*

Moreover, the proper functioning of the electrodes was evaluated by measuring different PBS solutions with different molarities and testing the linear response to different electrolyte resistivities (Figure 5.8 B). The cell constant of the electrodes was determined by plotting the measured electrical resistance and conductivity of each sample and extracting the slope by linear regression analysis. The obtained K_{cell} value was 400.33 m^{-1}, close to the theoretical one (420.17 m^{-1}) (Figure 5.8 B), thus indicating a homogenous distribution of the current density. With these results, we concluded that the platinized Au electrodes could measure impedances uniformly across a given cell culture area. After the electrical validation of the electrodes, the substrate was bonded to the middle part of the chip to complete the assembly and integrate them into the device for TEER measurements.

5.2.3. Assessment of epithelial barrier formation via TEER quantification in the 3D bioprinted gut-on-chip

TEER measurements were performed in real time to quantify the integrity and tightness of the intestinal epithelial barrier developed in our 3D gut-on-chip model. As proof of concept, we developed a new version of the previously described microfluidic chip with integrated electrodes to monitor the impedance of the barrier via impedance electrical spectroscopy (EIS).

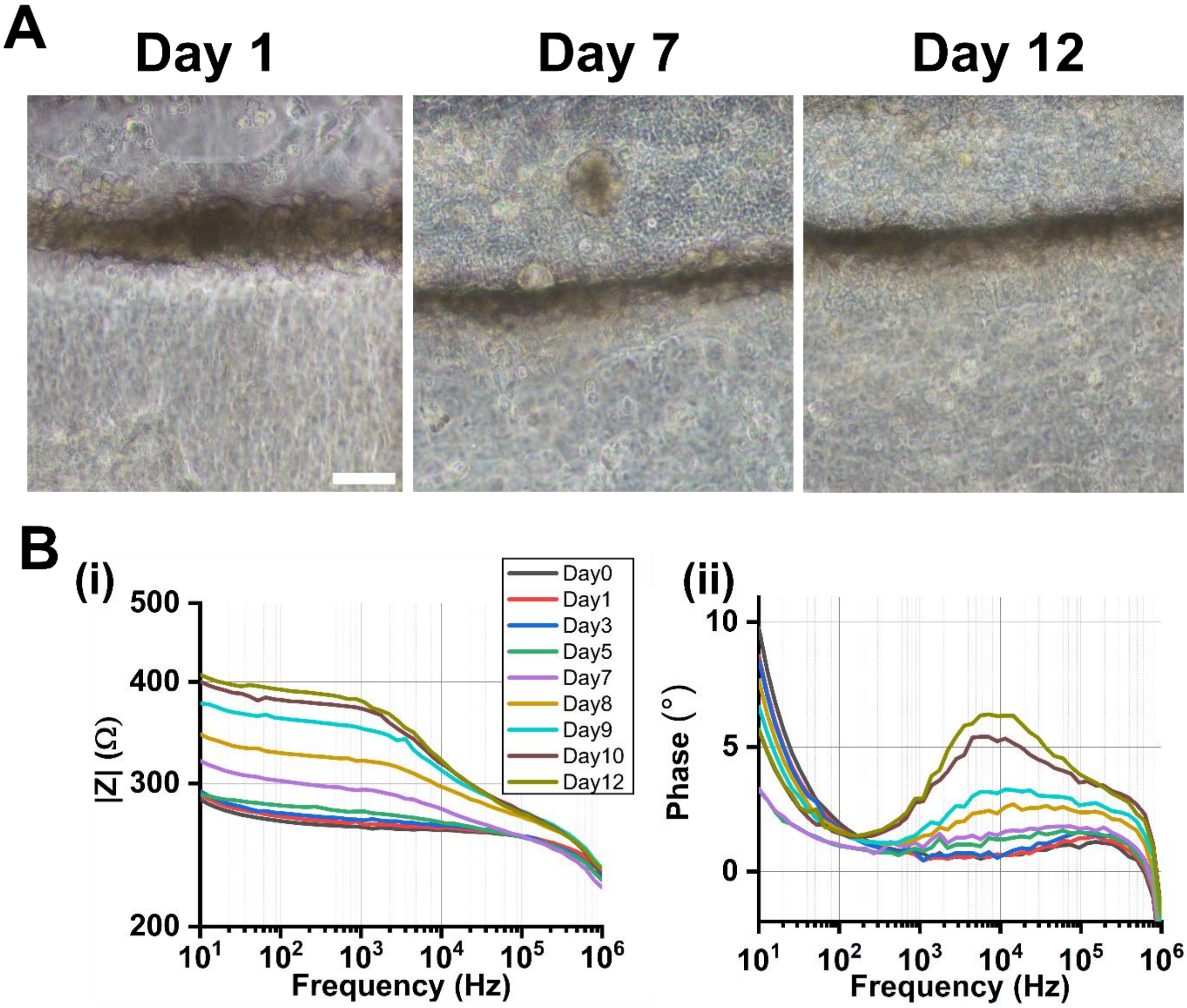

Figure 5.9: *EIS-based impedance measurements in the 3D gut-on-chip. (A) Brightfield images of the Caco-2 epithelial barrier formation in the chip with integrated electrodes at different days of cell culture. Scale bar: 100 µm. (B) Bode impedance (i) magnitude and (ii) phase plots of the forming epithelial cell barrier in the frequency range between 10 Hz and 1 MHz. From day 6 post-seeding, a significant increase in TEER can be observed up to day 12.*

Following the procedure described in chapter 4, Caco-2 cells were seeded in the central channel of the microfluidic chip with the encased 3T3 fibroblast-laden hydrogel (cell density: 7.5*10^5 cells/cm^2) and cultured under continuous cell medium perfusion for two weeks (flow rate: 5-10 µL/min). Cell impedance was measured periodically with the integrated platinized Au electrodes from the seeding of the epithelial cells (day 0) up to day 14 at different frequencies ranging from 10Hz to 1MHz. As observed in Figure 5.9 A, Caco-2 cells seeded on the rectangular-shaped hydrogel channels started to attach and expand on the lateral walls in close contact with the encapsulated 3T3 cells, forming an epithelial barrier from day 7 that reached confluency at day 12. The observed barrier formation was correlated with the measured impedances inside the chip (Figure 5.9 B). In the initial days of cell co-culture, from day 0 to day 5, the recorded impedance magnitude was flat and linked to the cell medium resistance R_s, as epithelial cells had not fully covered the hydrogel surface yet. From day 6 onwards, the total impedance increased in the lower frequencies (10^2-10^3 Hz), indicating a higher TEER as Caco-2 cells formed a tighter barrier. Also, in the middle frequencies (10^3-10^5 Hz), a significant increase was observed due to the cell layer capacitance C_{cl}, as cells covered the hydrogel surface and formed a confluent barrier. This effect was also visible in the impedance phase spectra, with a progressive phase increase in the corresponding frequencies (Figure 5.9 B).

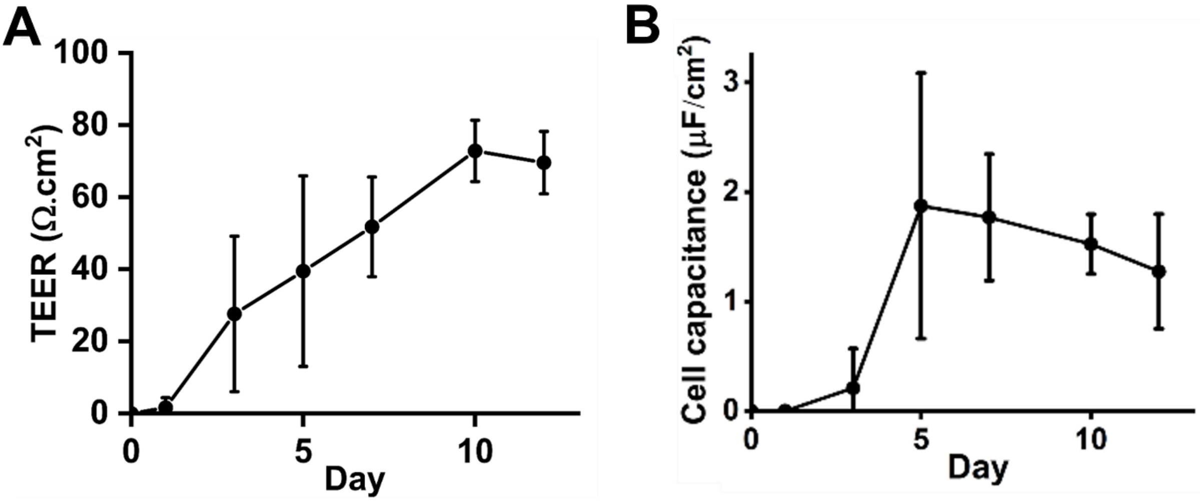

Figure 5.10: *Transepithelial electrical resistance TEER and cell layer capacitance C_{cl} quantification in the 3D gut-on-chip. (A) TEER and (B) Ccl plots of Caco-2 cell barrier. Values are represented as mean ± S.D. (N=3).*

Applying an equivalent electrical model on the impedance magnitude plots within the 10^2-10^5 Hz frequency range, TEER and cell capacitance C_{cl} values of the epithelial barrier were extracted for different days of cell culture on-chip (Figure 5.10). As shown by the electrical sensitivity simulations, current density distribution was uniform across the hydrogel walls of the channel for the selected electrode configuration, thus allowing normalization of the cell layer resistance by the total area. During the first days of cell co-culture, TEER values were low, with a slow increase up to 20 Ω.cm^2. From day 5-6, TEER increased faster as cells were forming a barrier, reaching values up to 80 Ω.cm^2 at day 12, similar to *in vivo* measurements of the native small intestine (Figure 5.10 A) [21,22]. After more than two weeks under cell medium flow, epithelial cells would start detaching from the hydrogel in certain regions of the channel, with a subsequent decrease of TEER (data not shown). This trend of cell barrier resistance increase is consistent with previous intestinal *in vitro* studies based on stromal-cell laden 3D hydrogels, where a boost in TEER was observed at day 9-11, coinciding with the time the fibroblasts needed to migrate towards the surface of the hydrogel and to secrete ECM proteins for epithelial cell attachment [23]. Moreover, the cell capacitance also increased significantly within the first week of cell culture on-chip, as cells gradually covered the hydrogel surface (Figure 5.10 B). After the first 7 days, C_{cl} reached a plateau, with values close to 2 μF/cm^2. Cell capacitance in mature barriers is constant and close to 1 μF/cm^2 for flat cell monolayers. Higher values in epithelial intestinal models with Caco-2 cells have also been reported and attributed to an increased cell surface by cell polarization and formation of microvilli at the apical brush border. Hence, these results could also suggest Caco-2 cells formed a polarized barrier in our 3D gut-on-chip model. Further characterization of epithelial cell polarization via immunofluorescence staining of key markers such as villin-2 could confirm this hypothesis.

5.2.4. Recovery of the epithelial barrier function after barrier disruption

As a next step on the validation of the electrical monitoring in our gut-on-chip system, a barrier disruption assay was performed to induce the rupture and recovery of the epithelial barrier in our 3D gut-on-chip via TEER quantification. To do this, the calcium ion chelating agent EDTA was perfused into the central channel for 5 min after 12 days of dynamic cell co-culture, causing a transient breakdown of the tight junctions in the Caco-2 cell barrier followed by a recovery of the barrier function over time. This rupture translated into an increased cell barrier permeability and a reduced cell layer resistance, as observed in the recorded impedance spectra (Figure 5.11 A). Preliminary results showed a rapid drop of more than 30% in TEER 20 min after EDTA exposure, consistent with other gut-on-chip models (Figure 5.11 B) [1]. Once EDTA-free cell medium was perfused again, a slow recovery could be observed up to 24h. Further work on the disruption and recovery of the epithelial barrier within the 3D gut-on-chip model could confirm the ability of the system to follow-up permeability changes in real time.

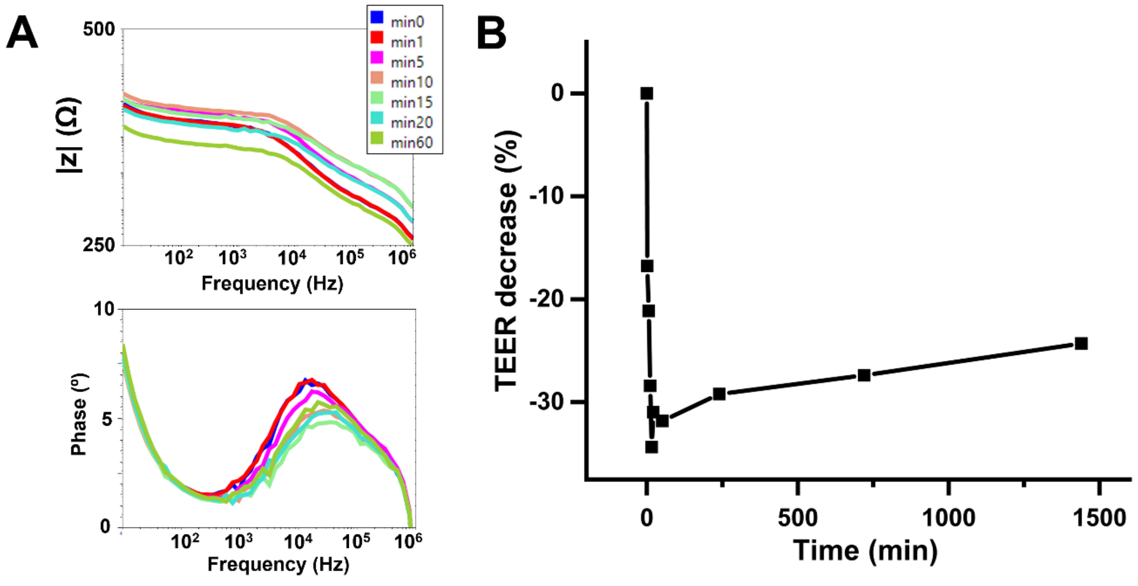

Figure 5.11: *TEER quantification during a barrier disruption assay in the 3D hydrogel gut-on-chip. (A) Bode impedance (i) magnitude and (ii) phase plots after EDTA adding and cell barrier recovery. (B) Percentage of TEER decrease compared to the initial value over time.*

5.3. Discussion

Over these last years, electrodes have been introduced in organ-on-chip systems to monitor the integrity of tissue barriers in real time via TEER measurements. In the case of gut-on-chips, a common approach has consisted in placing metal wires inside the chip to record the electrical resistance of the studied epithelial barrier [5,24]. But inserting these electrodes inside the device can induce potential measurement errors as non-uniform current densities can arise from their location and placement [8,25]. Alternatively, some groups have integrated thin film electrodes within microfluidic platforms to obtain more reliable TEER measurements [1,9]. However, these devices are based on stiff membranes that cannot replicate the 3D structure of the intestinal mucosa. In this work and for the first time, a hydrogel gut-on-chip with real time TEER sensing capabilities has been developed by integrating thin film Au electrodes inside the device. With our chip, a significant and progressive increase of the TEER linked to the formation of the epithelial barrier under flow conditions was recorded via EIS for 2 weeks, with values close to the *in vivo* ranges. This trend of TEER increase matched previous observations in static conditions with the same bioink, where hydrogel-embedded fibroblasts migrated towards the hydrogel surface to promote epithelial cell attachment and barrier formation after more than one week of cell co-culture [23]. It is worth mentioning that the maximum values of TEER in our hydrogel gut-on-chip were lower than in the static model, where TEER reached 250 $\Omega.cm^2$ after two weeks. Further investigation of the effect of flow on the tightness of the cell barrier could elucidate the reasons for this difference between models. Moreover, an increase of cell layer capacitance was monitored over time. Interestingly, the obtained high capacitance values could suggest the presence of a polarized epithelial barrier due to an increased cell membrane surface [9]. Moreover, unlike standard approaches where electrodes are placed at the top and bottom of the cell culture area, the coplanar configuration of our electrodes ensured both clear optical imaging of the epithelial cells and hydrogel-encapsulated fibroblasts, along with uniform current densities for accurate electrical readouts. The presented system is highly versatile as it can be adapted to other tissue barriers *in vitro* to quantitatively assess their properties in real time, with potential applications in drug screening studies.

5.4. References

1. Henry, O. Y. F. *et al.* Organs-on-chips with integrated electrodes for trans-epithelial electrical resistance (TEER) measurements of human epithelial barrier function. *Lab Chip* **17**, 2264–2271 (2017).
2. Nicolas, A. *et al.* High throughput transepithelial electrical resistance (TEER) measurements on perfused membrane-free epithelia. *Lab Chip* **21**, 1676–1685 (2021).
3. Tan, H. Y. *et al.* A multi-chamber microfluidic intestinal barrier model using Caco-2 cells for drug transport studies. *PLoS One* **13**, e0197101 (2018).
4. Yeste, J., Illa, X., Guimerà, A. & Villa, R. A novel strategy to monitor microfluidic in-vitro blood-brain barrier models using impedance spectroscopy. in *Bio-MEMS and Medical Microdevices II* vol. 9518 95180N (SPIE, 2015).
5. Odijk, M. *et al.* Measuring direct current trans-epithelial electrical resistance in organ-on-a-chip microsystems. *Lab Chip* **15**, 745–752 (2015).
6. Grimnes, S. & Martinsen, Ø. G. Sources of error in tetrapolar impedance measurements on biomaterials and other ionic conductors. *J Phys D Appl Phys* **40**, 9–14 (2007).

7. Yeste, J. *et al.* A perfusion chamber for monitoring transepithelial NaCl transport in an in vitro model of the renal tubule. *Biotechnol Bioeng* **115**, 1604–1613 (2018).
8. Yeste, J. *et al.* Geometric correction factor for transepithelial electrical resistance measurements in transwell and microfluidic cell cultures. *J Phys D Appl Phys* **49**, (2016).
9. van der Helm, M. W. *et al.* Non-invasive sensing of transepithelial barrier function and tissue differentiation in organs-on-chips using impedance spectroscopy. *Lab Chip* **19**, 452–463 (2019).
10. Edström, H. Porous Gold Surfaces for Implantable Neural Electrodes. **XXI**, (2014).
11. Koklu, A., Sabuncu, A. C. & Beskok, A. Rough Gold Electrodes for Decreasing Impedance at the Electrolyte/Electrode Interface. *Electrochim Acta* **205**, 215–225 (2016).
12. Gabriel, G. *et al.* Manufacturing and full characterization of silicon carbide-based multi-sensor micro-probes for biomedical applications. *Microelectronics J* **38**, 406–415 (2007).
13. Grimnes, S. & Martinsen, Ø. G. Bioimpedance and Bioelectricity Basics. *Bioimpedance and Bioelectricity Basics* (2008) doi:10.1016/B978-0-12-374004-5.X0001-3.
14. Gerasimenko, T. *et al.* Impedance Spectroscopy as a Tool for Monitoring Performance in 3D Models of Epithelial Tissues. *Front Bioeng Biotechnol* **7**, (2020).
15. Deli, M. A. Potential use of tight junction modulators to reversibly open membranous barriers and improve drug delivery. *Biochimica et Biophysica Acta (BBA) - Biomembranes* **1788**, 892–910 (2009).
16. Tomita, M., Hayashi, M. & Awazu, S. Absorption-enhancing mechanism of EDTA, caprate, and decanoylcarnitine in Caco-2 cells. *J Pharm Sci* **85**, 608–611 (1996).
17. Han, X. *et al.* Biomaterial–tight junction interaction and potential impacts. *J Mater Chem B* **7**, 6310–6320 (2019).
18. Noach, A. B. J., Kurosaki, Y., Blom-Roosemalen, M. C. M., de Boer, A. G. & Breimer, D. D. Cell-polarity dependent effect of chelation on the paracellular permeability of confluent caco-2 cell monolayers. *Int J Pharm* **90**, 229–237 (1993).
19. Yeste, J. *et al.* A compartmentalized microfluidic chip with crisscross microgrooves and electrophysiological electrodes for modeling the blood-retinal barrier. *Lab Chip* **18**, 95–105 (2018).
20. Marrero, D. *et al.* Organ-on-a-chip with integrated semitransparent organic electrodes for barrier function monitoring. *Lab Chip* (2023) doi:10.1039/D2LC01097F.
21. Biological Transport Phenomena in the Gastrointestinal Tract: Cellular Mechanisms. *Transport Processes in Pharmaceutical Systems* 163–200 (1999) doi:10.1201/9780203909478-9.
22. Sjöberg, Å. *et al.* Comprehensive study on regional human intestinal permeability and prediction of fraction absorbed of drugs using the Ussing chamber technique. *European Journal of Pharmaceutical Sciences* **48**, 166–180 (2013).
23. Torras, N. *et al.* A bioprinted 3D gut model with crypt-villus structures to mimic the intestinal epithelial-stromal microenvironment. *Biomaterials Advances* **153**, 213534 (2023).
24. Shah, P. *et al.* A microfluidics-based in vitro model of the gastrointestinal human-microbe interface. *Nat Commun* **7**, (2016).
25. Vigh, J. P. *et al.* Transendothelial electrical resistance measurement across the blood–brain barrier: A critical review of methods. *Micromachines (Basel)* **12**, 685 (2021).

Conclusions

3D hydrogel gut-on-chip models have recently become a promising alternative to conventional membrane-based systems as they can combine microfluidics and ECM-like scaffolds to generate a more biomimetic microenvironment for intestinal cells under dynamic conditions. However, most of these models are based on cumbersome procedures and expensive equipment that limit their potential applications in the field. To overcome these limitations, a 3D bioprinted gut-on-chip model has been presented in this PhD thesis. The system consists of a perfusable hydrogel channel containing villi-like structures that can support a multicellular *in vitro* model of the intestinal mucosa. Specific conclusions are listed below:

1. To generate the 3D hydrogels, a customized visible-light DLP printing setup was used with a photosensitive bioink, composed of PEGDA and GelMA. For the bioprinting process, a set of optimal printing parameters was selected to obtain hydrogel channels with lateral villi-like features that had similar dimensions to the ones found *in vivo*.

2. As this bioprinting technique has been proven cell-friendly, stromal cells were embedded in the hydrogel substrate for cell culture on-chip. After several days under fluid flow, the encapsulated cells showed high cell viability rates, with an observed migration towards the surfaces of the hydrogels.

3. A multicellular model of the intestinal mucosa was developed inside the chip for which epithelial cells were seeded on the central channel, and co-cultured with the embedded fibroblasts for two weeks under continuous perfusion. The device could support an intestinal barrier in direct contact with the hydrogel-embedded stromal cells for several weeks under dynamic conditions, showed by both permeability assays and immunostainings.

4. The proposed hydrogel gut-on-chip was also adapted for real time TEER monitoring by integrating electrodes inside the device. The formation of the intestinal epithelial barrier was monitored with real time TEER measurements for two weeks, showing a significant and progressive increase of the cell layer impedance over time.

In summary, I have developed a hydrogel-based and electrode-integrated 3D bioprinted gut-on-chip model that recapitulates cell-cell interactions of the intestinal stroma and epithelia in a physiologically relevant manner while also providing real time measurements of the intestinal barrier integrity. This system is highly versatile as it can potentially be adapted to other tissue barriers *in vitro* such as the brain-blood barrier or the renal tubule to quantitatively assess drug effectiveness for therapeutical research.

List of publications

[1] Vera, D., García-Díaz, M., Torras, N., Álvarez, M., Villa, R., & Martinez, E. (2021). Engineering Tissue Barrier Models on Hydrogel Microfluidic Platforms. In *ACS Applied Materials and Interfaces* (Vol. 13, Issue 12, pp. 13920–13933). American Chemical Society. https://doi.org/10.1021/acsami.0c21573

[2] Marrero, D., Pujol-Vila, F., **Vera, D**., Gabriel, G., Illa, X., Elizalde-Torrent, A., Alvarez, M., & Villa, R. (2021). Gut-on-a-chip: Mimicking and monitoring the human intestine. *Biosensors and Bioelectronics*, *181*, 113156. https://doi.org/10.1016/J.BIOS.2021.113156

[3] Vera, D., García-Díaz, M., Torras N., Castaño O., Villa, R., Álvarez M., Martinez E. (2023) A 3D bioprinted hydrogel gut-on-chip with integrated electrodes for trans-epithelial electrical resistance (TEER) measurements, (***submitted***)